

**Catalysis by Design Using Surface Organometallic Nitrogen-Containing
Fragments**

Dissertation by
Bilel Hamzaoui

In Partial Fulfillment of the Requirements
For the Degree of
Doctor of Philosophy

King Abdullah University of Science and Technology
Thuwal, Kingdom of Saudi Arabia, 2016

© May 2016
Bilel Hamzaoui
All Rights Reserved

The dissertation of Bilel Hamzaoui is approved by the examination committee:

Committee Chairperson: Pr. Jean Marie Basset

Committee Member: Pr. Didier Astruc

Committee Member: Pr. Kazuhiro Takanabe

Committee Member: Pr. Mani M. Sarathy

ABSTRACT

Catalysis by Design Using Surface Organometallic Nitrogen-Containing Fragments

Bilel Hamzaoui

The aim of this thesis is to explore the chemistry of well-defined silica-supported group 4 and group 5 complexes that contain one or more multiply-bonded nitrogen atoms. Such species have been recognized as crucial intermediates in many catalytic reactions (e.g. hydroaminoalkylation, olefin hydrogenation, imine metathesis...). The first chapter provided a bibliographic overview of the preparation and the reactivity of group 4 and 5 complexes towards hydroaminoalkylation and imine metathesis catalysis.

The second chapter deals with the isolation and the characterization of a series of well-defined group 4 η^2 -imine complexes surfaces species. 2D solid-state NMR (^1H - ^{13}C HETCOR, Multiple Quantum) experiments have revealed consistently a unique structural rearrangement, viz azametallacycle occurring on the immobilized metal-amido ligands. Hydrogenolysis of the sole Zr-C bond in such species gives selectively a silica-supported zirconium monohydride that can perform the catalytic hydrogenation of olefins.

The third chapter examines the mechanistic studies of the intermolecular hydroaminoalkylation using SOMC to identify the key metallacyclic surface intermediates (silica-supported three-membered and five-membered). The catalyst was regenerated by protonolysis and afforded pure amine. Catalytic testing of a selection of amine compounds with variable electronic properties was carried out.

The fourth chapter deals with the generation and the characterization of well-defined silica-supported zirconium-imido complexes. The resulting species effectively catalyzes imine/imine cross-metathesis and thus considered as the first heterogeneous catalysts active for imine metathesis reaction.

The fifth chapter studies the reaction of SBA₁₅₋₁₁₀₀ with dry aniline and derivatives leading to opening strained siloxane bridges into acid-base paired functionalities (formation of N-phenylsilanamine-silanol pairs). This approach was successfully applied to the design of a series of aniline derivatives bifunctional SBA₁₅. The efficiency of this methodology is strongly supported and unambiguously highlighted by strong solid state characterizations: FT-IR, 1D and 2D solid state NMR spectroscopy and even dynamic nuclear polarization enhanced ²⁹Si and ¹⁵N, XRD and TEM... Importantly, a plethora of well-organized bifunctional catalysts with different electronic properties were successfully synthesized and tested in the Knoevenagel condensation.

ACKNOWLEDGEMENTS

There are many people who I would like to thank who have helped me during my graduate studies. First and foremost, I would like to thank my supervisor, Pr. Jean Marie Basset, for giving me the opportunity to be a part of his research group. Your support and mentorship have significantly contributed to my growth as a chemist. The skills that I have gained by being a member of the Basset group are invaluable and will certainly help in my career path.

I would like to thank my committee members, Pr. Didier Astruc, Pr. Kazuhiro Takanabe, and Pr. Mani M. Sarathy, for their guidance and support throughout the course of this research.

Special thanks to Dr. Jeremie Pelletie, Dr. Anissa Bendjeriousedjerari and Dr. Yin Chen; without their timely guidance and learned suggestions it would have been difficult to see the successful completion of this work.

Much of the work in this project would not have been possible without the technical expertise of Dr. Edy Abuhamad for solid state NMR and Dr. Edrisse Chermak for DFT calculations.

I feel blessed to have worked with the past and present members of the Basset group during my graduate studies. It has been a truly rewarding experience to be a part of an engaging team to share ideas and hobbies together. I have learnt so much from you all. I want to extend a special thanks to Ali Hamieh, Baraa Werghi, Ghodhbane

Myriam, Aya Saidi, Reem Alshareef, Dr.Mohamad El Eter, Dr.Raju Dey, Dr.Eva B. Pump
and Dr. Jullian Vittenet

I would also like to acknowledge other members in the group, Hind Al- Johani,
Gabriel Jeantelot, Dr.Julien SofackKreutzer, Bertrand Rosmade, Dr.Manoja Samantaray,
Dr.Samy Ould Chikh, Claudia Carraro, Dr. Janet C Mohandas, Dr. Michael J. Kelly and Dr.
Ziyauddin Qureshi.

Finally, a deep thank you to my family for their love, support, and encouragement. I
could not have done this without you.

TABLE OF CONTENTS

ABSTRACT.....	3
ACKNOWLEDGEMENTS.....	5
TABLE OF CONTENTS.....	7
LIST OF SYMBOLS and ABBREVIATIONS.....	11
LIST OF ILLUSTRATIONS.....	13
LIST OF TABLES.....	17
Chapter 1: Bibliography	18
1.1 Introduction	18
1.2 Introduction to Surface organometallic chemistry.....	18
1.2.1 Surface organometallic chemistry on Silica	19
1.2.2 Catalysis by design: Surface Organometallic fragments.....	22
1.2.3 Towards new surface organometallic fragment?	24
1.3 Early Transition Metal- η^2 -imine Complexes	25
1.3.1 Synthetic pathway to group 4 and 5 metal- η^2 -imine complexes (metallaaziridines)..	26
1.3.2 Intramolecular C–H activation in metal methyl amide complexes.....	26
1.3.4 Rearrangement of the product of isocyanide.....	33
1.4 Reactivity of metallaaziridines.....	34
1.4.1 Zirconaaziridines	34
1.4.3 Tantalaaziridines	37
1.4.2 Titanaaziridines.....	38
1.4.4 Intermolecular hydroaminoalkylation of unactivated Alkenes	40
1.5 Imido complexes.....	45
1.6 Conclusions and thesis organization.....	48
1.6.1 Summary of the present chapter	48
1.6.2 Thesis organization	49
1.7 References	51
Chapter 2: Isolation of Silica-Supported Metallaaziridines and Generation of Well-Defined Single-Site Monohydride Zirconium Species	55
2.1 Introduction	55
2.1.1 Metal-amides complexes and surface organometallic chemistry	55
2.1.2 Silica-supported zirconium-hydride complexes.....	56
2.2 Scope of the chapter.....	59

2.3 Grafting of tetrakis-dimethylamide group 4 complexes on silica supports.....	61
2.3.1 Characterization of tetrakis-dimethylamide group 4 complexes on silica supports	61
2.3.1.1 Infrared characterization and elemental analysis	61
2.3.1.2 SS NMR characterization.....	67
2.3.1.3 EXAFS characterization	74
2.4 Silica-supported mono hydride zirconium complexes.....	76
2.4.1 FTIR Characterization and elemental analysis	76
2.4.2 SS NMR characterization.....	77
2.4.3 Catalytic testing for olefin hydrogenation	80
2.5 Conclusions	85
2.6 Experimental.....	87
2.6.1 General.....	87
2.6.2 Preparation procedures	89
2.6.3 EXAFS experiment.....	92
2.7 References	95
Chapter 3: Catalytic Intermediates Isolation and Mechanistic Studies for Heterogeneous Hydroaminoalkylation Reaction.....	97
3.1 Introduction	97
3.1.1 Alkene hydroaminoalkylation	97
3.1.2 Reactivity of zirconaaziridines	100
3.2 Scope of the chapter	101
3.3 Isolation and characterization of silica-supported azazirconacyclopentane intermediate	104
3.3.1 FTIR and elemental analysis.....	104
3.3.2 Solid state NMR experiments	105
3.3.3 Reactivity Studies	111
3.4 Synthesis of well-defined silica-supported tantalaaaziridines and application on catalytic hydroaminoalkylation	112
3.4.1 Synthesis and characterization of silica-supported tetra-dimethylamido tantalum complex.....	112
3.4.2 Synthesis and characterization of silica-supported tantalaaaziridine	115
3.4.3 Easy formation of tantaallaziridine by substituting NMe-alkyl ligand with NMe-Phenyl	118
3.4.4 Mechanistic study by DFT Calculations of tantalaaaziridines formation.....	121
3.5 Alkene Hydroaminoalkylation Catalytic Studies	124
3.5.1 Catalytic hydroaminoalkylation using II.6.....	124

3.5.2 Catalytic hydroaminoalkylation using III.2 - III.4.....	128
3.5.3 Catalytic hydroaminoalkylation conclusions.....	130
3.5 Conclusions	131
3.6 Experimental Section	132
General.....	132
Synthesis procedures	132
Computational Details	134
SS NMR details	135
3.7. References	137
Chapter 4. Imine Metathesis Catalysed by Well-Defined Silica-Supported Zirconium-Imido Complexes.....	139
4.1 Introduction	139
4.2 Scope of the chapter.....	140
4.3 Results and Discussions	142
4.3.1 Grafting of $Zr(NEt_2)_4$ on SiO_{2-700}	142
4.3.2 Formation of the zirconium-imido surface	145
4.3.3 Imide/imine stoichiometric metathesis reaction	147
4.3.3 Imine/imine catalytic metathesis reaction	150
4.3.4 Catalyst regeneration.....	152
4.4 Conclusion.....	153
5.5 Experimental.....	155
General.....	155
Preparation procedures.....	155
Details of the SS NMR spectra	156
4.6 References	158
Chapter 5. Atomic-Level Organization of Vicinal Acid-Base Pairs through the Chemisorption of Aniline and Derivatives onto Mesoporous SBA15	159
5.1 Introduction	159
5.2 Scoop of the chapter.....	161
5.3 Results and discussion	163
5.3.1 Reaction of $SBA15_{1100}$ with aniline.....	163
5.3.2 FT-IR characterization of the aniline modified SBA15	163
5.3.3 NMR characterization of the aniline modified SBA15 and silsesquioxane	164
5.3.4 Dynamic Nuclear Polarisation (DNP) characterization of the aniline modified SBA15.....	170
5.3.5 Textural characterization of the aniline modified SBA15	172

5.3.6 Catalytic behavior for the Knoevenagel condensation	175
5.3.7 Stability of the catalysts	180
5.4 Conclusion	183
5.5 Experimental	183
5.5.1 DNP-solid state NMR.....	183
5.5.2 Transmission Electron Microscopy (TEM).....	184
V.5.3 Preparation of V.1 (impregnation method).....	184
5.5.4 Preparation of N-phenylsilylanamine silsesquioxane V.4.....	184
5.5.6 Catalytic performances for Knoevenagel reaction	185
5.5.7 Determination of the surface coverage.....	185
5.6 References	187
Appendix A: Selected NMR spectra	189
Appendix B: Selected GC-MS spectra.....	192
Appendix C: DFT calculated energies, frequencies, rate constants and optimized coordinates.	195
LIST OF PUBLICATIONS.....	208

LIST OF SYMBOLS and ABBREVIATIONS

Symbol /abbreviation	Definition
Ar	Aromatic
BET	Brunauer, Emmett, Teller
CP/MAS	Cross Polarization/ Magic Angle Spinning
DCM	DiChloroMethane
eq.	equivalent
Et	Ethyl
EXAFS	Extended X-Ray Absorption Fine Structure
GC	Gas Chromatography
h	hour(s)
<i>i</i> Bu	isobutyl
IR	Infra-Red
Me	Methyl
mg	milligram(s)
MHz	megahertz
min	minute(s)
mL	milliliter(s)
mmol	millimole(s)
mol	mole(s)
Mw	weight average molecular weight
NMR	Nuclear Magnetic Resonance
Np	Neopentyl (-CH ₂ C(CH ₃) ₃)
Ph	Phenyl
POSS	PolySilSesquioxane
ppm	part per million
Pr	Propyl

rt	room temperature
SBA	Santa Barbara Amorphous
SOMC	Surface Organo Metallic Chemistry
<i>t</i> Bu	<i>tert</i> butyl
<i>T</i>	temperature
TEM	Transmission Electronic Microscopy
TEOS	TetraOrthoSilicate
TOF	Turn Over Frequency
TON	Turn Over Number
XRD	X-Ray Diffraction
°	degree
δ	chemical shift
η	hapticity

LIST OF ILLUSTRATIONS

Figure 2.1: In situ FTIR difference spectra of (a) self-supporting SBA ₁₅₋₇₀₀ pellet and (b) after reaction with Ti(NMe ₂) ₄ and (C) after reaction with Zr(NMe ₂) ₄ and (d) after reaction with Hf(NMe ₂) ₄	62
Figure 2.2: In situ FTIR difference spectra of (a) self-supporting SiO ₂₋₇₀₀ pellet and (b) after reaction with Ti(NMe ₂) ₄ and (C) after reaction with Zr(NMe ₂) ₄ and (d) after reaction with Hf(NMe ₂) ₄	62
Figure 2.3: FTIR of deuterated SiO ₂₋₇₀₀ (pink) and after reaction with Zr(NMe ₂) ₄ (red)	64
Figure 2.4: FTIR of SiO ₂₋₇₀₀ treated with Zr(NMe ₂) ₄ , t ₀ (purple) after 1 hour (black), 2 hour (red) and 3 hour (blue). The spectral width has been reduced to show the NH vibration range (3150 to 3500 cm ⁻¹).	64
Figure 2.5: FTIR of SiO ₂₋₇₀₀ treated with dimethyl amine then evacuated under vacuum (10 ⁻⁴ mbar) after 1 min (pink), 15 min (blue), 30 min (red) and 18 hrs (black).	66
Figure 2.6: ¹⁵ N CP/MAS NMR spectra of II.6.	73
Figure 2.7: Imaginary parts of the back Fourier transform (left) and Fourier transforms (right) of the EXAFS k ₂ .χ(k) functions for compound II.1. The solid lines are the experimental data while the dotted lines are the fit results obtained within a k-range between 4 and 14 Å ⁻¹ and within an R-range of 1 up to 2.8 Å. (phase shift not corrected)	74
Figure 2.8: FTIR of II.6 (red), 2 (black), and 2-1 (pink).	76
Figure 2.9: (a) ¹ H SS NMR of II.6, (b) ¹³ C SS NMR spectra of II.6, (c) ¹ H SS NMR of II.9 and (d) ¹³ C SS NMR spectra of II.9.	78
Figure 2.10: Two-dimensional (2D) ¹ H- ¹ H double-quantum (DQ)/Single-quantum (SQ) of II.9	79
Figure 2.11: ¹⁵ N CP/MAS NMR spectra of II.6 and II.9	80
Figure 2.12: Conversion vs. time of ethylene to ethane using II.9/H ₂ /150°C	82
Figure 2.13: N ₂ adsorption of SBA ₁₅₍₇₀₀₎ and II.1.	91
Figure 2.14: XRD Pattern of SBA ₁₅₍₇₀₀₎ and II.1.	91
Figure 2.15: Imaginary part of the back Fourier transform (left) and Fourier transforms (right) of the EXAFS k ₃ .χ(k) functions for a Zr foil reference. The solid lines are the experimental data while the dash lines are the fit results obtained within a k-range between 4 and 14 Å ⁻¹ and within an R-range of 1.8 up to 3.9 Å	93
Figure 3.16: FTIR spectra of a) II.6 b) III.1 c) III.1 after treatment with HNMe ₂ (0.8 bar) at 150°C for 20 h followed by evacuation (10 ⁻⁴ mbar) overnight d) III.1 after evacuation (10 ⁻⁴ mbar) and heating at 150°C for 20 h.	105
Figure 3.17: ¹ H SS NMR and ¹³ C SS NMR spectra of II.6 and III.1	106
Figure 3.18: (A) ¹ H MAS NMR of III.1. (B) and (C) 2D contour plots of the aliphatic region of the DQ and TQ proton SS-NMR correlation spectra of III.1 (see experimental part for details).	107
Figure 3.19: (A) 1D ¹³ C CP/MAS NMR (B) 2D contour plot of the aliphatic region of ¹ H ¹³ C HETCOR NMR spectrum of III.1 (see experimental part for details).	108
Figure 3.20: (A) 1D ¹³ C CP/MAS NMR (B) 2D contour plot of the aliphatic region of ¹ H ¹³ C HETCOR NMR spectrum of III.1 on SBA ₁₅₋₇₀₀ (see experimental part for details)	109
Figure 3.21: 2D ¹³ C ¹³ C spin-diffusion with DARR of (III.1) (see experimental part for details).	111
Figure 3.22: GC-FID Chromatogram of (a) gas mixture after reaction of HNMe ₂ and III.1 (b) N,2-dimethylpropan-1-amine (c) HNMe ₂	112
Figure 3.23: FTIR of SiO ₂₋₇₀₀ , III.2 [≡Si-O-Ta(NMe ₂) ₄], III.3 [≡Si-O-Ta(η ² NMeCH ₂)(NMe ₂) ₂] and III.4 [≡Si-O-Ta(η ² NPhCH ₂)(NMe ₂) ₂].	113
Figure 3.24: ¹ H SS NMR of III.2.	114
Figure 3.25: ¹³ C SS NMR of III.2.	115
Figure 3.26: (A) 1D ¹ H spin-echo MAS solid state NMR spectrum of III.3, (B) ¹³ C CP/MAS NMR spectrum of III.3 (C) 2D ¹ H- ¹ H double-quantum (DQ)/single-quantum (SQ), (D) ¹ H- ¹ H triple-quantum (TQ)/SQ and (E) 2D CP/MAS HETCOR NMR spectrum.	118
Figure 3.27: (A) 1D ¹ H spin-echo MAS solid state NMR spectrum of III.4, (B) ¹³ C CP/MAS NMR spectrum of III.4 (C) 2D ¹ H- ¹ H double-quantum (DQ)/single-quantum (SQ), (D) ¹ H- ¹ H triple-quantum (TQ)/SQ and (E) 2D CP/MAS HETCOR NMR spectrum.	120

Figure 3.28: DFT reaction profiles for the transformation of III.2 into III.3 or III.4.	123
Figure 3.29: GC-FID Chromatogram of (a) HNMe ₂ and (b) gas mixture after first reaction of HNMe ₂ and III.1 (c) second reaction (d) third reaction.	126
Figure 3.30: FTIR of a) SiO ₂₋₇₀₀ . b) After treating the SiO ₂₋₇₀₀ with HNMe ₂ and - propanamine,N,2-dimethyl, dimethylamine and hydrogen at 150°C during 20h then evacuating (10 ⁻⁴ mbar) over night at 150°C.	127
Figure 4.31: FTIR of SiO ₂₋₇₀₀ , IV.1 [≡Si-O-Zr(NEt ₂) ₃], IV.2 [≡Si-O-Zr(=NEt)NEt ₂] and IV.3 [≡Si-O-Zr(=NPh)NEt ₂].	143
Figure 4.32: (A) 1D ¹ H spin-echo MAS SS NMR spectrum of IV.1, (B) ¹³ C CP/MAS NMR spectrum of IV.1.	144
Figure 4.33: (A) 1D ¹ H spin-echo MAS SS NMR spectrum of IV.1, (B) ¹³ C CP/MAS NMR spectrum of IV.1. (C) 2D ¹ H- ¹ H double-quantum (DQ)/single-quantum (SQ), (D) ¹ H- ¹ H triple-quantum (TQ)/SQ and (E) 2D HETCOR SS NMR spectra(see section IV.5 for details).	144
Figure 4.34: 1D ¹ H spin-echo MAS SS NMR spectrum of IV.2.	146
Figure 4.35: ¹³ C CP/MAS NMR spectrum of IV.2.....	147
Figure 4.36: (A) 1D ¹ H spin-echo MAS SS NMR spectrum of IV.3,(B) 2D ¹ H- ¹ H double-quantum (DQ), (C) ¹³ C CP/MAS NMR spectrum of IV.3, (D) 2D CP/MAS HETCOR NMR spectrum of IV.3 (see section 4.5 for details).	149
Figure 4.37: Reusability studies of IV.3 for the metathesis of imine metathesis (TableV.2, entry 1).	153
Figure 4.38: FTIR spectra of the catalyst IV.3 (Entry 1) after the first catalytic cycle.	153
Figure 5.39: FT-IR spectra of the starting SBA15 ₁₁₀₀ (black) and V.1 (red).	164
Figure 5.40: (A) ¹ H MAS NMR spectrum of V.1. (B) DQ rotor-synchronized 2D ¹ H MAS NMR spectrum of V.1.	165
Figure 5.41: ¹ H liquid NMR of aniline and V.4 in C ₆ D ₆	166
Figure 5.42: (A) ¹³ C CP-MAS NMR of V.1. (B) 2D contour plot of the aromatic region of ¹ H- ¹³ C HETCOR spectrum of V.1.	169
Figure 5.43: ¹³ C liquid NMR of aniline and V.4 in C ₆ D ₆	169
Figure 5.44: 400 MHz DNP SENS spectra of V.1 (20mg) impregnated with a 16mM solution of TEKPOL in 1,1,2,2-tetrachloroethane at 8 kHz MAS frequency with a sample temperature of 100K. (a) ²⁹ Si DNP enhanced CP/MAS with a CP contact time of 5 ms, a 3 s polarization delay and 1024 scans. Exponential line broadening of 60 Hz was applied prior to Fourier transformation. (b) ¹⁵ N DNP enhanced CP/MAS with 5 ms CP contact time, a 3 polarization delay and 16000 scans. Exponential line broadening of 150 Hz was applied prior to Fourier transformation. In both (a) and (b) for comparison, spectra are shown with both for both μ wave on and off.....	171
Figure 5.45: ¹⁵ N liquid NMR of aniline and V.4 in C ₆ D ₆	172
Figure 5.46: Small angle XRD patterns of SBA1 ₁₀₀ and V.1.	173
Figure 5.47: Nitrogen adsorption/desorption isotherm at 77 K of SBA ₁₁₀₀ and V.1.	174
Figure 5.48: Transmission electron micrographs of V.1 at different tilt angles: in the direction perpendicular to the pore axis (B), and in the direction of the mesoporous axis (B).	175
Figure 5.49: FT-IR spectra of materials V.1-V.5.....	177
Figure 5.50: ¹ H MAS solid state NMR of catalyst V.2-V.5	178
Figure 5.51: (i) FT-IR spectrum of [NPh,O] SBA15, V.1 after 1hr in contact with dry ethanol and followed by evacuation at 10 ⁻⁵ mbar, 100 °C for 12h: the characteristic bands of ≡SiNHPh, [ν (NH) = 3435 cm ⁻¹] is still observed. (ii) FT-IR spectrum of [N,O] SBA15, after 5 min in contact with dry ethanol and followed by evacuation at 10 ⁻⁵ mbar, 100 °C for 12h: complete disappearance of the characteristic bands of ≡SiNH ₂ group [ν_s (NH ₂) = 3535, ν_{as} (NH ₂) =3445 and δ (NH ₂) = 1550 cm ⁻¹].	181
Figure 5.52:(i) GC-MD Chromatogram of pure dry aniline and GC chromatogram of reactant and product of Knoevenagel condensation.....	182

Scheme 1.1: Different types of hydroxyl groups present on the surface of silica	19
Scheme 1.2: Dehydroxylation process of the silica surface.....	20
Scheme 1.3: Reaction of organometallic precursor (ML _n) with dehydroxylated silica.....	21
Scheme 1. 4: Reaction of tetraeopentyl zirconium with SiO ₂₋₅₀₀	21
Scheme 1. 5: SOMC Examples of heterogeneous catalysis.	22
Scheme 1.6: Selected catalysis promoted by the surface organometallic fragments.	23
Scheme 1.7: Examples of different surface metal nitrogen fragments.....	25
Scheme 1. 8: Resonance structures for metal η ² -imine complexes.....	25
Scheme 1.9: General routes to metallaaziridines.	26
Scheme 1.10: Synthesis of zirconaaziridines I.6.	27
Scheme 1.11: Synthesis of zirconaaziridines from a ketimine or a cyclic aldimine.	27
Scheme 1.12: Synthesis of titanaaziridines I.9.	28
Scheme 1. 13: Synthesis of a bridging titanaaziridine.	28
Scheme 1.14: Structure of hafnaaziridine complex.	29
Scheme 1.15: Synthesis of Cp*NbCl ₂ (η ² -(Me) ₂ CN(2,6-Me ₂ C ₆ H ₃)) and Cp*NbMe ₂ (NMe ₂) ₂	29
Scheme 1.16: Synthesis of niobaaziridine-hydride I.17.....	30
Scheme 1.17: Synthesis of tantallaaziridines I.19 and I.20.....	31
Scheme 1.18: (i) Negishi reagent and (ii) Rosenthal reagent in the synthesis of zirconaaziridines.	31
Scheme 1.19: Synthesis of titanaaziridines I.24 and I.25.	32
Scheme 1.20: Structurally characterized vanadaaziridines.	33
Scheme 1.21: Synthesis of titanaaziridines I.27.	34
Scheme 1.22: Insertion reactions of zirconaaziridines.	35
Scheme 1.23: reactivity of zirconaaziridine I.28.....	36
Scheme 1. 24: Reactions of I.28 with ethylene carbonate.	36
Scheme 1.25: Reactions of tantalaaziridine I.32.	38
Scheme 1.26: Reactivity of titanaaziridines I.33.	39
Scheme 1.27: Reactivity of titanaaziridine I.9.....	40
Scheme 1.28: (i) Inter- and (ii) intra- molecular hydroaminoalkylation.	40
Scheme 1.29: Selected group 4 and group 5 metal hydroaminoalkylation catalysts.	41
Scheme 1.30: Intermolecular hydroaminoalkylation of vinyl arene.....	42
Scheme 1.31: Regiodivergent hydroaminoalkylation.	43
Scheme 1.32: Mechanism of intermolecular hydroaminoalkylation.	44
Scheme 1.33: examples of silica supported metal-imido complexes.	46
Scheme 1.34: Imide/Imine stoichiometric metathesis reaction.....	46
Scheme 1.35: Chauvin-type mechanism for imine metathesis.....	47
Scheme 1.36: General reaction of imine\imine crosses metathesis.....	47
Scheme 1.37: Synthetic strategy deployed in Chapter II.	50
Scheme 2.38: Resulting products after reaction of Ti(NR ₂) ₄ on SiO ₂₋₂₀₀ (II.1) and SiO ₂₋₇₀₀ (II.2).	55
Scheme 2.39: Resulting products after grafting of Zr(NMe ₂) ₄ on MSN.....	56
Scheme 2.40: Silica-supported zirconium precatalysts hydrogenation of olefins ^[7] , isotopic exchange in alkanes ^[8] and hydroisomerization and hydrogenolysis of alkanes. ^[9]	57
Scheme 2.41: Reported model of silica-supported zirconium hydrides.	58
Scheme 2. 42: Reactivity of group 4 M(NMe ₂) with highly dehydroxylated silica surfaces.	60
Scheme 2.43: Generation of silica-supported zirconium monohydride.	60
Scheme 2.44: Reaction of silica with dimethylamine.....	65
Scheme 2.45: Spontaneous transformation of silica supported zirconium dimethyl amines.	70
Scheme 2.46: Proposed mechanism for the hydrogenation of ethylene and propylene by II.6 and II.9. .	83
Scheme 2.47: Proposed mechanism for the generation of propylene and 1-pentene by reaction of ethylene with II.6D. For clarity in the mechanism, the inclusion of only one equivalent of D ₂ was considered.	85
Scheme 2.48: Silica supported complexes II.6 - II.9 and II.6' - II.8'.	86
Scheme 3.49: Proposed mechanism of hydroaminoalkylation reaction.	98

Scheme 3.50: Previously reported metallaziridine molecular complexes based on group 4 and 5 transition metals.	99
Scheme 3.51: Previously reported aziriconaacyclopentane molecular complexes.	101
Scheme 3.52: Elementary steps of the intermolecular hydroaminoalkylation by silica-supported zirconaziridine complex.	103
Scheme 3.53: Preparation pathway of $[\equiv\text{Si}-\text{O}-\text{Ta}(\text{NMe}_2)_4]$ (III.2) $[\equiv\text{Si}-\text{O}-\text{Ta}(\eta^2\text{NRCH}_2)(\text{NMe}_2)_2]$ R = Me (III.3), Ph(III.4).	104
Scheme 3.54: Reaction II.6 with propylene.	104
Scheme 3.55: Grafting of $\text{Ta}(\text{NMe}_2)_5$ on SiO_{2-700}	114
Scheme 3.56: Synthesis of silica-supported tantalaziridine III.3.	116
Scheme 3.57: Synthesis of silica-supported tantalaziridine III.4.	119
Scheme 3.58: Structures of key transition states along the reaction pathway involving $\text{HN}(\text{Ph})(\text{Me})$. The distances are in Å.	122
Scheme 4.59: Reaction of $\text{Zr}(\text{NEt}_2)_4$ with SiO_{2-700}	142
Scheme 4.60: Silica-supported zirconium imido formation with the hypothetical intermediate.	146
Scheme 4.61: Imide/imine stoichiometric metathesis via transient 4-membered metallacycle.	148
Scheme 4.62: Silica-supported imide/imine metathesis.	148
Scheme 4.63: Silica-supported zirconium-imido complexes mediated heterogeneous imine metathesis.	154
Scheme 5.64: Synthesis of paired N-phenylsilanamine/silanol V.1 via the chemisorption of dry aniline on $\text{SBA}_{15,1100}$ in toluene at 80 °C for 20h.	161
Scheme 5.65: Synthesis of a model molecular silsesquioxane bearing N-phenylsilanamine group.	166
Scheme 5.66: Schematic drawing showing of the observed proximities of the paired N-phenylsilanamine/silanol groups in V.1 in the 2D $^1\text{H}-^1\text{H}$ DQ NMR spectroscopy.	167
Scheme 5.67: Knoevenagel condensation using benzaldehyde with diethylmalonate. (i) The reaction was performed in sealed flask in which each reactant (2 mmol) and the catalyst (20 mg) were dissolved in dry ethanol (5 mL) and the reaction mixture was refluxed in an oil bath at 80 °C for 24 h.	176
Scheme 5.68: Synthesis of acid-base paired catalysts via (i) the chemisorption of dry aniline derivatives on $\text{SBA}_{15,1100}$ in toluene at 80 °C for 20h.	176

LIST OF TABLES

Table 2.1. ^1H NMR spectrum of silica and SBA supports treated with $\text{M}(\text{NMe}_2)_4$	68
Table 2.2: ^{13}C NMR spectrum of SBA_{15-700} treated with $\text{M}(\text{NMe}_2)_4$	69
Table 2.3: Carbon- proton, DQ and TQ Solid-state NMR spectra of $\text{Zr}(\text{NMe}_2)_4$ after reation with SBA_{15-700}	72
Table 2.4: Parameters extracted from the fit of EXAFS data related to compound 1. Underlined characters denote fixed parameters while § indicate constrained parameters.....	75
Table 2.5: Elemental analysis of II.6 and II.9.....	77
Table 2.6: Reactivity study of II.6 and II.9 contacted by different gas mixtures (24 hrs, 200 °C).....	81
Table 2. 7. Specific surface and size distribution of the pores.....	90
Table 3.9. Hydroaminoalkylation substrates testing using catalysts III.2 -4.	129
Table 4.10: Catalytic imine metathesis substrates testing using catalysts IV.3 and IV.2.	150
Table 4.11: Conversion, yield and TON of the catalytic imine metathesis substrates testing using catalysts IV.3 and IV.2.	152
Table 5.12. Textural parameters of V.1 from Nitrogen sorption combined with small angle X-ray diffraction.	173
Table 5.13 Knoevenagel condensation testing.	179

Chapter 1: Bibliography

1.1 Introduction

1.2 Introduction to Surface organometallic chemistry

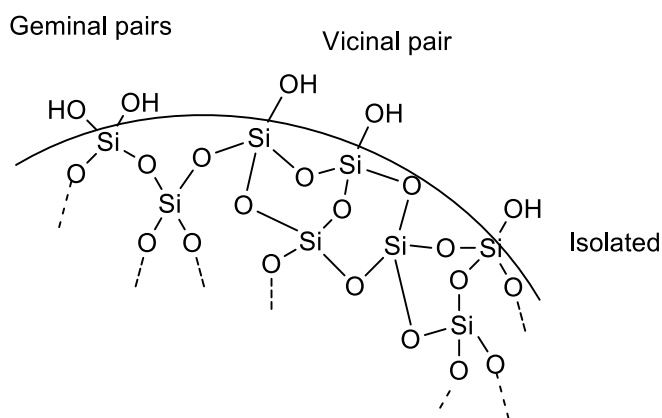
Heterogeneous catalysis plays a fundamental instrumental role in industrial processes for its advantages including simple preparation and separation of products, reactant and catalysts, chemical and thermal stability.^[1] Yet the catalytically active species, remains poorly characterized and are assumed to be a distribution of a plurality of sites. By contrast, homogenous catalysis permits a far more detailed mechanistic understanding of microscopic process and catalytic mechanisms.

The reaction of organometallic compounds with the surfaces of metal-oxides or metals (along with their subsequent reactions) is defined as the field of surface organometallic chemistry (SOMC).^[2] In principle, it attempts to bridge the two types of catalysis. Although superficially resembling heterogeneous catalysts, the relatively uniform structure, the reactivity and the distribution on the support of the surface organometallic complexes make them closely related to their homogenous counterparts. In principle, the methodology of SOMC allowed to prepare single-site heterogeneous catalysts in which most of the active sites are quasi identical and evenly distributed. It became possible to have a molecular understanding of the coordination sphere of the metal using a wide range of solid state characterizations and to attain well-defined surface species. They offer the possibility to explore their reactivity step wise and to isolate highly reactive species or intermediate.^[3]

The support selected to carry the grafting is pivotal to the surface complexes and it should be considered as a very bulky ligands. A key feature of this system is that the supported sites are distant and cannot interact with each other, hence preventing bimolecular deactivation.

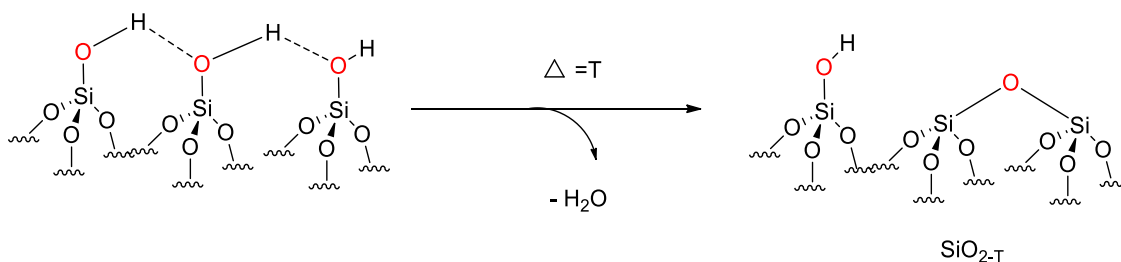
1.2.1 Surface organometallic chemistry on Silica

Fumed silica is one of the most commonly used metal-oxides on SOMC. Its surface consists of Si-O-Si siloxane units showing low reactivity and hydroxyl groups (viz silanols, SiOH), which are usually the grafting sites. There are three types of hydroxyl groups, isolated, germinal and vicinal pairs (Scheme 1.1). The silica mostly used in this research is fumed silica, marked by Degussa under the trade-name Aerosil. Additional studies have been carried out using SBA15; a mesoporous silica in which the mesopores are cylindrical and organised in a hexagonal lattice between the cylindrical pores; there are micropores which connect the cylinders to each other. The size of the mesopores in SBA-15 varies between 6.5–15 nm and the thickness of the pore walls range from 3.1 to 4.8 nm.^[4]



Scheme 1.1: Different types of hydroxyl groups present on the surface of silica.

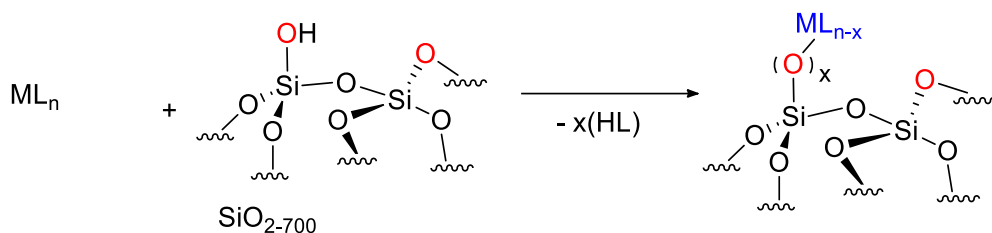
Upon heating under high vacuum, hydrogen-bonded pairs of hydroxyl groups condense to afford siloxane bridges while releasing water (scheme 1.2). It follows that the temperature of dehydroxylation of the silica controls the density and the nature of the hydroxyl groups displayed by the surface. After dehydroxylation at 200°C, the surface hydroxyl groups exist primarily as vicinal pairs. Dehydroxylation at high temperature (450-700 °C) results in further condensation; only isolated hydroxyl groups remains onto the surface.^[5]



Scheme 1.2: Dehydroxylation process of the silica surface.

Transition metals complexes with a wide range of ligands have been grafted on surface silanols. These reactions generally occur via electrophilic attack of the protons from the hydroxyl groups on the donor atoms of one or more ligands (protolysis).^[5]

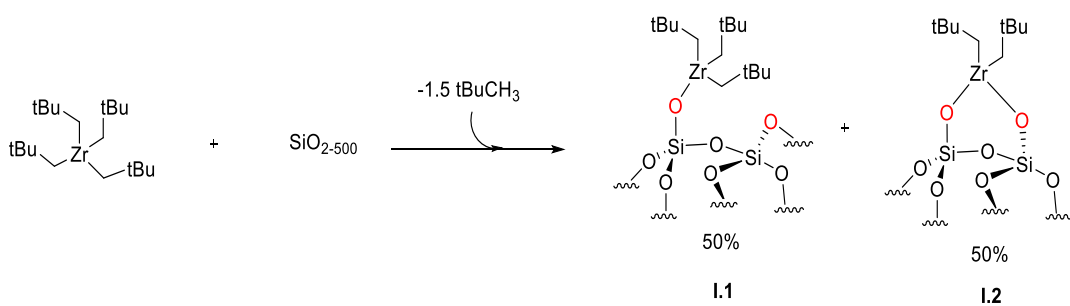
Sublimation or impregnation of suitable organometallic precursor (ML_n), onto the partially dehydroxylated silica surface leads then to the formation of the grafted organometallic species, $[(\equiv SiO)ML_{n-1}]$.^[6] The quantification of the by-products released during the grafting reaction (viz. the ligand L) gives an indication of the stoichiometry of the grafting. Several characterization techniques (IR, EXAFS, SS MAS NMR, microanalysis, GC...) provide precise structural information of the grafted complexes (Scheme 1.3).



Scheme 1.3: Reaction of organometallic precursor (ML_n) with dehydroxylated silica.

Well-defined surface organometallic species $[(\equiv\text{SiO})M(\text{CH}_2\text{tBu})_3]$ and $[(\equiv\text{SiO})_2M(\text{CH}_2\text{tBu})_2]$ (Scheme 1.4) with $M = \text{Zr}^{[7]}$, $\text{Ti}^{[8]}$, $\text{Hf}^{[9]}$ have been obtained. These catalysts have shown outstanding activity and selectivity toward different reactions (homologation/hydrogenolysis of alkenes, polymerisation/oligomerization alkenes, alkanes and alkenes metathesis). The nature of the active sites allows a deeper mechanistic understanding of the reaction.^[5]

By analogy to the previous general organometallic species, group 4 metals alkyls have been prepared by reacting tetrakisneopentyl metal (zirconium, titanium and hafnium) with silica dehydroxylated at 500 °C (Scheme 1.4).

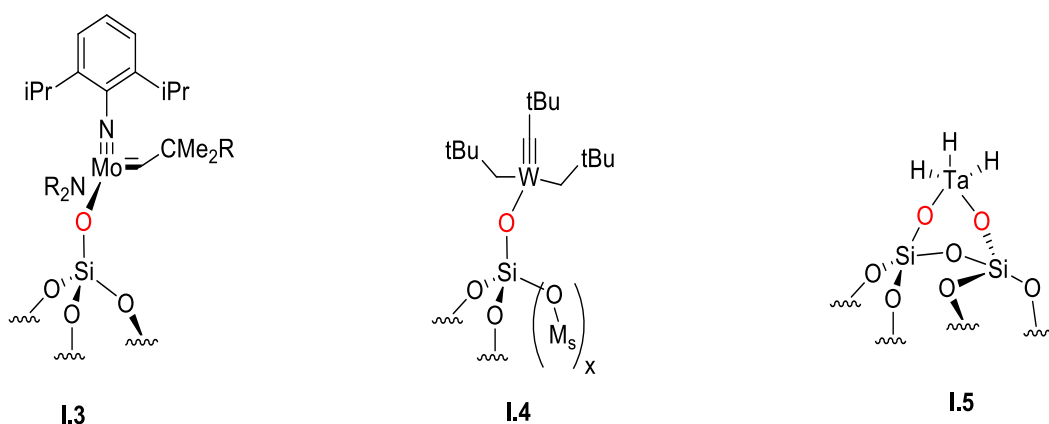


Scheme 1.4: Reaction of tetraneopentyl zirconium with SiO_{2-500} .

1.2.2 Catalysis by design: Surface Organometallic fragments

Surface Organometallic Chemistry (SOMC) has allowed the access to a rich library of surface complexes active for a wide range of catalytic reactions. The nature of the fragments (M=C, M-C, M-H, M≡C, M-NC) bore by the supported metal is pivotal to its reactivity and can promote various catalysis (e.g. alkane metathesis,^[10] alkene metathesis,^[11] methane non oxidative coupling^[12]).

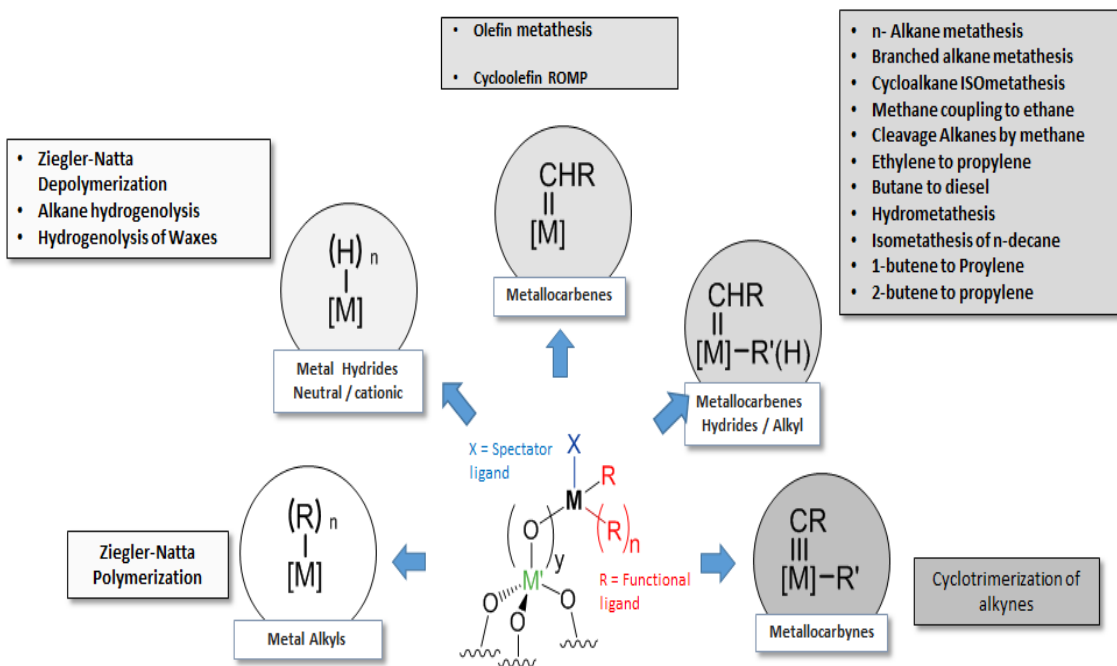
Notable examples of SOMC successes in heterogeneous catalysis can be outlined (scheme 1.5): silica-grafted olefin metathesis catalysts with TON of 23000 in 25 hours for propene,^[13] the trifunctional tungsten-based catalyst (I.3, Scheme 1.5) for direct conversion of ethylene to propylene,^[14] and tantalum-based catalytic system for the non-oxidative coupling of methane to ethane,^[12] and other remarkable activity toward C-C and C-H bonds in stoichiometric activation and catalytic reactions such as alkane metathesis,^[15] cross-metathesis between ethane and toluene.^[16]



Scheme 1. 5: SOMC Examples of heterogeneous catalysis.

The large body of work available about the surface organometallic catalysts has led to the recent conceptual development of the surface organometallic fragment

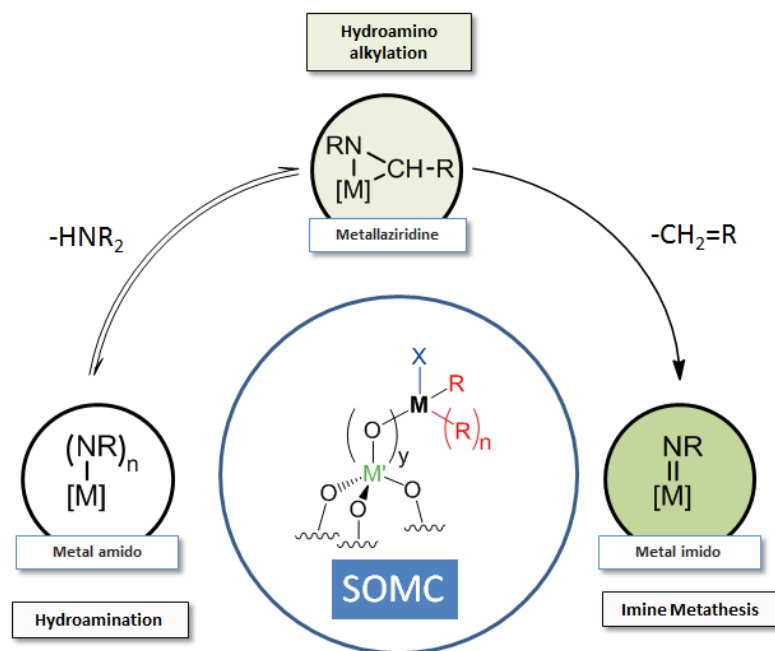
(SOMF).^[17] It aims to rationalize and even predict the catalytic behavior of supported transition metals by investigating the reactivity of specific group bore by the metal centers. Mechanistic studies have identified key metal fragments that are prone to characteristic elementary steps. Due to the hydrocarbon transformations being investigated first, the reactions involving metal-carbon and metal hydrogen have been the prime subject of interest. In addition, larger metals center can combine fragments simultaneously or sequentially such as metal alkyl (M-R) or metal hydride (M-H) with metal carbene (M=C) or metal carbyne (M≡C) and have remarkable catalysis performance (scheme 1.6).



Scheme 1.6: Selected catalysis promoted by the surface organometallic fragments.

1.2.3 Towards new surface organometallic fragment?

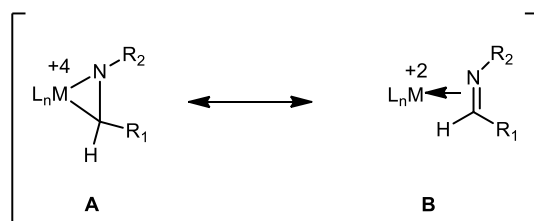
The same methodology deployed on organometallic metal fragment can certainly be applied to metal fragments including heteroatoms with the view to isolate and identify key catalytic intermediates. Specifically, using highly dehydroxylated silica presents the advantage to lead potentially to well-defined and single-site species and with crucial structural information accessible. The most common heteroatoms are nitrogen and oxygen with the former being more undeveloped. Furthermore, nitrogen-containing compounds are valuable fine chemicals. By similarity with organometallic fragments (M-C, M=C, M≡C), we can propose and target metal-nitrogen analogs (M-N, MNC, M=N, M≡N) (scheme 1.7). The metallaaziridine fragment is particularly interesting as it contains a metal carbon bond (that can characterize directly and easily) generated from a metal nitrogen bond. It also implies that its reactivity can resemble that of metal-alkyl (MR) and that of metal-nitrogen (MN). The metal imido surface fragment (M=N) is also intriguing as it is present in numerous complexes to tune their reactivity but almost never as a direct catalytic intermediate (It can nonetheless promote imine metathesis). The following sections will attempt to document both surface metal fragments' reactivity using reported molecular examples (MNC in section 1.3 and 1.4 and M=N in section 1.5).



Scheme 1.7: Examples of different surface metal nitrogen fragments.

1.3 Early Transition Metal- η^2 -imine Complexes

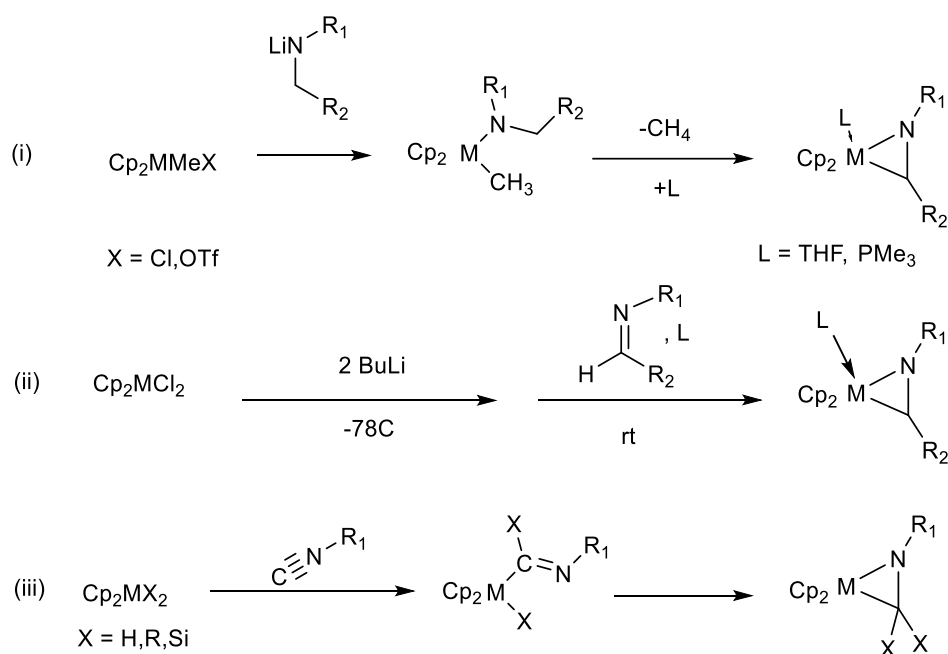
A variety of transition metals η^2 -imine complexes ^[18] have been documented. Within this class of compounds, many early transition metal η^2 -imine complexes have been structurally characterized or proposed as reaction intermediates. The bonding in η^2 -imine complexes can best be described by two models (Scheme 1.8): a metallacycle (A) or a η^2 -imine π complex (B).



Scheme 1.8: Resonance structures for metal η^2 -imine complexes.

1.3.1 Synthetic pathway to group 4 and 5 metal- η^2 -imine complexes (metallaaziridines)

There are three general routes to metallaaziridines generated from the corresponding cyclopentadienyl (Scheme 1.9): (i) C–H activation within a metal methyl amide complex, (ii) imine addition to a metallocene equivalent, and (iii) rearrangement of the product of isocyanide insertion into the M–H, M–C, or M–Si bond.^[19] In the following subsection, selected examples of metallaaziridines complexes will be discussed.

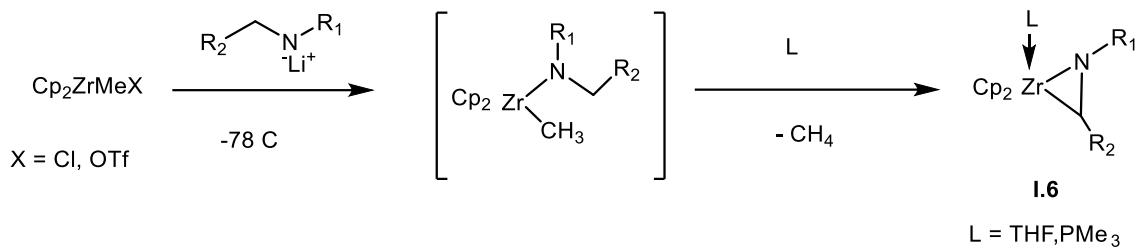


Scheme 1.9: General routes to metallaaziridines.

1.3.2 Intramolecular C–H activation in metal methyl amide complexes

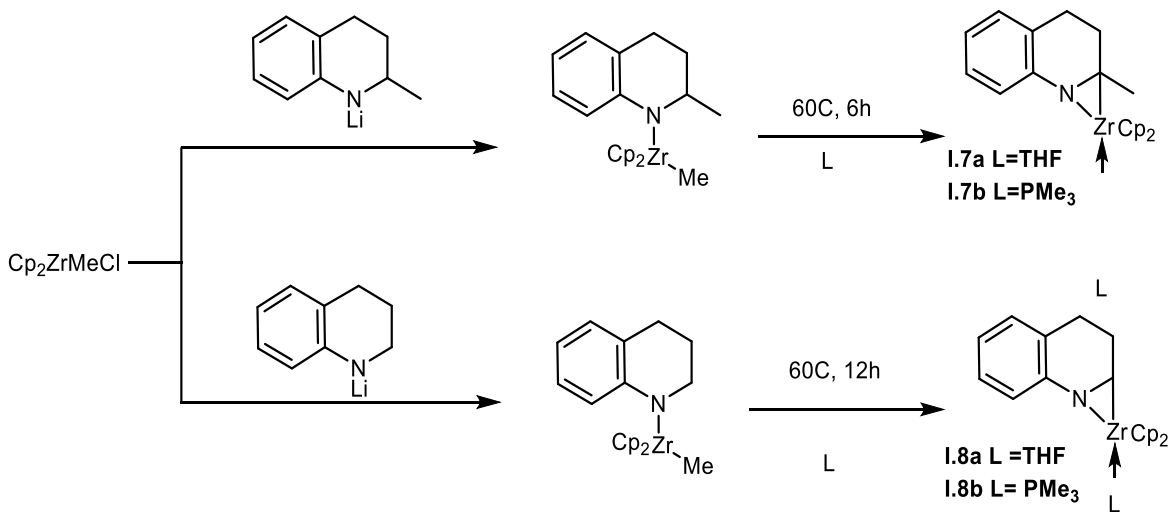
A wide variety of zirconaaziridines $\text{Cp}_2\text{Zr}(\eta^2\text{-C}(\text{H})\text{R}^2\text{NR}^1)\text{L}$ (**I.6**) have been synthesized and isolated using a route discovered by Buchwald (Scheme I.10).^[20] The zirconaaziridines could be isolated in reasonable yields and easily purified by recrystallization. The crystal structure of **I.6** showed a CN bond length of 1.41 Å, consistent with a reduction in C=N

double bond character. These zirconaaziridines were shown to readily insert alkenes, alkynes, imines, isocyanates, and aldehydes to form metallacyclic products. [21]



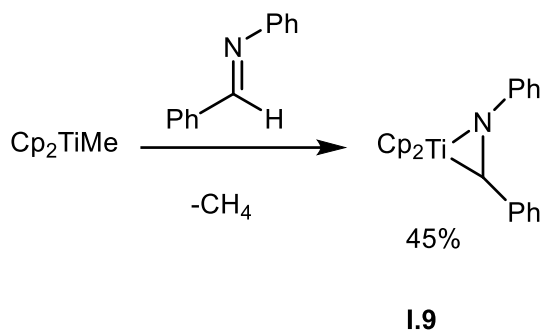
Scheme 1.10: Synthesis of zirconaaziridines 1.6.

Whitby^[22] and coworkers reported the synthesis of the first isolated zirconaaziridines **1.7b** and **1.7b** prepared from a ketimine or a cyclic aldimine by Buchwald's method (Scheme I.11). The formation of the η^2 -cyclic ketimine complex **1.7b** from the Cp₂Zr(Me)(NR₂) complex was observed to proceed significantly faster than the formation of the η^2 -cyclic aldimine complex **1.8b**.



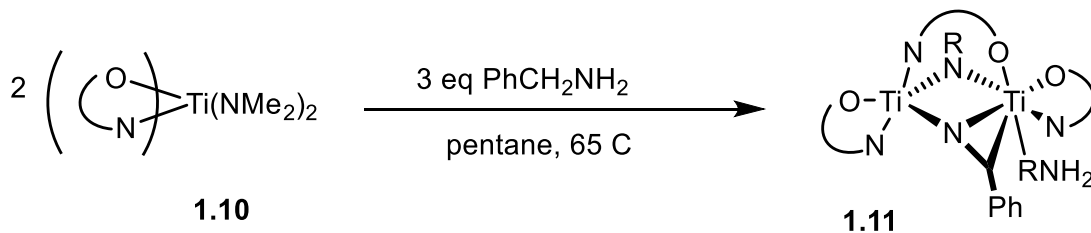
Scheme 1.11: Synthesis of zirconaaziridines from a ketimine or a cyclic aldimine.

Teuben^[23] reported the synthesis of $\text{Cp}_2\text{Ti}(\eta^2\text{-N(Ph)CH(Ph)})$ (**I.9**) by the reaction of Cp_2TiR and N-benzylidene aniline (Scheme 1.12). The green crystalline product was characterized by ^1H NMR and IR, as well as by an elemental analysis and molecular weight determination that are in poor agreement with the calculated values for **I.9** (the crystal structure was not determined).



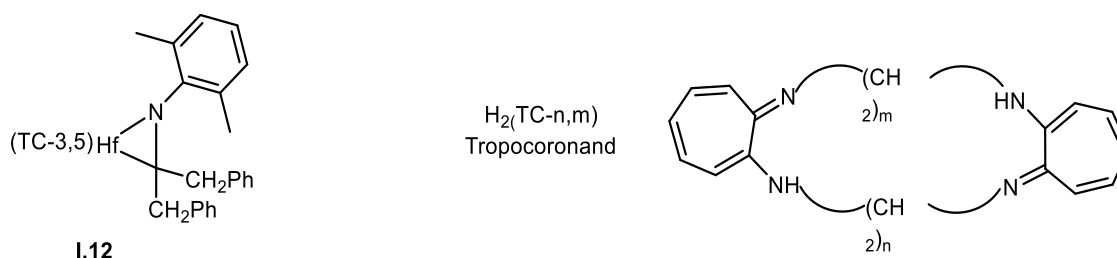
Scheme 1.12: Synthesis of titanaaziridines I.9.

More recently, Schafer reported the reaction of the bis(amidate)-ligated titanium amido complex **I.10** with benzylamine yielded the bridging titanaaziridine **I.11** in excellent yield (Scheme 1.13).^[24]



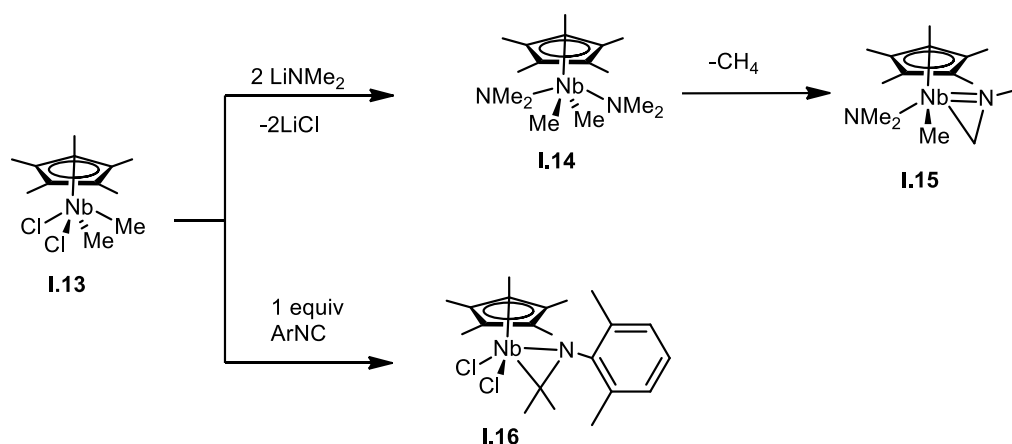
Scheme 1.13: Synthesis of a bridging titanaaziridine.

The only reported hafnaaziridine complex $(\text{TC-3,5})\text{Hf}(\eta^2\text{-C(CH}_2\text{Ph)}_2\text{N(2,6-Ph(CH}_3)_2))$ (**I.12**, TC-3,5 = tropocoronand, Scheme 1.14) has been synthesized via insertion of an arylisocyanate into the bis(CH_2Ph) complex^[25] and was characterized by X-ray crystallography.



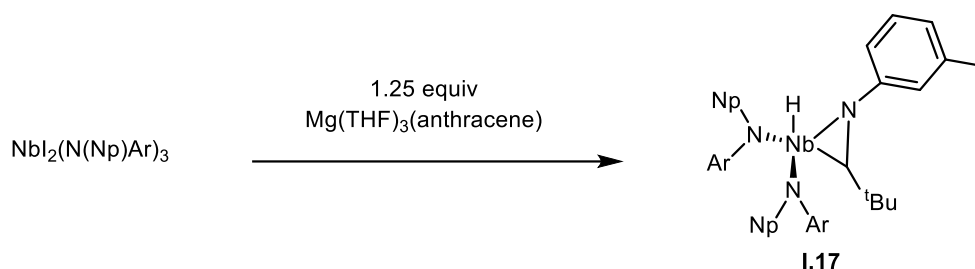
Scheme 1.14: Structure of hafniaaziridine complex.

Three niobium η^2 -imine complexes have been isolated and characterized. The reaction of $\text{Cp}^*\text{NbCl}_2\text{Me}_2$ (**I.13**) with $(2,6\text{-Me}_2\text{C}_6\text{H}_3)\text{NC}$ and subsequent methyl group migration (Scheme I.15) resulted in the formation of $\text{Cp}^*\text{NbCl}_2(\eta^2\text{-(Me)}_2\text{CN}(2,6\text{-Me}_2\text{C}_6\text{H}_3))$ (**I.16**).^[26] The niobaaziridine $\text{Cp}^*\text{Nb}(\text{Me})(\text{NMe}_2)(\eta^2\text{-CH}_2\text{NMe})$ was formed by cyclometallation of an -NMe_2 moiety in the complex $\text{Cp}^*\text{NbMe}_2(\text{NMe}_2)_2$ (**I.13**, Scheme 1.15). These niobaaziridines were isolated and characterized by ^1H NMR, but crystals suitable for X-ray diffraction analysis were not obtained.



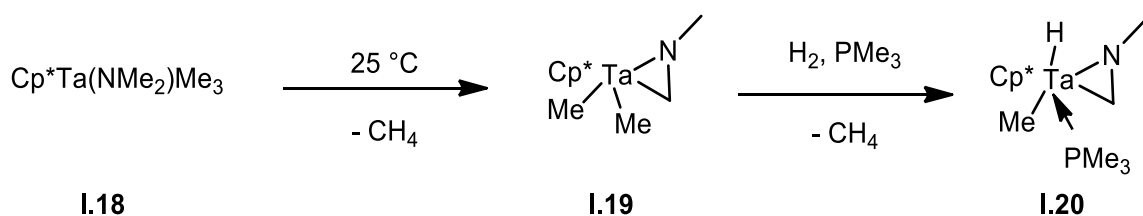
Scheme 1.15: Synthesis of $\text{Cp}^*\text{NbCl}_2(\eta^2\text{-(Me)}_2\text{CN}(2,6\text{-Me}_2\text{C}_6\text{H}_3))$ and $\text{Cp}^*\text{NbMe}_2(\text{NMe}_2)_2$.

A niobaaziridine hydride,^[27] $\text{Nb}(\text{H})(\eta^2\text{-(}^t\text{Bu)}(\text{H})\text{C=NAr})(\text{N}[\text{Np}]\text{Ar})_2$ (**I.17**, Np = neopentyl), has been characterized by ^1H NMR, IR, and X-ray crystallography.^[28] (Scheme 1.16)



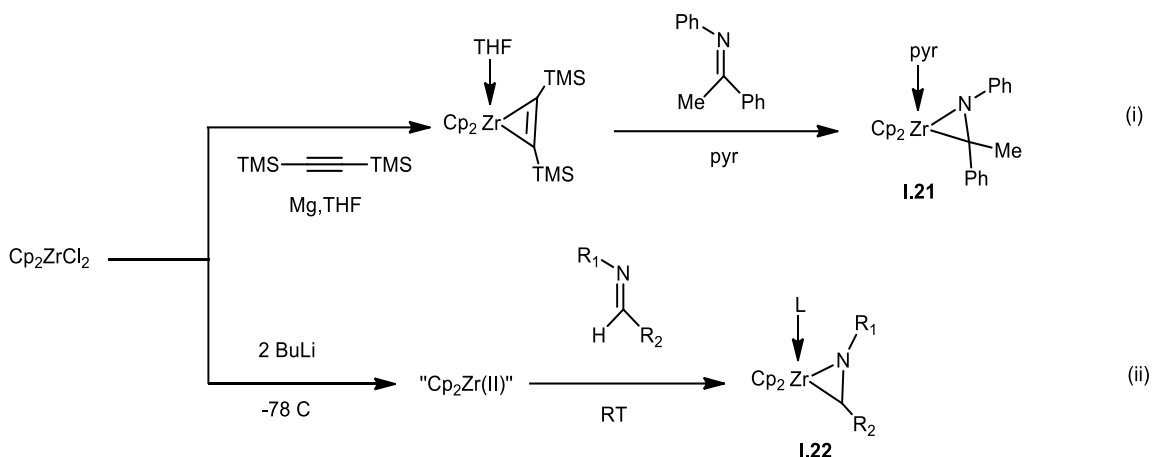
Scheme 1.16: Synthesis of niobaaziridine-hydride I.17.

Tantalum analogues of several of these niobaaziridines have also been synthesized and characterized more completely.^[18b] In 1978, Bercaw^[29] reported the synthesis of Cp*TaMe₂(η²-CH₂NMe) (**I.19**) via the decomposition of Cp*Ta(NMe₂)Me₃ (**I.18**) with release of CH₄ (Scheme 1.17). The structure of **I.19** was confirmed by ¹H and ¹³C NMR, IR, and elemental analysis. The formation of **I.19** from **I.18** was found to be a unimolecular process with a kinetic isotope effect of kH/kD = 9.7 ± 1, strongly supporting a mechanism involving hydrogen abstraction, (3-hydrogen elimination to form a tantalum-hydride intermediate, or a pathway in between these two extremes. Tantalaaaziridine **I.20** reacted with H₂ in the presence of PMe₃ to form the tantalaaaziridine hydride complex Cp*Ta(η²-CH₂NMe)Me(PMe₃)H (**I.20**), which decomposes slowly at room temperature. Recently, Hartwig has proposed tantalaaaziridine intermediates similar to **I.19** in the hydroaminoalkylation of olefins.^[30] Other structurally characterized tantalaaaziridines include Ta(O(2,6-ⁱPr₂C₆H₃)₂Cl₂(η²-C(H)(PMe₃)N(2,6-ⁱPr₂C₆H₃))^[31] and TaCl₃(DME)(η²-C(H)PhNCH₂Ph)^[32].



Scheme 1.17: Synthesis of tantalazaaziridines I.19 and I.20.

Zirconaaziridines can be synthesized by either (i) addition of an imine to the Negishi reagent^[33] or(ii) by addition to other "Cp₂Zr" equivalent, such as Rosenthal's reagent^[34] (Scheme 1.18).



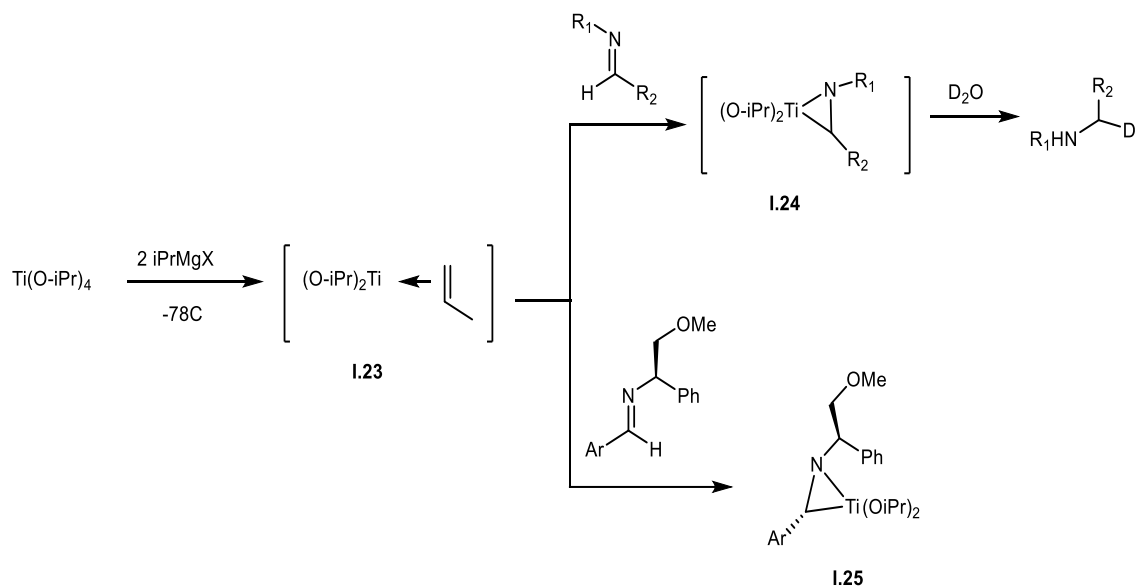
Scheme 1.18: (i) Negishi reagent and (ii) Rosenthal reagent in the synthesis of zirconaaziridines.

Unfortunately, zirconaaziridines produced by this method are often isolable only in low yields and poor purity, in part due to competition with reductive coupling of the imine reactant.

Titanaaziridines have been proposed as intermediates for a variety of synthetic transformations. Sato^[35] has developed the use of Ti(O-*i*Pr)₄/2 *i*PrMgX as a source of "Ti(O-*i*Pr)₂" *in situ* (Scheme I.19) and proposed that the reagent forms the η²-propylene complex **I.23** after addition of the Grignard reagent, β-hydride elimination and reductive

elimination. The propylene is easily displaced by alkynes, alkenes, and imines to form organometallic species.

Generation of **I.23** followed by addition of the imine and deuteration yields the corresponding monodeuterated amines (Scheme 1.19). The imine complexes also insert alkenes and alkynes into the Ti-C bond and afford the corresponding amines upon workup.^[36] These results support the proposed formation of the imine complexes **I.24** yet these complexes have never been successfully isolated or even characterized *in situ*.

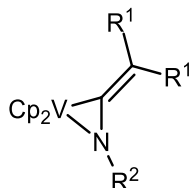


Scheme 1.19: Synthesis of titanaaziridines I.24 and I.25.

Sato reported also the asymmetric synthesis of allyl- and α -allenyl amines via the reaction of the chiral complexes $\text{Ti}(\text{O}i\text{Pr})_2(\eta^2\text{-C}(\text{H})\text{ArNR}^*)$ with terminal alkynes or propargyl halides (Scheme 1.19).^[37] In this system, the chiral induction originates from the N-substituent of the imine, which contains a chelating methoxy group and a chiral center. Based on the stereochemistry of the organic products in (Scheme 1.19), Sato has

proposed that the imine complex **1.25** adopts a chair-like conformation in which the aryl substituents on the imine ligand are both in equatorial positions.

One η^2 -imine complex of vanadium^[38] was synthesized by the reaction of $[\text{Cp}_2\text{V}]$ with ketene imines $\text{R}^1_2\text{C}=\text{C}=\text{NR}^2$ to form complexes **1.26** (Scheme 1.20). The solid state structure of **1.26** ($\text{R}^1 = \text{Me}$, $\text{R}^2 = \text{Ph}$) was determined, confirming η^2 coordination of the imine ($\text{C}=\text{N}$) moiety. The C-N bond length is 1.371(9) Å, significantly longer than the C=N of a free imine. The reactivity of this complex was not investigated.

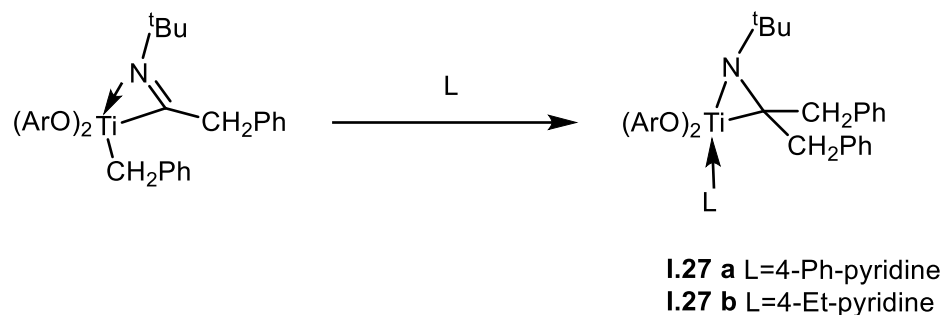


1.26

Scheme 1.20: Structurally characterized vanadaaziridines.

1.3.4 Rearrangement of the product of isocyanide

Two structurally-characterized monomeric titanaaziridines reported in the literature are Rothwell's complexes $\text{ArO}_2\text{Ti}(\eta^2\text{-N}(\text{tBu})\text{C}(\text{CH}_2\text{Ph})_2)\text{L}$ (**1.27a** and **1.27b**, $\text{ArO} =$ 2,6-diisopropylphenoxide) (Scheme 1.21).^[39]



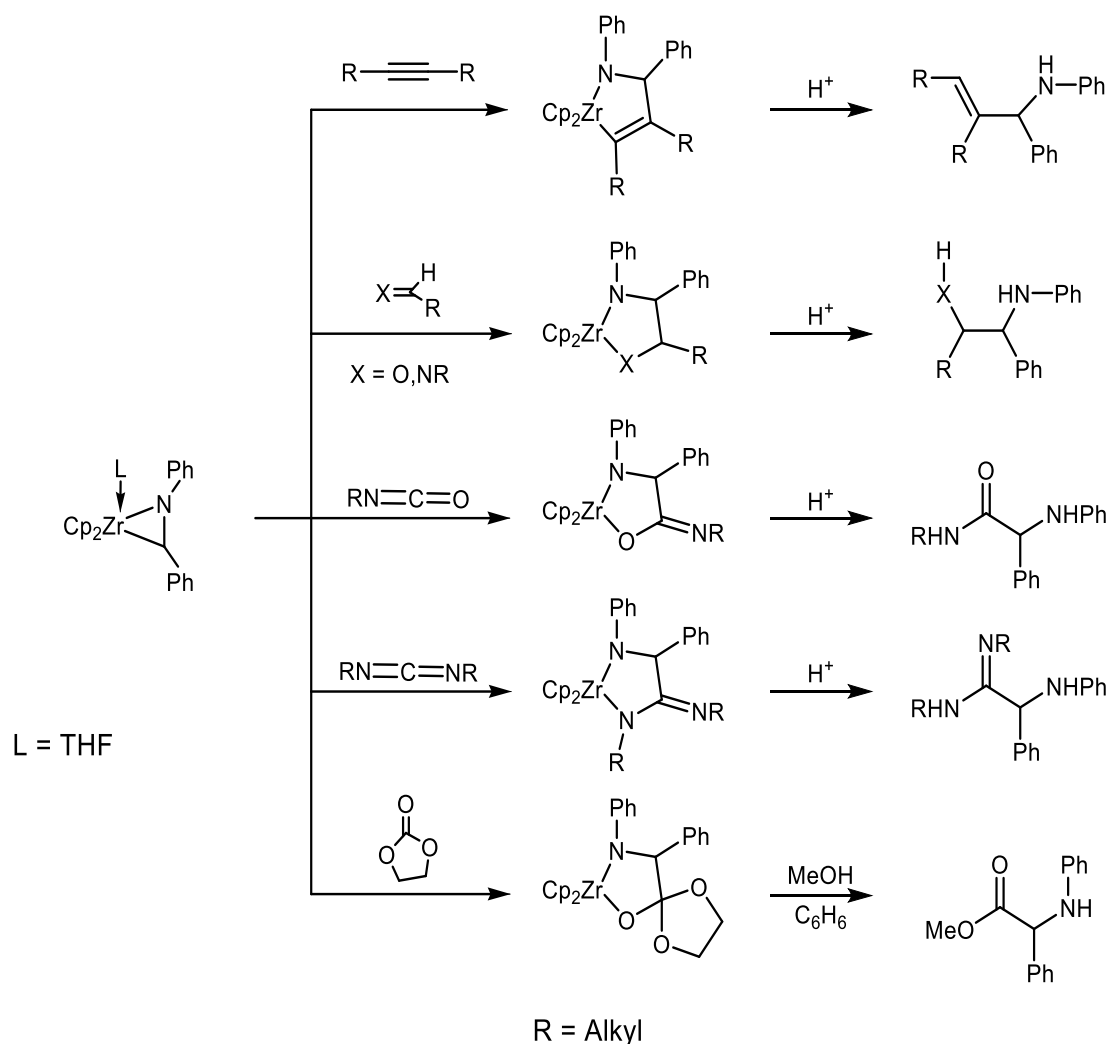
Scheme 1.21: Synthesis of titanaaziridines 1.27.

1.4 Reactivity of metallaaziridines

Group 4 and 5 metallaaziridine have reactivity similar to the related M-R alkyl; they readily insert various compounds (e.g. H₂, unsaturated hydrocarbon, isocyanate, etc) into the metal-carbon bond and undergo coupling reactions. Although extremely air- and moisture- sensitive, they tend to be stable under inert atmosphere. They have also been generated *in situ* for further use in organic synthesis. The following section will discuss selected example of the reactivity of metallaaziridine.

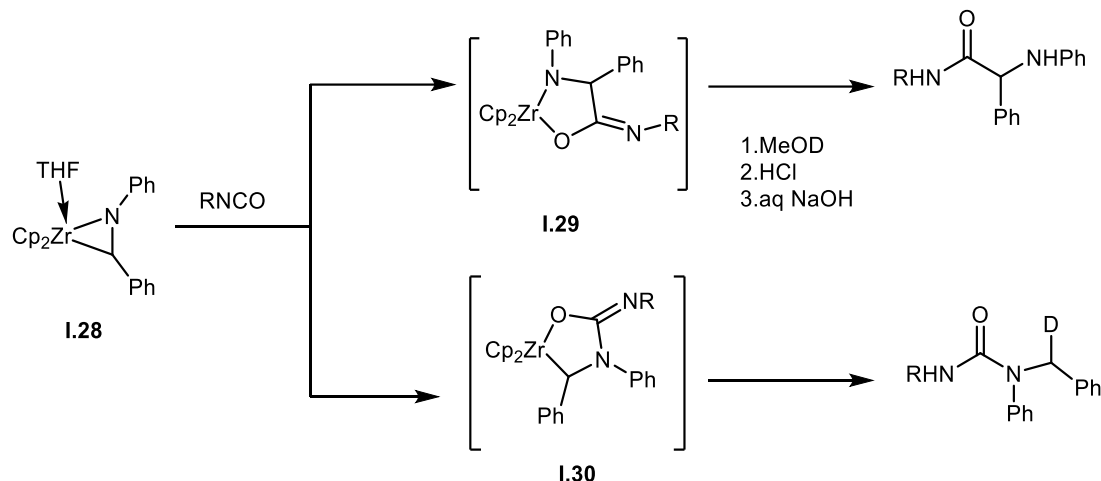
1.4.1 Zirconaaziridines

Imines are prone to nucleophilic attack at the carbon atom, however the analogous carbon in a zirconaaziridine reacts as a nucleophilic α -amino carbanion that is subject to electrophilic attack as well as insertion of unsaturated C=C and C=X bonds. A variety of electrophiles have been employed with zirconaaziridines and yielded the corresponding 5-membered rings (Scheme 1.22).



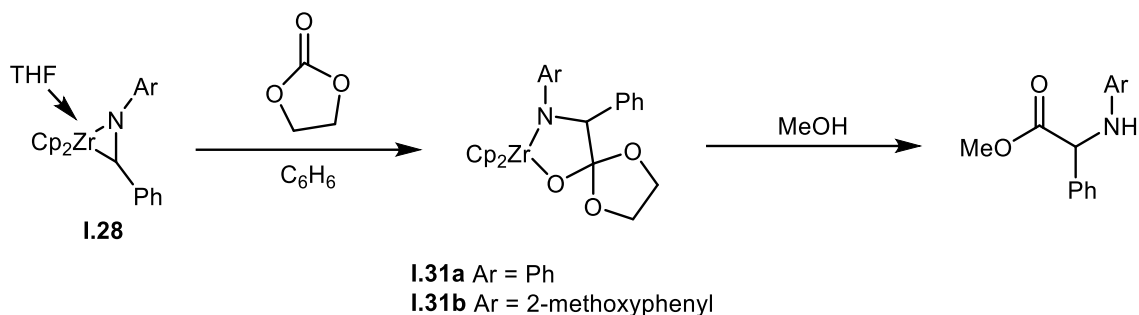
Scheme 1.22: Insertion reactions of zirconaaziridines.

Norton's group investigated the reactivity of Buchwald's zirconaaziridine **1.6** as well as **1.28** with CO and CO₂ with the goal of synthesizing amino acids.^[40] Isocyanates RNCO (which are isoelectronic with CO₂) tend to insert into the Zr-C bond for bulky R group and into the Zr-N bond for small R (Scheme 1.23). Upon workup, these products afford amides or ureas. The insertion reactions were found to be irreversible and were proposed to require dissociation of THF before insertion occurs. Reaction with CO gave unidentifiable products while reaction with CO₂ resulted in insoluble precipitates.



Scheme 1.23: reactivity of zirconaaziridine 1.28.

The reactions of **1.28** with ethylene carbonate yielded the spirocyclic complexes **1.31**, which upon hydrolysis gave the β -hydroxyethyl ester product (Scheme 1.24). Methanolysis of **1.31** yielded the methyl ester. The insertion of racemic or enantiopure diphenylethylene carbonate yielded the analogous zirconacycle products.



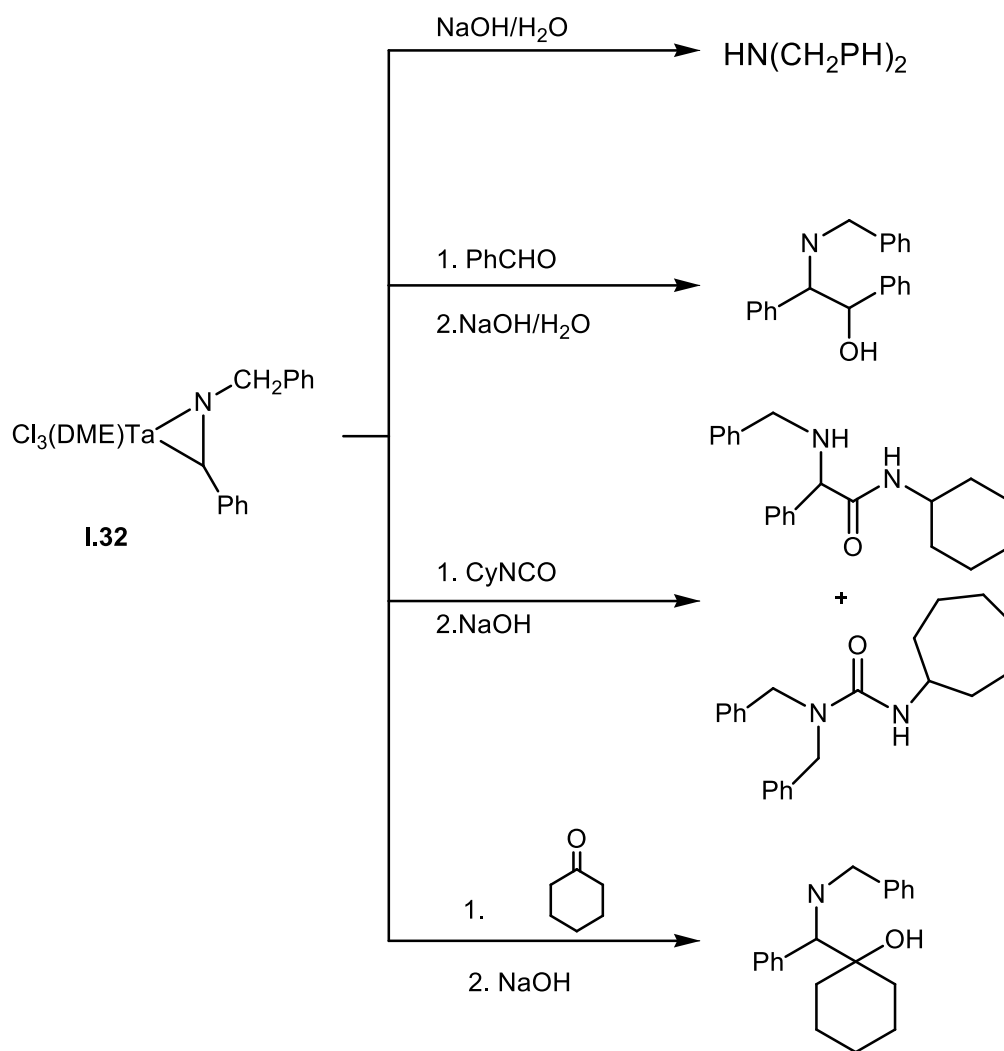
Scheme 1. 24: Reactions of 1.28 with ethylene carbonate.

Subsequent work by the Norton group demonstrated that carbodiimides insert into the Zr-C bond of zirconaaziridines, yielding zirconacycles that are hydrolyzed to α -amino amidines.^[41] Mechanistic studies of this reaction showed that dissociation of THF is required before insertion can occur; strongly supporting the idea that heterocumulenes must coordinate to zirconium in order to insert.

1.4.3 Tantalaziridines

The chemistry of tantalum η^2 -imine complexes has been investigated more thoroughly than that of the niobium and vanadium analogues. Compound **1.32** was implicated as intermediates in Pedersen's reactions; it inserts ketones and aldehydes into the Ta-C bond, and inserts isocyanates into both Ta-C and Ta-N bonds (Scheme 1.25).

For instance, hydrolysis of the imine complex **1.32** with an alkaline solution produced dibenzylamine almost quantitatively. The coupling of N-(benzylidene)benzylamine and various carbonyl compounds (i.e. cyclohexanone could also be accomplished in 88% yield and lead to coupled products after hydrolysis. No intermediate were isolated but it can be assumed the existence of a transient 5-membered ring formed by insertion in to the azametallacycle

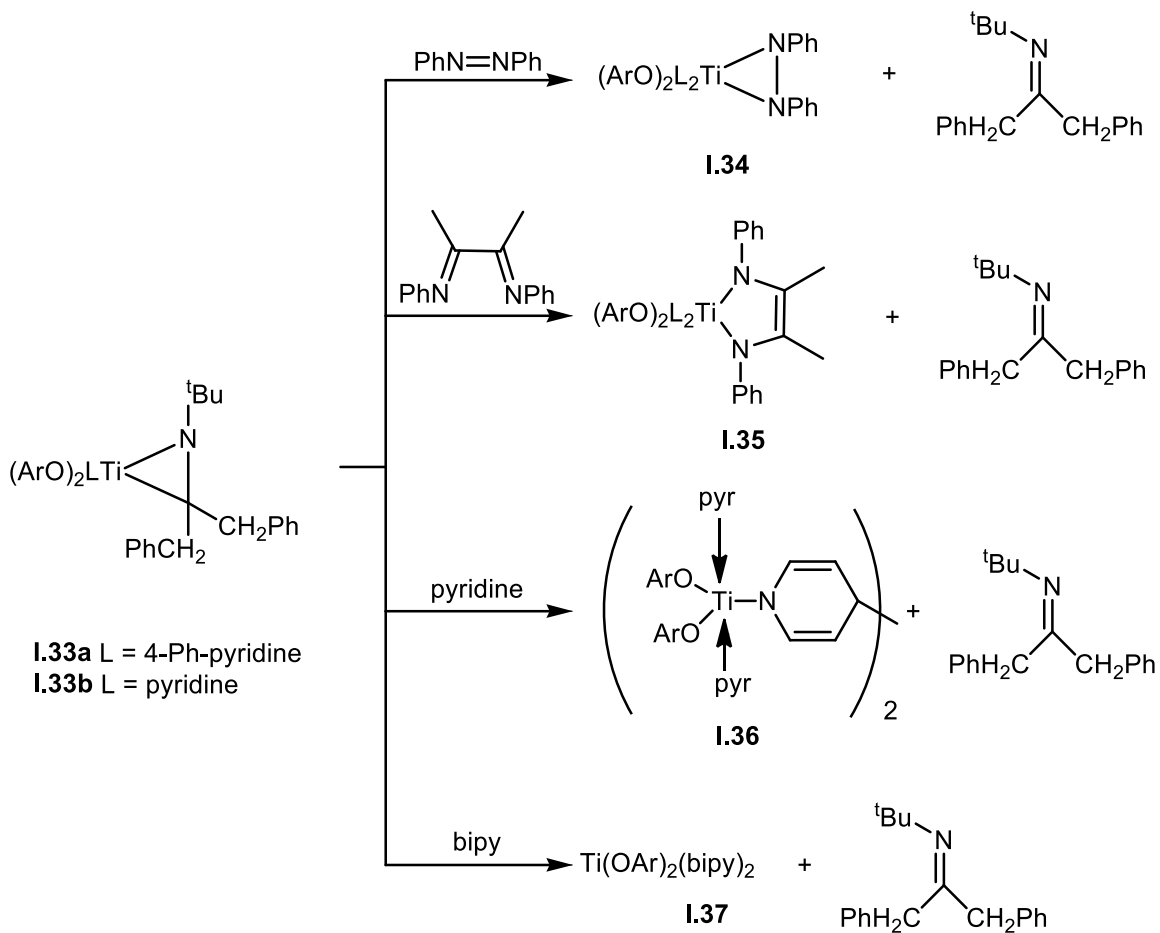


Scheme 1.25: Reactions of tantalazaaziridine I.32.

1.4.2 Titanaaziridines

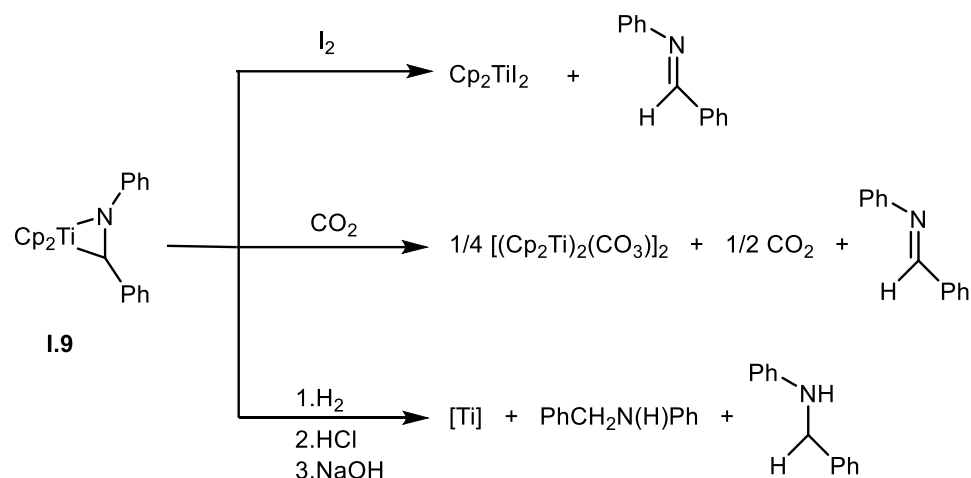
The titanaaziridine **I.32** was structurally characterized by Rothwell.^[39] Reactivity studies did not reveal any inclination toward expansion of the 3-member metallacycle but for ligand exchange and release of the corresponding imine. Treatment with the α -diimine PhN=C(Me)C(Me)=NPh and with azobenzene resulted in displacement of the imine ligand. After treatment of **I.33** with excess pyridine, elimination of 1 equivalent of free imine (PhCH₂)₂C=NCBu) was observed and the dimeric species **I.33** was formed (scheme 1.26), in which the titanium atom have been reduced to +3 oxidation state. Reaction

with excess 2,2'-bipyridine (bipy) resulted in the formation of $\text{Ti}(\text{OAr})_2(\text{bipy})_2$ (Scheme 1.26).



Scheme 1.26: Reactivity of titanaaziridines I.33.

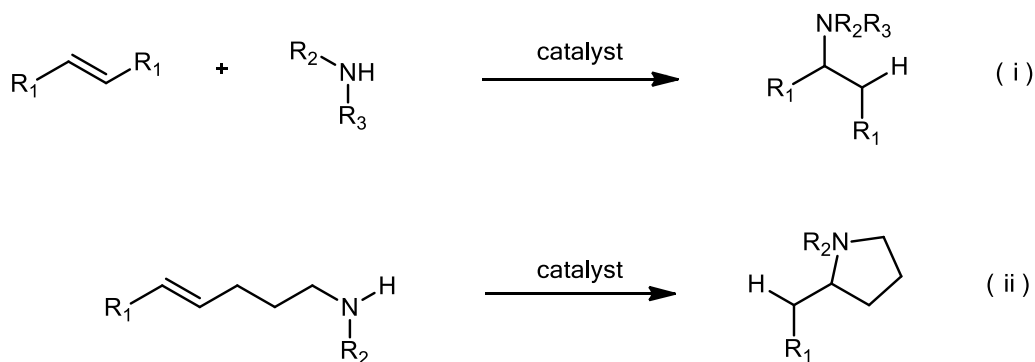
$\text{Cp}_2\text{Ti}(\eta^2\text{-N}(\text{Ph})\text{CH}(\text{Ph}))$ (**I.9**) react with I_2 and CO_2 and H_2 and lead to the elimination of the corresponding imine. Treatment H_2 yield benzylphenylamine by hydrogenation of the imine (Scheme 1.27).^[23]



Scheme 1.27: Reactivity of titanaaziridine I.9.

1.4.4 Intermolecular hydroaminoalkylation of unactivated Alkenes

The hydroaminoalkylation is an emerging atom-efficient direct alkene-to-amine transformation complementary to hydroamination reaction. It has the potential to become a versatile synthetic approach to various important amines^[42] using both intra- and inter- molecular variants of the reaction (Scheme 1.28).

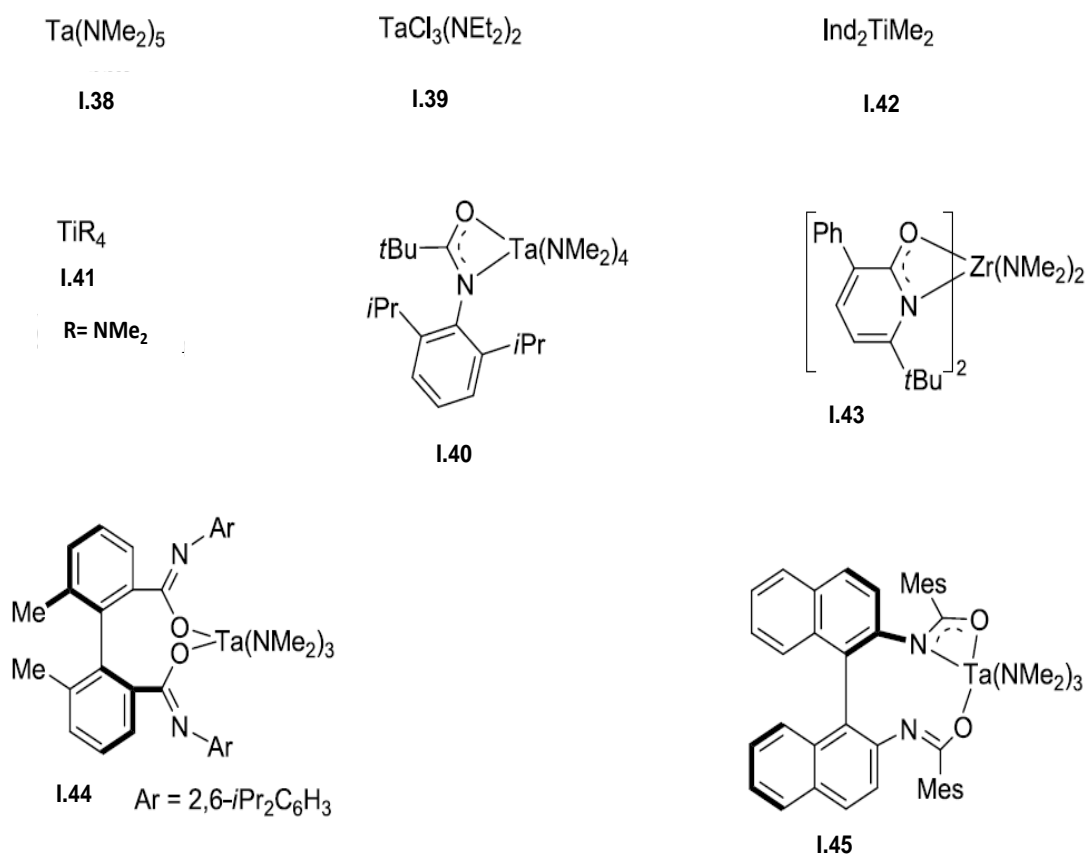


Scheme 1.28: (i) Inter- and (ii) intra- molecular hydroaminoalkylation.

While initial observations of catalytic hydroaminoalkylation have been published since more than three decades,^[43] it has received more attention recently.^[42] Most hydroaminoalkylation catalysts in literature are based on d^0 group 4^[24, 44] and group 5^[30, 45] metal complexes (Scheme 1.29). The observation of hydroaminoalkylation as a side

reaction of hydroamination^[44a] has sparked the development of group 4 metal hydroaminoalkylation catalysts.

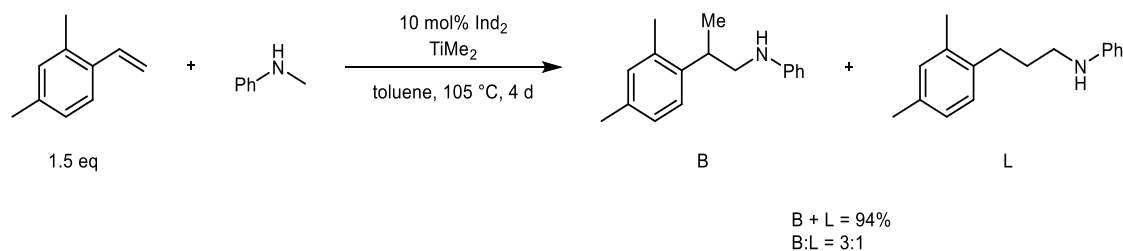
In agreement with earlier observations,^[43] Herzon and Hartwig showed that the heteroleptic chloro bisamide **I.39**^[30] and the homoleptic tantalum amide **I.38**^[45a] are active catalysts for the intermolecular hydroaminoalkylation of unactivated alkenes with secondary amines, **I.39** is more active for a variety of substrates, including dialkylamines (reaction a; R₃ = H, alkyl; R₂ = alkyl) while amide **I.38** was only effective for the activation of more reactive arylalkylamines.



Scheme 1.29: Selected group 4 and group 5 metal hydroaminoalkylation catalysts.

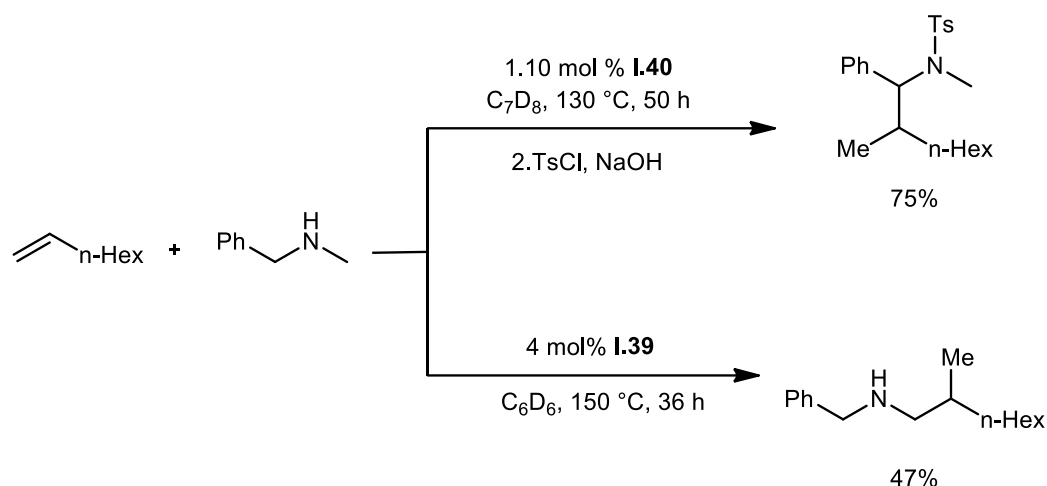
Branched addition products were obtained exclusively and it was found that polysubstituted olefins are significantly less prone to undergo hydroaminoalkylation. More recently, Schafer and coworkers have developed a family of various amidate tantalum catalysts, such as **I.40** and similar structures.^[45b] Tantalum amidates displayed reactivities similar to that of **I.38** and **I.39**. The homoleptic tetrabenzyl titanium **I.41**^[44b, 44c] or bis(indenyl) complex **I.42**^[44d] were shown to catalyze intra- and inter- molecular hydroaminoalkylations, although the latter reaction was found to be feasible only in the case of alkylarylamines.

Another notable characteristic of group 4 catalysts is their reactivity towards primary amines. Only intramolecular (b) process could be achieved and no reports on group 5 metal-catalyzed additions of primary amines to alkenes are known so far. The intermolecular hydroaminoalkylation of terminal alkenes with secondary amines proceeds with excellent branched:linear selectivities exceeding 99:1 in most cases. A notable and somewhat expected exception is the case of vinyl arenes which were reported to produce large quantities (up to 25%) of the linear isomer (Scheme 1.30).^[44d]



Scheme 1.30: Intermolecular hydroaminoalkylation of vinyl arene.

When a non-symmetric secondary dialkylamine is employed in hydroaminoalkylation reaction, two possible products resulting from the activation of the two different alkyl groups can be formed.



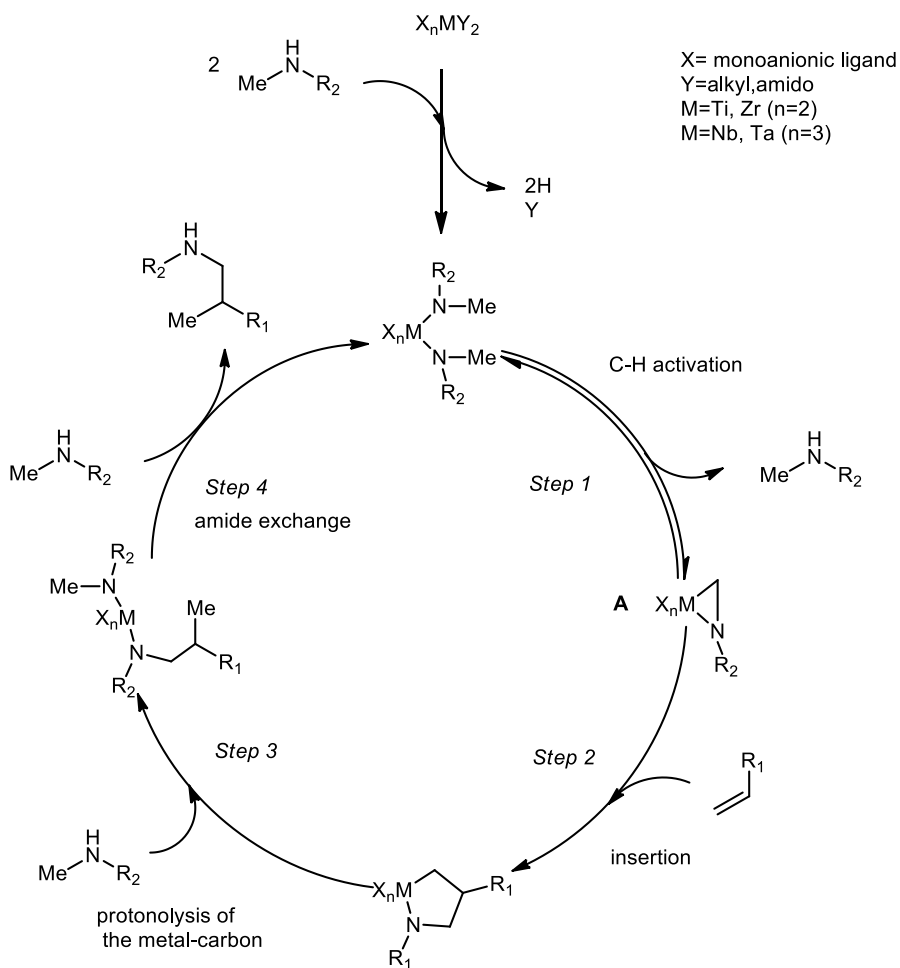
Scheme 1.31: Regiodivergent hydroaminoalkylation.

The vast majority of known group 4 and 5 catalysts reported to date displayed a pronounced preference for the activation of the less substituted alkyl group (i.e. methyl over methylene). The activation of a tertiary alkyl C–H bond in the hydroaminoalkylation is unreported to our knowledge. Remarkably, catalyst **I.44** displayed a very different behavior by yielding the sterically more encumbered reaction products.^[45b]

Reports on relative activity of different group 5 metals have been controversial. While early studies showed that $Nb(NMe_2)_5$ was displaying slightly higher reactivity than its tantalum counterpart **I.38**,^[43a] it was claimed that the niobium analogue of the bis(amidate) complex **I.45** was completely catalytically inactive.^[45c]

The general mechanism of catalytic hydroaminoalkylation was proposed in the early studies dealing with group 5 metal catalysts (Scheme 1.32).^[43a] The key step of the catalytic cycle is believed to be the C–H activation of the bisamide leading to the metallaaziridine **A** (Scheme 1.32, step 1). Subsequent alkene insertion (Scheme 1.32, step 2), protonolysis of the metal-carbon bond (Scheme 1.32, step 3) and amide exchange (step 4) completes the catalytic cycle. The insertive reactivity of

metallaaziridines towards unsaturated carbon-carbon and carbon-heteroatom bonds has already been used in other synthetic applications and is well-known.^[46] Only few mechanistic details on the reversibility and relative feasibility of steps 1–4 of the catalytic cycle are available in the literature. Herzon and Hartwig have suggested that the formation of the metallaaziridine **A** is reversible in the reaction catalyzed by **I.38**,^[45a] whereas step 1 is virtually irreversible in the case of catalyst **I.39**^[30] as indicated by isotopic labeling studies.



Scheme 1.32: Mechanism of intermolecular hydroaminoalkylation.

The preferred reactivity for a methyl over a methylene group in case of **I.39** was explained by a more feasible aziridine formation due to a more accessible C–H bond.^[30]

However, no explanation for the opposite behavior of **1.40** (Scheme 1.34) was provided.^[45b] Recently, Doye and coworkers reported that the intramolecular hydroaminoalkylation of primary aminoalkenes catalyzed by $\text{Ti}(\text{NMe}_2)_4$ (**1.41**) involves a rate limiting C–H activation step, as indicated by a pronounced kinetic isotope effect.^[44e] The lack of a sterically demanding spectator ligand in **1.41** resulted in catalyst aggregation and a complex kinetic behavior at higher catalyst concentrations.^[44e, 47]

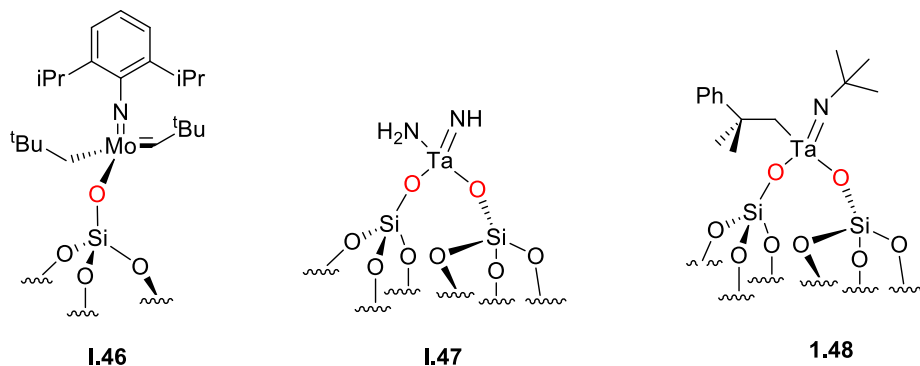
In summary, several research groups have demonstrated that the hydroaminoalkylation is a promising method for direct, atom-economic alkene-to-amine transformation. An obvious gap in the understanding of the mechanistic details of this process needs to be addressed in order to overcome its current limitations, such as narrow substrate scope, low catalytic activity and the need of harsh reaction conditions. In addition, the asymmetric hydroaminoalkylation yielding chiral amines remains underdeveloped and stereo-selectivities are, with a few exceptions, moderate at best.

1.5 Imido complexes

The imido ligand has been generally employed as an ancillary group to support high oxidation state metal centers, and an increasing number of complexes having reactive imido ligands have been shown to participate in C–H bond activation^[48] and metathesis reactions^[49]. In particular, group 4 imido^[50] complexes play a pivotal role in various important catalytic processes, such as, the intermolecular hydroamination of alkynes^[51] alkenes,^[52] hydrohydrazination of alkynes,^[53] and carboamination processes.^[54]

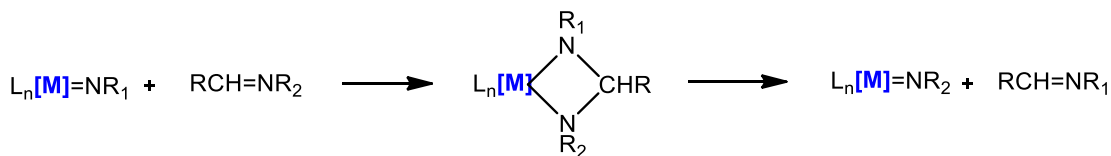
The use of imido complexes has been extended to surface organometallic chemistry as ‘inert’ ligands in the case of a tungsten imido complex based on the

Schrock complex^[55] as olefin metathesis catalysts. Another example was the dinitrogen activation with silica-supported tantalum hydrides complex in presence of hydrogen leading to the formation of the amido imido complex of tantalum $(=\text{SiO})_2\text{Ta}(=\text{NH})(\text{NH}_2)$.^[56] More recently, the surface imido complex $(=\text{SiO})_2\text{Ta}(=\text{N}^t\text{Bu})(\text{CH}_2\text{CMe}_2\text{Ph})$ was found to promote various catalytic oxo/imido hetero-metathesis transformations.^[57]



Scheme 1.33: examples of silica supported metal-imido complexes.

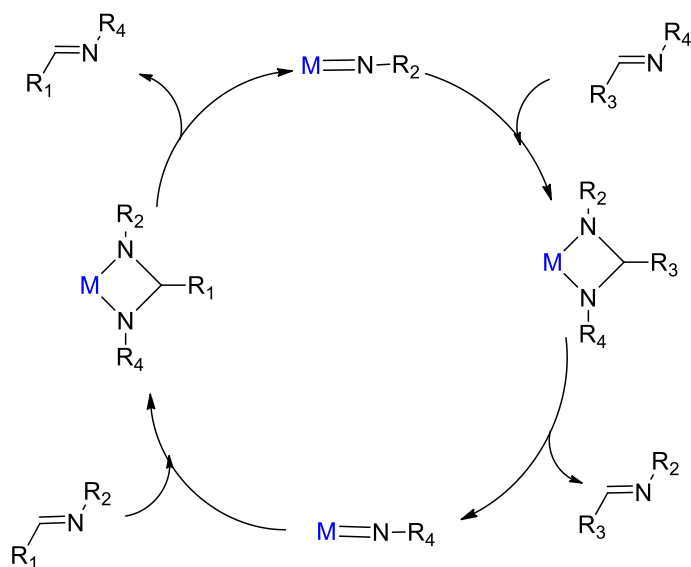
Previous works mainly described two types of $\text{M}=\text{NR}$ transfer reactions: stoichiometric and catalytic. The former passes by imide/imine stoichiometric metathesis of a metal imide with a one molecule of imine substrate (Scheme 1.33). New metal imide and imine products can be formed by transient $\text{M}=\text{N}$ bond transfer.



Scheme 1.34: Imide/Imine stoichiometric metathesis reaction.

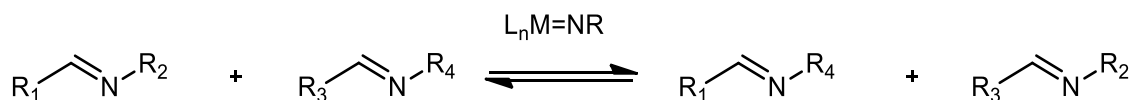
The latter, catalytic imine metathesis is somehow analogous to olefin metathesis. Two different imines afford a statistical mixture of all possible $\text{M}=\text{NR}$ exchange products. To note, the imine substrates do not react directly with each other

but may be mediated by monomeric imido-metalloocene complexes.^[58] Examples of imine metathesis for which mechanistic data were reported apparently proceed by different pathways. The viability of a Chauvin-type mechanism^[59] (Scheme 1.35) was established by Bergman and co-workers in their observation of isolable diazametallacyclic intermediates in the reaction of $\text{CpCp}'\text{Zr}(=\text{NR})(\text{THF})$ ($\text{Cp}' = \text{Cp}, \text{Cp}^*$) with imines.^[58, 60]



Scheme 1.35: Chauvin-type mechanism for imine metathesis.

In contrast, Mountford and co-workers observed no diazametallacycles and the kinetics of the reaction were consistent with a [2+2] mechanism and proposed an aminecatalyzed process to explain the reaction of $(\text{py})_3\text{Cl}_2\text{Ti}(=\text{NR})$ with imines.^[61]



Scheme 1.36: General reaction of imine\imine crosses metathesis.

More recently, imine metathesis catalyzed by a variety of transition metals (Zr, Mo, Re, Nb) became the object of increasing scrutiny in a number of research groups, most likely on account of the mechanistic analogy with the more famous and

synthetically relevant olefin metathesis. It was found that imine metathesis takes place in organic solvents at high temperature, typically around 80- 100 °C.^[62]

1.6 Conclusions and thesis organization

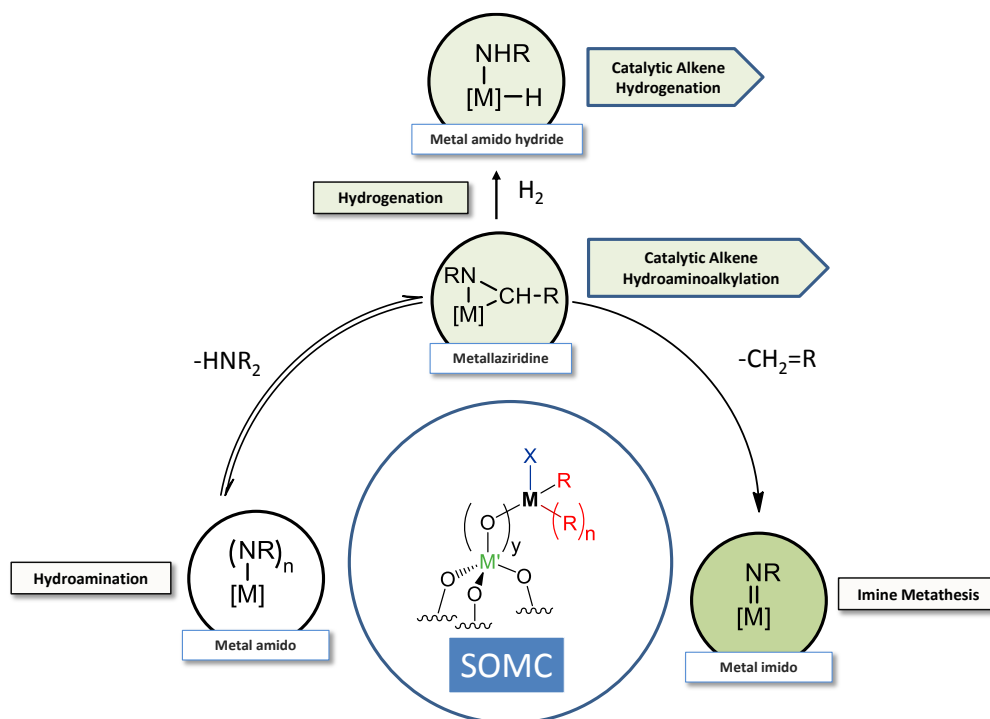
1.6.1 Summary of the present chapter

This chapter first covers concisely the field of surface organometallic chemistry including the recent advances related the surface metal fragments in catalytic applications (see 1.2) and attempted to illustrate several aspects of the chemistry of group 4 metal-nitrogen complexes relevant to this thesis. It has shown that transition metals η^2 -imine complexes display a promising and diversified reactivity, which leads, directly or indirectly, to several homogeneous catalysis such as hydroaminoalkylation (see 1.3 and 1.4), imine metathesis 1.5). It is noteworthy that while the reactivity of these metallaaziridines has been investigated, catalytic applications are scarcer. More systematic work is necessary to develop new classes of compounds which may work as starting points for exploring new chemical reactivity and explaining existing reaction better. A major obstacle to better mechanistic understanding is the scarcity of well-defined model systems for metals η^2 -imine –based catalysts. It is also desirable to develop heterogeneous catalysts that will allow hydroaminoalkylation and imine metathesis to be employed more conveniently and in a broader range of substrate. The starting point of the present work is that SOMC can provide response to both issues by providing new supported catalyst, and key intermediates that are well-defined and single-site.

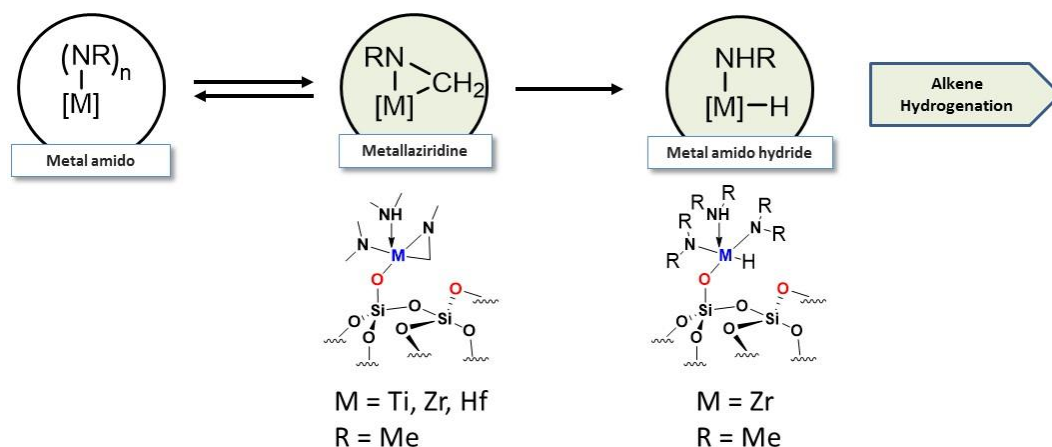
The creation of a single-site catalyst would be an important contribution to the field; in this light SOMC aims to define the reactivity of well-defined surface species as models for heterogeneous catalysts. The systematic study of the reactivity of organometallic compounds with surfaces may eventually have an impact on surface catalysis rivaling that of organometallic chemistry on homogenous catalysis.

1.6.2 Thesis organization

This thesis aims to explore the chemistry of well-defined silica-supported group 4 and group 5 complexes that contain one or more multiply-bonded nitrogen atoms. Such species have been recognized as crucial intermediates in many catalytic reactions (e.g. hydroaminoalkylation, olefin hydrogenation, imine metathesis...). The first chapter provided a bibliographic overview of the preparation and the reactivity of group 4 and 5 complexes grafted onto silica towards hydroaminoalkylation and imine metathesis catalysis.



The second chapter deals with the isolation and the characterization of a series of well-defined group 4 η^2 -imine complexes surface species. 2D solid-state NMR (^1H - ^{13}C HETCOR, Multiple Quantum) experiments have revealed consistently a unique structural rearrangement, viz azametallacycle occurring on the immobilized metal-amido ligands. Hydrogenolysis of the sole Zr-C bond in such species gives selectively a silica-supported zirconium monohydride that can perform the catalytic hydrogenation of olefins.



Scheme 1.37: Synthetic strategy deployed in Chapter II.

The third chapter examines the mechanistic studies of the intermolecular hydroaminoalkylation using SOMC to identify the key metallacyclic surface intermediates (silica-supported three-membered and five-membered). The catalyst was regenerated by protonolysis and afforded pure amine. Catalytic testing of a selection of amine compounds with variable electronic properties was carried out.

The fourth chapter deals with the generation and the characterization of well-defined silica-supported zirconium-imido complexes. The resulting species effectively catalyzes imine/imine cross-metathesis and thus considered as the first heterogeneous catalysts active for imine metathesis.

The fifth chapter studies the reaction of SBA₁₅₋₁₁₀₀ °C with dry aniline and derivatives leading to opening strained siloxane bridges into acid-base paired functionalities (formation of N-phenylsilanamine-silanol pairs). This approach was successfully applied to the design of a series of aniline derivatives bifunctional SBA₁₅. The efficiency of this methodology is strongly supported and unambiguously highlighted by strong solid state characterizations: FT-IR, 1D and 2D solid state NMR spectroscopy and even dynamic nuclear polarization enhanced ²⁹Si and ¹⁵N, XRD and TEM... Importantly, a plethora of well-organized bifunctional catalysts with different electronic properties were successfully synthesis and tested in the Knoevenagel condensation.

1.7 References

- [1] G. W. Parshall, R. E. Putscher, *J Chem Educ* **1986**, *63*, 189-191.
- [2] S. L. Scott, J. M. Basset, G. P. Niccolai, C. C. Santini, J. P. Candy, C. Lecuyer, F. Quignard, A. Choplin, *New J Chem* **1994**, *18*, 115-122.
- [3] S. L. Scott, J. M. Basset, *J Mol Catal* **1994**, *86*, 5-22.
- [4] A. Bendjeriou-Sedjerari, J. D. A. Pelletier, E. Abou-Hamad, L. Emsley, J. M. Basset, *Chem Commun* **2012**, *48*, 3067-3069.
- [5] A. B. J.-M. Basset, F. Bayard, J.-P. Candy, C. Coperet, A. De Mallmann, G., E. K. Godard, F. Lefebvre, C. Lucas, S. Norsic, K. Pelzer, A. Quadrelli, C., D. S. Santini, F. Stoffelbach, M. Taoufik, C. Thieuleux, J. Thivolle-Cazat, L., L. Veyre, *Mod. Surf. Organomet. Chem*, **2009**.
- [6] V. R. Dufaud, J. M. Basset, *Angew Chem Int Edit* **1998**, *37*, 806-810.
- [7] aF. Quignard, A. Choplin, J. M. Basset, *J Chem Soc Chem Comm* **1991**, 1589-1590; bF. Quignard, C. Lecuyer, C. Bougault, F. Lefebvre, A. Choplin, D. Olivier, J. M. Basset, *Inorg Chem* **1992**, *31*, 928-930; cC. Thieuleux, E. A. Quadrelli, J. M. Basset, J. Dobler, J. Sauer, *Chem Commun* **2004**, 1729-1731.
- [8] C. Larabi, N. Merle, S. Norsic, M. Taoufik, A. Baudouin, C. Lucas, J. Thivolle-Cazat, A. de Mallmann, J. M. Basset, *Organometallics* **2009**, *28*, 5647-5655.
- [9] G. Tosin, M. Delgado, A. Baudouin, C. C. Santini, F. Bayard, J. M. Basset, *Organometallics* **2010**, *29*, 1312-1322.
- [10] E. Callens, N. Riache, K. Talbi, J. M. Basset, *Chem Commun* **2015**, *51*, 15300-15303.
- [11] N. Riache, E. Callens, J. Espinas, A. Dery, M. K. Samantaray, R. Dey, J. M. Basset, *Catal Sci Technol* **2015**, *5*, 280-285.
- [12] D. Soulivong, S. Norsic, M. Taoufik, C. Coperet, J. Thivolle-Cazat, S. Chakka, J. M. Basset, *J. Am. Chem. Soc.* **2008**, *130*, 5044-+.
- [13] F. Blanc, J. Thivolle-Cazat, J. M. Basset, C. Coperet, A. S. Hock, Z. J. Tonzetich, R. R. Schrock, *J. Am. Chem. Soc.* **2007**, *129*, 1044-1045.
- [14] M. Taoufik, E. Le Roux, J. Thivolle-Cazat, J. M. Basset, *Angew Chem Int Edit* **2007**, *46*, 7202-7205.
- [15] J. M. Basset, C. Coperet, D. Soulivong, M. Taoufik, J. T. Cazat, *Accounts Chem Res* **2010**, *43*, 323-334.

- [16] M. Taoufik, E. Schwab, M. Schultz, D. Vanoppen, M. Walter, J. Thivolle-Cazat, J. M. Basset, *Chem Commun* **2004**, 1434-1435.
- [17] J. D. Pelletier, J. M. Basset, *Acc Chem Res* **2016**.
- [18] aS. A. T. Cummings, J. A.; Norton, J. R., *Synthesis and Reactivity of Zirconaaziridines. In New Aspects of Zirconium Containing Organic Compounds*, Vol. 10, Springer-Verlag ed., **2005**; bM. Gomez, *Eur J Inorg Chem* **2003**, 3681-3697.
- [19] J. A. T. Sarah A. Cummings, Jack R. Norton, *New Aspects of Zirconium Containing Organic Compounds, Vol. I. Marek*, Springer, **2005**.
- [20] aS. L. Buchwald, M. W. Wannamaker, B. T. Watson, *J Am Chem Soc* **1989**, *111*, 776-777; bS. L. Buchwald, B. T. Watson, M. W. Wannamaker, J. C. Dewan, *J Am Chem Soc* **1989**, *111*, 4486-4494.
- [21] R. B. Grossman, W. M. Davis, S. L. Buchwald, *J Am Chem Soc* **1991**, *113*, 2321-2322.
- [22] aN. Coles, R. J. Whitby, J. Blagg, *Synlett* **1990**, 271-272; bN. Coles, R. J. Whitby, J. Blagg, *Synlett* **1992**, 143-145; cM. C. J. Harris, R. J. Whitby, J. Blagg, *Tetrahedron Lett* **1994**, *35*, 2431-2434; dM. C. J. Harris, R. J. Whitby, J. Blagg, *Tetrahedron Lett* **1995**, *36*, 4287-4290; eN. Coles, M. C. J. Harris, R. J. Whitby, J. Blagg, *Organometallics* **1994**, *13*, 190-199; fJ. M. Davis, R. J. Whitby, A. Jaxachamiec, *Tetrahedron Lett* **1994**, *35*, 1445-1448.
- [23] E. Klei, J. H. Teuben, *J Organomet Chem* **1981**, *214*, 53-64.
- [24] J. A. Bexrud, P. Eisenberger, D. C. Leitch, P. R. Payne, L. L. Schafer, *J Am Chem Soc* **2009**, *131*, 2116-+.
- [25] M. J. Scott, S. J. Lippard, *Organometallics* **1997**, *16*, 5857-5868.
- [26] A. Castro, M. V. Galakhov, M. Gomez, P. Gomez-Sal, A. Martin, F. Sanchez, P. Velasco, *Eur J Inorg Chem* **2000**, 2047-2054.
- [27] J. S. Figueroa, C. C. Cummins, *J Am Chem Soc* **2003**, *125*, 4020-4021.
- [28] E.-i. H. Negishi, S., *Synthesis and Reactivity of Zirconocene Derivatives. In Titanium and Zirconium in Organic Synthesis*, Marek, I., Ed. Wiley-VCH, **2002**.
- [29] J. M. Mayer, C. J. Curtis, J. E. Bercaw, *J Am Chem Soc* **1983**, *105*, 2651-2660.
- [30] S. B. Herzon, J. F. Hartwig, *J Am Chem Soc* **2008**, *130*, 14940-+.
- [31] J. R. Clark, P. E. Fanwick, I. P. Rothwell, *Organometallics* **1996**, *15*, 3232-3237.
- [32] K. Takai, T. Ishiyama, H. Yasue, T. Nobunaka, M. Itoh, T. Oshiki, K. Mashima, K. Tani, *Organometallics* **1998**, *17*, 5128-5132.
- [33] aE.-i. H. Negishi, S., *Synthesis and Reactivity of Zirconocene Derivatives. In Titanium and Zirconium in Organic Synthesis*, **2002**; bM. Jensen, T. Livinghouse, *J Am Chem Soc* **1989**, *111*, 4495-4496; cE. Negishi, F. E. Cederbaum, T. Takahashi, *Tetrahedron Lett* **1986**, *27*, 2829-2832; dF. Soleil, R. Choukroun, *J Am Chem Soc* **1997**, *119*, 2938-2939.
- [34] U. B. Rosenthal, V. V., *Marek, I., Ed. Wiley-VCH: Weinheim* **2002**, 355-387.
- [35] aF. U. Sato, H., *Titanium(II) Alkoxides in Organic Synthesis. In Titanium and Zirconium in Organic Synthesis*, **2002**; bF. U. Sato, H., *Titanium(II) Alkoxides in Organic Synthesis. In Titanium and Zirconium in Organic Synthesis*, Wiley-VCH: Weinheim, **2002**.
- [36] Y. Gao, Y. Yoshida, F. Sato, *Synlett* **1997**, 1353-1354.
- [37] K. Fukuhara, S. Okamoto, F. Sato, *Org Lett* **2003**, *5*, 2145-2148.
- [38] T. Sielisch, U. Behrens, *J Organomet Chem* **1986**, *310*, 179-187.
- [39] aL. D. Durfee, P. E. Fanwick, I. P. Rothwell, K. Folting, J. C. Huffman, *J Am Chem Soc* **1987**, *109*, 4720-4722; bL. D. Durfee, J. E. Hill, P. E. Fanwick, I. P. Rothwell, *Organometallics* **1990**, *9*, 75-80.

- [40] D. A. Gately, J. R. Norton, P. A. Goodson, *J Am Chem Soc* **1995**, *117*, 986-996.
- [41] J. A. Tunge, C. J. Czerwinski, D. A. Gately, J. R. Norton, *Organometallics* **2001**, *20*, 254-260.
- [42] P. Eisenberger, L. L. Schafer, *Pure Appl Chem* **2010**, *82*, 1503-1515.
- [43] aM. G. Clerici, F. Maspero, *Synthesis-Stuttgart* **1980**, 305-306; bW. A. Nugent, D. W. Ovenall, S. J. Holmes, *Organometallics* **1983**, *2*, 161-162.
- [44] aC. Muller, W. G. Saak, S. Doye, *Eur J Org Chem* **2008**, 2731-2739; bR. Kubiak, I. Prochnow, S. Doye, *Angew Chem Int Edit* **2009**, *48*, 1153-1156; cI. Prochnow, R. Kubiak, O. N. Frey, R. Beckhaus, S. Doye, *Chemcatchem* **2009**, *1*, 162-172; dR. Kubiak, I. Prochnow, S. Doye, *Angew Chem Int Edit* **2010**, *49*, 2626-2629; eI. Prochnow, P. Zark, T. Muller, S. Doye, *Angew Chem Int Edit* **2011**, *50*, 6401-6405.
- [45] aS. B. Herzon, J. F. Hartwig, *J Am Chem Soc* **2007**, *129*, 6690-+; bP. Eisenberger, R. O. Ayinla, J. M. P. Lauzon, L. L. Schafer, *Angew Chem Int Edit* **2009**, *48*, 8361-8365; cG. F. Zi, F. R. Zhang, H. B. Song, *Chem Commun* **2010**, *46*, 6296-6298; dF. R. Zhang, H. B. Song, G. F. Zi, *Dalton T* **2011**, *40*, 1547-1566.
- [46] S. A. Cummings, J. R. Norton, *Abstr Pap Am Chem S* **2005**, *229*, U1087-U1087.
- [47] R. Kempe, *Angew Chem Int Edit* **2000**, *39*, 468-493.
- [48] aD. W. Stephan, J. C. Stewart, F. Guerin, R. E. V. H. Spence, W. Xu, D. G. Harrison, *Organometallics* **1999**, *18*, 1116-1118; bN. Yue, E. Hollink, F. Guerin, D. W. Stephan, *Organometallics* **2001**, *20*, 4424-4433.
- [49] M. W. Bouwkamp, A. A. Batinas, P. T. Witte, T. Hubregtse, J. Dam, A. Meetsma, J. H. Teuben, B. Hessen, *Organometallics* **2008**, *27*, 4071-4082.
- [50] aP. J. Walsh, A. M. Baranger, R. G. Bergman, *J Am Chem Soc* **1992**, *114*, 1708-1719; bJ. K. F. Buijink, J. H. Teuben, H. Kooijman, *Abstr Pap Am Chem S* **1994**, *207*, 248-Inor.
- [51] D. D. Devore, J. D. Lichtenhan, F. Takusagawa, E. A. Maatta, *J Am Chem Soc* **1987**, *109*, 7408-7416.
- [52] E. A. Maatta, *Inorg Chem* **1984**, *23*, 2560-2561.
- [53] aF. Preuss, H. Becker, *Z Naturforsch B* **1986**, *41*, 185-190; bF. Preuss, H. Becker, H. J. Hausler, *Z Naturforsch B* **1987**, *42*, 881-888; cF. Preuss, H. Becker, J. Kaub, W. S. Sheldrick, *Z Naturforsch B* **1988**, *43*, 1195-1200; dF. Preuss, E. Fuchslocher, E. Leber, W. Towae, *Z Naturforsch B* **1989**, *44*, 271-277.
- [54] aJ. I. Song, S. Gambarotta, *Chem-Eur J* **1996**, *2*, 1258-1263; bC. C. Cummins, R. R. Schrock, W. M. Davis, *Inorg Chem* **1994**, *33*, 1448-1457.
- [55] aB. Rhers, E. A. Quadrelli, A. Baudouin, M. Taoufik, C. Coperet, F. Lefebvre, J. M. Basset, B. Fenet, A. Sinha, R. R. Schrock, *J Organomet Chem* **2006**, *691*, 5448-5455; bB. Rhers, A. Salameh, A. Baudouin, E. A. Quadrelli, M. Taoufik, C. Coperet, F. Lefebvre, J. M. Basset, X. Solans-Monfort, O. Eisenstein, W. W. Lukens, L. P. H. Lopez, A. Sinha, R. R. Schrock, *Organometallics* **2006**, *25*, 3554-3557.
- [56] P. Avenier, M. Taoufik, A. Lesage, X. Solans-Monfort, A. Baudouin, A. de Mallmann, L. Veyre, J. M. Basset, O. Eisenstein, L. Emsley, E. A. Quadrelli, *Science* **2007**, *317*, 1056-1060.
- [57] P. A. Zhizhko, A. A. Zhizhin, O. A. Belyakova, Y. V. Zubavichus, Y. G. Kolyagin, D. N. Zarubin, N. A. Ustynyuk, *Organometallics* **2013**, *32*, 3611-3617.
- [58] aK. E. Meyer, P. J. Walsh, R. G. Bergman, *J Am Chem Soc* **1995**, *117*, 974-985; bK. E. Meyer, P. J. Walsh, R. G. Bergman, *J Am Chem Soc* **1994**, *116*, 2669-2670.
- [59] J. L. Herisson, Y. Chauvin, *Makromolekul Chem* **1971**, *141*, 161-&.
- [60] R. L. Zuckerman, S. W. Krska, R. G. Bergman, *J Am Chem Soc* **2000**, *122*, 751-761.

- [61] aJ. M. McInnes, P. Mountford, *Chem Commun* **1998**, 1669-1670; bP. Mountford, *Chem Commun* **1997**, 2127-2134.
- [62] M. Ciaccia, R. Cacciapaglia, P. Mencarelli, L. Mandolini, S. Di Stefano, *Chem Sci* **2013**, *4*, 2253-2261.

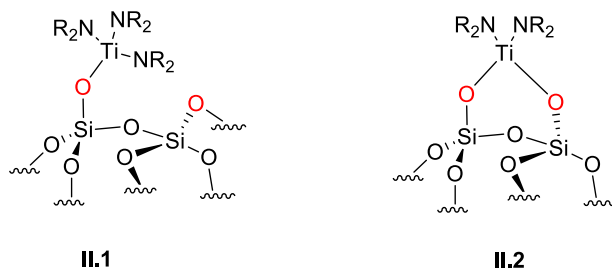
Chapter 2: Isolation of Silica-Supported Metallaaziridines and Generation of Well-Defined Single-Site Monohydride Zirconium Species

2.1 Introduction

This chapter is dedicated to the examination of metallaaziridine complexes based on group 4 transition metals and supported onto silicon oxide materials. Grafting metal-amide complexes on silica surfaces have scarcely been investigated within the surface organometallic chemistry (SOMC) framework. As discussed in the previous chapter, this also present an opportunity to isolate surface organometallic fragment (SOMF) related to metal amide (viz. MN and MNC).

2.1.1 Metal-amides complexes and surface organometallic chemistry

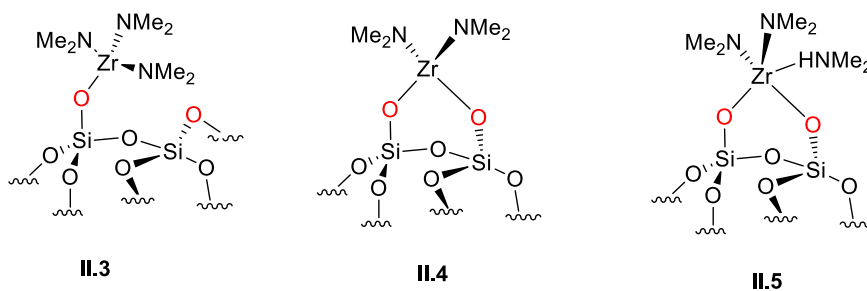
Most of the examples documented on supported group 4 metal bearing amido ligands were focused more on the podality and the coordination sphere of the complexes than on the reactivity of the M-N fragment. This is due, in part, to the assumption that the metal coordination sphere would remain unchanged, except for the M-O bond formed from the grafting, compared to the homoleptic precursors. Scott *et al* examined the grafting of $Ti(NR_2)_4$ (R = Me, Et) with partially dehydroxylated Aerosil.



Scheme 2.38: Resulting products after reaction of $Ti(NR_2)_4$ on SiO_{2-200} (II.1) and SiO_{2-700} (II.2).

Irreversible grafting occurred on dehydroxylated silica at 200 and 500 °C giving bis- and tris- (dialkylamido) titanium (IV) surface fragments, respectively (scheme 2.38).^[1]

Sadow *et al* reported recently the reaction of $Zr(NMe_2)_4$ and mesoporous silica nanoparticle (MSN) giving $Zr(NMe_2)_n@MSN$. A series of SSNMR experiments, such as ^{15}N Hetero experiments and DNP-enhanced CPMAS ^{15}N SSNMR, showed that zirconium is primarily bonded to dimethylamide groups, with a small quantity of coordinated dimethylamine. The resulting surface are a mixture of mainly monopodal $[≡Si-O-Zr(NMe_2)_3]$ (more than 90%) with a small amount as diamido- amine $[≡Si-O)_2Zr(NMe_2)_2(NHMe_2)]$ (Scheme 2.39).^[2]

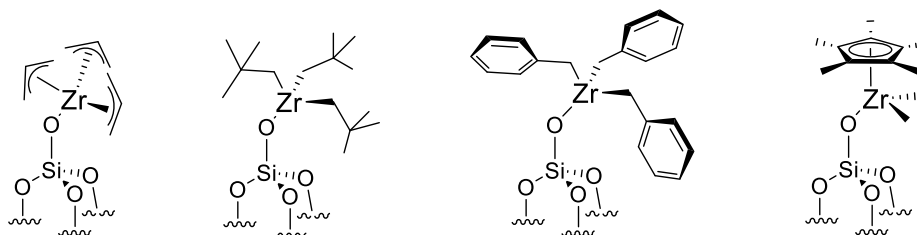


Scheme 2.39: Resulting products after grafting of $Zr(NMe_2)_4$ on MSN.

2.1.2 Silica-supported zirconium-hydride complexes

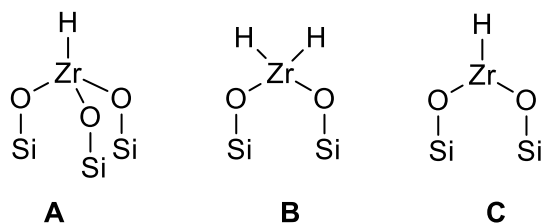
Zirconium hydrides supported on metal-oxide are notoriously difficult to prepare selectively.^[3] Interests in such species are high due to their unique catalytic performances, particularly regarding hydrocarbons transformations (e.g. Ziegler Natta reverse polymerization).^[4] This remarkable reactivity toward C-H or C-C bond activation has been observed for supported group 4 metal hydrides. It has been successfully harnessed to promote heterogeneous catalysis:^[5] olefin polymerization,^[6] the

hydrogenation of olefins,^[7] isotopic exchange in alkanes,^[8] as well as hydroisomerization and hydrogenolysis of alkanes.^[9] The most investigated zirconium precatalysts were prepared by grafting homoleptic organometallic complexes (MR₄ with M = Zr; R = allyl,^[10] neopentyl,^[5] benzyl,^[11] etc.) onto the surface of partially dehydroxylated silica (Scheme 2.40).



Scheme 2.40: Silica-supported zirconium precatalysts hydrogenation of olefins^[7], isotopic exchange in alkanes^[8] and hydroisomerization and hydrogenolysis of alkanes.^[9]

The catalytically active zirconium hydride species can then be generated by hydrogenolysis (*viz* hydrogen treatment at temperature from 150 to 200 °C).^[4a] The resulting solid exhibits always a mixture of metal hydrides species. In those, the zirconium atom bears one or two hydrogen ligands and be tethered to the surface by two or three covalent bonds.^[12] The major species established are Zr^{IV}, [(≡Si-O)₃ZrH] (**A**) and [(≡Si-O)₂ZrH₂] (**B**) with the existence of the minor Zr^{III}, [(≡Si-O)₂ZrH] (**C**), being reported (Figure 2.41). A consistent body of works carried over the last two decades had allowed the identification of their distinct spectroscopic signatures both in FTIR and ¹H SS NMR.



Scheme 2.41: Reported model of silica-supported zirconium hydrides.

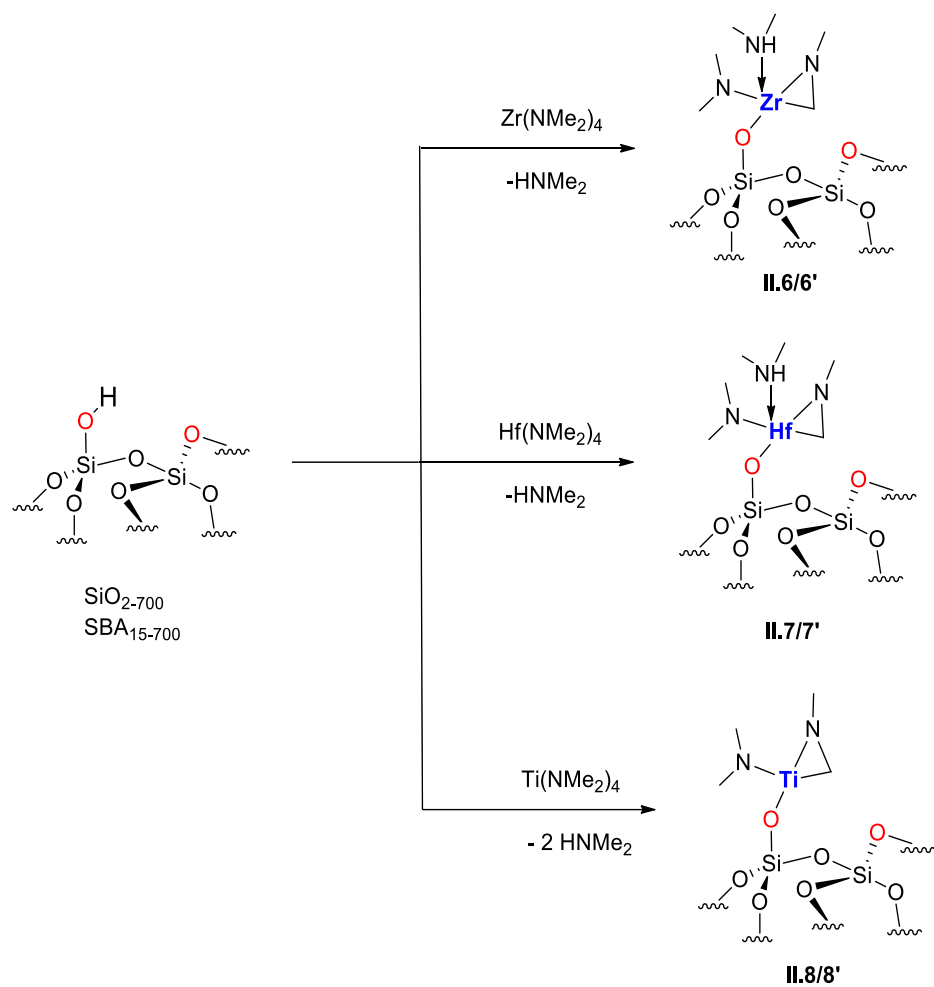
Yet no example of a selective preparation of one type of zirconium hydride had been reported to date. The interactions between siloxane groups displayed on the surface and the oxophilic zirconium hydride intermediates are generally assumed to be responsible for this lack of selectivity. This is particularly important as the reactivity of the mono hydride is assumed to differ considerably from that of the bis hydride.^[7a] According to DFT calculations, the latter is reactive enough to conduct alkane hydrogenolysis while the former can only perform alkene hydrogenation.^[7a, 9] Experimentally, both zirconium hydrides are generated simultaneously when neopentyl zirconium grafted on silica is contacted with hydrogen.^[4a] The intermediates are then believed to react with the vicinal siloxane groups with concomitant production of surface silane ($\equiv\text{Si-H}$) and bipodal Zr hydride(s). Directing the reactivity of the grafted zirconium atom during the hydrogenolysis is hence desirable as a mean to selectively produce either the mono- or the bis- hydride. One possible way is to use precursors different that zirconium alkyls (e.g. ZrNp_4).^[13] In these complexes, the equivalent ligands can all undergo hydrogenolysis to generate the corresponding highly reactive hydrides, which can then react with the closest oxygen of the silica surface. Heteroleptic complexes with electron-rich ligands, such as Cp^* , can stabilize the zirconium center but also render the corresponding hydride less active.

2.2 Scope of the chapter

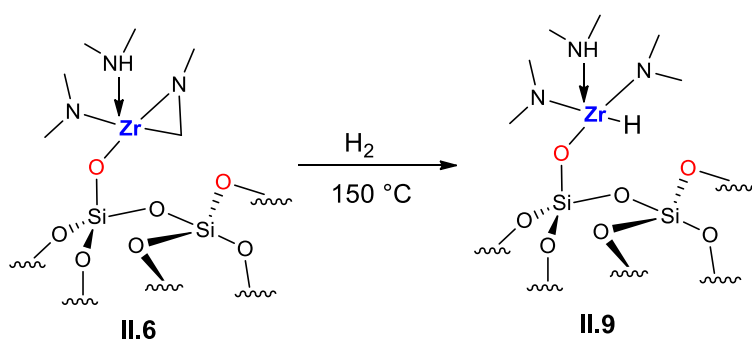
A brief overview of the background of group 4 silica supported metal bearing amido ligands and zirconium hydride has been provided (see section 2.1). The preparation and the characterization of examples including titanium, zirconium and hafnium will be tackled first (see section 2.3). The reactivity of the one selected zirconaaziridine has been investigated further by testing its performance for alkene hydrogenation and alkene metathesis (see section 2.4).

The first part of this chapter deals with the reaction of group 4 metal-dimethyl amine $M(\text{NMe}_2)_4$ complexes with partially dehydroxylated silica surfaces. We report the isolation of the zirconaaziridine surface $[\equiv\text{Si-O-M}(\text{HNMe}_2)(\eta^2\text{NMeCH}_2)(\text{NMe}_2)]$ ($M = \text{Zr}, \text{Hf}$) and $[\equiv\text{Si-O-M}(\eta^2\text{NMeCH}_2)(\text{NMe}_2)]$ ($M = \text{Ti}$) (Scheme 2.42). The metallacycle group was obtained by spontaneous rearrangement of the amide ligands during the reaction of $M(\text{NMe}_2)_4$ with surface silanols. These structures were evidenced by sophisticated Solid-State SS NMR experiments, infrared spectroscopy, elemental analysis and EXAFS.

The second part of this chapter deals with the hydrogenolysis of the sole Zr-C bond in **II.6** to target selectively a silica-supported zirconium monohydride. We report the first single-site silica-supported mono-hydride $[\equiv\text{Si-O-Zr}(\text{HNMe}_2)(\text{NMe}_2)_2\text{H}]$ (**II.9**) (Scheme 2.43) obtained by hydrogenolysis of azazirconacyclopropane $[\equiv\text{Si-O-Zr}(\text{HNMe}_2)(\eta^2\text{NMeCH}_2)(\text{NMe}_2)]$ (**II.6**). The amido ligands are capable to provide increased stability to the zirconium hydride species compared to their alkyl counterpart. Both **II.6** and **II.9** were characterized using elemental analysis, FTIR and combining multidimensional solid state NMR experiments (^1H , ^{13}C , ^{15}N).



Scheme 2.42: Reactivity of group 4 $\text{M(NMe}_2)_4$ with highly dehydroxylated silica surfaces.



Scheme 2.43: Generation of silica-supported zirconium monohydride.

2.3 Grafting of tetrakis-dimethylamide group 4 complexes on silica supports

Exposition of fumed silica and SBA₁₅ pretreated at 700°C to an excess of M(NMe₂)₄ results in an irreversible chemisorption of the metal complex onto the surface. Silica supports, initially colorless, acquires a yellow color over the course of the reaction when using titanium precursor but remain colorless in the cases of its zirconium and hafnium counterparts.

2.3.1 Characterization of tetrakis-dimethylamide group 4 complexes on silica supports

2.3.1.1 Infrared characterization and elemental analysis

Comparison of the FTIR spectra of the silica support before and after contact with M(NMe₂)₄ reveals the consumption of all available surface silanols and the appearing of bands typical of the alkyl vibrations. With either SBA₁₅₋₇₀₀ or SiO₂₋₇₀₀, the intense $\nu(\text{O-H})$ mode of silica located at 3747 cm⁻¹ disappears (Figures 2.1 and 2.2). New bands appear with the high frequency modes in the C-H stretching and bending regions (intense bands at 2967-2776 cm⁻¹; CH stretching and weak bands in the 1500-1400 cm⁻¹; C-H bending). It is noteworthy that a broad and weak signal is observed at around 3294 cm⁻¹, ascribed to N-H band, and consistently with the presence of physisorbed dimethylamine.

After reaction of Zr(NMe₂)₄, Ti(NMe₂)₄ and Hf(NMe₂)₄ with either SBA₁₅₋₇₀₀ or SiO₂₋₇₀₀, the IR spectra of the corresponding grafted metal complexes were almost similar except for the absence of the peak at 3294 cm⁻¹ in the case of the grafted of Ti(NMe₂)₄ (Figure 2.1 and 2.2).

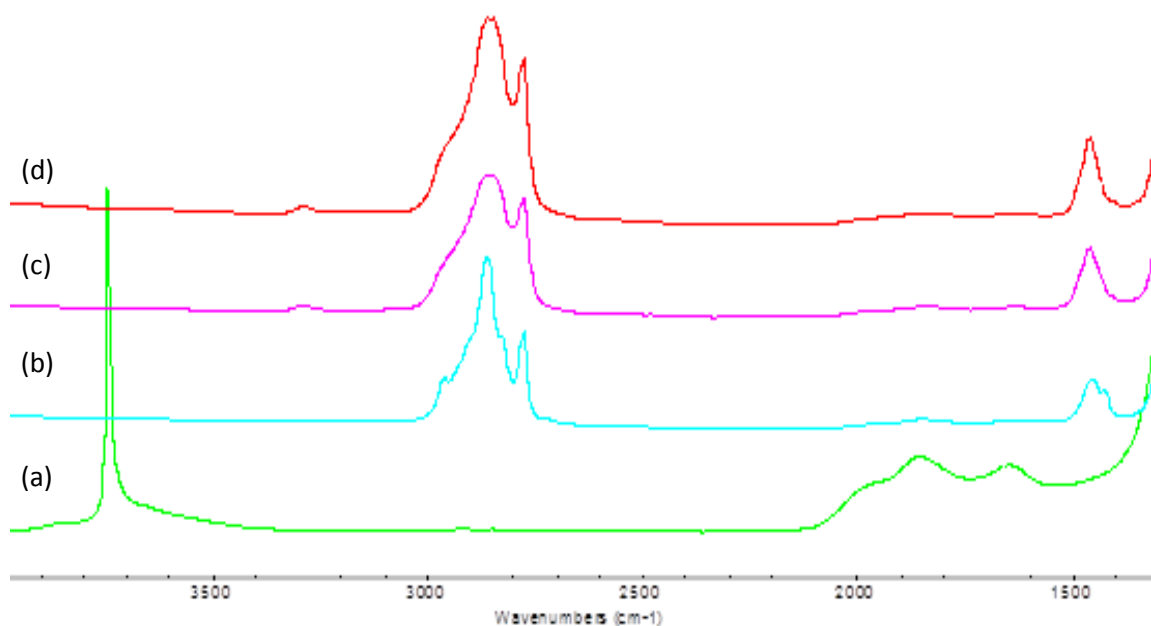


Figure 2.1: In situ FTIR difference spectra of (a) self-supporting SBA₁₅₋₇₀₀ pellet and (b) after reaction with Ti(NMe₂)₄ and (c) after reaction with Zr(NMe₂)₄ and (d) after reaction with Hf(NMe₂)₄.

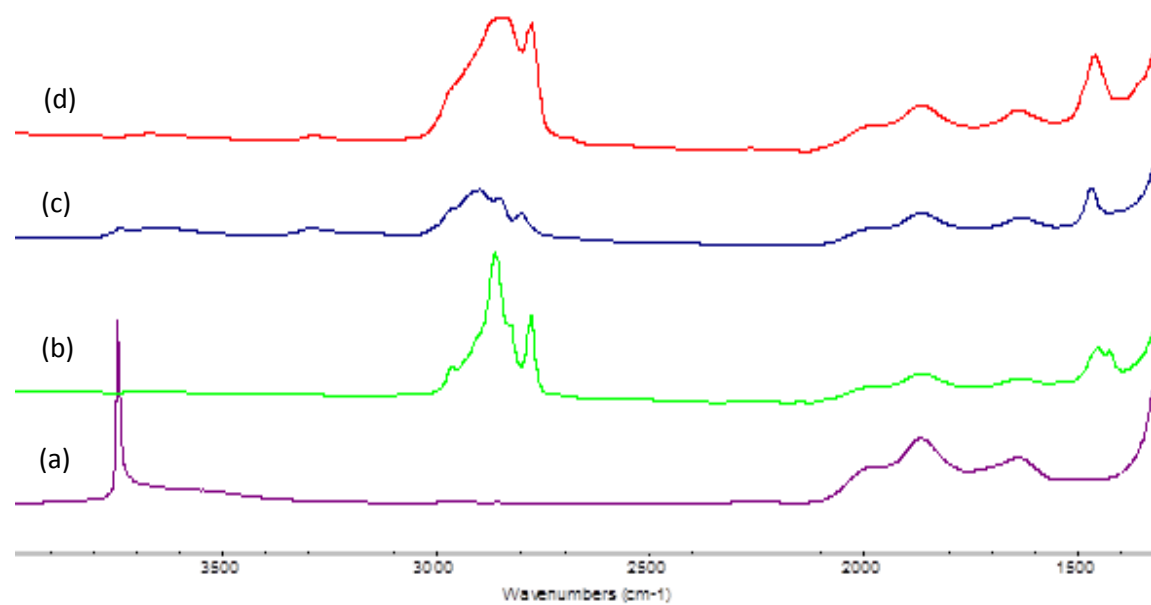


Figure 2.2: In situ FTIR difference spectra of (a) self-supporting SiO₂₋₇₀₀ pellet and (b) after reaction with Ti(NMe₂)₄ and (c) after reaction with Zr(NMe₂)₄ and (d) after reaction with Hf(NMe₂)₄.

Elemental analysis of the SBA₁₅₋₇₀₀ zirconium grafted surface gave 10.1% Zr, 10.1% C and 5.58% N. The metal content of the solid at about 1.03 zirconium per silanols confirms the total reaction of the silanols. The ratios of nitrogen and carbon against the zirconium content, respectively (3.61 N/Zr (expd 3) and 7.60 C/Zr (expd 6)) were higher than expected for a tris-amido monopodal surface species. It was then postulated that a significant amount of dimethylamine (released by the protolysis by the silanols on the amido ligand) may remain adsorbed on the surface and thus explain the band observed at $\nu = 3294 \text{ cm}^{-1}$ (N-H stretching).^[14] Longer drying time of the powder did not reveal any decrease of the 3292 cm^{-1} signal, hence suggesting the presence of dimethylamine strongly physisorbed onto the silica support.^[14] To assess the validity of the proposed hypothesis, we devised a series of experiments to examine the grafting. Silica enriched with deuterium (up to 90%) was prepared by three cycles of treatment of D₂O followed by dehydroxylation under high vacuum. After grafting of Zr(NMe₂)₄ on the deuterated silica, FTIR spectra of a pressed pellet was recorded. The 3294 cm^{-1} signal cannot be observed while a weak and broad signal around 2500 cm^{-1} can be detected (Figure 2.3). This indicates that the proton in HNMe₂ originates from the surface silanols and is the result of the grafting process.

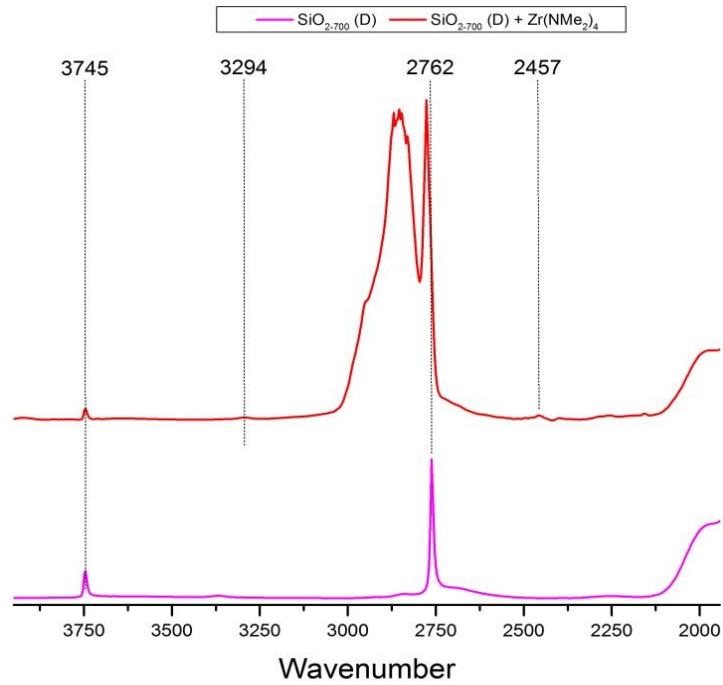


Figure 2.3: FTIR of deuterated SiO_{2-700} (pink) and after reaction with $\text{Zr}(\text{NMe}_2)_4$ (red).

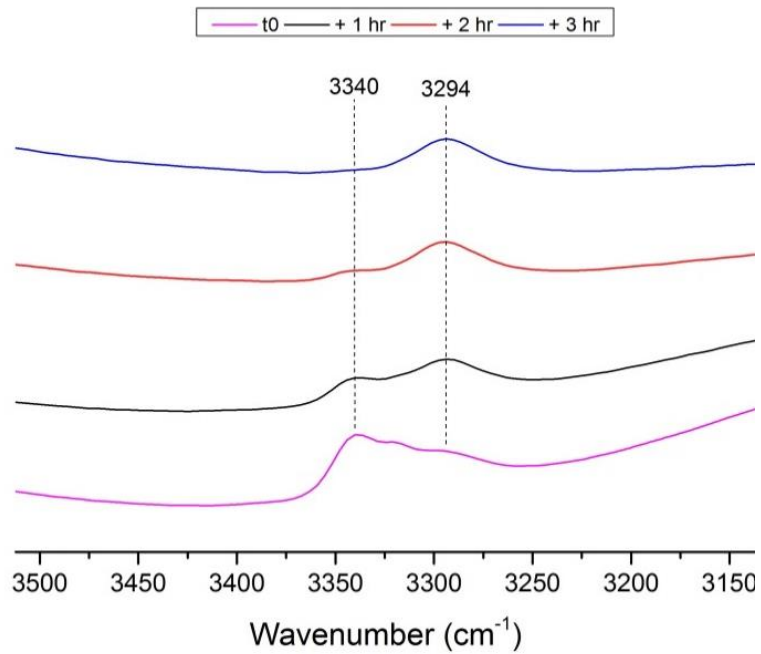
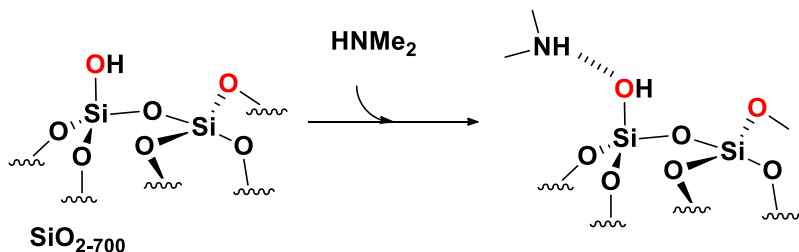


Figure 2.4: FTIR of SiO_{2-700} treated with $\text{Zr}(\text{NMe}_2)_4$, t_0 (purple) after 1 hour (black), 2 hour (red) and 3 hour (blue). The spectral width has been reduced to show the NH vibration range (3150 to 3500 cm^{-1}).

In another experiment, we carried the grafting without any solvent using a pellet of silica (not enriched with deuterium) on which $\text{Zr}(\text{NMe}_2)_4$ was sublimed. Immediately after the first contact, two overlapping small bands at 3294 and 3340 cm^{-1} were observed (Figure 2.4). As the grafting progresses, the proportion between them changes as the 3294 cm^{-1} signal, initially the smallest one becomes the only one after 3 hrs. This confirms that during the grafting an HNMe_2 is interacting probably weakly and temporally with the surface silanols, presumably by hydrogen bonding with the hydroxyl.

Complementary experiments attempted to recreate these phenomena by contacting SiO_{2-700} with gaseous dimethyl amine in the absence of zirconium complex (Scheme 2.44). The only band consistent with that of an amine NH is observed at 3337 cm^{-1} (Figure 2.5). It differs from the persistent band observed during the grafting reaction (3294 cm^{-1}) and it disappears by evacuation under high vacuum overnight.



Scheme 2.44: Reaction of silica with dimethylamine.

Moreover, the intensity of the silanols band at 3747 cm^{-1} is inversely correlated to that of the amine; low after contacting with HNMe_2 and high when the NH signal has disappeared. After the evacuation, weak signals in the alkyl region indicate that some dimethylamine remains physisorbed onto the surface. However, no NH signal can be

then detected. This suggests that silanols are the main interacting group for retaining the amine on a silica surface prior grafting; only trace amount remains physisorbed onto the surface and do not seem to generate an observable NH vibration.

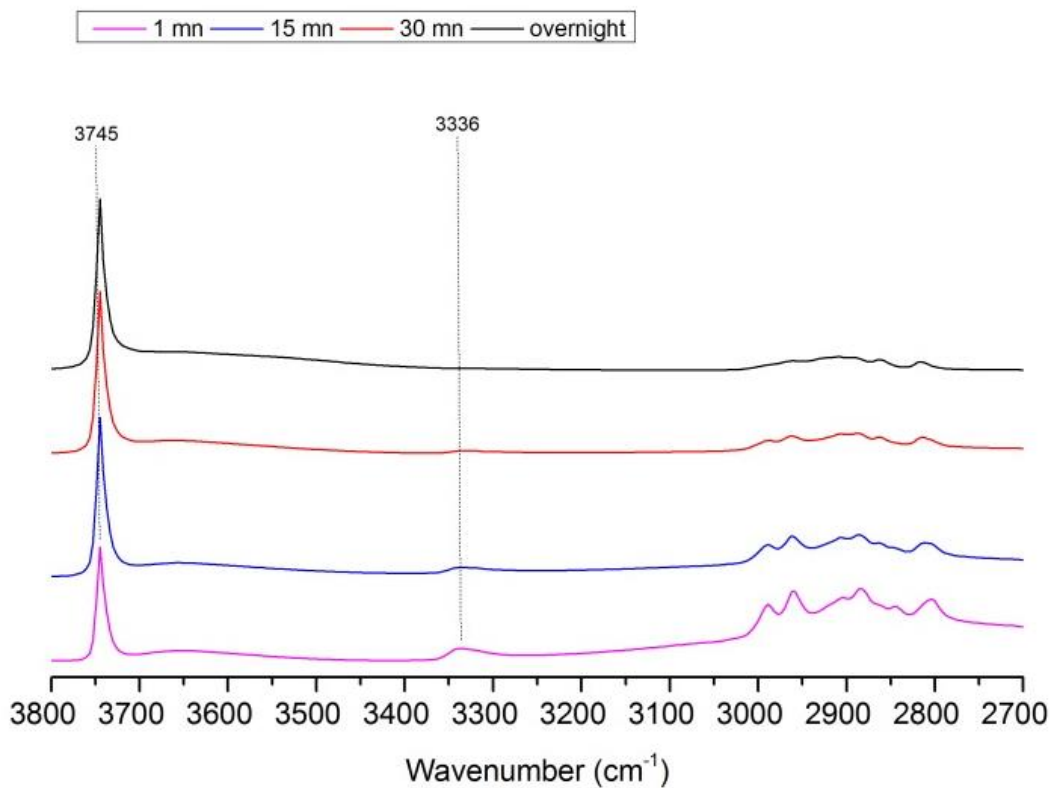


Figure 2.5: FTIR of SiO₂₋₇₀₀ treated with dimethyl amine then evacuated under vacuum (10⁻⁴ mbar) after 1 min (pink), 15 min (blue), 30 min (red) and 18 hrs (black).

As a results of these experiments the NH band at 3294 cm⁻¹ is only observed when zirconium is grafted on silica and not when HNMe₂ is adsorbed on SiO₂₋₇₀₀. Consequently it can be assumed that it is corresponding to the $\nu(\text{NH})$ vibration of HNMe₂ coordinated to zirconium.

2.3.1.2 SS NMR characterization

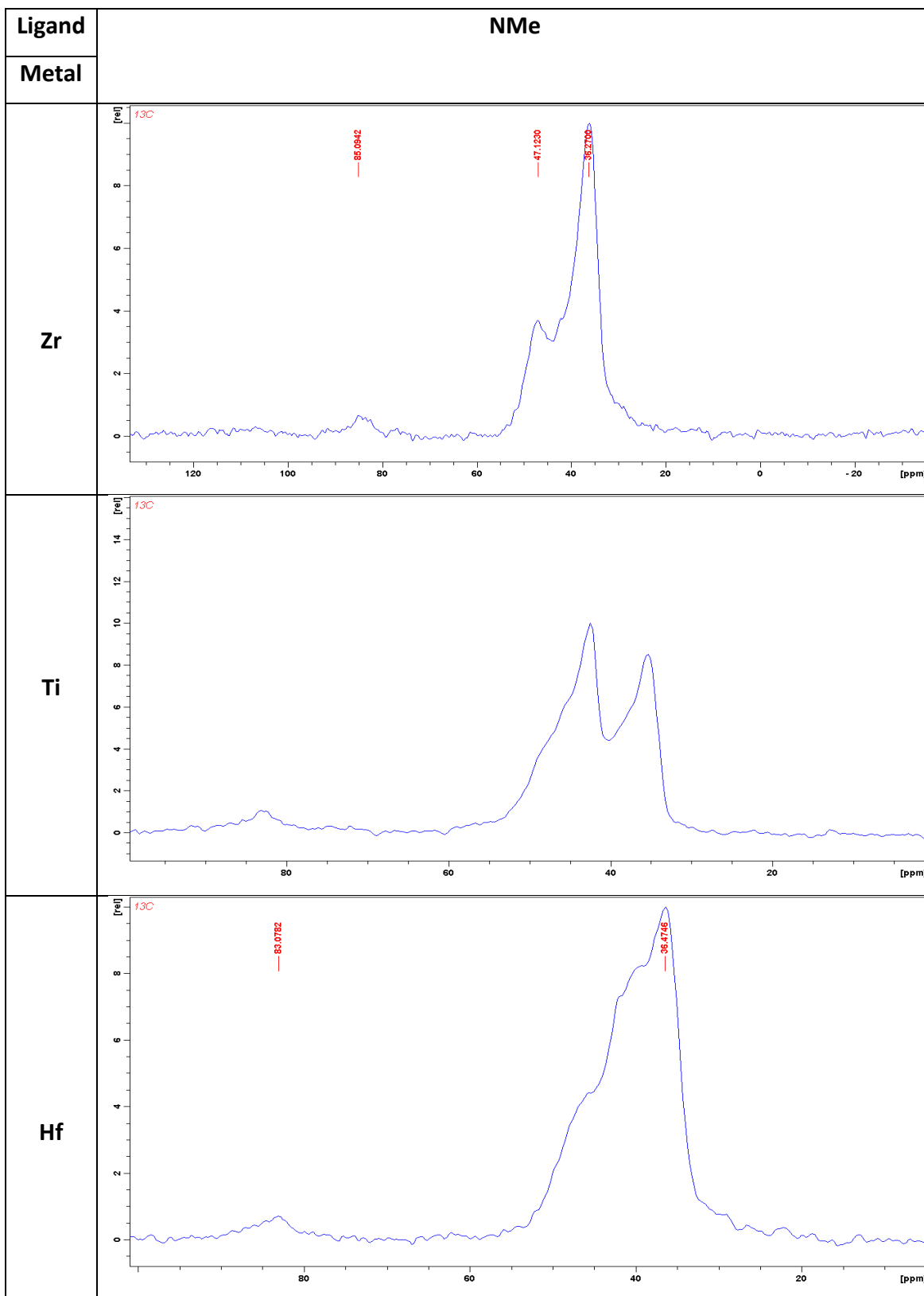
SS NMR, specifically when combining advanced experiments, has proven instrumental to determine the coordination sphere of supported metal centres.^[15]

The ^1H NMR spectra of supported $\text{M}(\text{NMe}_2)_4$ ($\text{M} = \text{Ti}, \text{Zr}$) and Hf consist of one peak centered at 2.8 ppm (Table 2.1). It is assigned to the proton present in the dimethylamido ligands. Characterization with ^{13}C NMR of supported metal complexes shows more complex structures of the supported $\text{M}(\text{NMe}_2)_4$. ^{13}C NMR revealed a more complex pattern as three signals could be clearly identified: one large at 36 ppm, one much smaller at 47 ppm and a weak and broad signal at 85 ppm (Table 2.2).

Table 2.1. ¹H NMR spectrum of silica and SBA supports treated with M(NMe₂)₄.

Support	SiO ₂ -700	SBA ₁₅ -700
Metal		
Zr		
Ti		
Hf		

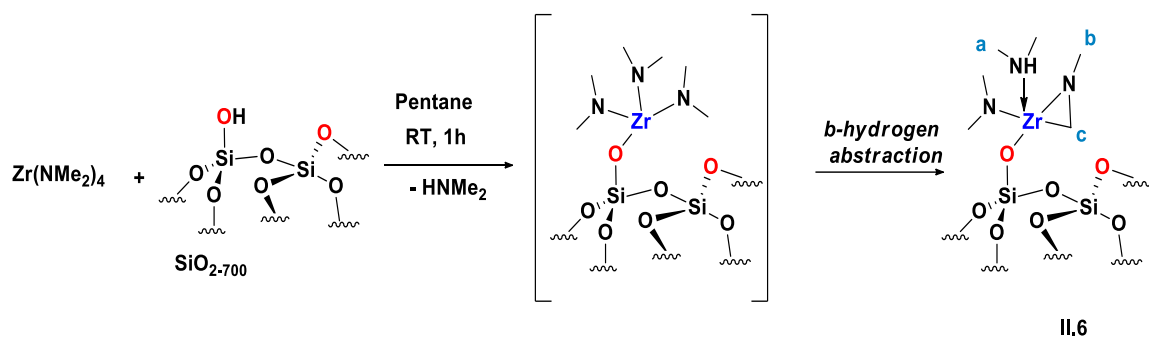
Table 2.2: ^{13}C NMR spectrum of SBA₁₅₋₇₀₀ treated with M(NMe₂)₄.



NB: Similar results were found with SiO₂₋₇₀₀.

The concomitance of these resonances is inconsistent with surface complexes displaying three equivalent dimethylamido ligands. The presence of another unexpected structure, azametallacyclopropane (metallaaziridine) fragment, in which a methylene was directly coordinated to the zirconium atom was suspected. The three peaks in the ^{13}C NMR may be assigned according to the literature^[16] to the carbons a, b and c respectively (Scheme 2.45).

In fact, the silica-supported group 4 metal dialkylamide complexes resulting from the reaction of $\text{M}(\text{NR}_2)_4$ ($\text{R} = \text{Me}$) with both silica₇₀₀ and SBA₁₅₋₇₀₀ may undergo intramolecular β -H abstraction by a coordinated amido-ligand and subsequent liberation of amine, this reaction yields an metallaaziridines complex (**II.6**).



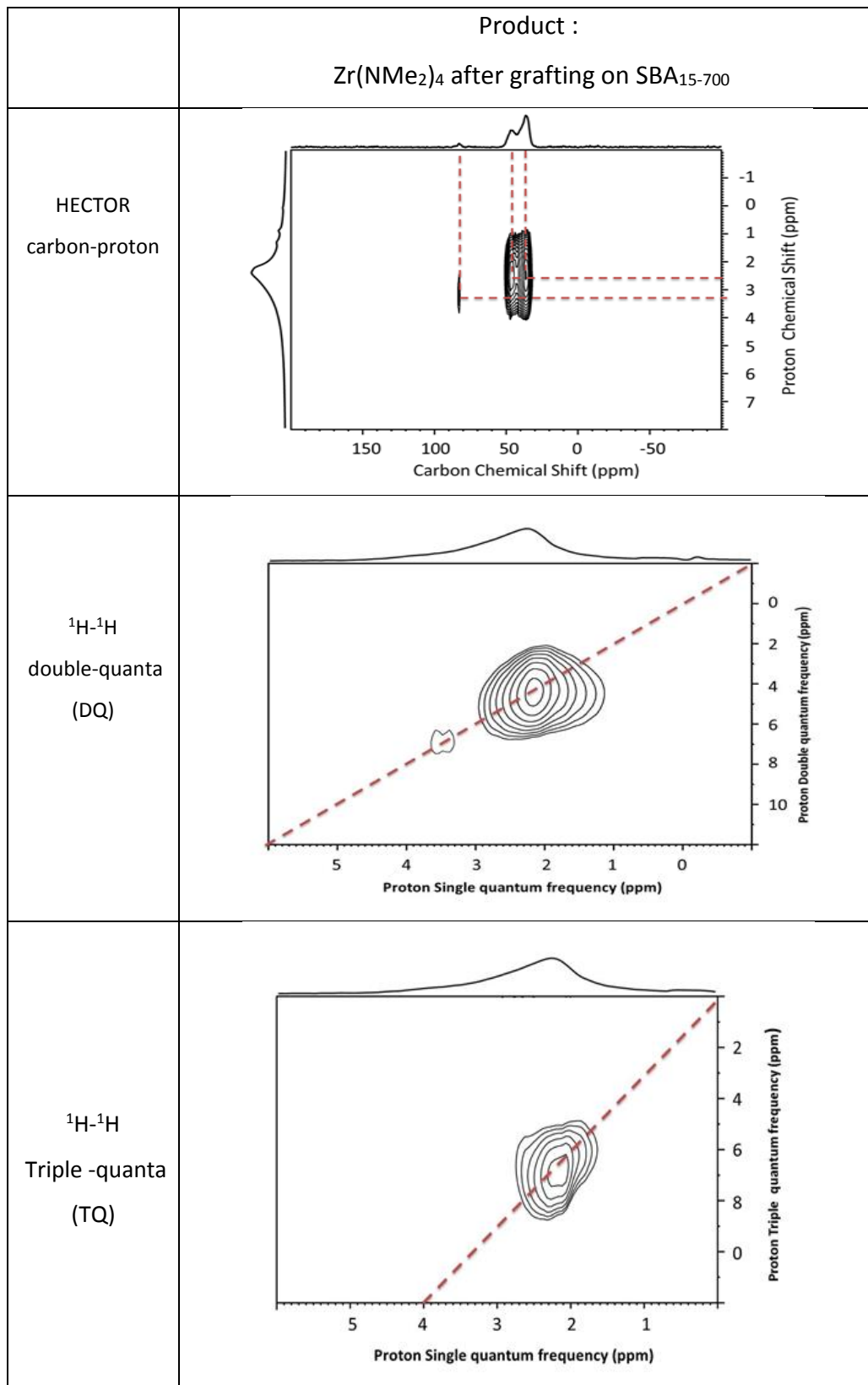
Scheme 2.45: Spontaneous transformation of silica supported zirconium dimethyl amines.

Further advanced SS NMR experiments were undertaken to probe this hypothesis. Combining 2D experiments such as 2D ^1H - ^{13}C heteronuclear correlation (HETCOR) and ^1H - ^1H multiple quantum (DQ and TQ) can provide the access to intimate understanding of the zirconium coordination sphere.^[17]

In the case of zirconium complex, the HETCOR spectrum revealed the correlations only between attached ^1H - ^{13}C spins using a short contact time of 0.5 ms. Clear correlations were seen between methyl protons at 2.4 ppm and the carbons at 36 and 47 ppm (Table 2.3). Another more interesting correlation was revealed between the signals at 85 ppm and the proton at 3.2 ppm, the latter being quasi invisible in the mono dimensional spectrum. Two-dimensional Proton Double- (DQ) and Triple- Quantum (TQ) correlation experiments were performed to determine the number of protons attached to the same carbon, hence discriminating between CH_2 and CH_3 groups. The DQ frequency in the indirect ω_1 dimension corresponds to the sum of the two SQ that give an autocorrelation peak located on the $\omega_1 = 2\omega_2$. Similarly TQ frequencies correspond to the sum of the frequencies of three protons that are close in space with $\omega_1 = 3\omega_2$.

A strong autocorrelation peak is observed for the proton resonance at 2.4 ppm in both DQ and TQ spectra (4.8 and 6.6 ppm in the ω_1 dimensions, respectively), which is compatible with the assignment of this resonance to methyl protons (Table 2.3). The proton resonance at 3.2 ppm shows a correlation at 6.4 ppm (ω_1) in the DQ spectrum, whereas no autocorrelation peak is observed in the TQ spectrum. It can be thus assigned to a CH_2 group.

Table 2.3: Carbon- proton, DQ and TQ Solid-state NMR spectra of $Zr(NMe_2)_4$ after reation with SBA_{15-700} .



In support of this conclusion, the corresponding high field signal in the ^{13}C spectrum (85 ppm) is also in line with a CH_2 directly bound to a zirconium atom. This leaves very little doubt that **II.6** is a zirconaaziridine surface $[\equiv\text{Si-O-Zr}(\text{HNMe}_2)(\text{NMe}_2)(\text{NMeCH}_2)]$. Examples in which the $\text{Zr}^{(\text{IV})}$ metal center is stabilized by electron-rich ligands such as alkylzirconocene cations^[18] or carborane^[19] have been reported. Comparison of the chemical shifts of the carbon and hydrogen in the methylene directly bound to the metal revealed a significant increase in chemical shift measured in **II.6** (85 vs. 46.5 or 31 ppm). This large variation in chemical shift may be indicative of the enhanced activation of the CH_2 by the zirconium center, possibly due to the higher electron density in the molecular compounds compared to the surface ones.

Further confirmation of the amido ligands being not equivalent in **II.6** are provided by the ^{15}N CP/MAS NMR spectroscopy. Indeed, the spectrum of **II.6** exhibit two broad resonances at 357 and -378 ppm (Figure 2.6).

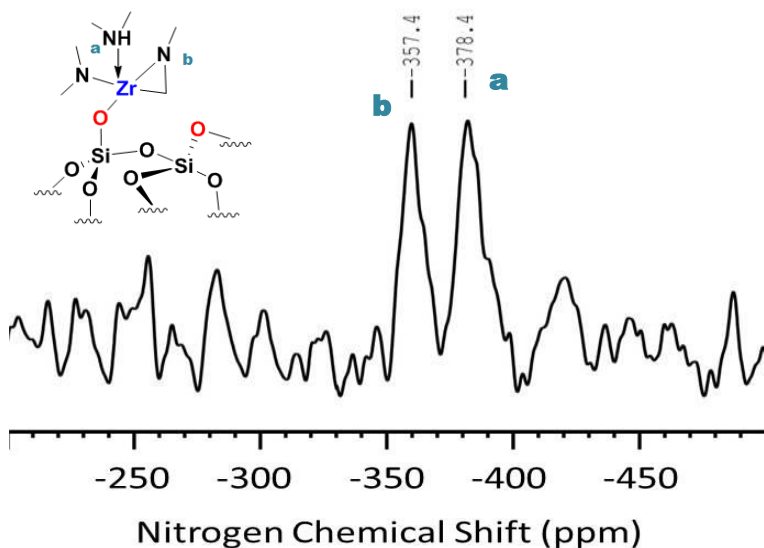


Figure 2.6: ^{15}N CP/MAS NMR spectra of **II.6**.

2.3.1.3 EXAFS characterization

The EXAFS data of **II.6** was collected with Zr K-edge (17.998 keV). For analysis of the EXAFS experiments data, we used the atomic coordinates derived from DFT calculation. The structural model of **II.6** was simplified as the first coordination shell involves three light scatters being carbon, nitrogen and oxygen. All have close atomic numbers ($Z = 6, 7, 8$) and similar bond distances to zirconium, which prevents any differentiation by EXAFS. Oxygen and a carbon scatterer were selected to model the first shell and its total coordination number was constrained during the fit to be equal to 5 while the Debye-Waller factors were also constrained to damp the correlations between parameters (Figure 2.7 and table 2.4).

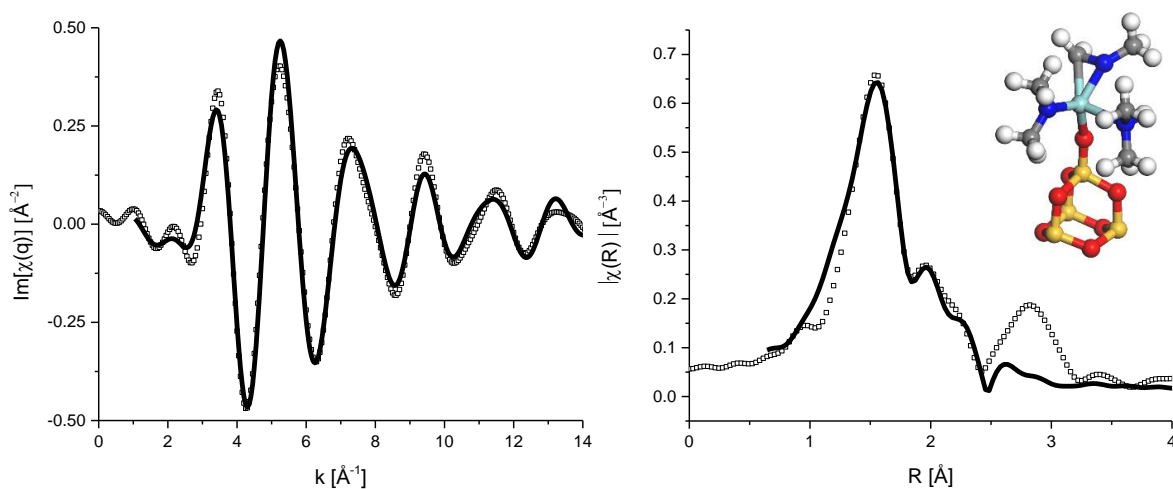


Figure 2.7: Imaginary parts of the back Fourier transform (left) and Fourier transforms (right) of the EXAFS $k^2 \cdot \chi(k)$ functions for compound **II.1**. The solid lines are the experimental data while the dotted lines are the fit results obtained within a k -range between 4 and 14 \AA^{-1} and within an R -range of 1 up to 2.8 \AA . (phase shift not corrected)

The best fit was obtained using 2.9 ± 0.5 oxygen scatters at $2.02 \pm 0.03 \text{\AA}$ and 2.1 ± 0.5 carbon scatters at $2.24 \pm 0.02 \text{\AA}$. Thus, the results are in agreement with the grafting of $\text{Zr}(\text{NMe}_2)_4$ on surface hydroxyls which produce one Zr-O and two Zr-N covalent bonds

at 2.02 ± 0.02 Å, one Zr-C covalent bond from the azametallacyclopropane at 2.24 ± 0.03 Å and one Zr-N dative bond at the same distance.^[20] The fit was also largely improved by taking into account the second shell with the contribution of either O, N or C scatters at 2.74 ± 0.04 Å. In this case, carbon scatter gave the best agreement with the experimental data although its quantification is not reliable because of the correlations between parameters.

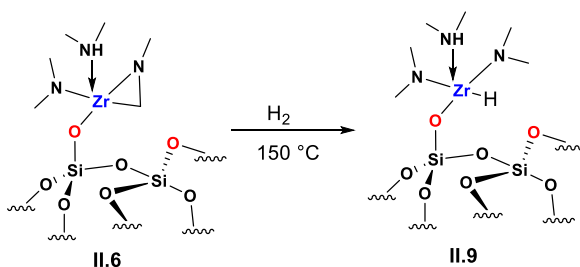
Table 2.4: Parameters extracted from the fit of EXAFS data related to compound 1. Underlined characters denote fixed parameters while § indicate constrained parameters

Scattering paths	N	R [Å]	$\sigma^2 \times 10^{-3}$ [Å ²]	ΔE [eV]	R-factor
Zr-O/N	2.9 ± 0.5 §	2.02 ± 0.03	4 ± 1 §	4 ± 3	0.017
Zr-C/N	2.1 ± 0.5 §	2.24 ± 0.02	4 ± 1 §		
Zr-C	2 ± 1	2.74 ± 0.04	5		

2.4 Silica-supported mono hydride zirconium complexes

2.4.1 FTIR Characterization and elemental analysis

Single-site silica-supported mono-hydride $[\equiv\text{Si-O-Zr}(\text{HNMe}_2)(\text{NMe}_2)_2\text{H}]$ (**II.9**) was obtained by hydrogenolysis of the zirconaaziridines (**II.6**) (Scheme 2.34).



The subtraction of FTIR spectra corresponding to **II.9** – **II.6** reveals the appearance of one new vibration band at 1587 cm^{-1} simultaneously to the disappearance of bands at 2827 , 2773 and 1461 cm^{-1} (Figure 2.8).

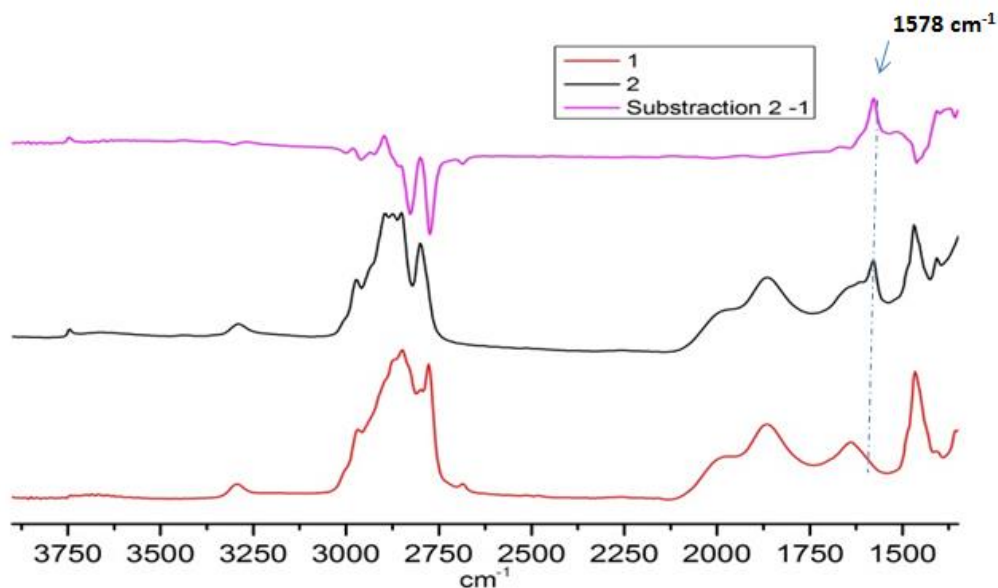


Figure 2.8: FTIR of **II.6** (red), **2** (black), and **2-1** (pink).

The former modification can be assigned to a zirconium hydride species while the latter suggests a rearrangement of the alkyl fragments. Elemental analysis of **II.9** shows almost no significant variation with that of **II.6** (table 2.5).

Table 2.5: Elemental analysis of II.6 and II.9.

	%Zr	%C	%N	%H	C/N	N/Zr	C/Zr
II.6	2.6	2.41	1.48	0.56	1.89	3.70	7.02
II.9	2.65	2.39	1.44	0.58	1.93	3.53	6.84

Interestingly, the NH vibration observed previously (3294 cm^{-1}) in **II.6** remains and seems little affected by the hydrogen. This suggests that the hydrogenolysis may not have affected the Zr-N bonds. Considering a Zr-H vibration at 1587 cm^{-1} , the value of this wavelength is lower compared to that of the reported $[(\equiv\text{Si-O})_3\text{ZrH}]$ (**A**, see scheme 2.4) ($1600 - 1630\text{ cm}^{-1}$ range),^[3a, 4a] probably an indication of the effect of the difference of coordination (O, O, O vs N, N, N, O).

2.4.2 SS NMR characterization

The coordination sphere of **II.9** was further examined by comparison of SS NMR spectra experiment from **II.6**. ^1H NMR of **II.9** contains an intense peak at 2.5 ppm and a very broad peak at 8.0 ppm (Figure 2.9). That of **II.6** contains only one broad peak for all the resonances of the proton of the methyl and methylene fragments.^[21] In the double-quantum (DQ) spectrum (Figure 2.10), the peak at 2.5 ppm displays a strong auto-correlation that can be assigned to the NMe_2 group similarly to that observed in **II.6** (Figure 2.9).

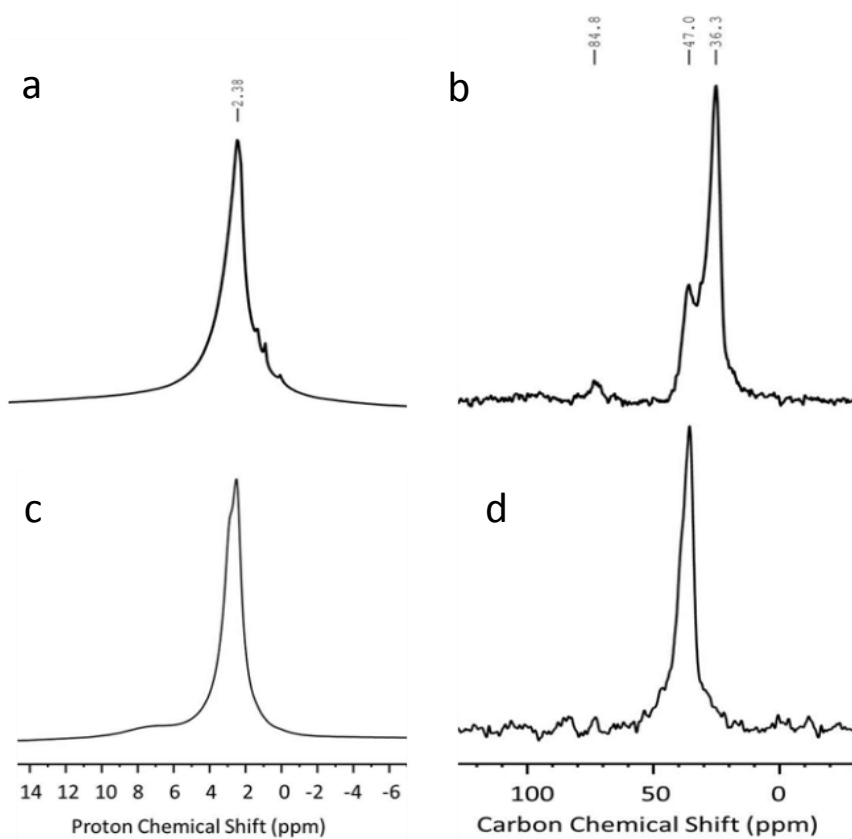


Figure 2.9: (a) ¹H SS NMR of II.6, (b) ¹³C SS NMR spectra of II.6, (c) ¹H SS NMR of II.9 and (d) ¹³C SS NMR spectra of II.9.

The peak at 8.0 ppm shows no auto-correlation in DQ (Figure 6) and may be assigned to the proton of a zirconium monohydride. Furthermore, a correlation in the DQ NMR spectrum between the methyl group at 2.5 ppm and hydride at 8.0 ppm supports the formation of a hydride close to the amide group. This value is lower than that reported for related surface zirconium hydride species: $[(\equiv\text{Si-NH})(\equiv\text{Si-O})_2\text{ZrH}]$ and $[(\equiv\text{Si-NH})_2(\equiv\text{Si-O})\text{ZrH}]$ at 10.2 ppm, and $[(\equiv\text{Si-N})(\equiv\text{Si-O})\text{ZrH}]$ at 14.5 ppm. Recent examples of the molecular complexes have reported similar values for the hydrides signals.^[3a]

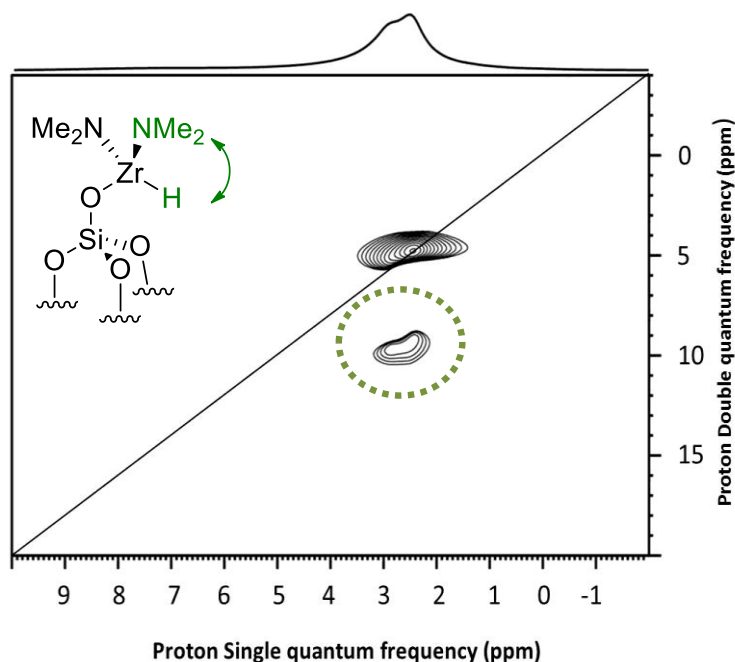


Figure 2.10: Two-dimensional (2D) ^1H - ^1H double-quantum (DQ)/Single-quantum (SQ) of **II.9**.

In contrast, other nuclei NMR experiments with ^{13}C and ^{15}N showed a simplification of the peaks detected when comparing **II.9** with **II.6**. For instance, the only one peak at 36 ppm in the ^{13}C CP/MAS NMR spectrum is very similar of that observed prior to the hydrogen treatment (36 ppm) (Figure 2.9). The two peaks at 47 and 86 ppm have disappeared. They were attributed to the methyl and the methylene group borne by the nitrogen ligand of the azazirconacyclopropane in **II.6**. Moreover, the chemical shift is consistent with an NMe_2 ligand.^[21] Further confirmation of the amido ligands being all equivalent in **II.9** is provided by the ^{15}N CP/MAS NMR spectroscopy. Indeed, the spectrum of **II.9** contains a single sharp peak at -380 ppm while **II.6** exhibits two broad resonances at -357 and -378 ppm (Figure 2.11).

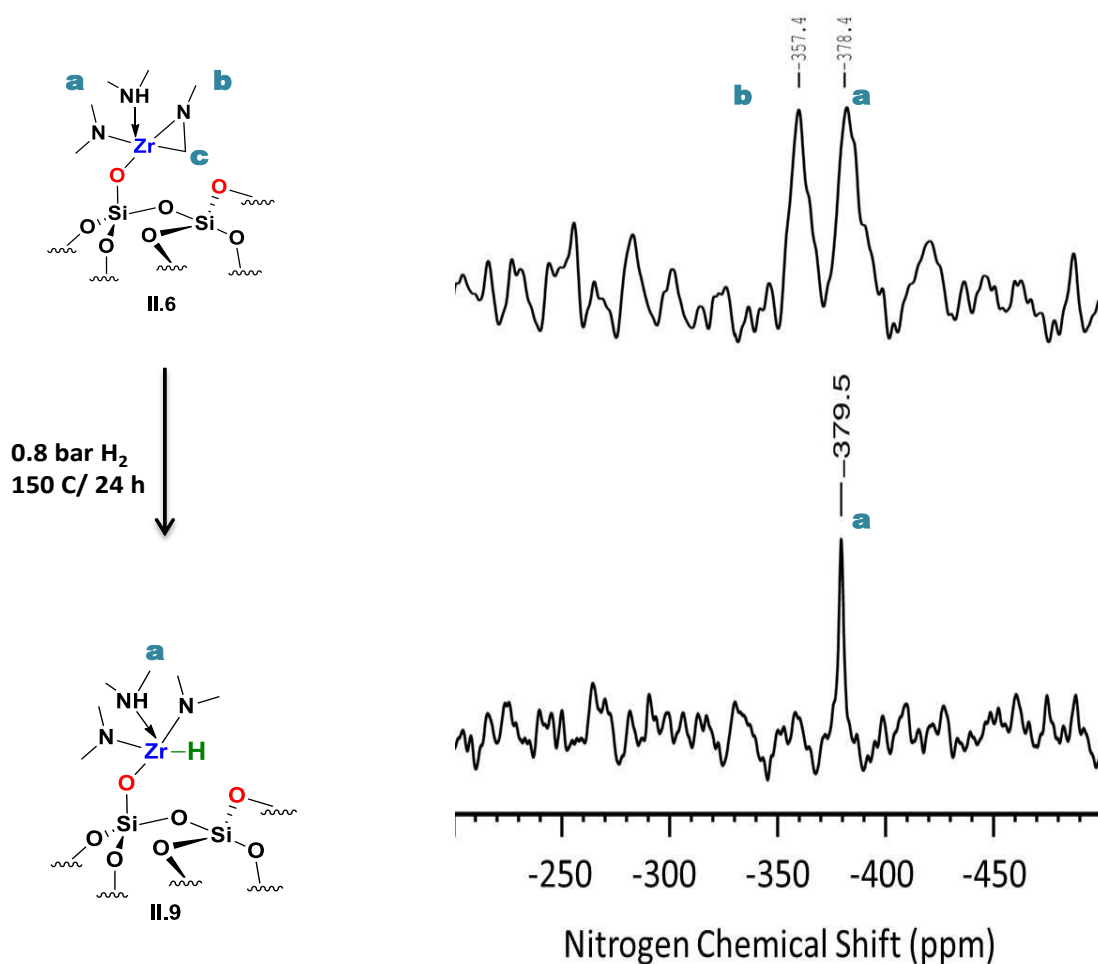


Figure 2.11: ¹⁵N CP/MAS NMR spectra of II.6 and II.9.

II.4.3 Catalytic testing for olefin hydrogenation

The performances of II.6 and II.9 were examined for the catalytic transformations such as hydrogenation of olefin and the hydrogenolysis of alkane. In the initial series of experiments, surface complexes II.6 and II.9 (typically 150 mg of silica supported complexes inside a reactor of 230 ml) were contacted by different gases (propane, ethylene or propene, 0.5 bars). Further experiments employed mixtures of ethylene or propene (0.3 bars) with hydrogen (0.5 bars). For each run, the composition of the gas phase was monitored by GC-FID for 24 hrs (Table 2.6 & Figure 2.12).

Table 2.6: Reactivity study of II.6 and II.9 contacted by different gas mixtures (24 hrs, 200 °C).

Entry	Complex	Reactants	Gas phase Composition
1	II.6	C ₃ H ₆ + H ₂	C ₃ H ₆ (60%); C ₃ H ₈ (40%)
2	II.9	C ₃ H ₆ + H ₂	C ₃ H ₆ (57%); C ₃ H ₈ (43%)
3	II.6	C ₃ H ₆	C ₃ H ₆ (100%)
4	II.9	C ₃ H ₆	C ₃ H ₆ (100%)
5	II.6	C ₂ H ₄ + H ₂	C ₂ H ₆ (87%); C ₂ H ₄ (8%); C ₄ H ₈ (3%); C ₃ H ₆ (1%); C ₃ H ₈ (1%); C ₅ H ₁₀ (1%)
6	II.9	C ₂ H ₄ + H ₂	C ₂ H ₆ (85%); C ₂ H ₄ (8.3%); C ₄ H ₈ (3%); C ₃ H ₆ (2%); C ₃ H ₈ (1%); C ₅ H ₁₀ (1%)
7	II.6	C ₂ H ₄	C ₂ H ₄ (75%); C ₃ H ₆ (17%); C ₅ H ₁₀ (8%)
8	II.9	C ₂ H ₄	C ₂ H ₄ (100%)

When **II.9** is exposed to propane (0.3 bar) and hydrogen (0.6 bar), no reaction was observed. Of note, our recent investigation of mixtures of zirconium hydrides and dihydrides were able to hydrogenolyze propane under comparable conditions.^[3a] When **II.9** is exposed to a mixture of propene and hydrogen (Table 2.6: entry 1), only hydrogenation occurs with a conversion of around 40% and propane as the sole product. This is consistent with a hydrogenation process in which the surface zirconium complex adds hydrogens to the double bond. Under similar conditions, **II.6** gave very comparable results (Table 2.6: entry 2) indicating that the hydride has been generated *in situ*. When **II.6** or **II.9** are treated with only propene, no transformation can be observed

in the gas phase (Table 2.6: Entry 3 & 4). When **II.6** and **II.9** were treated with a mixture of ethylene and hydrogen (0.3 bars: 0.5 bars, respectively), identical distributions of products were observed in both cases (Table 2.6: Entry 5 & 6). Ethane is the main product (>85%) with only 8% ethylene remaining (Figure 2.12). In addition, small amounts of by-products were observed: 1-butene (2.5%), propene (ca 1.5%), propane (ca 0.8%) and 1-pentene (ca 0.5%). Finally, treating **II.6** with pure ethylene leads to small amounts of propene and 1-pentene (17% and 8%, respectively) while **II.9** is seemingly unreactive (Entry 7 & 8). This short study highlights the capability of **II.9** as a hydrogenation catalyst and is consistent with the proposed structure as a silica-supported zirconium hydride compound (Scheme 2.34).

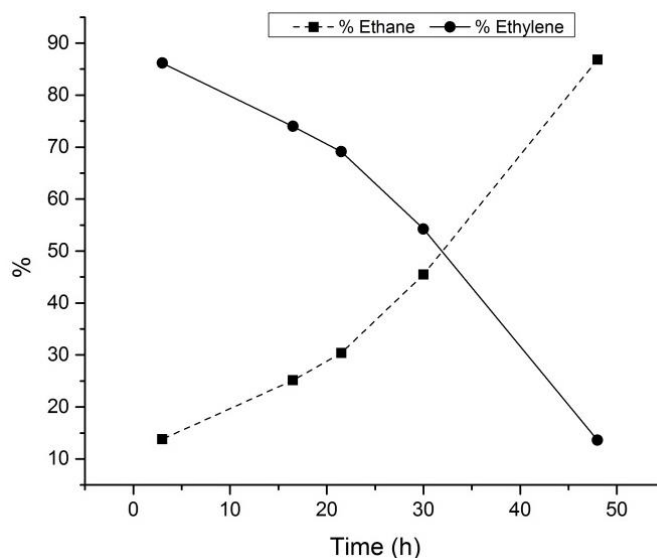
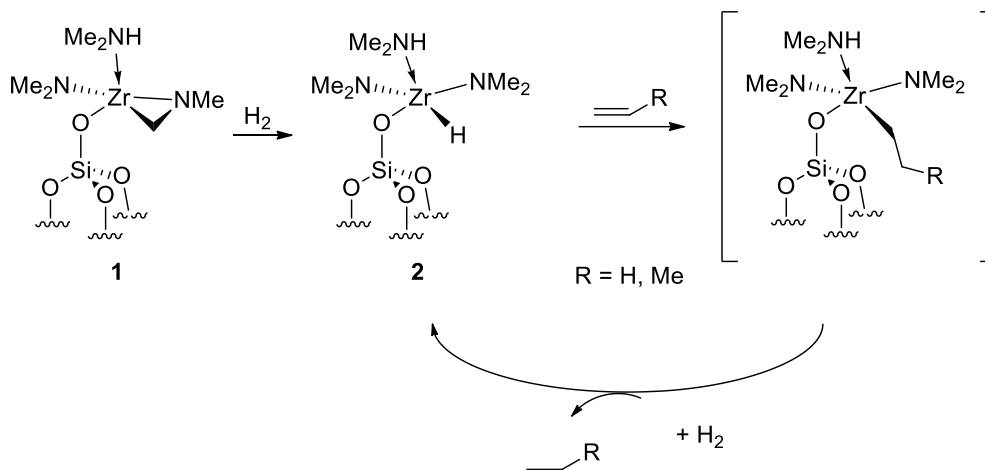


Figure 2.12: Conversion vs. time of ethylene to ethane using **II.9**/ H_2 /150°C.

Indeed, it is clear that **II.6**, when exposed to a mixture of hydrogen with either ethylene or propene, is converting into **II.9** *in situ*. Regardless of the catalyst employed, the conversion of ethylene to ethane is higher compared to that of propene to propane.



Scheme 2.46: Proposed mechanism for the hydrogenation of ethylene and propylene by **II.6** and **II.9**.

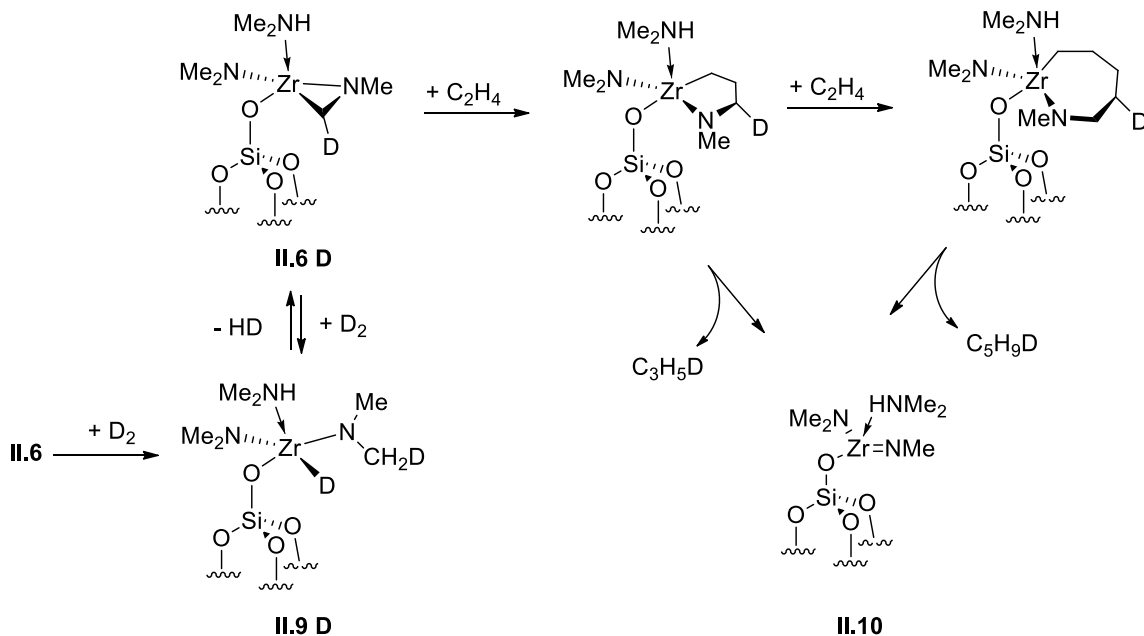
The minor by-products obtained when using **II.9** and ethylene suggests the occurring of parallel pathways leading to odd numbered alkene and their hydrogenated counterparts, and to 1-butene. Transition metal can conduct C=C hydrogenation known^[22] via metal hydride intermediates.^[23] Abundant documentation covers late transition metal-based catalysts (*i.e.*, Pd, Pt and Rh)^[24] including homogeneous and heterogeneous examples while instances of early transition metal-based counterparts are rarer. Yet zirconium hydrides complexes have a track record to conduct hydrogenation reactions (zirconocene derivatives on linear^[25] and aromatic alkene,^[26] silica supported zirconium hydrides on benzene and cyclohexene^[27] or ethylene and diene).^[28] Recently, our group reported zirconium hydrides coexisting with dihydrides counterparts supported on aminated silica surfaces activating the C-H bond of

alkanes.^[3a] From the present study, we can conclude that **II.9** conducts the hydrogenation of only the shortest olefins (i.e. ethylene and propylene) as neither pentane or butane were observed. Further experiment employing 1-butene as substrate confirms that lack of reactivity.

The minor by-products obtained when using **II.6** and ethylene suggests the occurring of parallel pathways leading to 1-butene and odd numbered alkene and their hydrogenated counterparts. It can be proposed that the C₃ and C₅ alkene and alkane are generated by one or two insertions of ethylene within the azazirconacycloprane moiety of **II.6** followed by the elimination of the corresponding olefins. It can be postulated that surface species [$\equiv\text{Si-O-Zr}(\text{NMe}_2)(=\text{NMe})$] (**II.10**) would be formed in this decomposition process (Scheme II.46).^[1] The propane may be generated by hydrogenation of the propene generated. No pentane has been detected.

This hypothesis was assessed by using deuterium D₂ instead of H₂. The deuteride equivalent of **II.9** (**II.9 D**) $\equiv\text{Si-O-ZrD}(\text{NMe}_2)(\text{NMeCH}_2\text{D})$ was obtained by deuterolysis of **II.6**. The gas mixture resulting from treating it under the same conditions as entries 5 & 6 was analyzed by GC-MS. The product distribution was comparable to that observed for entry 5 and 6. It is noteworthy that the C₃ and C₅ peaks are clearly containing deuterium (Scheme II.47). This is compatible with the mechanism proposed (Scheme 2.11), as the deuterium may come from the deuterated methylene in the metallaziridine. In this pathway, the zirconium hydride must regenerate the metallaziridine fragment to undergo the decomposition of the ligand. This is also a strong indication that **II.6** and **II.9**

are in equilibrium under the screening conditions. Further support for this mechanism can be found with the reaction of **II.6** with pure ethylene. Propene and 1-pentene were the sole products detected. This reaction appears to be stoichiometric to that of the zirconium complex present at the beginning of the reaction.



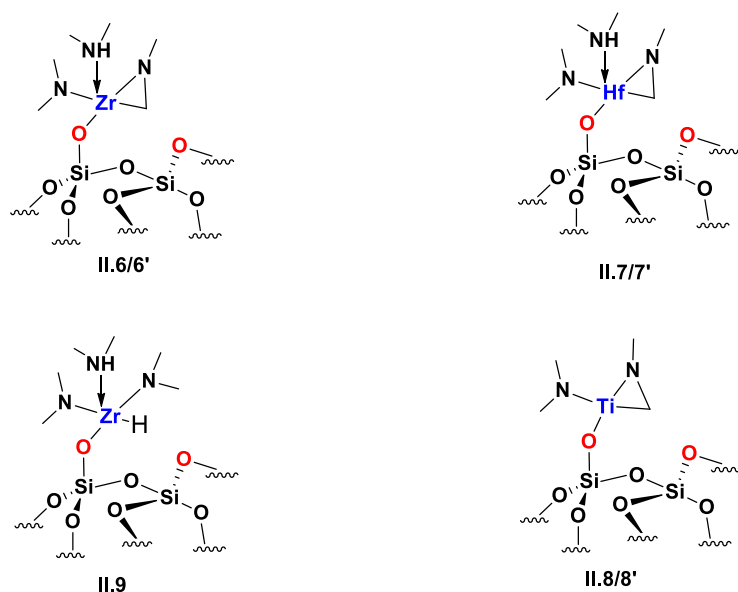
Scheme 2.47: Proposed mechanism for the generation of propylene and 1-pentene by reaction of ethylene with **II.6D**. For clarity in the mechanism, the inclusion of only one equivalent of D_2 was considered.

Finally the 1-butene is believed to occur by separate pathways in which ethylene insert into an ethyl fragment generated from the reaction of ethylene with hydride. No product of dimerization is observed when using propene nor deuterium-enriched butane could be detected.

2.5 Conclusions

In this chapter, three new silica-supported metallaaziridines have been isolated [$\equiv\text{Si-O-M}(\text{HNMe}_2)(\eta^2\text{NMeCH}_2)(\text{NMe}_2)$] $\text{M} = \text{Zr}$ (**II.6**, **II.6'**), Hf (**II.7**, **II.7'**) and [$\equiv\text{Si-O-M}$

$(\eta^2\text{NMeCH}_2)(\text{NMe}_2)]$ ($\text{M}=\text{Ti}$ (**II.8**, **II.8'**) from the grafting of the corresponding homoleptic precursor ($\text{M}(\text{NMe}_2)_4$; $\text{M} = \text{Ti, Zr, Hf}$) onto SiO_{2-700} and SBA_{15-700} . This reactivity has been evidenced by combining multiple quanta experiments, FTIR and elemental analysis. In addition the structure of **II.6** was confirmed by EXAF studies. **II.6** - **II.8'** are the first experimental evidences of these new surface organometallic fragments MCN.



Scheme 2.48: Silica supported complexes II.6 - II.9 and II.6' - II.8'.

Single-site silica-supported zirconium monohydride [$\equiv\text{Si-O-Zr}(\text{HNMe}_2)(\text{NMe}_2)_2\text{H}$] **II.9** has been synthesized and fully characterized by FTIR, elemental analysis and SS NMR experiments. To our knowledge, this species is the first selective isolation of a silica-supported zirconium monohydride. **II.9** can perform the catalytic hydrogenation of short-chain olefins (ethylene and propylene). Minor amounts of C_3 , C_4 and C_5 byproducts are collected when using ethylene. A formation mechanism in which the insertion of one or two molecules of ethylene into the azazirconacyclopropane followed by elimination of C_3 and C_5 byproducts to lead to an imido inactive species **3** has been

proposed. However, **II.9** does not promote hydrogenolysis of propane even under severe conditions. Several reasons can be invoked: (i) **II.9** is exclusively monohydride (ii) the electron count (10 electrons) is high (iii) the higher electron density on the zirconium atom due to the nitrogen ligands environment.

2.6 Experimental

2.6.1 General

All experiments were carried out under controlled atmosphere. The syntheses and the treatments of the surface species carried out using high vacuum lines ($< 10^{-5}$ mbar) and glove-box techniques. Pentane was collected from a Solvent Purification System following by a freeze-pump. Elemental analyses were performed at the Mikroanalytisches Labor Pascher. LiNMe_2 and ZrCl_4 were purchased from Sigma Aldrich. $\text{Zr}(\text{NMe}_2)_4$ was prepared by allowing ZrCl_4 to react with LiNMe_2 according to the literature procedures.

Fourier Transformed Infrared Spectroscopy. FTIR spectra were recorded on a Nicolet 6700 FTIR spectrometer equipped with a cell under controlled atmosphere. Typically, 16 scans were accumulated for each spectrum (resolution 4 cm^{-1}).

Solid State Nuclear Magnetic Resonance Spectroscopy:

One dimensional ^1H MAS, ^{13}C and ^{15}N CP-MAS solid state NMR spectra were recorded on a Bruker AVANCE III spectrometer operating at 400 MHz for ^1H , with a conventional double resonance 4 mm CPMAS probe. The samples were introduced under argon into zirconia rotors, which were then tightly closed. The spinning frequency was set to 17

KHz for ^1H and 10 KHz for ^{13}C and ^{15}N spectra, respectively. NMR chemical shifts are reported with respect to TMS as an external reference for ^1H , ^{13}C and pyridine for ^{15}N . For CP/MAS ^{13}C and ^{15}N NMR, the following sequence was used: 900 pulses on the proton (pulse length 2.4 s), then a cross-polarization step with a contact time typically 2 ms, and finally acquisition of the ^{13}C and ^{15}N signal under high power proton decoupling. The delay between the scan was set to 5 s, to allow the complete relaxation of the ^1H nuclei and the number of scans was between 3,000-5,000 for carbon, 100,000 for ^{15}N and 32 for proton. An apodization function (exponential) corresponding to a line broadening of 80 Hz was applied prior to Fourier transformation.

^1H - ^1H multiple-Quantum Spectroscopy: Two-dimensional double-quantum (DQ) experiment was performed on Bruker AVANCE III spectrometer with a regular double resonance 3.2 mm CPMAS probe, as stated by the following common scheme: excitation of DQ coherences, t_1 evolution, Z-filter, and detection. The spectra were recorded in a rotor synchronized fashion in t_1 ; that is the t_1 increment was set equal to one rotor period (4.545 μs). One cycle of the standard back-to-back (BABA) recoupling sequence was used for the excitation and reconversion period. Quadrature detection in w_1 was achieved using the States-TPPI method. A spinning frequency of 22 KHz was used. The 900 proton pulse length was 2.5 μs , while a recycle delay of 5 s was used. A total 128 t_1 increments with 32 scan each were recorded.

Nitrogen Adsorption–Desorption. Isotherms at 77 K were measured using a Micromeritics ASAP 2420 physisorption analyzer. Specific surface areas were calculated

following typical BET procedures. Pore size distribution was obtained using BJH pore analysis applied to the desorption branch of the nitrogen adsorption/desorption isotherm.

X-Ray Powder Diffraction. The small-angle X-ray powder diffraction (XRD) data were acquired on a Bruker D8 advance diffractometer using Cu K α monochromatic radiation ($\lambda = 1.054184 \text{ \AA}$) to confirm the hexagonal ordered structure of the samples.

2.6.2 Preparation procedures

Preparation of $[\equiv\text{Si-O-Zr}(\text{NMe}_2)(\text{NMeCH}_2)]$ (II.9). Zr(NMe₂)₄ in slight excess (1.1 equivalent, 0.100 g) with respect to the amount of surface accessible silanols (1.28 mmol silanols groups per gram) was reacted with SBA-15 (0.260 g) at room temperature in pentane for 1 h. After filtration and four washing cycles, all volatile compounds were evaporated and the solid was dried for 1 h under dynamic vacuum ($< 10^{-5}$ mbar).

Hydrogenation reaction: (II.9) (0.300 g) was heated at 150 °C under H₂ atmosphere (60 cm Hg). The reaction mixture was allowed 20 hrs. Upon reaction no gases was generated.

Hydrogenolysis of olefin: All reactions were made in glass reactor (230 mL), at 200 °C (1 C/min from RT to 200 °C). The reaction time was 24 hrs. For reactions with only C₂H₄ or C₃H₆, the pressure of the gas introduced is about 0.5 bars. For reaction in the presence of H₂, PH₂ was always 0.5 bars and PC₂H₄, C₃H₆ was about 0.3 bars.

Preparation and characterization of SBA-15. SBA-15 was synthesized according to literature.^[29] The BET analysis shows a specific area of 822 m²/g and a pore size of 5.21

nm. This prepared SBA₋₁₅ was treated at 700 °C for 12 h under high vacuum (< 10⁻⁵ mbar) to obtain SBA₁₅₋₇₀₀. After thermal treatment, the overall structure features of SBA₋₁₅ and its properties as large specific area and narrow pore distribution are retained. However, a small decrease in these parameters was remarked after grafting the zirconium complex. SBA₋₁₅ and the subsequent products were characterized by nitrogen adsorption at 77 K (N₂ adsorption) for determination of the specific surface and size distribution of the pores (Table 5).

Table 2. 7. Specific surface and size distribution of the pores.

Material	specific area (m²/g)	Pore size (nm)
SBA₁₅	822	5.21
SBA₁₅₋₇₀₀	885	5.25
II.6	691	5.16

PXRD pattern clearly reveals four well-resolved peaks in the 2θ domain at 0.95, 1.60, and 1.83°. They can be respectively indexed as (100), (110), and (200) diffraction peaks associated with 6mm hexagonal symmetry. This symmetry remains unchanged, even after dehydroxylation at 700 °C and grafting of zirconium complexes, showing the chemical and thermal stability of this material.

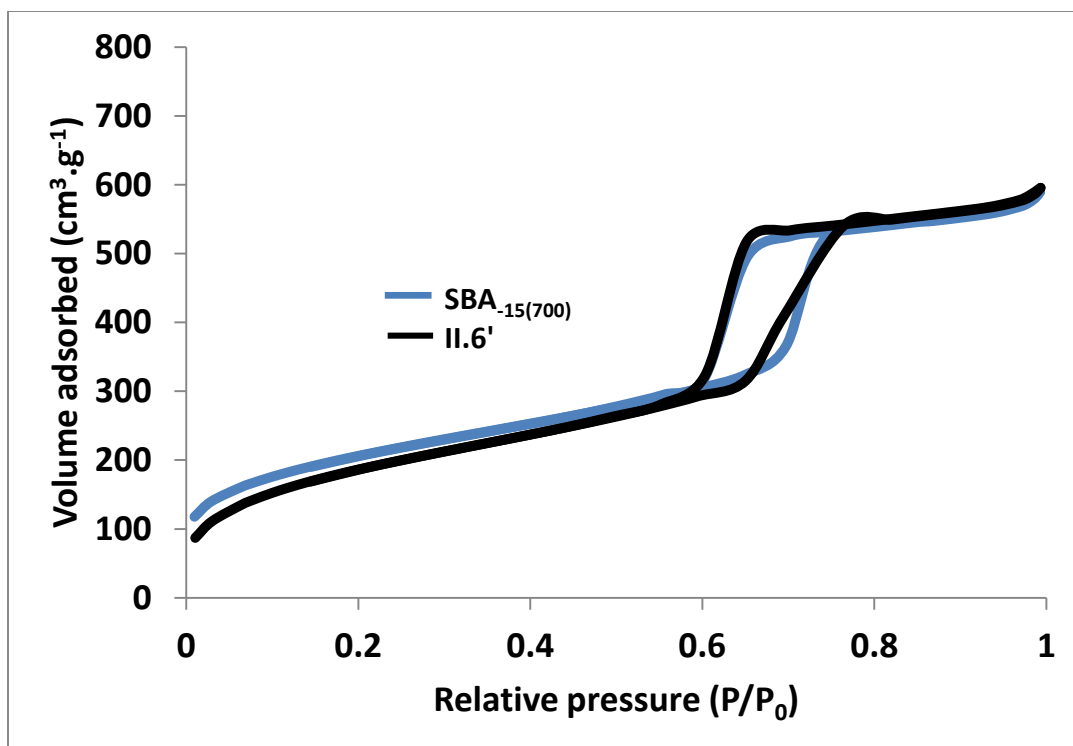


Figure 2.13: N₂ adsorption of SBA₁₅₍₇₀₀₎ and II.1.

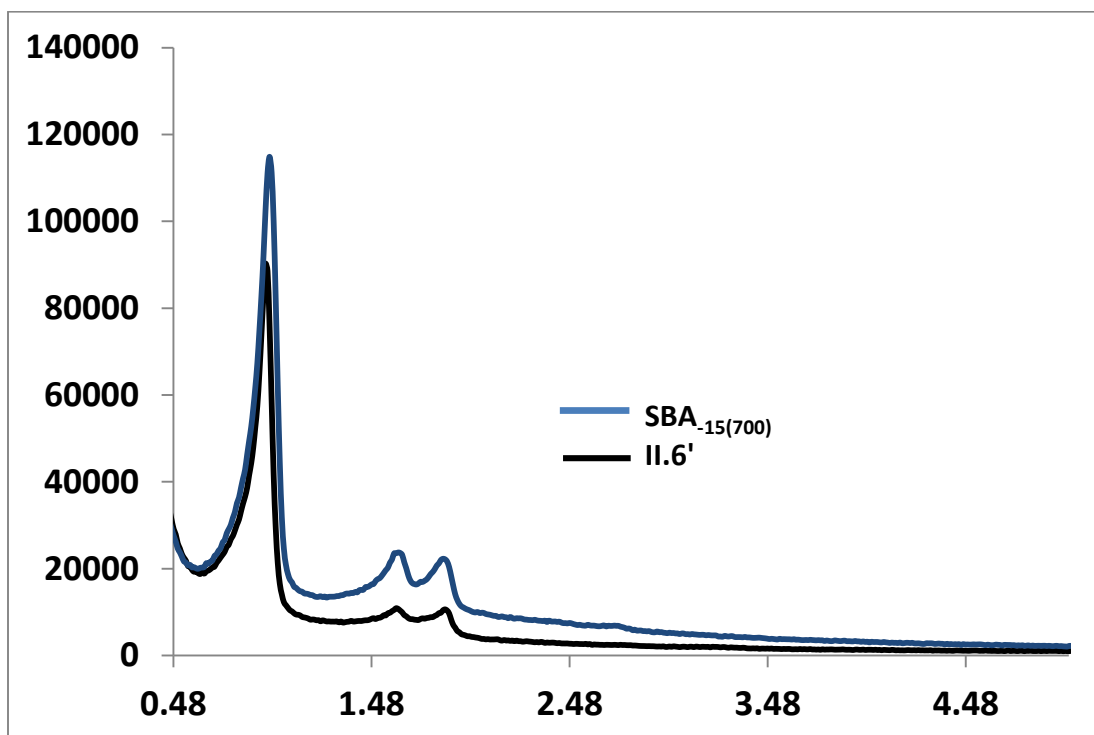


Figure 2.14: XRD Pattern of SBA₁₅₍₇₀₀₎ and II.1.

2.6.3 EXAFS experiment

Zr K-edge (17.998 keV) EXAFS and XANES data were collected on the bending magnet beam line of the Materials Research Collaborative Access Team (MRCAT, Sector 10) at the Advanced Photon Source, Argonne National Laboratory. The beam line was detuned to 50% in order to minimize the presence of harmonics. Data were taken in step scan mode with data points of 0.3 eV in the XANES region and 0.07 Å⁻¹ in the EXAFS region. Measurements were made in the transmission mode with the ionization chambers optimized for the maximum current with linear response) using gas mixtures (75% N₂ + 25% Ar) to give 10% absorption in the incident X-ray detector and 35% absorption (argon) in the transmission X-ray detector. A zirconium metal foil spectrum was acquired simultaneously with each measurement for energy calibration. Catalyst samples were pressed into a cylindrical holder of ca. 5 mm diameter inside an argon-filled glovebox and then sealed in a quartz tube with stainless steel endcaps and Kapton windows for data collection at the beam line. Samples were prepared with a thickness chosen to give an absorption change of ca. 1.0 at the Zr K-edge.

XAS data were analyzed using the HORAE package, a graphical interface to the AUTOBK and IFEFFIT code. The EXAFS spectrum was obtained after performing standard procedures for pre-edge subtraction, normalization, polynomial removal and wave vector conversion. Determination of the energy level (E_0) was performed at the first inflection point of the edge. For each atomic shell, the following structural parameters were adjusted: coordination number (N), bond length distance (R), and the so-called Debye–Waller factor via the mean-square relative displacement (σ^2) of the considered

bond length. The parameter ΔE_0 , which accounts for the difference between the experimental absorption-edge energy and its estimate made by the code, was also fitted. The amplitude factor (S_0^2) was fitted to the EXAFS spectrum obtained for a zirconium metallic foil reference, with a hexagonal crystal structure. S_0^2 was found equal to 0.87 (see Figure 2.15 and table 6) and subsequently fixed at this value for the analysis of compound II.6.

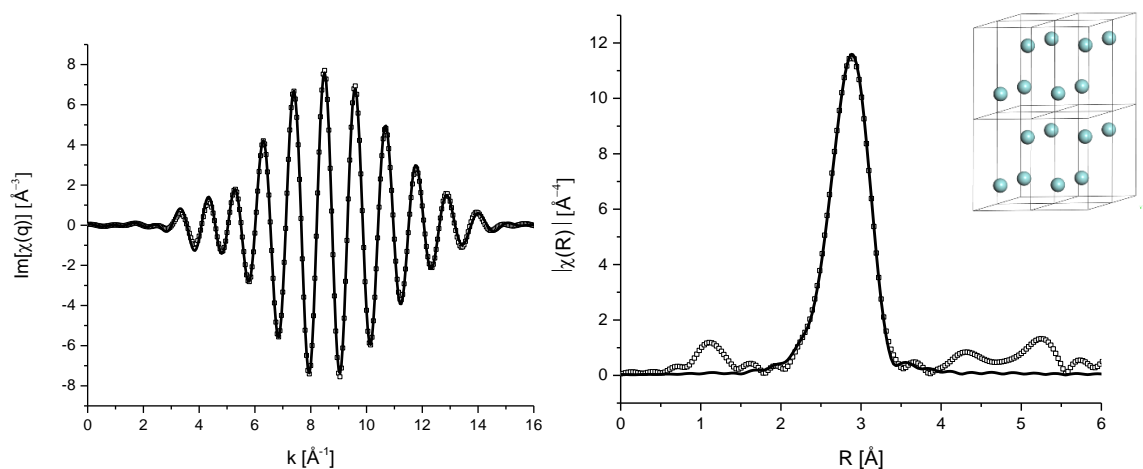


Figure 2.15: Imaginary part of the back Fourier transform (left) and Fourier transforms (right) of the EXAFS $k^3 \cdot \chi(k)$ functions for a Zr foil reference. The solid lines are the experimental data while the dash lines are the fit results obtained within a k -range between 4 and 14 \AA^{-1} and within an R -range of 1.8 up to 3.9 \AA .

Table 6. Parameters extracted from the fit of EXAFS data related to the Zr metallic foil reference.

Scattering paths	S_0	N	R [Å]	$\sigma^2 \times 10^{-3}$ [Å ²]	ΔE [eV]	R-factor
Zr-Zr	0.87 ± 0.05	6	3.157 ± 0.004	5.3 ± 0.6	5.4 ± 0.5	1×10^{-4}
Zr-Zr		6	3.262 ± 0.005	5.9 ± 0.7		

DFT calculation (EXAFS): used as support for EXAFS experiment in which we started from a guess structure we built and optimized at the UFF1 level with the Avogadro molecular builder and visualization tool. We fully optimized then the geometry of the whole structure at the Density Functional Theory level from Gaussian093 code using the MO64 functional and TZVP5 basis set for all the atoms except for the Zirconium atom to which we described the electronic structure of s and p core electrons from the Stuttgart/Dresden6 effective core potential.

2.7 References

- [1] M. Beaudoin, S. L. Scott, *Organometallics* **2001**, *20*, 237-239.
- [2] N. Eedugurala, Z. R. Wang, U. Chaudhary, N. Nelson, K. Kandel, T. Kobayashi, I. I. Slowing, M. Pruski, A. D. Sadow, *Acs Catal* **2015**, *5*, 7399-7414.
- [3] aA. Bendjeriou-Sedjerari, J. M. Azzi, E. Abou-Hamad, D. H. Anjum, F. A. Pasha, K. W. Huang, L. Emsley, J. M. Basset, *J Am Chem Soc* **2013**, *135*, 17943-17951; bC. Lecuyer, F. Quignard, A. Choplin, D. Olivier, J. M. Basset, *Angewandte Chemie-International Edition in English* **1991**, *30*, 1660-1661.
- [4] aF. Rataboul, A. Baudouin, C. Thieuleux, L. Veyre, C. Coperet, J. Thivolle-Cazat, J. M. Basset, A. Lesage, L. Emsley, *J. Am. Chem. Soc.* **2004**, *126*, 12541-12550; bL. Y. Ustynyuk, A. S. Fast, Y. A. Ustynyuk, V. V. Lunin, *Russ J Phys Chem a+* **2012**, *86*, 942-952.
- [5] J. Corker, F. Lefebvre, C. Lecuyer, V. Dufaud, F. Quignard, A. Choplin, J. Evans, J. M. Basset, *Science* **1996**, *271*, 966-969.
- [6] R. Duchateau, *Chem Rev* **2002**, *102*, 3525-3542.
- [7] aD. V. Besedin, L. Y. Ustynyuk, Y. A. Ustynyuk, V. V. Lunin, *Top Catal* **2005**, *32*, 47-60; bV. R. Dufaud, J. M. Basset, *Angew. Chem., Int. Ed.* **1998**, *37*, 806-810.
- [8] G. L. Casty, M. G. Matturro, G. R. Myers, R. P. Reynolds, R. B. Hall, *Organometallics* **2001**, *20*, 2246-2249.
- [9] D. V. Besedin, L. Y. Ustynyuk, Y. A. Ustynyuk, V. V. Lunin, *Russ J Phys Chem a+* **2008**, *82*, 193-200.
- [10] V. Salinier, J. M. Corker, F. Lefebvre, F. Bayard, V. Dufaud, J. M. Basset, *Adv. Synth. Catal.* **2009**, *351*, 2155-2167.
- [11] N. Popoff, B. Macqueron, W. Sayhoun, J. Espinas, J. Pelletier, O. Boyron, C. Boisson, N. Merle, K. C. Szeto, R. M. Gauvin, A. De Mallmann, M. Taoufik, *Eur. J. Inorg. Chem.* **2014**, *2014*, 888-895.
- [12] aF. Rataboul, C. Coperet, L. Lefort, A. de Mallmann, J. Thivolle-Cazat, J. M. Basset, *Dalton Trans.* **2007**, 923-927; bG. Tosin, C. C. Santini, A. Baudouin, A. De Mallman, S. Fiddy, C. Dablemont, J. M. Basset, *Organometallics* **2007**, *26*, 4118-4127.
- [13] aM. Jezequel, V. Dufaud, M. J. Ruiz-Garcia, F. Carrillo-Hermosilla, U. Neugebauer, G. P. Niccolai, F. Lefebvre, F. Bayard, J. Corker, S. Fiddy, J. Evans, J. P. Broyer, J. Malinge, J. M. Basset, *J. Am. Chem. Soc.* **2001**, *123*, 3520-3540; bN. Millot, S. Soignier, C. C. Santini, A. Baudouin, J. M. Basset, *J. Am. Chem. Soc.* **2006**, *128*, 9361-9370.
- [14] L. Du, H. G. Kjaergaard, *J Phys Chem A* **2011**, *115*, 12097-12104.
- [15] F. Blanc, C. Coperet, A. Lesage, L. Emsley, *Chem. Soc. Rev.* **2008**, *37*, 518-526.
- [16] J. M. Mayer, C. J. Curtis, J. E. Bercaw, *J Am Chem Soc* **1983**, *105*, 2651-2660.
- [17] J. Espinas, J. D. A. Pelletier, E. Abou-Hamad, L. Emsley, J. M. Basset, *Organometallics* **2012**, *31*, 7610-7617.
- [18] J. Pflug, A. Bertuleit, G. Kehr, R. Frohlich, G. Erker, *Organometallics* **1999**, *18*, 3818-3826.
- [19] M. S. Cheung, H. S. Chan, Z. W. Xie, *Organometallics* **2005**, *24*, 4468-4474.
- [20] X. C. Shi, G. X. Jin, *Organometallics* **2012**, *31*, 7198-7205.
- [21] M. El Eter, B. Hamzaoui, E. Abou-Hamad, J. D. A. Pelletier, J. M. Basset, *Chem. Commun. (Cambridge, U. K.)* **2013**, *49*, 4616-4618.
- [22] aD. A. Evans, M. M. Morrissey, *J Am Chem Soc* **1984**, *106*, 3866-3868; bF. Alonso, P. Riente, M. Yus, *Tetrahedron* **2009**, *65*, 10637-10643.
- [23] G. S. McGrady, G. Guilera, *Chem Soc Rev* **2003**, *32*, 383-392.
- [24] F. Zaera, *Phys Chem Chem Phys* **2013**, *15*, 11988-12003.
- [25] D. W. Hart, J. Schwartz, *J Am Chem Soc* **1974**, *96*, 8115-8116.
- [26] X. Xu, G. Kehr, C. G. Daniliuc, G. Erker, *J Am Chem Soc* **2013**, *135*, 6465-6476.

- [27] Y. I. Yermakov, Y. A. Ryndin, O. S. Alekseev, D. I. Kochubey, V. A. Shmachkov, N. I. Gergert, *J. Mol. Catal.* **1989**, *49*, 121-132.
- [28] V. A. Zakharov, V. K. Dudchenko, E. A. Paukshtis, L. G. Karakchiev, Y. I. Yermakov, *J. Mol. Catal.* **1977**, *2*, 421-435.
- [29] aA. Bendjeriou-Sedjerari, J. D. A. Pelletier, E. Abou-Hamad, L. Emsley, J. M. Basset, *Chem Commun* **2012**, *48*, 3067-3069; bA. E. Bennett, C. M. Rienstra, M. Auger, K. V. Lakshmi, R. G. Griffin, *J Chem Phys* **1995**, *103*, 6951-6958.

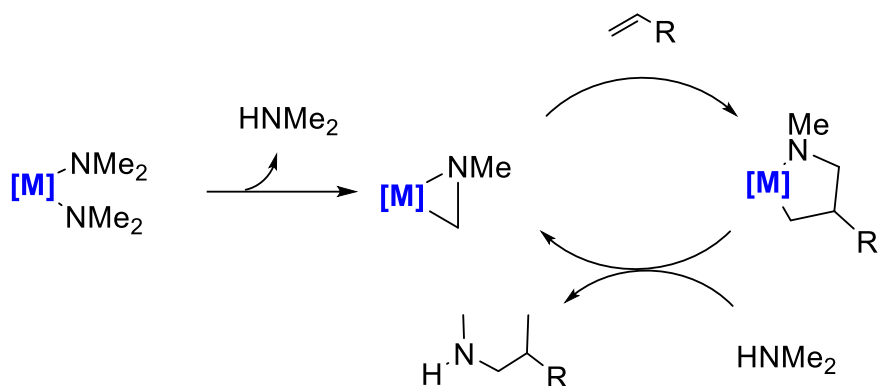
Chapter 3: Catalytic Intermediates Isolation and Mechanistic Studies for Heterogeneous Hydroaminoalkylation Reaction

3.1 Introduction

The development of economically relevant heterogeneous catalysts for alkene hydroaminoalkylation would be a significant step to access a broad range of amines from simple unsaturated hydrocarbons. The type of azametallacyclopropane species evidenced in chapter II are key intermediates for this reaction in homogenous catalysis with many examples being reported using group 4 and 5 based catalysts. The investigation in this chapter covers both zirconium and tantalum metallaaziridnes to compare their reactivity and their catalytic performances.

3.1.1 Alkene hydroaminoalkylation

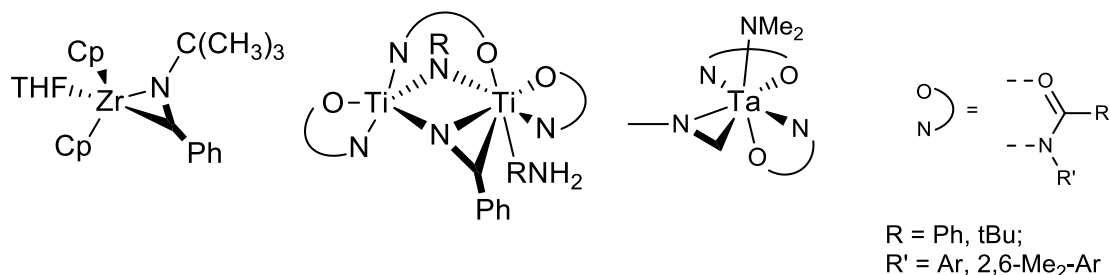
Converting simple organic molecules to functionalized organic compounds is of great interest for academic and industrial research.^[1] Examples have been reported for cross-coupling,^[2] ring expansion^[3] and carbonylation^[4] reactions. Catalytic hydroaminoalkylation reactions are of particular significance, as they provide a selective synthetic route to substituted amines from simple alkene feedstock.^[5] These reactions typically involve the addition of a α -C-H bond (of an amine) across an unsaturated C-C bond (Scheme 3.49).^[6]



Scheme 3.49: Proposed mechanism of hydroaminoalkylation reaction.

Group 4^[7] and 5^[6b, 8] dimethylamido complexes have been well-established as effective precatalysts for the α -alkylation of dimethylamine with simple alkenes.^[8a, 9] High productivities on a broad range of substrates have been reported for electrophilic, catalytic hydroaminoalkylation using sterically demanding amidate^[6a, 10] or electron-withdrawing chloro ligands.^[8b] The active species of the mechanism is commonly assumed to be an azametallacyclopropane because they promote alkylation on the α -position of the amine. The catalytic hydroaminoalkylation cycle (Scheme 3.1) has been proposed but has only been supported by a limited number of experiments.^[8b, 11] In 1982, Nugent et al. investigated the α -deuteration of dimethylamine by reversible α -metallation–demetallation reaction.^[12] More recently, Hultzech^[8c] and Doye^[11] conducted kinetic studies on niobium- and titanium- based catalysts. Elimination of an amine from a bis(amido) metal precursor produces an intermediate that is assumed to be a metallaziridine.^[13] Insertion of an olefin into the new metal-carbon bond generates a five-membered ring complex intermediate. Finally, the starting bis(amido) complex is regenerated through protonolysis by the amine substrate concomitantly with the release of the product.^[1a, 8a, 8b]

The formation of metallaziridine intermediates was always postulated as the key step in the catalytic cycle. Such species have been formally elucidated in few reports.^[14] For instance, Cp*Ta(NMe₂)Me₃ undergoes intramolecular β-H migration to give Cp*Ta(η²-CH₂NMe)Me₂ and the release of methane.^[15] Similar azametallacyclopropane complexes have been isolated and structurally elucidated by single crystal X-ray crystallography (Scheme 3.50).

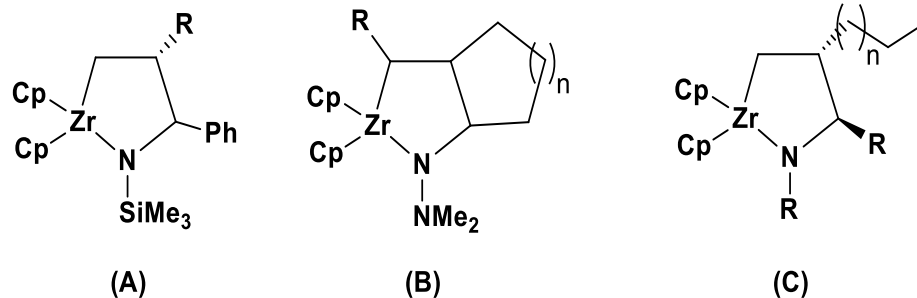


Scheme 3.50: Previously reported metallaziridine molecular complexes based on group 4 and 5 transition metals. Herzon and Hartwig examined the reactivity of tantalum amido derivatives as catalysts for the α-alkylation of alkylaryl amines and dialkyl amines with terminal olefin substrates.^[8a] They showed that the selectivity of hydroaminoalkylation reactions with alkene can be affected by the electronic properties of the amine. To note, N-aryl substrates consistently lead to higher yields than the dialkyl analogues.^[8a] Whitby and co-workers explained this improved reactivity by the lone pair of nitrogen being less available in N-Aryl than in N-alkyl for donation to the metal center due to conjugation with the aromatic π-system.^[16] This observation is in agreement with the report by Herzon and Hartwig in which Ta(NMe₂)₅ and [Cl₃Ta(NMePh)₂]₂ were tested as precatalysts for the reaction of N-(methyl-d₃)-aniline with 1-octene. Interestingly,

highest incorporation of deuterium on the α -carbon was observed when using $[\text{Cl}_3\text{Ta}(\text{NMePh})_2]_2$ as precatalyst.^[8b]

3.1.2 Reactivity of zirconaaziridines

The application of zirconaaziridine complexes toward organic transformations had been abundantly documented.^[17] Precedent examples for such reactivity can be found in the work of Buchwald,^[18] Norton,^[19] Whitby,^[16, 20] Blagg two decades ago.^[20a, 21] Zirconaaziridines can generate, after workup, functionalized amines by reaction with unsaturated C–C bonds^[1b] (olefins and acetylenes) and C–X bonds^[1b] (aldehydes, carbonates^[19a, 19b, 19e, 22] and imines^[1b]). This passes by the formation of a 5-membered zirconacycle through inter-^[1b] or intra-^[23] molecular insertion into the Zr–C bond of the metallaaziridine. Buchwald^[1b] and Whitby^[20a] studied the intermolecular unsaturated hydrocarbon insertion into zirconaaziridines.^[1b] Significant regioselectivity in 1,2-insertion fashion was observed for the formation of the corresponding five-membered metallacycles (Scheme III.51 A and C). Intramolecular insertion of olefins and acetylenes into the Zr–C bonds of zirconaaziridines can lead to annulation reactions. Livinghouse showed that alkyl-, silyl-, and aryl- substituted C–C multiple bonds readily insert into the Zr–C bonds of zirconaaziridines yielding cyclic products (Scheme III.3 B).^[23] To note, mostly zirconium complexes with bulky and electron-rich cyclopentadienyl (Cp) ligands were employed; no catalytic screening for hydroaminoalkylation was reported then.



Scheme 3.51: Previously reported azazirconaacyclopentane molecular complexes.

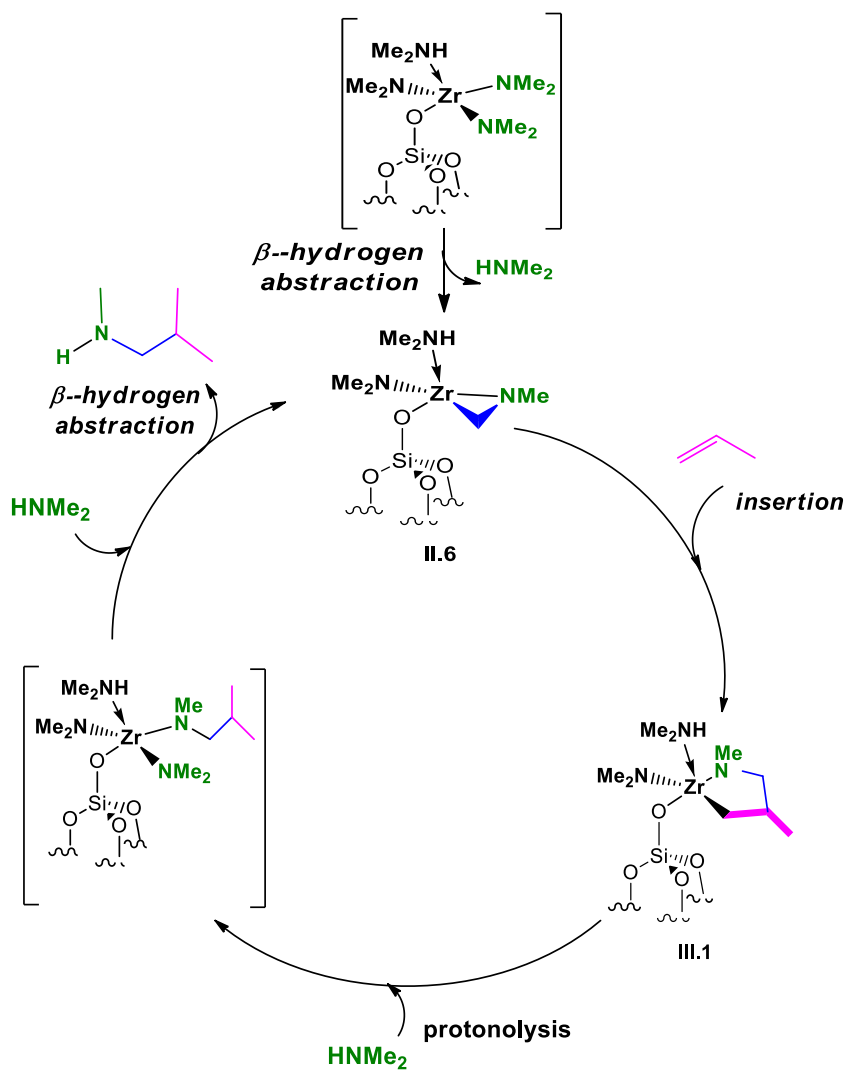
3.1.3 Metallaaziridine-based catalysts for intramolecular hydroaminoalkylation of alkenes

Metallaaziridine-based catalysts were reported only recently (since 2007) by various groups, including Schafer's,^[5a, 6b, 10a, 24] Doye's,^[7b, 11, 25] and Hartwig's,^[8a, 8b] as intermediates of the hydroaminoalkylation of alkenes. The insertion of a double-bond into the M-C bond of the metallaaziridine is supposed to be the C-C bond forming step. Schafer *et al.* prepared a bimetallic titanium species containing an azametallacyclopropane ligand bridging two metal centers.^[7a, 10a] In a separate experiment, they also observed the formation of a tantalazaaziridine moiety from mono- and bis- amidate tantalum complexes.^[10a] Doye and Beckhaus reported the synthesis of titanaaziridine complexes starting from secondary *N*-methylamines and a sterically demanding bis (η^5 : η^1 adamantylidene pentafulvene) titanium complex.^[25b]

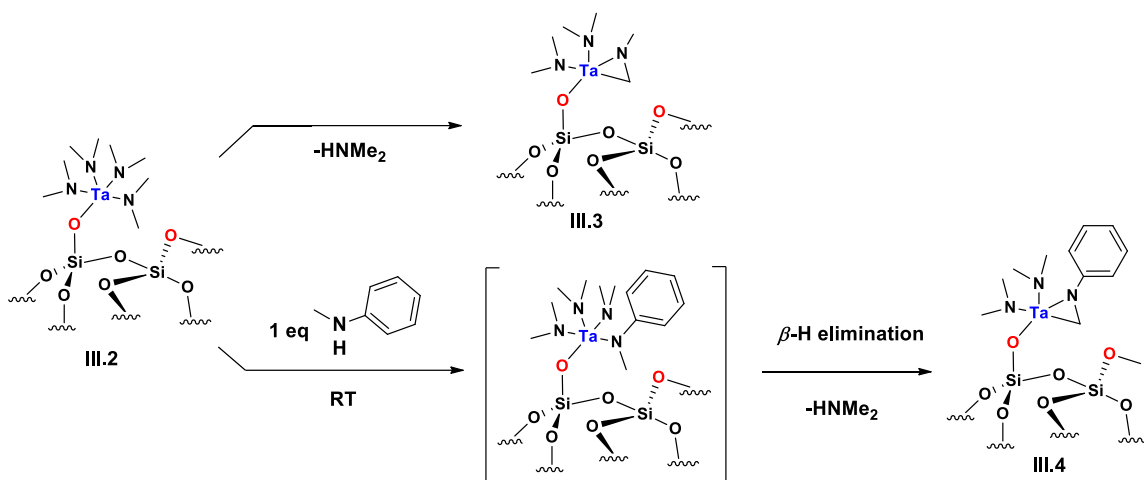
3.2 Scope of the chapter

In this chapter, we are investigating the elementary steps in the heterogeneous intermolecular hydroaminoalkylation mechanism (Scheme 3.52) that is initiated using silica-supported zirconaaziride [\equiv Si-O-Zr (HNMe₂)(η^2 NMeCH₂)(NMe₂)] (II.6) (see

Chapter II). We report the isolation and the characterization of the five-membered metallacyclic intermediate supported on silica [$\equiv\text{Si-O-Zr}(\text{HNMe}_2)(\eta^2\text{NMeCH}_2\text{CH}(\text{Me})\text{CH}_2)(\text{NMe}_2)$] (**III.1**) (Scheme 3.52). We fully characterize the structure of the prepared surface species by SS NMR, elemental analysis and FTIR spectroscopy. After dimethylamine protonolysis, **III.1** gave a hydroaminoalkylation product and regenerated **II.6** that can be reused several times. These results encouraged us also to study surface metallaazaridine complexes as other surface hydroaminoalkylation catalysts candidates. Tantalum was considered first due to the better performance of its molecular complexes over zirconium counterparts.^[8a, 12] The effect of the substrate employed (N-dialkyl vs N-alkylaryl) over the performance of active catalytic species was also of interest. In this chapter, we report the preparation and the characterization of the first single-site well-defined silica-supported tantallaaziridines ($[\equiv\text{Si-O-Ta}(\eta^2\text{NRCH}_2)(\text{NMe}_2)_2]$, R = Me (**III.3**), Ph (**III.4**)) (Scheme 3.53) starting from $[\equiv\text{Si-O-Ta}(\text{NMe}_2)_4]$ (**III.2**). All surface species were characterized by SS NMR experiments, elemental analysis and FTIR spectroscopy.



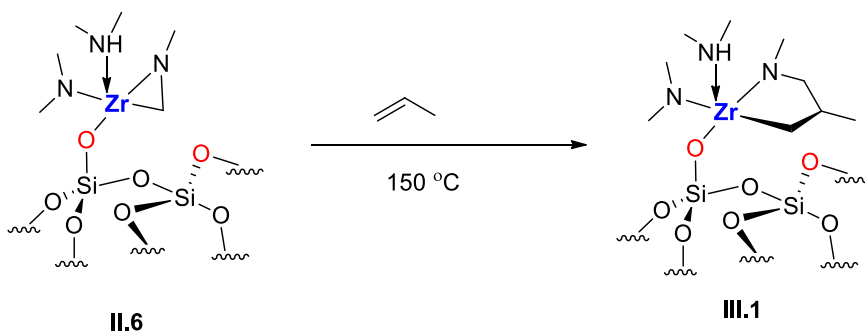
Scheme 3.52: Elementary steps of the intermolecular hydroaminoalkylation by silica-supported zirconaziridine complex.



Scheme 3.53: Preparation pathway of $[\equiv\text{Si-O-Ta}(\text{NMe}_2)_4]$ (III.2) $[\equiv\text{Si-O-Ta}(\eta^2\text{NRCH}_2)(\text{NMe}_2)_2]$ R = Me (III.3), Ph(III.4).

3.3 Isolation and characterization of silica-supported azazirconacyclopentane intermediate

After treatment of II.6 by pure propylene (0.6 bar, 20 h and 150°C), a yellow powder III.1 was formed and was collected after evacuation (10^{-4} mbar at ambient temperature for 1 h).



Scheme 3.54: Reaction II.6 with propylene.

3.3.1 FTIR and elemental analysis

Comparison of the FTIR spectra of II.6 and III.1 reveals a change in the envelope of bands related to alkyl vibrations ($3000\text{--}2800\text{ cm}^{-1}$) with a notable increase of $\nu(\text{CH}_2)$ at

2958 cm^{-1} (Figure 3.16 a and b). This may be interpreted as a modification of the alkyl groups in **III.1**. Elemental analysis gives 2.71% Zr, 3.26% C and 1.37% N with a ratio of Zr/C/N = 1.0/9.1/3.2 \pm 1.0 (theoretical ratio 1/9/3). This ratio strongly suggests that one molecule of propylene has been incorporated by **II.6**.

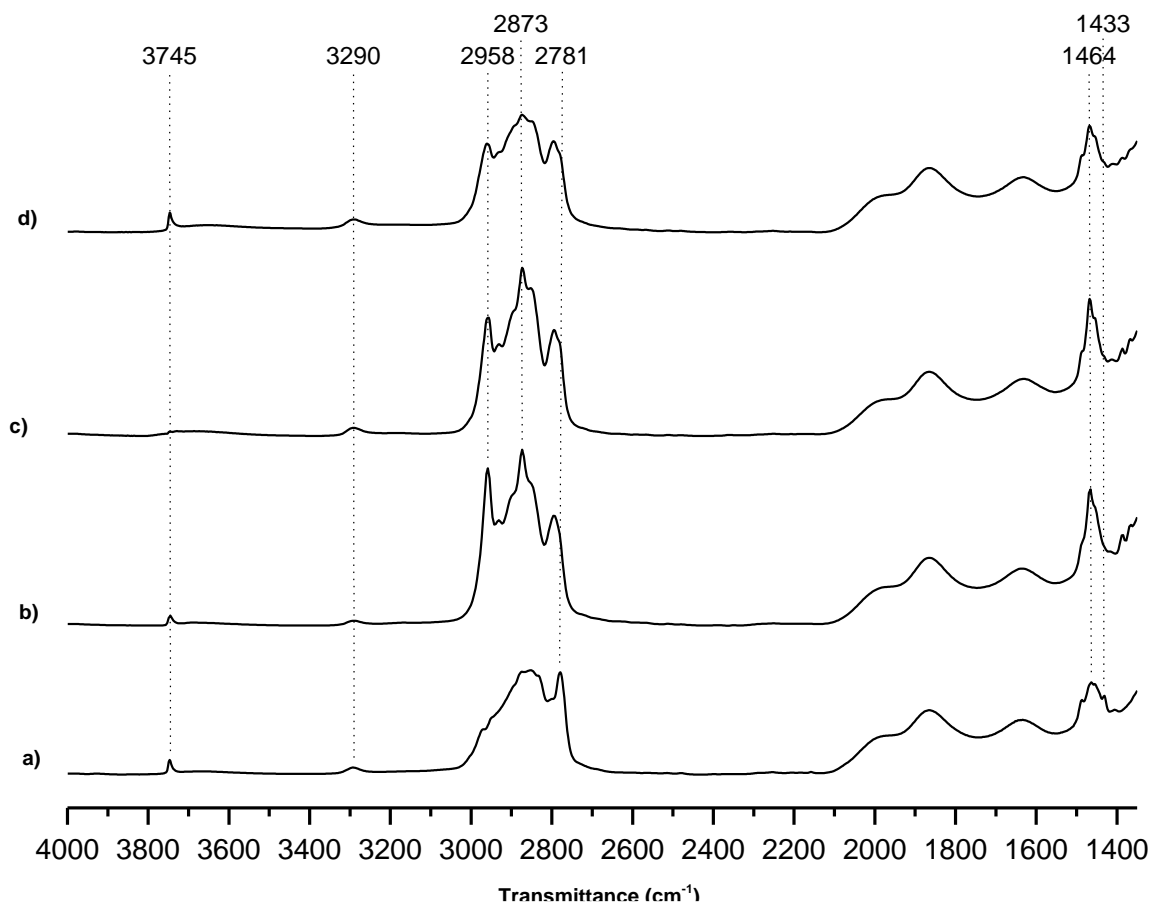


Figure 3.16: FTIR spectra of a) **II.6** b) **III.1** c) **III.1** after treatment with HNMe_2 (0.8 bar) at 150°C for 20 h followed by evacuation (10^{-4} mbar) overnight d) **III.1** after evacuation (10^{-4} mbar) and heating at 150°C for 20 h.

3.3.2 Solid state NMR experiments

The ^1H SS NMR spectrum of **III.1** (Figure 3.17) exhibits two major signals at 1.2 and 2.9 ppm and two minor overlapping signals at 1.7 and 2.0 ppm. The most intense peak at 2.9 ppm is reminiscent of that seen previously at 2.4 ppm in **II.6** that was assigned to the

NCH₃ group in aminomethyl ligands. The other three peaks clearly represent the more complex hydrocarbon motif around the zirconium centre in **III.1** compared to **II.6**.

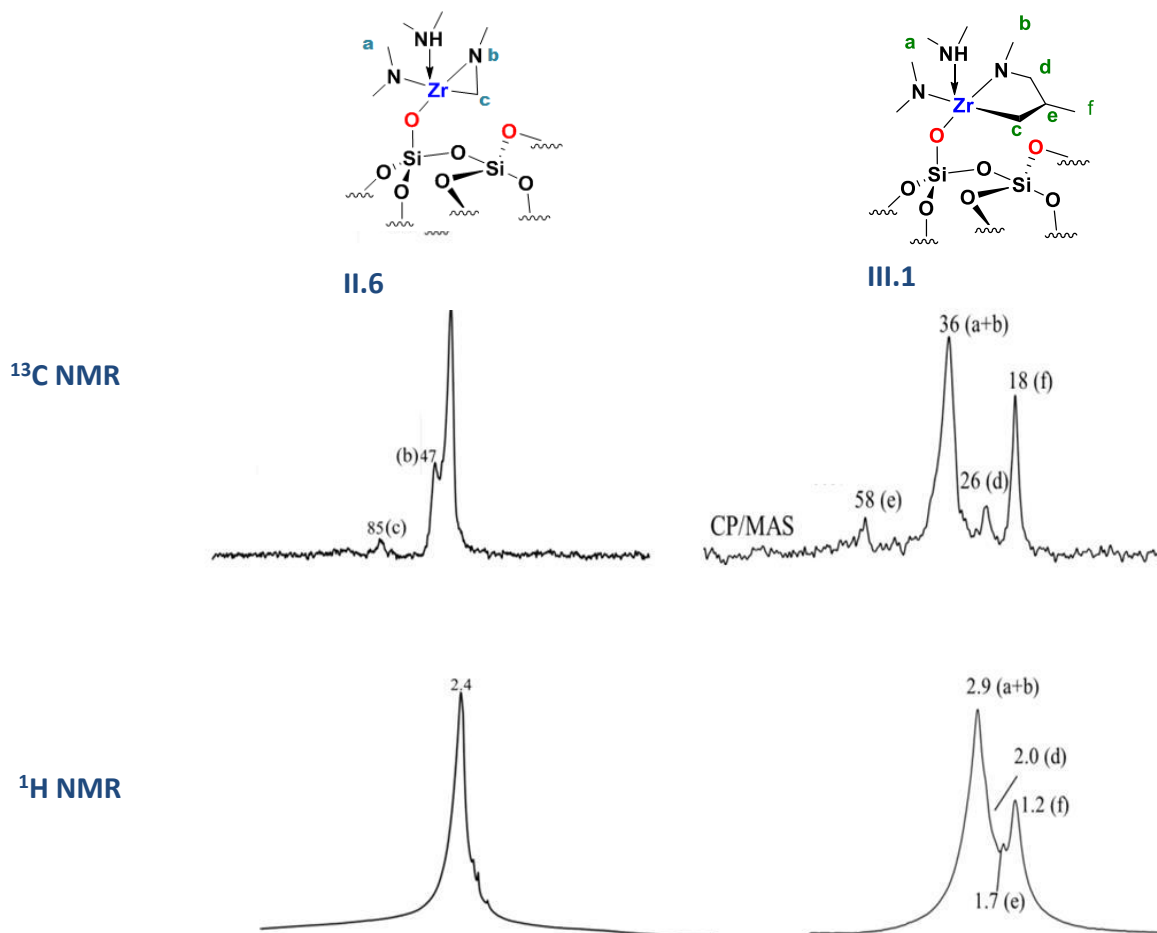


Figure 3. 17: ¹H SS NMR and ¹³C SS NMR spectra of **II.6** and **III.1**.

The ¹³C SS NMR spectrum (Figure 3.17) of **III.1** is consistent with four signals detected at 18, 26, 36 and 58 ppm. The resonance at 36 ppm was significantly more intense than the others, which can be explained by the five aminomethyl fragments. This interpretation is compatible with multiple-quantum 2D experimental spectra of **III.1** that reveal autocorrelations in double-quantum (DQ) and triple-quantum (TQ) frequencies (Figure 3.18 B and C) for signals at 2.9 ppm.

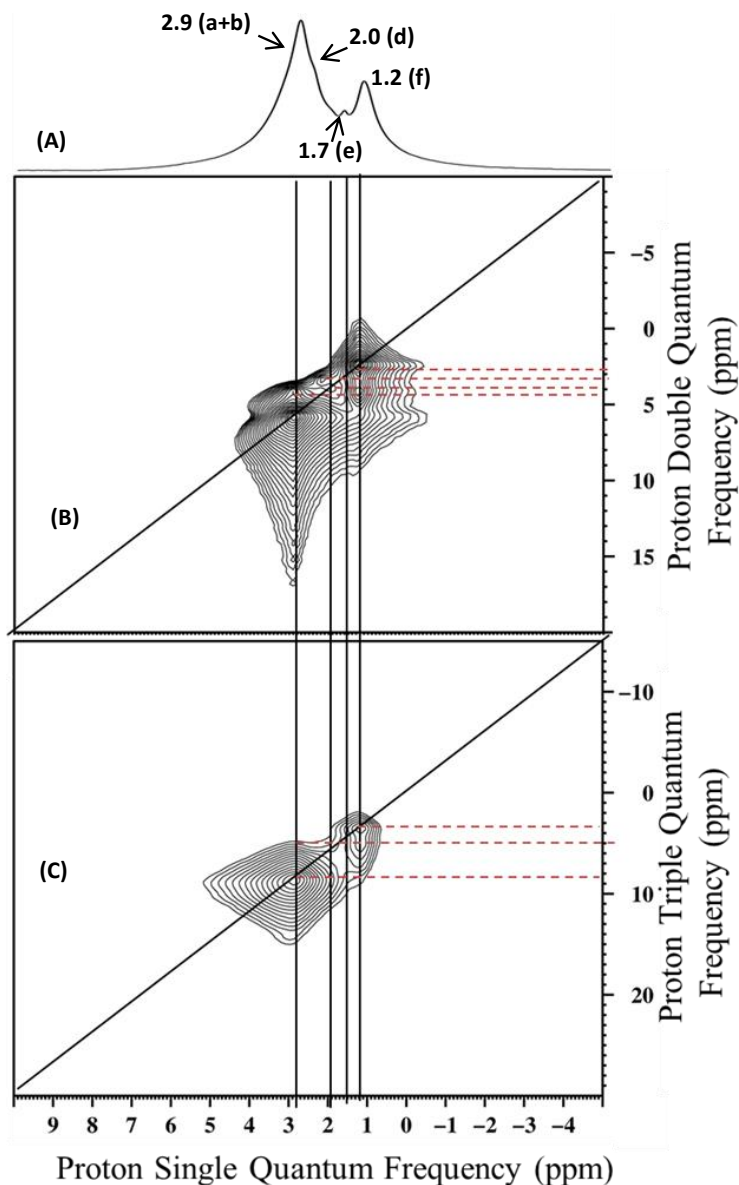


Figure 3.18: (A) ^1H MAS NMR of III.1. (B) and (C) 2D contour plots of the aliphatic region of the DQ and TQ proton SS-NMR correlation spectra of III.1 (see experimental part for details).

In addition, the 2D ^1H ^{13}C HETCOR NMR spectrum (Figure 3.4 B) of III.1 shows a correlation between the carbon peak at 36 ppm and the proton peak at 2.9 ppm. Referring to the assignments proposed for II.6, similar fragments^[4c] can be attributed to these two peaks in dimethyl amine $\text{HN}(\text{CH}_3)_2$ dimethyl amide $\text{N}(\text{CH}_3)_2$ ligands (labeled as a) and the methyl amide $\text{N}(\text{CH}_3)$ fragment (labeled as b) (Figure 3.18).

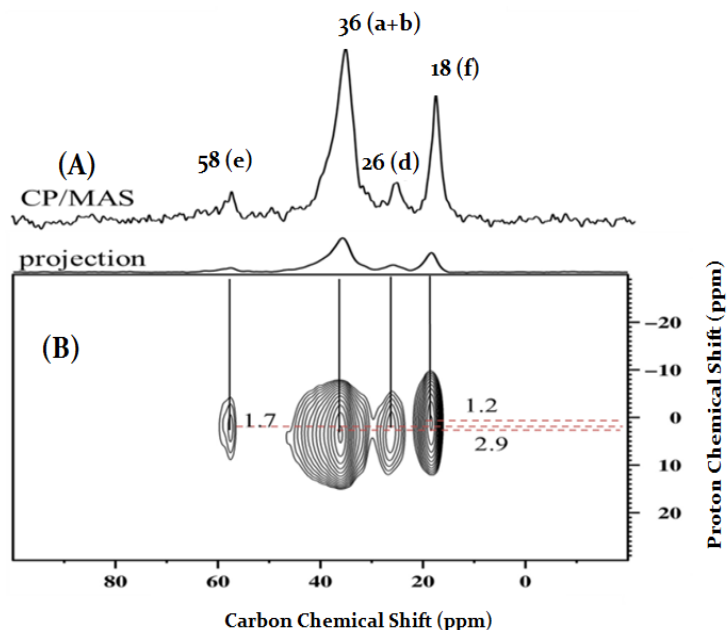


Figure 3. 19: (A) 1D ^{13}C CP/MAS NMR (B) 2D contour plot of the aliphatic region of ^1H ^{13}C HETCOR NMR spectrum of III.1 (see experimental part for details).

Signals at 18 ppm (^{13}C) and 1.2 ppm (^1H) correlate in the 2D ^1H ^{13}C HETCOR NMR spectrum (Figure 3.19 B); both have chemical shifts consistent with a methyl fragment. The methyl assignment is validated by the autocorrelation at 1.2 ppm in DQ and TQ frequencies (Figure 3.18 B and C). These signals are more shielded than (a) and (b), which is attributed to a CH_3 (f) bonded to an alkyl fragment. The minor peak at 1.7 ppm displays no auto-correlation in DQ or TQ frequencies (Figure 3.18 B and C), while the peak at 2.0 ppm shows an auto-correlation only in the DQ experiments; these can be assigned to CH and CH_2 , respectively. A strong correlation is observed between the proton peak at 1.7 ppm and the carbon peak at 58 ppm (Figure 3.19 B). These signals can be attributed to CH (e). Similarly, carbon resonance at 26 ppm correlates with that of the proton at 2.0 ppm and is assigned to CH_2 (d). The absence of CH_2 (c) may be due to the low concentration of III.1 (Mw: 2.7%).

To increase the amount of zirconium on the surface, synthesis of **III.2** was reproduced using SBA₁₅ dehydroxylated at 700 °C (with higher surface area comparing to silica; 2.6 vs 0.3 mmol OH/g). The carbon peak corresponding to CH₂ (c) was observed at 63 ppm in the ¹³C CP/MAS NMR spectrum (Figure 3.20). It correlates with the new protons peak at 2.2 ppm in the 2D ¹H ¹³C HETCOR NMR. Resonance at 63 ppm is indicative of a carbon in the α-position of the zirconium centre.^[25b, 26] It is known that the signal of such a methylene carbon is difficult to detect in the solid state given its low abundance and highly restricted mobility.^[27] Examples of NMR characterization of related molecular complexes were documented; A ¹³C chemical shift (δ = 66.2 ppm) has been reported as a characteristic signal of TiCH₂ group of titanaaziridine complexes;^[25b] the corresponding ¹H signal has been observed between 1.13 and 2.62 ppm.

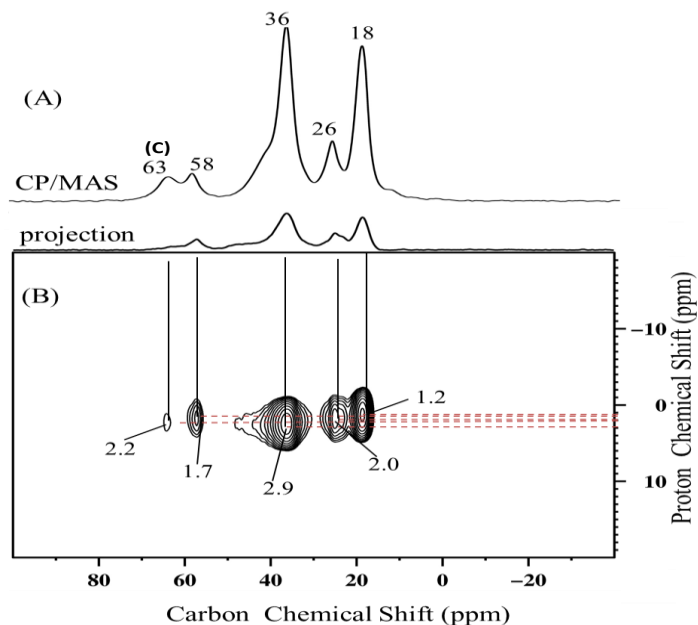


Figure 3.20: (A) 1D ¹³C CP/MAS NMR (B) 2D contour plot of the aliphatic region of ¹H ¹³C HETCOR NMR spectrum of **III.1** on SBA₁₅₋₇₀₀ (see experimental part for details)

In another report by Buchwald,^[1b] ZrCH₂ group gave ¹H signals in the range of 1.08 to 2.07, slightly lower than that observed for **III.1** (2.2 ppm). The ¹³C signals for ZrCH₂ and ZrCH₂CH were not assigned unambiguously but were between 53.96 and 74.73 ppm. These values are roughly compatible with our own finding (58 and 63 ppm). It is noteworthy that the zirconium complexes prepared by Doyes and Buchwald were both based on cyclopentadienyl ligands, hence with higher electron count than **III.1** (16 against 10 electrons).

¹³C-¹³C spin-diffusion correlation with DARR (Dipolar-assisted Rotational Resonance) was performed to examine through-space correlations between the carbons in **III.1** (Figure 3.21). We observed a correlation between signals at 58 ppm in the tertiary CH (e) and signals at 18 and 26 ppm in CH₃ (f) and CH₂ (d), respectively. No correlations were evident between the latter two; this is direct evidence that (e) is directly bonded with (f) and (d). The carbon peak at 36 ppm evidences the logical intensification of the autocorrelation because of its distance from the other carbons. Furthermore, space correlations in DQ and TQ (Figure 3.18) spectra between the CH₃ (f) protons at 1.2 ppm and the protons at 1.7 and 2.0 ppm that correspond with tertiary CH (e) and secondary CH₂ (d) confirm the vicinity of these carbons. All these data support the structure of **III.1** as $[\equiv\text{Si-O-Zr}(\text{HNMe}_2)(\eta^2\text{NMeCH}_2\text{CH}(\text{Me})\text{CH}_2)(\text{NMe}_2)]$.

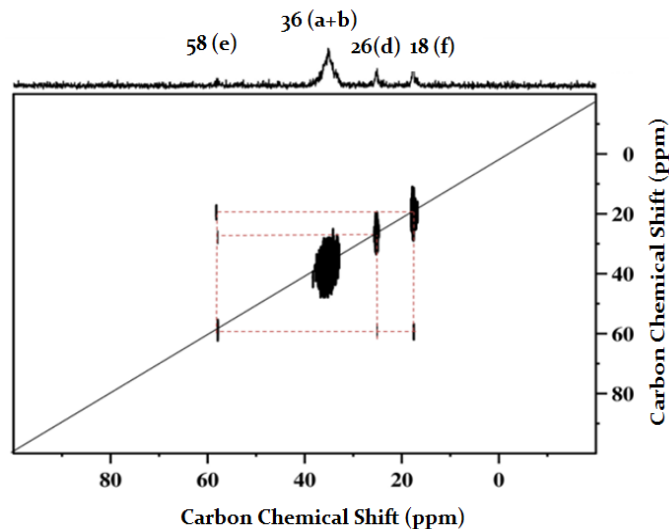


Figure 3.21: 2D ^{13}C ^{13}C spin-diffusion with DARR of (III.1) (see experimental part for details).

3.3.3 Reactivity Studies

A single product was observed after the reaction of **III.1** with dimethylamine (0.8 bar) at 150°C for 20 h (Figure 3.7 a). It was identified as N,2-dimethylpropan-1-amine by a GC-FID (by comparison with a blank run of commercial N,2-dimethylpropan-1-amine mn (Figure 3.22 b, RT = 4.5 mn). This provide direct evidence that the hydroaminoalkylation mechanism promoted by **II.6** includes the 1,2-insertion of olefin into the metal-carbon bond.

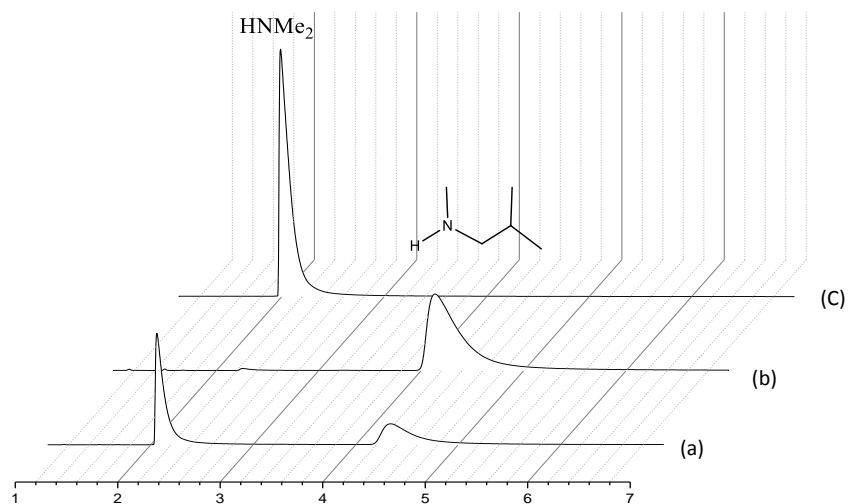


Figure 3.22: GC-FID Chromatogram of (a) gas mixture after reaction of HNMe₂ and III.1 (b) N,2-dimethylpropan-1-amine (c) HNMe₂.

3.4 Synthesis of well-defined silica-supported tantalumaziridines and application on catalytic hydroaminoalkylation

3.4.1 Synthesis and characterization of silica-supported tetra-dimethylamido tantalum complex

Treating SiO₂₋₍₇₀₀₎ with pentakis dimethylamido tantalum in pentane at ambient temperature for 1 hr leads to the formation of a yellow powder (III.2). Comparison of FTIR spectra of SiO₂₋₍₇₀₀₎ and III.2 indicates the grafting of Ta(NMe₂)₅ onto silica (Figure III.23). The signal corresponding to the isolated silanols in SiO₂₋₍₇₀₀₎ (3745 cm⁻¹ ν_(O-H)) has completely disappeared in III.2. New bands have appeared in the regions corresponding to ν_(C-H) (3000-2800 cm⁻¹) and δ_(C-H) (1500-1300 cm⁻¹). They may be assigned to dimethylamine ligand vibrations (Figure III.10).^[28] The combination and overtone bands from the silica (1990, 1867 and 1639 cm⁻¹) remained unchanged.

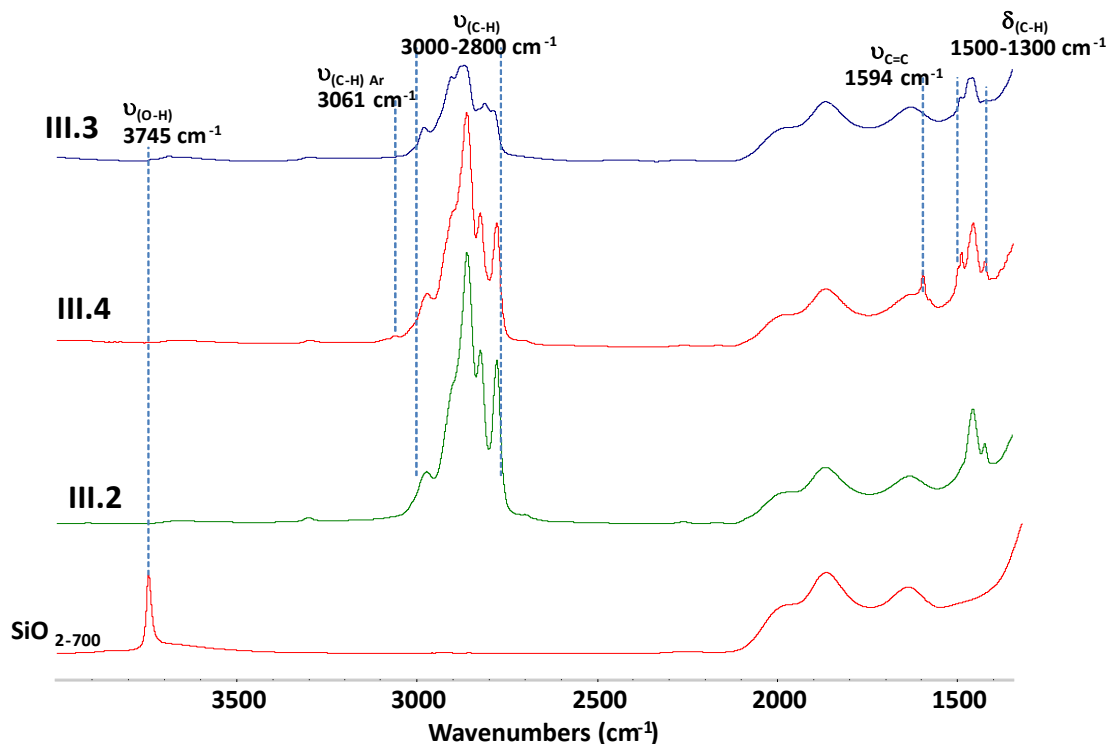
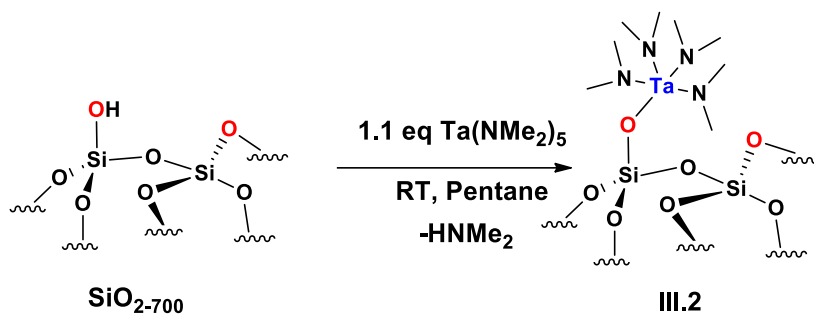


Figure 3.23: FTIR of SiO_{2-700} , **III.2** [$\equiv\text{Si-O-Ta}(\text{NMe}_2)_4$], **III.3** [$\equiv\text{Si-O-Ta}(\eta^2\text{NMeCH}_2)(\text{NMe}_2)_2$] and **III.4** [$\equiv\text{Si-O-Ta}(\eta^2\text{NPhCH}_2)(\text{NMe}_2)_2$].

Elemental analysis of **III.2** gives 4.8% Ta, 2.7% C and 1.6% N with a molar ratio of Ta/C/N = 1/8.4/4.2 (+/-0.3). Considering the respective amounts of grafted tantalum with that of silanols available for grafting (0.27 vs. 0.30 mmol) and the disappearance of vibrations due to silanols, we can propose for **III.2** a tantalum grafted on most of the isolated silanols. The ratio Ta/N (1:4.2 +/- 0.3) is consistent with a monopodal surface

complex with four NMe₂ ligands.



Scheme 3.55: Grafting of Ta(NMe₂)₅ on SiO₂₋₇₀₀.

¹H SS NMR spectrum of III.2 exhibits a single broad signal centered around 3.2 ppm (Figure 3.24).

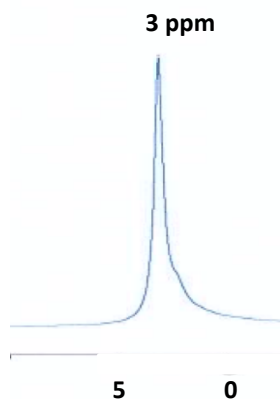


Figure 3.24: ¹H SS NMR of III.2.

¹³C SS NMR revealed one major signal at 45 ppm (Figure 3.25). Both spectra are consistent with quasi-equivalent CH₃ fragments bound to nitrogen atoms.^[15] A tetradimethylamido monopodal structure [≡Si-O-Ta(NMe₂)₄] can be confirmed for tantalum

surface complex **III.2**. Interestingly, a small peak at 35 ppm (^{13}C SS NMR) and a shoulder at 2.5 ppm (^1H SS NMR) may be interpreted as one NMe_2 in axial position.^[15]

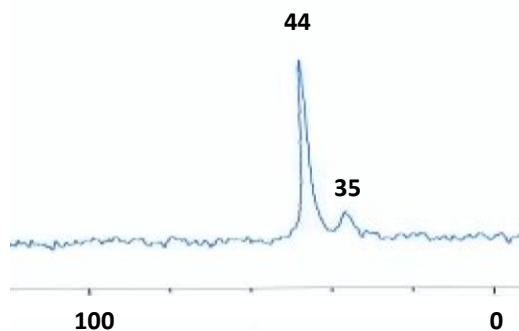


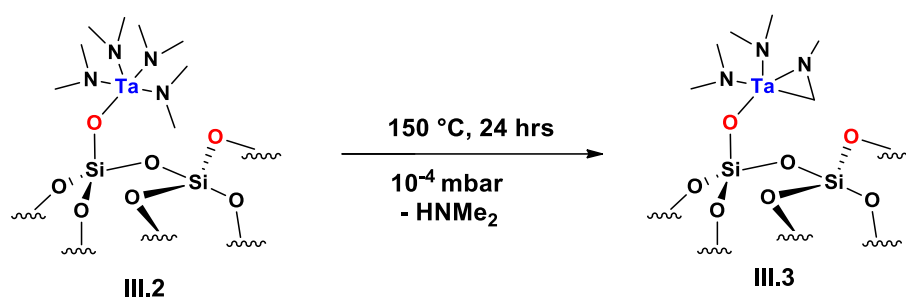
Figure 3.25: ^{13}C SS NMR of **III.2**.

This result illustrates a different reactivity than that observed in our previous studies on the grafting of $\text{Zr}(\text{NMe}_2)_4$ on SBA_{15-700} (Chapter II)^[28] on which the azametallacyclopropane fragment is formed spontaneously at room temperature to afford $[\equiv\text{Si-O-Zr}(\eta^2\text{NMeCH}_2)(\text{NHMe}_2)\text{NMe}_2]$ (**II.6**). Furthermore, the zirconium center was also strongly coordinated to the dimethylamine formed during grafting. It was rationalized that the lesser reactivity of the $[\equiv\text{Si-O-Ta}(\text{NMe}_2)_4]$ regarding the activation the N-Methyl ligand might be overcome by controlled heating under vacuum.

3.4.2 Synthesis and characterization of silica-supported tantallaaziridine

Thermal treatment of **III.2** was conducted at 10^{-4} mbar (Scheme 3.8) to give **III.3**. Initial evacuation of **III.3** at room temperature left the IR spectrum unchanged, although evacuation at a higher temperature ($150\text{ }^\circ\text{C}$) resulted in diminishing intensity of signals in the alkyl vibration region (Figure 3.23). The volatiles identified by GC-FID, consist

exclusively of dimethylamine. Elemental analysis of **III.3** gives 4.8% Ta, 2.0% C and 1.2% N with ratios Ta/C/N = 1/6.1/3.1 (+/-0.3). This strongly suggests that one molecule of HNMe₂ has been eliminated from **III.2**.



Scheme 3.56: Synthesis of silica-supported tantalum aziridine **III.3**.

Furthermore, a new band is observed at 1490 cm⁻¹ and the small band visible in **III.3** at 1422 cm⁻¹ disappeared in **III.2**. These bands correspond to the vibration of the C-H bond of the CH₂ group formed in **III.3**.^[29] In comparison to [≡Si-O-Zr(HNMe₂)(η²NMeCH₂)(NMe₂)] (**II.6**), the wavenumber of this CH₂ is, as expected, lower. Both ¹H and ¹³C SS NMR spectra of **III.3** are notably more complex than that of **III.2**. ¹H NMR of **III.3** contains an intense peak at 2.3 ppm and a broad peak at 3.2 ppm (Figure 3.26 A). The 2.3 ppm signal is attributed to the NCH₃ fragments, as in **III.2**. The resonance at 3.2 ppm can be assigned tentatively to the Ta-CH₂ moieties (note, the Zr-CH₂ analogue show a similar resonance at 3.2 ppm).^[28] The ¹³C SS NMR spectra of the solid products (Figure 3.26 B) shows two signals; one large at 34 ppm, one smaller at 45 ppm. Those two peaks are reminiscent to those previously seen with zirconium,^[28] except for the absence of the broad signal corresponding to the CH₂ group at 85 ppm. It

is known that the signals of such methylene with highly restricted mobility are difficult to detect by SS NMR.^[27] The HETCOR spectrum revealed clear correlations between the protons at 2.3 ppm and the carbons at 34 and 45 ppm (Figure 3.26 E), hence confirming that all the signals observed in ¹³C SS NMR can be assigned to NMe carbons. ¹H–¹H multiple quantum (double-quantum (DQ) and triple-quantum (TQ)) were applied to **III.3** to confirm the presence of the Ta-CH₂ fragment (Figure 3.26 C and D). The peak at 3.2 ppm shows an auto-correlation only in DQ spectrum, but not in the TQ spectrum and it can be thus assigned to a Ta-CH₂ fragment. Examples of NMR characterization of related molecular complexes, containing M-CH₂ fragment, have been documented.^[1b] The corresponding ¹H signal has been observed in the range of 1.08 to 2.07 ppm, slightly lower than that observed for **III.3**. The peak at 2.3 ppm displays a strong auto-correlation, hence validating the NMe₂ assignment.

To conclude, we can propose with certainty the structure $[\equiv\text{Si-O-Ta}(\eta^2\text{NMeCH}_2)(\text{NMe}_2)_2]$ for **III.3**. Its formation can be explained by an intramolecular β -H abstraction of one dimethylamine ligand (Scheme 3.7). This pathway draws strong similarities with that described for $[\equiv\text{Si-O-Zr}(\text{HNMe}_2)(\eta^2\text{NMeCH}_2)(\text{NMe}_2)]$, yet requires stronger conditions (T = 150 °C vs T = RT).

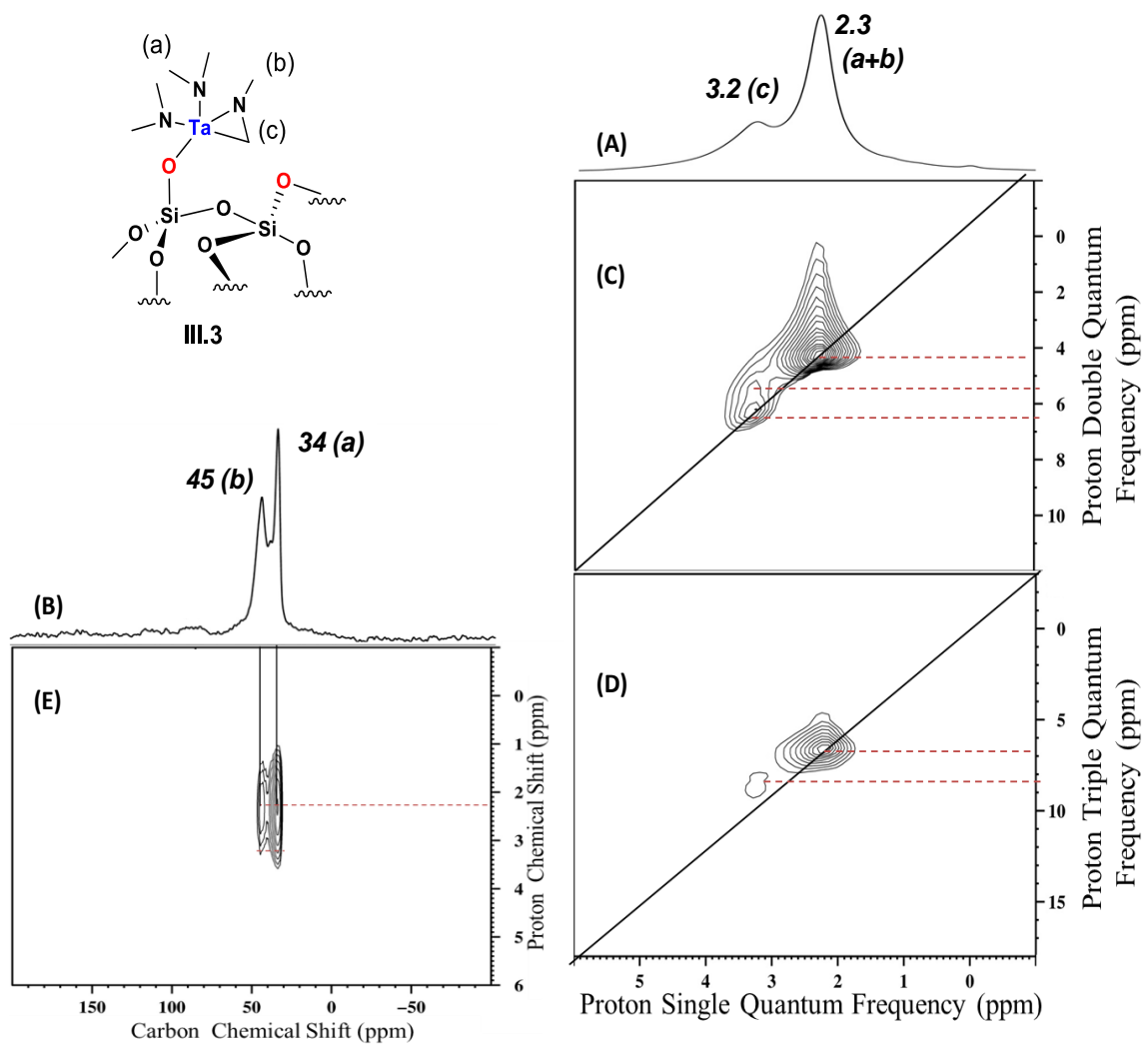
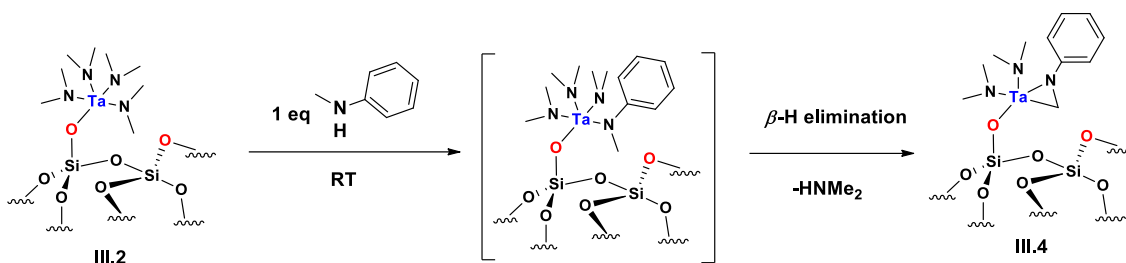


Figure 3.26: (A) 1D ¹H spin-echo MAS solid state NMR spectrum of III.3, (B) ¹³C CP/MAS NMR spectrum of III.3 (C) 2D ¹H-¹H double-quantum (DQ)/single-quantum (SQ), (D) ¹H-¹H triple-quantum (TQ)/SQ and (E) 2D CP/MAS HETCOR NMR spectrum.

3.4.3 Easy formation of tantaallaziridine by substituting NMe-alkyl ligand with NMe-Phenyl

Taking in account the work of Whitby,^[16] we postulated that substituting NMeR ligand (R = alkyl) with another in which R = phenyl may improve the reactivity of the corresponding grafted species toward the formation of the tantaallaziridine complex.

$[\equiv\text{Si-O-Ta}(\text{NMe}_2)_4]$ (**III.2**) was treated with one equivalent of methyl(phenyl)amine in pentane at room temperature (Scheme 3.57).



Scheme 3.57: Synthesis of silica-supported tantalum aziridine **III.4**.

After 4 hr of reaction, the powder was washed three times with pentane and the volatiles were removed *in vacuo*. The resulting powder was a brighter yellow colour than **III.2**. The exclusive gaseous product detected by GC-FID was HNMe_2 . FTIR spectra of the solid products **III.4** showed that the bands characteristic of the arylamide ligands are clearly visible (Figure 3.23). A very broad signal at 3061 cm^{-1} (aromatic C-H bending) and another sharp one at 1594 cm^{-1} ($\nu_{\text{C}=\text{C}}$) can be detected. Elemental analysis of **III.4** gives 5.1% Ta, 3.8% C and 1.3% N with a ratio of Ta/C/N = 1/11.2/3.2 (+/-0.3). This indicates that methyl(phenyl)amine molecules reacted with **III.2**.

^1H SS NMR spectrum of **III.4** (Figure 3.27 A) exhibits, prominently, one major signal at 3.4 ppm with two overlapping minor ones at 2.0 and 6.9 ppm. In the ^{13}C SS NMR spectrum (Figure III.27 B), one very intense resonance at 45 ppm overlapping a weaker one at 35 ppm are displayed in addition to two small signals at 117 and 128

ppm. The two latter resonances have chemical shifts consistent with overlapping aromatic carbons resonances, which is compatible with the resonance at 6.9 ppm in ^1H NMR (Figure 3.27 A). This is confirmed by the correlation observed in the HETCOR spectrum between these ^1H and ^{13}C signals (Figure 3.27 E).

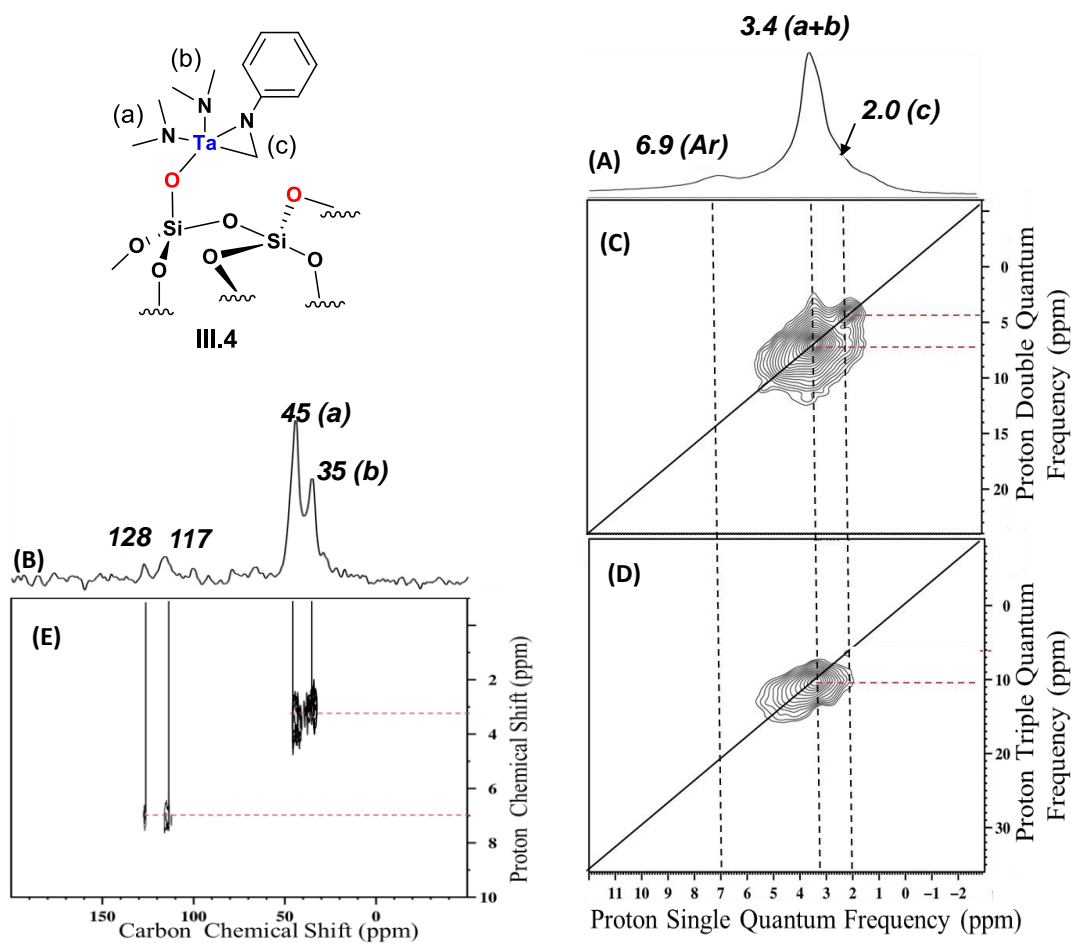


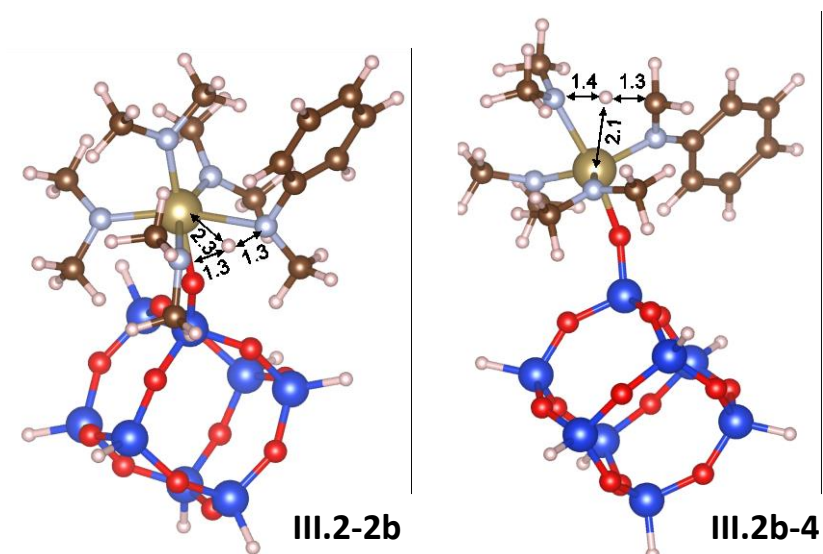
Figure 3.27: (A) 1D ^1H spin-echo MAS solid state NMR spectrum of III.4, (B) ^{13}C CP/MAS NMR spectrum of III.4 (C) 2D ^1H - ^1H double-quantum (DQ)/single-quantum (SQ), (D) ^1H - ^1H triple-quantum (TQ)/SQ and (E) 2D CP/MAS HETCOR NMR spectrum.

Hence, the signals can be assigned to the NCH_3 from the aminomethyl ligands. Finally, the signal at 2.0 ppm (^1H) auto-correlates only in DQ (but not in the TQ spectrum) and can be thus attributed to a CH_2 group. Its chemical shift is lower than that

in **III.3** (3.2 ppm). This may be explained by the presence of the aromatic ring in **III.4**. Indeed, the mesomeric effects of the aromatic cycle (as a electro n-donor) can induce a shift to lower frequency (ppm).^[16] To note, the generation of η^2 -imine complex by activation of the methyl from the amido ligand occurred at room temperature in this case.

3.4.4 Mechanistic study by DFT Calculations of tantallaaziridines formation

In order to shed some light on the mechanism of the metallaaziridines $[\equiv\text{Si-O-Ta}(\eta^2\text{NMeCH}_2)(\text{NMe}_2)_2]$ (**III.3**) and $[\equiv\text{Si-O-Ta}(\eta^2\text{NPhCH}_2)(\text{NMe}_2)_2]$ (**III.4**) from initial $[\equiv\text{Si-O-Ta}(\text{NMe}_2)_4]$ (**III.2**), DFT calculations were conducted for their respective formation pathways including β -hydride elimination. The silica support surface was modelled using a cluster model based on the silsesquioxane $\text{Si}_8\text{O}_{12}\text{H}_8$ cage structure with one $[\equiv\text{Si-O-Ta}(\text{NMe}_2)_4]$ moiety grafted on one of the Si-OH bonds (Scheme 3.58). The initial $[\equiv\text{Si-O-Ta}(\text{NMe}_2)_4]$ species (**III.2**) was considered as the reference structure at 0 kcal/mol. The formation of both metallacycles species **III.3** and **III.4** were found to follow energies reactions pathways (Figure 3.15). For the one leading to methyl-substituted metallaaziridine **III.3** (blue on Figure 3.28), a transition state (**III.2-3** in Figure 3.28) was considered corresponding to the transfer of a hydrogen from the carbon atom of one of the NMe_2 ligands to the nitrogen atom of another NMe_2 ligand.



Scheme 3.58: Structures of key transition states along the reaction pathway involving HN(Ph)(Me). The distances are in Å.

The overall geometry of the ligands around the tantalum center in **III.2-3** is best described as an octahedral geometry. Transition state **III.2-3** is located 32.8 kcal/mol above the starting species **III.2**. This relatively high barrier is in agreement with the reaction requiring experimentally heating at 150°C. Collapsing transition state **III.2-3** onto the products side leads then to the dissociation of HNMe₂ and the formation of metallacycle **III.3**. The total Gibbs free energy cost is of 18.0 kcal/mol relatively to the initial species **III.2**. For the pathway leading to phenyl-substituted metallaaziridine (green on Figure III.28), two steps were considered starting by the ligand exchange between NMe₂ and NPhMe followed by the β-H elimination. HN(Ph)(Me) can replace a NMe₂ ligand on the tantalum center of **III.2** leading to intermediate [≡Si-O-Ta(NMe₂)₃(NPhMe)] (**III.2b**) that has not been observed experimentally. The second step consists in the hydrogen transfer from the NPhMe ligand to one of the NMe₂ ligands similarly to the conversion from **III.2** to **III.3**.

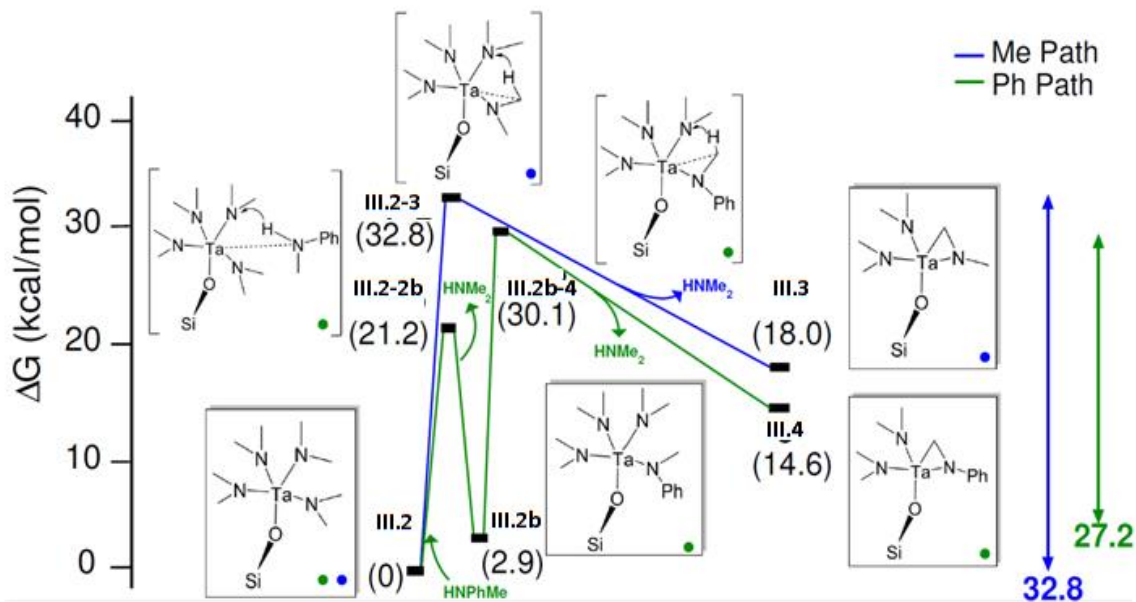


Figure 3.28: DFT reaction profiles for the transformation of III.2 into III.3 or III.4.

Focusing on the first step, transition state **III.2-2b** has an energy barrier of 21.2 kcal/mol compared to the initial structure **III.2**. This relatively low barrier is consistent with the reaction occurring at room temperature. Transition state **III.2-2b** is a hydrogen transfer from the nitrogen atom of the external HN(Ph)(Me) ligand to the nitrogen atom of one of the NMe₂ ligands. This hydrogen transfer leads to the dissociation of HNMe₂ and to the formation of intermediate **III.2b**, that lays above **III.2** by 2.9 kcal/mol. The second transition state **III.2b-4** (Figure III.28) is obtained by hydrogen transfer between the carbon atom of the N(Ph)(Me) ligand to one of the NMe₂ ligand, leading to metallacycle **III.4**. Transition state **III.2b-4** is located 30.1 and 27.2 kcal/mol above **III.2** and **III.2b**, respectively. It is noteworthy that the reaction is carried out under high vacuum, in which the formed HNMe₂ is removed. Hence, it can be assumed that the most correct estimate for the overall barrier corresponding to the formation of **III.4** is

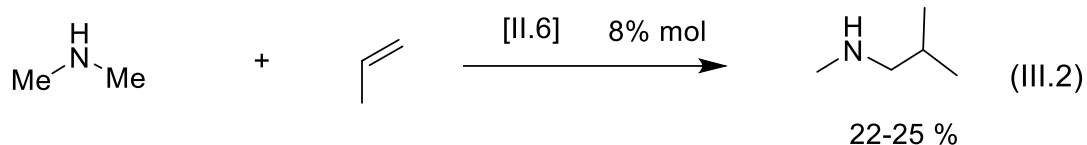
that corresponding to the energy difference between transition state **III.2b-4** and intermediate **III.2b**, 27.2 kcal/mol, rather than the largest energy difference between the highest in energy transition state **III.2b-4** and the most stable intermediate **III.2**, 30.1 kcal/mol. In this scenario, the barrier of 27.2 kcal/mol can be nonetheless considered consistent with this reaction occurring at room temperature. Finally, collapsing transition state **III.2b-4** on the products side leads to the $[\equiv\text{Si-O Ta}(\eta^2\text{NPhCH}_2)(\text{NMe}_2)_2]$ metallacycle **III.4**, 14.6 kcal/mol above **III.2** in terms of free energy. In conclusion, our calculations show that the presence of an aryl group on the NR_2 ligand reduces the free energy barrier for metallacycle formation from 32.8 to 27.2 kcal/mol, which is line with the experimental observations.^[8a]

3.5 Alkene Hydroaminoalkylation Catalytic Studies

This subsection examines the catalytic performances for the hydroamination of alkenes of zirconium and tantalum metallaziridine supported on silica (**II.6** and **III.2** - **III.4**, respectively). Different catalytic conditions were selected for each metal to take in account their difference in activity. Zirconium-based catalysts tend to be significantly less active than their tantalum counterparts so **II.6** was contacted with gaseous propene/dimethylamine while **III.2** - **III.4** were treated with heavier alkene/amine pairs (1-octene and liquid dialkylamines).

3.5.1 Catalytic hydroaminoalkylation using **II.6**

For catalytic hydroaminoalkylation testing, a mixture of one equivalent propylene and an excess of dimethylamine^[30] was added to **II.6** at 150°C for 20 h; *N*-methylisobutylamine was detected as the reaction product (Equation III.2).



We attempted to monitor the reaction progress by comparing the evolution of propene quantities using GC-FID. The yield of the reaction was about 22% after 20 h. Using a minor excess of the propylene compared to the dimethyl amine resulted in a similar yield around 25%.^[31] The catalytic reactivity of **II.6** for hydroaminoalkylation was tested in a complementary experiment using a small amount of **II.6** (100 mg) in a Schlenk vessel (250 ml). The powder was contacted sequentially with gases, vacuum and/or heating. The reaction was followed by FTIR spectroscopy under an inert argon atmosphere (Figure 3.23). Complex **II.2** was contacted with propene (0.8 bar) to generate **III.1**. After evacuation under 10^{-4} mbar for 1 h, **III.1** was heated under a mixed atmosphere of dimethylamine (0.8 bar)^[27] at 150°C for 20 h. The FTIR spectrum (Figure 3. 16 C) of the product collected after a rapid evacuation shows no significant differences in the pattern of $\nu(\text{C-H})$ vibrations with that of **III.1**. Note that the bands assigned to isolated silanols at 3747 cm^{-1} observed in both **II.6** and **III.1** disappeared, suggesting that they likely interact with the products via hydrogen bonding. GC-FID and GCMS found comparable amounts of N-methylisobutylamine and dimethylamine in the gas phase after the reaction (Figure 3.29 b).

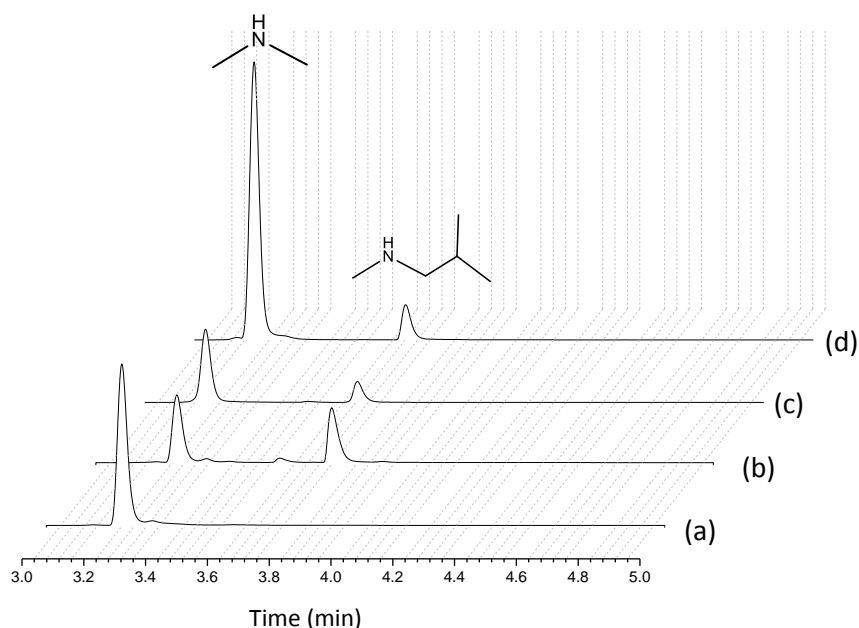


Figure 3.29: GC-FID Chromatogram of (a) HNMe₂ and (b) gas mixture after first reaction of HNMe₂ and III.1 (c) second reaction (d) third reaction.

The compound was then evacuated under 10^{-4} mbar at 150°C for 20 h and the FTIR (Figure 3.16 d) spectrum shows the peak corresponding to the silanols at 3745 cm^{-1} with similar intensity to that in Figure 3.16a and Figure 3.16b. These data suggest that the hydroaminoalkylation of propylene occurs but that only small amounts of the *N*-methylisobutylamine produced remain physisorbed on the silica surface after the reaction (see ChapterII, section 3 for comparable experiment). This was confirmed with a blank experiment,^[32] where SiO_{2-700} was treated with the evolved gas phase (containing *N*-methylisobutylamine and dimethylamine). Comparing the FTIR spectra of silica and SiO_{2-700} revealed an envelope in the CH stretching region between $2959\text{-}2808\text{ cm}^{-1}$ (Figure 3.30). This result validates the hypothesis that physisorption of the amine onto silica occurs in the absence of a grafted complex (Figure 3.16d).

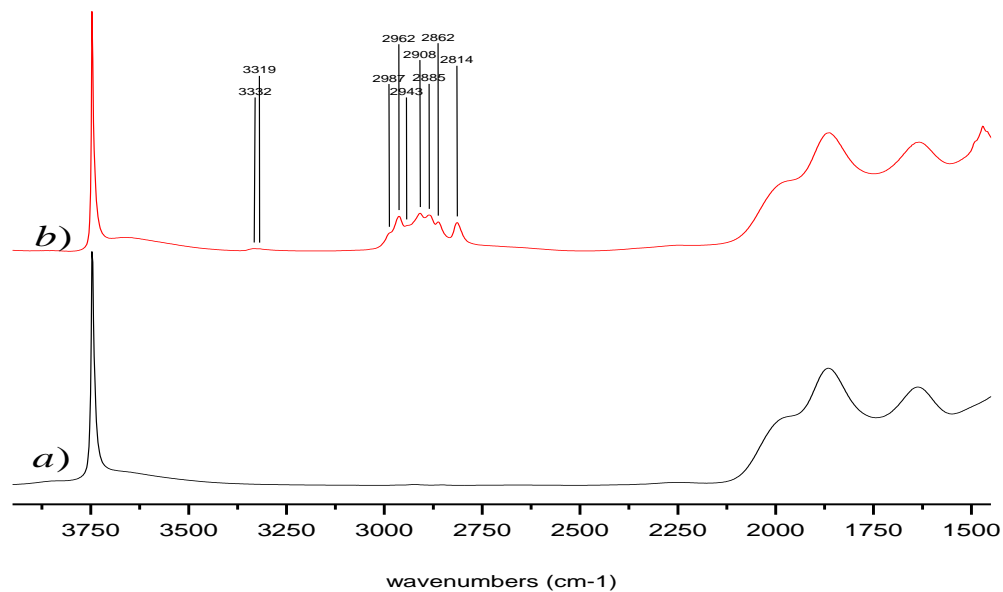


Figure 3.30: FTIR of a) $\text{SiO}_2\text{-700}$. b) After treating the $\text{SiO}_2\text{-700}$ with HNMe_2 and -propanamine, N,2-dimethyl, dimethylamine and hydrogen at 150°C during 20h then evacuating (10^{-4} mbar) over night at 150°C .

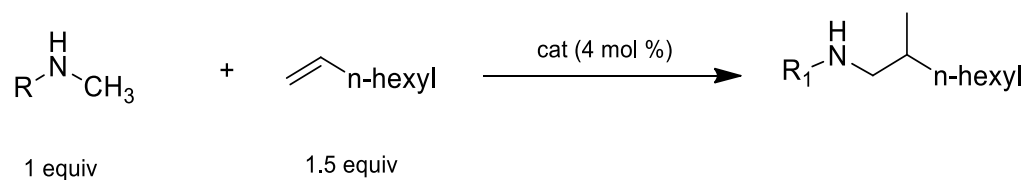
The catalyst was reused three times by repeating the following steps: i) heating with propylene (0.8 bar) at 150°C for 20 h, ii) evacuation under 10^{-4} mbar and iii) heating with dimethylamine (0.8 bar) at 150°C for 20 h. The components in the gas phases were monitored by GC-FID after each sequence (Figure 3.29 a, b and c). After three runs, *N*-methylisobutylamine continued to be obtained, yet in declining amounts due likely to the decomposition of the catalyst.

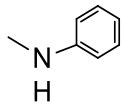
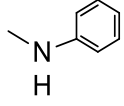
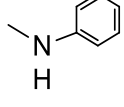
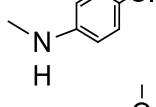
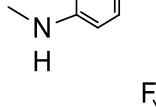
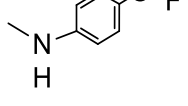
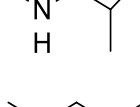
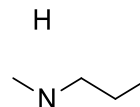

Zirconium catalysts have only been reported at very low activity levels for this reaction.^[8a] Potentially this explains the relative stability of azazirconacyclopentane **III.1** that allows for its isolation and characterisation. It is well-known that a silica surface enhances catalysis and stabilizes the active species.^[33]

3.5.2 Catalytic hydroaminoalkylation using III.2 - III.4

Species (III.2-III.4) were tested as catalyst for hydroamination reaction. The screening was conducted using selected substrates such as dialkylamines (NMeR; R = propyl, i-butyl) and N-methylanilines (NMe(4-R-Ar); R = H, OMe, OCF₃, Cl). All the runs were carried out under similar conditions (165 °C, 1-octene (1.5 eq), 4 mol % catalyst, toluene (0.4 ml)) and terminated after 1, 3 or 6 days (Table 3.9). As a general observation, the branched alkylation products were the sole regioisomer detected hence indicating insertion occurring in 1,2 fashion. Precatalysts III.2-III.4 were screened using methyl(phenyl)amine and formed the branched hydroaminoalkylation product (Entries 1-3). All precatalysts resulted in comparable yields (typically around 45% after 6 days) regardless the duration of the experiments. This indicates that the catalytically active species is likely to be the same in entries 1-3 and assumed to be III.4.

Table 3.8. Hydroaminoalkylation substrates testing using catalysts III.2 -4.



Entry	aryl amines	Catalyst	%yield ^a		
			24h	3 days	6 days
1		III.2	23	38	41
2		III.3	19	29	42
3		III.4	22	35	46
4		III.2	20	42	51
5		III.2	21	39	48
6		III.2	31	42	53
7		III.2	10	26	30
8		III.2	12	27	33
9		III.4	14	29	34

^a Determined by GC-FID using amine as default product.

Reactions using electron-rich N-methyl anilines such as (4-chlorophenyl)-methyl-amine (Entry 4), (4-methoxyphenyl)-methyl-amine (Entry 5), and methyl-[4-(trifluoromethoxy)phenyl] amine (Entry 6), occurred in slightly higher yields (around 50% after 6 days). The introduction of electro-attractive substituent on the para position of the N-aryl ligands seems to have a limited effect. Dialkylamides such as N,2-Dimethyl-1-propanamine (Entry 7) and methyl(propyl)amine (entries 8) reacted in lower yields (around 30% after 6 days). In contrast with entries 7-8, substituting amine with electro-donating groups, reduce the yield significantly. These results are in agreement with catalytic α -alkylation of amines being more efficiently with N-aryl alkylamines than with dialkylamines (see subsection 3.4.4).

3.5.3 Catalytic hydroaminoalkylation conclusions

It is not possible to compare directly the results obtained from runs using zirconium with those using tantalum as they were operating in very different conditions. However, both have shown that it is possible to employ single-site and well-defined metallaaziridine to promote hydroaminoalkylation heterogeneous catalysis. In addition, the validity of the SOMF approach applied to metal nitrogen fragment is reinforced. Nonetheless, a significant amount of work is necessary to design improved supported catalysts.

3.5 Conclusions

Our investigation, which includes the isolation of elusive azazirconacyclopentane **III.1** as a key intermediate, is in agreement with the accepted mechanism of the hydroaminoalkylation reaction. Its precursor **II.6** was prepared by grafting $\text{Zr}(\text{NMe}_2)_4$ onto the surface of $\text{SiO}_2\text{-700}$. Azazirconacyclopentane (**III.1**) was obtained after controlled insertion of propylene. The initial complex (**II.6**) can be regenerated by introducing excess gaseous dimethyl-amine, which led to the opening of metallacyclic fragment and the release of *N*-methylisobutylamine.

Complex **II.6** can undergo further cycles but also shows catalytic activity when using a mixture of propene and amine. These results confirm that supporting zirconium complexes onto silica is a viable preparative route to heterogeneous hydroaminoalkylation catalysts. Yet the catalytic performances remain modest but are encouraging to pursue towards the development of better heterogeneous catalysts to be used in broader range of processes.

Single-site well-defined silica-supported tetra-dimethylamido tantalum [$\equiv \text{Si-O-Ta}(\text{NMe}_2)_4$] (**III.2**) can undergo β -H elimination of dimethyl amine leading to the corresponding silica-supported tantallaaziridine. By combining SS NMR spectroscopy of the isolated intermediates and DFT study of the reaction mechanism, we can conclude that the electronic properties of the amine direct the reactivity of the tantalum center. [$\equiv \text{Si-O-Ta}(\eta^2\text{NMeCH}_2)(\text{NMe}_2)_2$] (**III.3**) can be conveniently obtained by thermal treatment of **III.2** (150 °C, 24 h). In contrast, the tantallaaziridine species [$\equiv \text{Si-O-Ta}(\eta^2\text{NPhCH}_2)(\text{NMe}_2)_2$] (**III.4**) can be prepared at room temperature, via treatment of

III.2 with methylarylamine. Catalytic testing of a selection of amine compounds with variable electronic properties was carried out. The α -alkylation of amines was consistently more efficient with N-aryl alkylamines substrates than with their dialkylamines counterparts.

3.6 Experimental Section

General

The description of the general procedures, including technical description and reagent preparation can be consulted in chapter II section 5.

Synthesis procedures

Preparation of $\equiv\text{Si-O-Zr}(\text{NMe}_2)(\text{HNMe}_2)(\text{NMeCH}_2)$ (II.6): see chapter II

Preparation of $\equiv\text{Si-O-Zr}(\text{HNMe}_2)(\eta^2\text{NMeCH}_2\text{CH}(\text{Me})\text{CH}_2)(\text{NMe}_2)$ (III.1): In a glass reactor (230 mL), an excess of dried propylene gas (0.8 mbar) was reacted with 1 g of (II.6). The reaction was heated with the gradient room temperature to 150°C (1°C per minute) and then at 150°C for 24 hours. After the reaction, the remaining gas was analyzed by GC-MS and found to contain only propylene, which was evacuated for 1 h under dynamic vacuum ($< 10^{-5}$ mbar) conditions.

Alkylation of dimethyl amine with propylene: In a glove box, a glass reactor tube (230 mL) was charged with (II.6) (0.840 g, 0.22 mmol, 0.08 eq.). The reactor was evacuated using a high-vacuum line. 2.81-mmol propylene (0.3 bar, 1 eq.) was introduced and condensed by cooling with liquid nitrogen. Next, HNMe_2+H_2 (0.4 mbar)

was added. After closing the reactor, the mixture was heated (150°C) for 20 h and then was cooled to 22°C.

Preparation of $[\equiv\text{Si-O-Ta}(\text{NMe}_2)_4]$ (III.2): In a double Schlenk, $\text{Ta}(\text{NMe}_2)_5$ (0.132 g) in slight excess (1.1 eq.) with respect to the amount of surface accessible silanols (0.3 mmol silanols groups per gram) was reacted with 1 g of $\text{SiO}_2\text{-700}$ at room temperature in pentane for 1 hr. After filtration and four washing cycles, all volatile compounds were evaporated and the white solid was dried for 1 hr under dynamic vacuum ($< 10^{-5}$ mbar).

Preparation of $[\equiv\text{Si-O-Ta}(\eta^2\text{NMeCH}_2)(\text{NMe}_2)_2]$ (III.3): In a glass reactor (230 mL), **III.2** (1.000 g) was heated with the gradient room temperature to 150 °C (1 °C per minute) and then at 150 °C for 24 hours under dynamic vacuum ($< 10^{-5}$ mbar). The resulting powder was then cooled to 22 °C analysed by FTIR and SS NMR.

Preparation of $[\equiv\text{Si-O-Ta}(\eta^2\text{NPhCH}_2)(\text{NMe}_2)_2]$ (III.4): In a double Schlenk, methyl(phenyl)amine (0.14 ml, 1 eq.) was reacted with 500 mg of **III.2** at room temperature in pentane for 4 hr. After filtration and four washing cycles, all gas-phase products were analyzed by GC-FID and the resulting solid was dried for 1 hr under dynamic vacuum ($< 10^{-5}$ mbar).

Alkylation of N-alkyl-arylamines and N-dialkylamines with 1-octene: Three vacuum sealed ampules were loaded sequentially with the catalyst (0.04 equiv), toluene (400 μL), secondary amine (1 eq.), a Teflon-coated stir bar, and 1-octene (1.50 eq.). The

ampules were then removed from the glove box and connected to a high vacuum line. The mixture was condensed by cooling with liquid nitrogen and the ampules were evacuated ($< 10^{-5}$ mbar). After sealing, the ampules were placed in an oil bath (165 °C). The reaction mixture was heated for 1 day, 3 days and 6 days and each time after reaction it was cooled to 22 °C. The product solution was filtrated to remove the catalyst and the remaining liquid product was analyzed by GC-FID and GC-MS.

Computational Details

All calculations were performed with Gaussian09.^[34] For geometry optimizations, transition states search and vibration frequencies evaluations we used the Perdew-Burke-Erznhof (PBE)^[35] functional along with the single valence polarization basis set of Ahlrichs for main group atoms (basis set SVP in G09)^[36] except the tantalum metallic center for which we described the core electrons with the Stuttgart SDD^[36] quasi-relativistic effective core potential. Minima and transition states were characterized by the appropriate number of negative eigenvalues in the Hessian. We also checked that the imaginary frequency of all the transition states structures corresponds to a vibration along the reactive path between reactants and products. We ran the final single point energy calculations over the PBE optimized geometries using the hybrid Perdew-Burke-Erznhof (PBE0) functional^[37] with the empirical dispersion correction of Grimme (D3)^[38] along with the triple- ζ valence plus one polarization function basis set of Ahlrichs (basis set TZVP in G09).^[39] We evaluated the final Gibbs free energies of all stationary point of the potential energy surface by adding the PBE0-D3/TZVP/SDD single point energies to

the thermal corrections including zero point vibrational energy at the PBE/SVP/SDD level. (See more details in Appendices C)

SS NMR details

Details of figure 3.13. (A) 1D ^1H spin-echo MAS solid state NMR spectrum of **III.3** (acquired on a 600 MHz NMR spectrometer under a 20 KHz MAS spinning frequency, number of scans = 8, repetition delay = 5 s), (B) ^{13}C CP/MAS NMR spectrum of **III.3** (acquired on 600 MHz NMR spectrometer with 10 KHz MAS, number of scan = 20000, repetition delay = 4 s contact time = 2 ms, line broadening = 80 Hz). (C) 2D ^1H - ^1H double-quantum (DQ)/single-quantum (SQ), (D) ^1H - ^1H triple-quantum (TQ)/SQ (acquired on a 600 MHz NMR spectrometer under 22 KHz MAS spinning frequency with a back-to-back re-coupling sequence, number of scans = 128, repetition delay = 5 s number of t_1 increments = 128, with the increment set equal to one rotor period of 45.45 μs) and (E) 2D CP/MAS HETCOR NMR spectrum with short contact times of 0.2 ms under 8.5 KHz MAS, number of scans per increment = 4000, repetition delay = 4 s, number of t_1 increments = 32, line broadening = 80 Hz).

Details of figure 3.14. (A) 1D ^1H spin-echo MAS solid state NMR spectrum of **III.4** (acquired on a 600 MHz NMR spectrometer under a 20 KHz MAS spinning frequency, number of scans = 8, repetition delay = 5 s), (B) ^{13}C CP/MAS NMR spectrum of **III.4** (acquired on 600 MHz NMR spectrometer with 10 KHz MAS, number of scan = 20000, repetition delay = 4 s contact time = 2 ms, line broadening = 80 Hz). (C) 2D ^1H - ^1H double-quantum (DQ)/single-quantum (SQ), (D) ^1H - ^1H triple-quantum (TQ)/SQ (acquired on a

600 MHz NMR spectrometer under 22 KHz MAS spinning frequency with a back-to-back re-coupling sequence, number of scans = 128, repetition delay = 5 s number of t_1 increments = 128, with the increment set equal to one rotor period of 45.45 μ s) and (E) 2D CP/MAS HETCOR NMR spectrum with short contact times of 0.2 ms under 8.5 KHz MAS, number of scans per increment = 4000, repetition delay = 4 s, number of t_1 increments = 32, line broadening = 80 Hz).

3.7. References

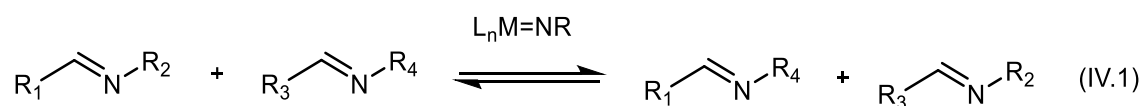
- [1] aH. Tsurugi, K. Yamamoto, H. Nagae, H. Kaneko, K. Mashima, *Dalton T* **2014**, *43*, 2331-2343; bS. L. Buchwald, B. T. Watson, M. W. Wannamaker, J. C. Dewan, *J Am Chem Soc* **1989**, *111*, 4486-4494; cI. Omae, *J Organomet Chem* **2007**, *692*, 2608-2632; dR. D. Broene, S. L. Buchwald, *Science* **1993**, *261*, 1696-1701.
- [2] G. D. Frey, C. P. Reisinger, E. Herdtweck, W. A. Herrmann, *J Organomet Chem* **2005**, *690*, 3193-3201.
- [3] D. Sole, L. Vallverdu, X. Solans, M. Font-Bardia, J. Bonjoch, *Organometallics* **2004**, *23*, 1438-1447.
- [4] Takahashi, H., J. Tsuji, *J Organomet Chem* **1967**, *10*, 511-&.
- [5] aE. Chong, J. W. Brandt, L. L. Schafer, *J Am Chem Soc* **2014**, *136*, 10898-10901; bS. Raouf-moghaddam, *Org Biomol Chem* **2014**, *12*, 7179-7193.
- [6] aJ. Dorfler, S. Doye, *Angew Chem Int Edit* **2013**, *52*, 1806-1809; bP. Eisenberger, R. O. Ayinla, J. M. P. Lauzon, L. L. Schafer, *Angew Chem Int Edit* **2009**, *48*, 8361-8365.
- [7] aJ. A. Bexrud, P. Eisenberger, D. C. Leitch, P. R. Payne, L. L. Schafer, *J Am Chem Soc* **2009**, *131*, 2116-+; bR. Kubiak, I. Prochnow, S. Doye, *Angew Chem Int Edit* **2009**, *48*, 1153-1156; cR. Kubiak, I. Prochnow, S. Doye, *Angew Chem Int Edit* **2010**, *49*, 2626-2629; dT. Preuss, W. Saak, S. Doye, *Chem-Eur J* **2013**, *19*, 3833-3837; eD. Jaspers, W. Saak, S. Doye, *Synlett* **2012**, 2098-2102.
- [8] aS. B. Herzon, J. F. Hartwig, *J Am Chem Soc* **2007**, *129*, 6690-+; bS. B. Herzon, J. F. Hartwig, *J Am Chem Soc* **2008**, *130*, 14940-+; cA. L. Reznichenko, K. C. Hultsch, *J Am Chem Soc* **2012**, *134*, 3300-3311; dA. L. Reznichenko, T. J. Emge, S. Audorsch, E. G. Klauber, K. C. Hultsch, B. Schmidt, *Organometallics* **2011**, *30*, 921-924; eF. R. Zhang, H. B. Song, G. F. Zi, *Dalton T* **2011**, *40*, 1547-1566.
- [9] P. W. Roesky, *Angew Chem Int Edit* **2009**, *48*, 4892-4894.
- [10] aJ. M. P. Lauzon, L. L. Schafer, *Dalton T* **2012**, *41*, 11539-11550; bZ. X. Zhang, J. D. Hamel, L. L. Schafer, *Chem-Eur J* **2013**, *19*, 8751-8754; cP. Garcia, P. R. Payne, E. Chong, R. L. Webster, B. J. Barron, A. C. Behrle, J. A. R. Schmidt, L. L. Schafer, *Tetrahedron* **2013**, *69*, 5737-5743.
- [11] I. Prochnow, P. Zark, T. Muller, S. Doye, *Angew Chem Int Edit* **2011**, *50*, 6401-6405.
- [12] W. A. Nugent, D. W. Ovenall, S. J. Holmes, *Organometallics* **1983**, *2*, 161-162.
- [13] E. Chong, P. Garcia, L. L. Schafer, *Synthesis-Stuttgart* **2014**, *46*, 2884-2896.
- [14] aL. W. Francisco, P. S. White, J. L. Templeton, *Organometallics* **1996**, *15*, 5127-5136; bL. H. Polm, G. Vankoten, C. J. Elsevier, K. Vrieze, B. F. K. Vansanten, C. H. Stam, *J Organomet Chem* **1986**, *304*, 353-370; cH. Hoberg, V. Gotz, C. Kruger, Y. H. Tsay, *J Organomet Chem* **1979**, *169*, 209-217; dJ. Browning, H. D. Empsall, M. Green, F. G. A. Stone, *J Chem Soc Dalton* **1973**, 381-387.
- [15] J. M. Mayer, C. J. Curtis, J. E. Bercaw, *J Am Chem Soc* **1983**, *105*, 2651-2660.
- [16] N. Coles, M. C. J. Harris, R. J. Whitby, J. Blagg, *Organometallics* **1994**, *13*, 190-199.
- [17] S. A. C. J. A. T. J. R. Norton, *Topics Organomet Chem, Vol. 10*, **2005**.
- [18] aR. B. Grossman, W. M. Davis, S. L. Buchwald, *J Am Chem Soc* **1991**, *113*, 2321-2322; bS. L. Buchwald, R. B. Nielsen, *J Am Chem Soc* **1988**, *110*, 3171-3175; cS. L. Buchwald, R. B. Nielsen, J. C. Dewan, *Organometallics* **1988**, *7*, 2324-2328.
- [19] aD. A. Gatley, J. R. Norton, P. A. Goodson, *J Am Chem Soc* **1995**, *117*, 986-996; bJ. X. Chen, J. A. Tunge, J. R. Norton, *J Org Chem* **2002**, *67*, 4366-4369; cT. V. Lubben, K. Plossl, J. R. Norton, M. M. Miller, O. P. Anderson, *Organometallics* **1992**, *11*, 122-127; dJ. A. Tunge, C. J. Czerwinski, D. A. Gatley, J. R. Norton, *Organometallics* **2001**, *20*, 254-260; eJ. A. Tunge, D. A. Gatley, J. R. Norton, *J Am Chem Soc* **1999**, *121*, 4520-4521.

- [20] aM. C. J. Harris, R. J. Whitby, J. Blagg, *Tetrahedron Lett* **1995**, *36*, 4287-4290; bJ. M. Davis, R. J. Whitby, A. Jaxachamiec, *Tetrahedron Lett* **1992**, *33*, 5655-5658; cJ. M. Davis, R. J. Whitby, A. Jaxachamiec, *Tetrahedron Lett* **1994**, *35*, 1445-1448.
- [21] aN. Coles, R. J. Whitby, J. Blagg, *Synlett* **1990**, 271-272; bN. Coles, R. J. Whitby, J. Blagg, *Synlett* **1992**, 143-145.
- [22] D. A. Gately, J. R. Norton, *J Am Chem Soc* **1996**, *118*, 3479-3489.
- [23] M. Jensen, T. Livinghouse, *J Am Chem Soc* **1989**, *111*, 4495-4496.
- [24] E. Chong, L. L. Schafer, *Org Lett* **2013**, *15*, 6002-6005.
- [25] aJ. Dorfler, T. Preuss, A. Schischko, M. Schmidtman, S. Doye, *Angew Chem Int Edit* **2014**, *53*, 7918-7922; bM. Manssen, N. Lauterbach, J. Dorfler, M. Schmidtman, W. Saak, S. Doye, R. Beckhaus, *Angew Chem Int Edit* **2015**, *54*, 4383-4387.
- [26] aY. Takahashi, N. Onoyama, Y. Ishikawa, S. Motojima, K. Sugiyama, *Chem Lett* **1978**, 525-528; bC. Airoidi, D. C. Bradley, G. Vuru, *Transit Metal Chem* **1979**, *4*, 64-64.
- [27] M. Beaudoin, S. L. Scott, *Organometallics* **2001**, *20*, 237-239.
- [28] M. El Eter, B. Hamzaoui, E. Abou-Hamad, J. D. A. Pelletier, J. M. Basset, *Chem Commun* **2013**, *49*, 4616-4618.
- [29] B. Hamzaoui, J. D. A. Pelletier, M. El Eter, Y. Chen, E. Abou-Hamad, J.-M. Basset, *Advanced Synthesis & Catalysis* **2015**, *357*, 3148-3154.
- [30] For all our experiments, Me₂NH gas was generated by hydrogenation in situ of Me₂NLi at 150 °C. After drying and deoxygenation using a gas trap (molecular sieves (3A) + copper oxide). The excess of H₂ remained mixed with the dimethylamine. A blank test was conducted and showed that 2 was unreactive to pure hydrogen in the same conditions.
- [31] The amount of dimethylamine introduced in the experiment can be only roughly estimated as it was generated in situ.
- [32] A. Kempe, C. Dempsey, J. Whitefield, J. Bothner, T. MacKenzie, S. Poole, *Arch Pediatr Adol Med* **2000**, *154*, 355-360.
- [33] Y. Chen, E. Abou-hamad, A. Hamieh, B. Hamzaoui, L. Emsley, J. M. Basset, *J Am Chem Soc* **2015**, *137*, 588-591.
- [34] M. J. Frisch, G. W. Trucks, H. B. Schlegel, G. E. Scuseria, M. A. Robb, J. R. Cheeseman, G. Scalmani, V. Barone, B. Mennucci, G. A. Petersson, H. Nakatsuji, M. Caricato, X. Li, H. P. Hratchian, A. F. Izmaylov, J. Bloino, G. Zheng, J. L. Sonnenberg, M. Hada, M. Ehara, K. Toyota, R. Fukuda, J. Hasegawa, M. Ishida, T. Nakajima, Y. Honda, O. Kitao, H. Nakai, T. Vreven, J. A. Montgomery Jr., J. E. Peralta, F. Ogliaro, M. J. Bearpark, J. Heyd, E. N. Brothers, K. N. Kudin, V. N. Staroverov, R. Kobayashi, J. Normand, K. Raghavachari, A. P. Rendell, J. C. Burant, S. S. Iyengar, J. Tomasi, M. Cossi, N. Rega, N. J. Millam, M. Klene, J. E. Knox, J. B. Cross, V. Bakken, C. Adamo, J. Jaramillo, R. Gomperts, R. E. Stratmann, O. Yazyev, A. J. Austin, R. Cammi, C. Pomelli, J. W. Ochterski, R. L. Martin, K. Morokuma, V. G. Zakrzewski, G. A. Voth, P. Salvador, J. J. Dannenberg, S. Dapprich, A. D. Daniels, Ö. Farkas, J. B. Foresman, J. V. Ortiz, J. Cioslowski, D. J. Fox, Gaussian, Inc., Wallingford, CT, USA, **2009**.
- [35] J. P. Perdew, K. Burke, M. Ernzerhof, *Physical Review Letters* **1996**, *77*, 3865-3868.
- [36] A. Schafer, H. Horn, R. Ahlrichs, *Journal of Chemical Physics* **1992**, *97*, 2571-2577.
- [37] C. Adamo, V. Barone, *Journal of Chemical Physics* **1999**, *110*, 6158-6170.
- [38] S. Grimme, S. Ehrlich, L. Goerigk, *Journal of Computational Chemistry* **2011**, *32*, 1456-1465.
- [39] A. Schafer, C. Huber, R. Ahlrichs, *J Chem Phys* **1994**, *100*, 5829-5835.

Chapter 4. Imine Metathesis Catalysed by Well-Defined Silica-Supported Zirconium-Imido Complexes

4.1 Introduction

Imine metathesis (equation IV.1) catalyzed by transition metals (Zr,^[10] Ti,^[5] Mo,^[12] Re,^[13] Ta,^[14] Nb^[3b]) was investigated in a number of research groups, most likely on account of the mechanistic analogy with the more famous and synthetically relevant olefin metathesis.^[15]



To date, heterogeneous catalysts for imine metathesis has not been reported. Our recent foray into silica supported zirconium amido catalysts ^[16] (chapter I and chapter II) encouraged us to examine the formation and the reactivity of the related metal imido complexes.

As discussed in chapter I, Surface Organometallic Chemistry (SOMC) has built to a rich library of surface complexes active for numerous catalytic reactions. In this context, the role of surface metal fragments (M=C, M-C, M-H, M-NC) has been evidenced to be essential for the reactivity of the surface species. Surface [M]=NR fragments have not been examined within this framework and their characterization and reactivity studies remain limited to this date.

In the general context of both homogeneous and heterogeneous catalysis, transition metals forming multiple bonds with ligands are key in several industrially important chemical processes such as alkane oxidation^[3] (M=O) or alkene metathesis^[4] (M=CR₂). In

contrast, their metal imides ($M=NR$) counterparts have received less attention yet can intermediate imido group ($=NR$) transfer reactions.^[5] The importance of imido complexes and their isolable analogues is well-established in organic synthesis and catalysis.^[6] Stoichiometric or catalytic reactions may occur at the $M=NR$ fragment itself,^[7] or the imido group may remain spectator, as in Schrock's group 6 olefin metathesis catalysts^[8] and imido-based Ziegler–Natta type olefin polymerisation catalysts.^[9] Catalytic imine metathesis is analogous to olefin metathesis in that two different imines afford a statistical mixture of all possible $=NR$ exchange products.

Examples of imine/imide exchange for which mechanistic data were reported apparently may proceed by two separate pathways. On the one hand, Bergman and co-workers established a Chauvin type mechanism based on isolable diazametallacyclic intermediates in the reaction of $CpCp'Zr(=NR)(THF)$ ($Cp'=Cp, Cp^*$) with imines.^[10] On the other hand, kinetic studies by Mountford and co-workers supports an amine-catalyzed process to explain the reaction of $(py)_3Cl_2Ti(=NR)$ with imines.^[5, 11]

4.2 Scope of the chapter

In this chapter, we describe the first catalytic imine metathesis reactions using silica supported imido-zirconium complexes. Reactions of molecular $Zr(NEt_2)_4$ with the surface hydroxyl groups of highly dehydroxylated silica (SiO_{2-700}) yield selectively a well-defined mononuclear surface species $[\equiv Si-O-Zr(NEt_2)_3]$ (**IV.1**). A synthetic route to silica-supported zirconium-imido complex $[\equiv Si-O-Zr(=NEt)NEt_2]$ (**IV.2**) was developed by prolonged thermal treatment of **IV.1** under vacuum. Subsequent reactions of compound **IV.2** with imine gives $=NR$ exchange (metathesis) product and new zirconium imido

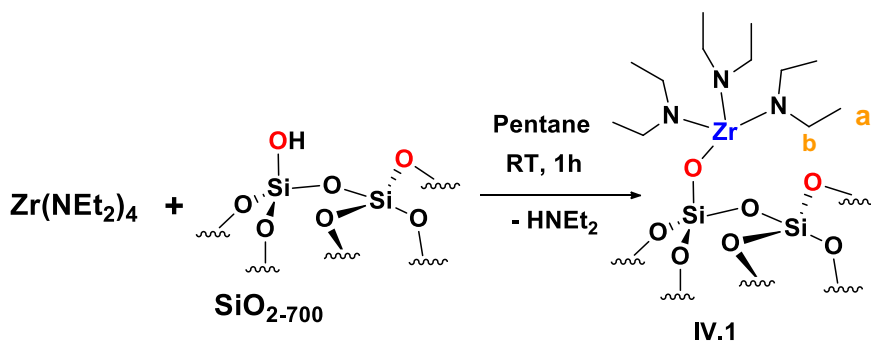
complex $[\equiv\text{Si-O-Zr(=NPh)NEt}_2]$ (**IV.3**). The observation of =NR exchange was evidenced by FTIR, elemental analysis, ^1H ^{13}C HETCOR and DQ SS NMR. Compound **IV.3** effectively catalyzes imine/imine cross-metathesis and thus considered as the first heterogeneous catalyst active in imine metathesis

4.3 Results and Discussions

4.3.1 Grafting of $\text{Zr}(\text{NEt}_2)_4$ on SiO_{2-700}

The surface complex **IV.1** was prepared by treating SiO_{2-700} with a solution of $\text{Zr}(\text{NEt}_2)_4$ in pentane (1.1 equivalents with respect to surface silanols). After workup, **IV.1** was obtained as a yellow powder containing 2.7% Zr, 4.3% C and 1.3% N with a molar ratio of $\text{Zr}/\text{C}/\text{N} = 1/12/3.1$ (± 0.3) (expected 1/12/3) and thus suggests a monopodal surface complex with three NEt_2 ligands (Scheme IV.59). Comparison of the FTIR spectra of SiO_{2-700} and **IV.1** (Figure IV.31) are consistent with the chemical grafting of $\text{Zr}(\text{NEt}_2)_4$ onto the silica surface.

The IR peaks associated with the isolated surface silanols (3745 cm^{-1}) have completely disappeared. Conversely, new bands associated with the $\nu(\text{CH})$ and $\delta(\text{CH})$ of the diethylamine ligands are observed in the $2970\text{--}2843\text{ cm}^{-1}$ and $1546\text{--}1496\text{ cm}^{-1}$ regions, respectively. All these observations and chemical analyses are consistent with the proposed structure of **IV.1** (Scheme 4.59).



Scheme 4.59: Reaction of $\text{Zr}(\text{NEt}_2)_4$ with SiO_{2-700} .

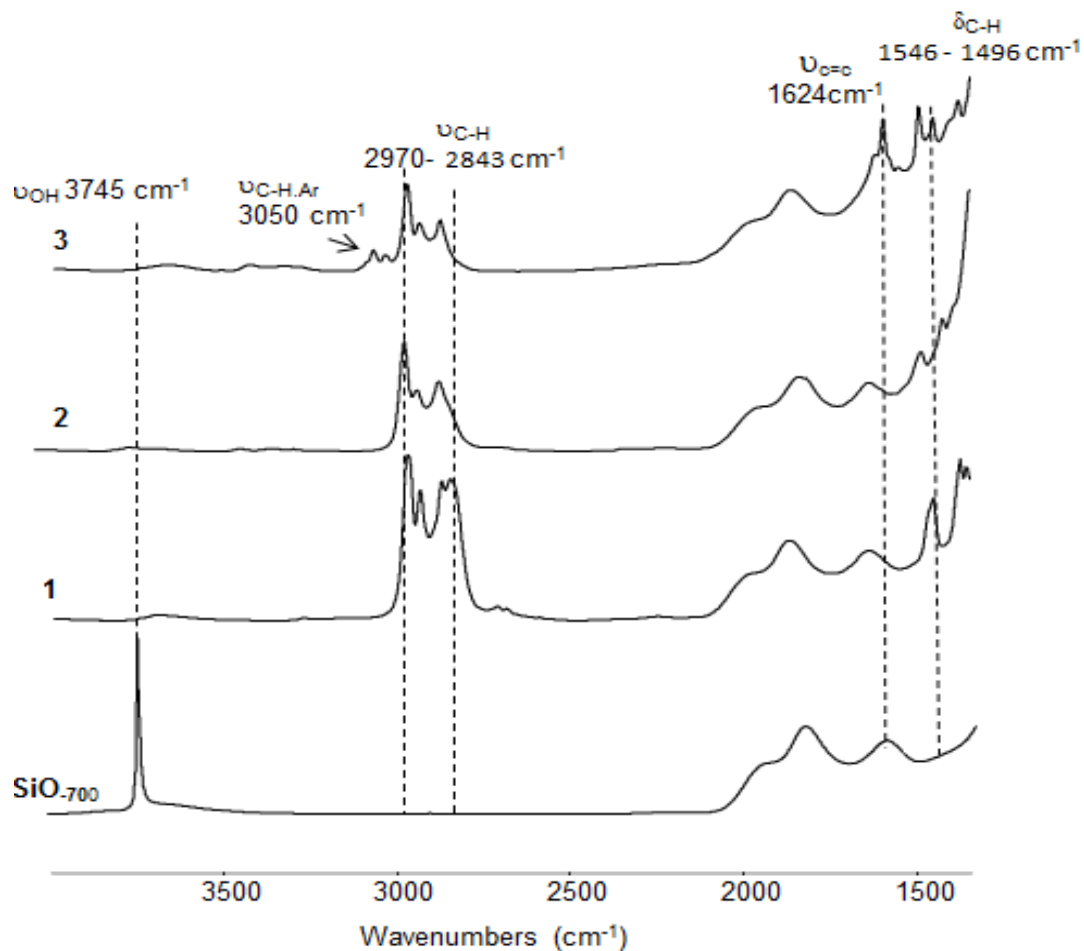


Figure 4.31: FTIR of SiO₂₋₇₀₀, IV.1 [≡Si-O-Zr(NEt₂)₃], IV.2 [≡Si-O-Zr(=NEt)NEt₂] and IV.3 [≡Si-O-Zr(=NPh)NEt₂].

Further corroborations at the molecular level have been sought using SS NMR spectroscopy of the grafted species. The solid-state ¹H NMR spectrum of **IV.1** shows two broad resonance at 1.1 and 3.2 ppm (Figure 4.32 A) and its ¹³C solid-state cross polarization/magic angle spinning (CP/MAS) NMR spectrum displays strong signals at 14 and 43 ppm (Figure 4.32 B).^[16b]

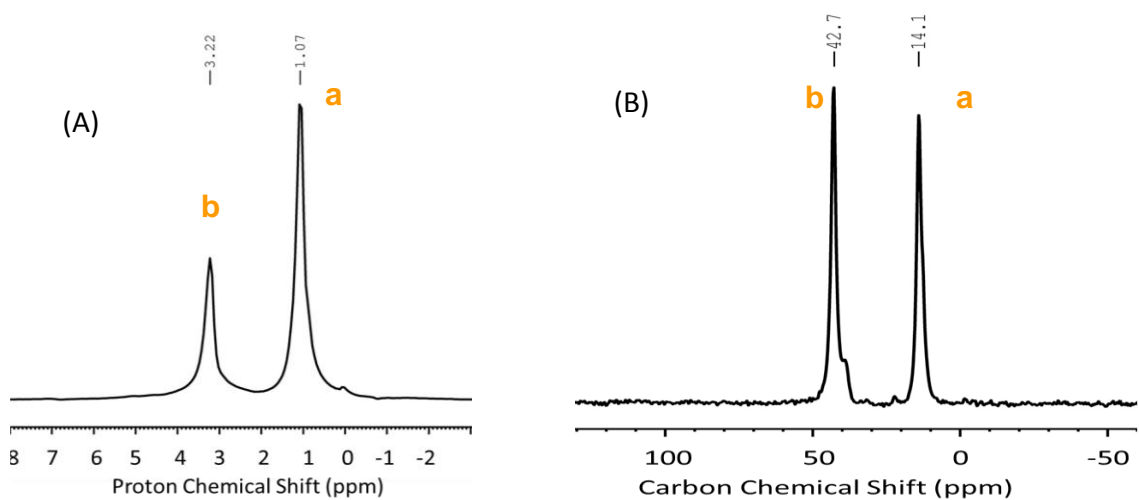


Figure 4.32: (A) 1D ^1H spin-echo MAS SS NMR spectrum of IV.1, (B) ^{13}C CP/MAS NMR spectrum of IV.1.

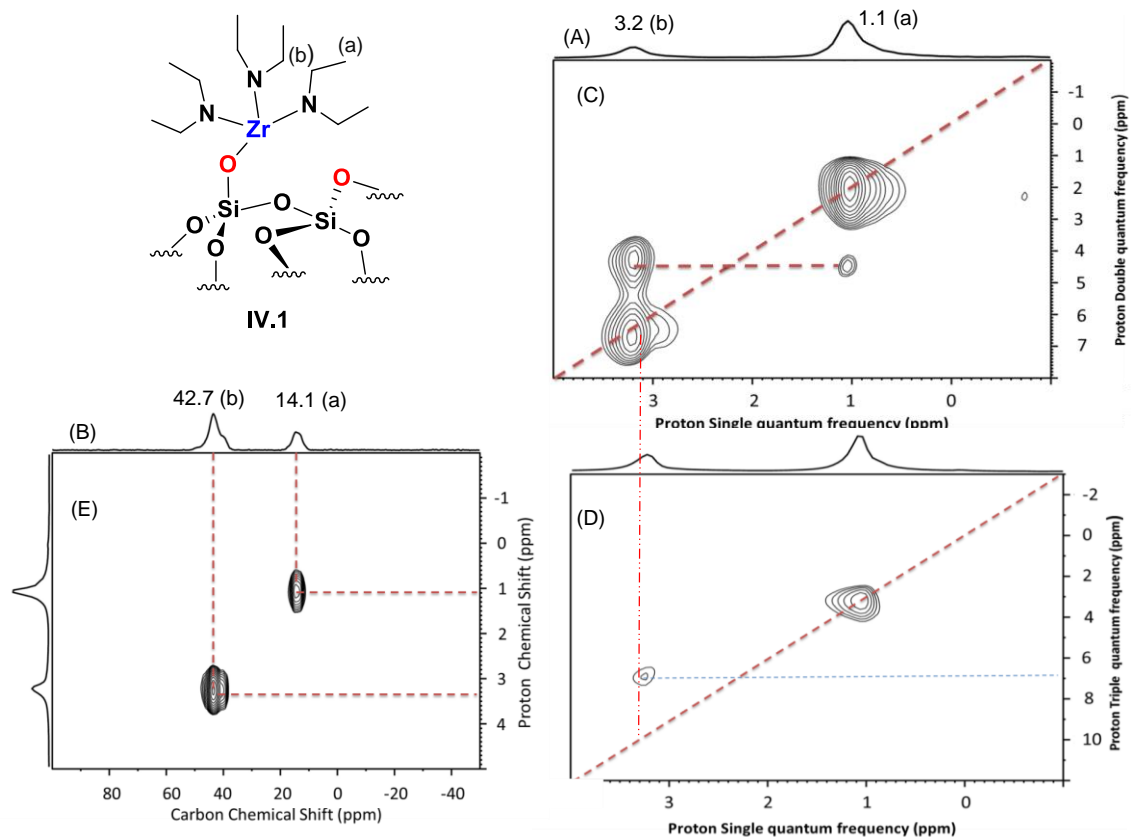
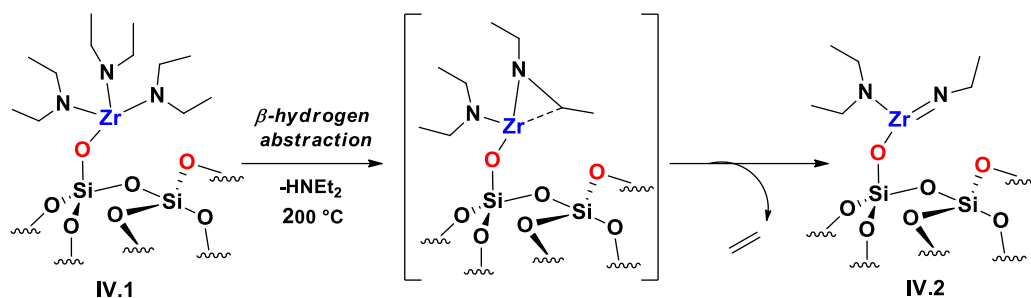


Figure 4.33: (A) 1D ^1H spin-echo MAS SS NMR spectrum of IV.1, (B) ^{13}C CP/MAS NMR spectrum of IV.1. (C) 2D ^1H - ^1H double-quantum (DQ)/single-quantum (SQ), (D) ^1H - ^1H triple-quantum (TQ)/SQ and (E) 2D HETCOR SS NMR spectra (see section IV.5 for details).

Moreover, the 2D HETCOR SS NMR spectra revealed correlations only between pairs of attached ^1H - ^{13}C spins using a short contact time of 0.5 ms. Clear correlations were noticeable between the protons at 1.1 and 3.2 ppm and the carbons at 14 and 43 ppm, respectively (Figure 4.33 E). Two-dimensional Proton Double- (DQ) and Triple-Quantum (TQ) correlation experiments were applied to determine the number of protons attached to the same carbon, hence discriminating between CH_2 and CH_3 groups. A strong autocorrelation peak is observed for the proton resonances at 1.1 ppm in both DQ and TQ spectra (Figure 4.33 C and D). This is compatible with the assignment of this resonance to methyl protons. The resonances at 3.2 ppm shows a correlation at 6.4 ppm (ω_1) in the DQ spectrum, but no autocorrelation peak is observed in the TQ spectrum. It can be thus assigned to a CH_2 group. Furthermore, a correlation in the DQ NMR spectrum between the CH_3 group at 1.1 ppm and the CH_2 group at 3.2 ppm confirms that both groups are in proximity of each other. In conclusion, these data validate **IV.1** as a surface zirconium complex exhibiting three equivalent diethyl-amido ligands $[(\equiv\text{Si-O})\text{Zr}(\text{NEt}_2)_3]$.

4.3.2 Formation of the zirconium-imido surface

The formation of imido ligands during the synthesis of molecular dialkylamido metal complexes is known to occur after thermal treatment under vacuum.^[18] The release of gaseous alkenes and dialkylamines has also been detected upon thermal transformation of isolable dialkylamido^[19] and imine complexes of the early transition metals.^[20] We decided to monitor the thermal treatment of **IV.1** to observe possible the conversion to zirconium-imido surface species (Scheme 4.60).



Scheme 4.60: Silica-supported zirconium imido formation with the hypothetical intermediate.

Initial evacuation of **IV.1** at room temperature left the FTIR spectrum unchanged, although evacuation at elevated temperature (200 °C) resulted in a modification of the signals pattern (Figure 4.31) concurrently to an overall reduction of the signal's intensity in the alkyl vibration region. Elemental analysis of **IV.2** gives 2.7% Zr, 2.3% C and 0.9% N with a ratio of $\text{Zr/C/N} = 1/6.4/2.1$ (+/-0.3) (expected 1/6/2). The volatiles identified and quantified by GC consist exclusively in diethylamine and ethylene (1/0.9). ^1H SS NMR of **IV.2** contains two broad signals centered at 1.1 and 3.1 ppm (Figure 4.34).

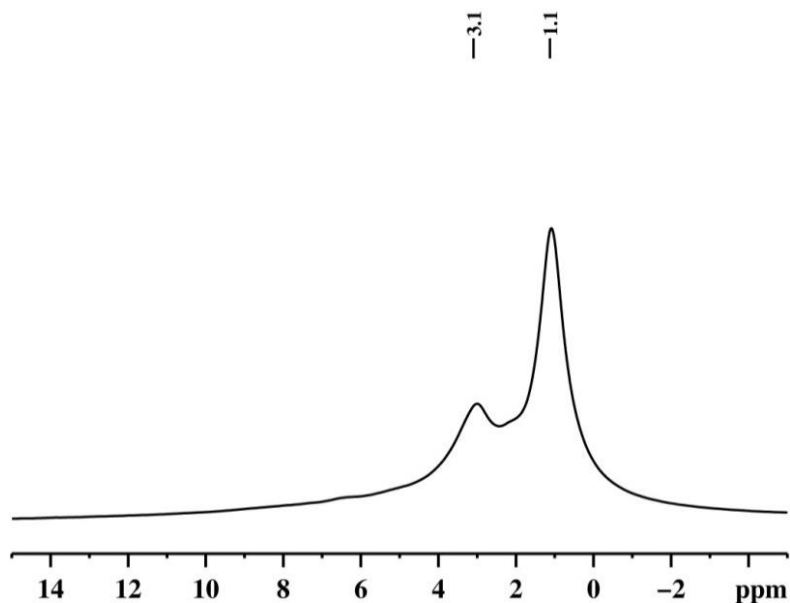


Figure 4.34: 1D ^1H spin-echo MAS SS NMR spectrum of IV.2.

^{13}C SS NMR spectrum of **IV.2** (Figure 4.35) exhibits two major signals at 14 and 41 ppm and two minor signals at 19 and 36 ppm. The most intense peaks at 14 and 40 ppm are reminiscent of that previously seen in **IV.1** at 14 ppm and 43 ppm. They were assigned to the carbon atoms of amino-ethyl group in the $\text{N}(\text{CH}_2\text{CH}_3)_2$ ligands. The other two peaks at 19 and 36 ppm were consistent with an N-Ethyl group different to that already present on the zirconium center. Considering all the data, we can attribute them to the methyl and the methylene group borne by the nitrogen of an ethylimido ligand ($=\text{NCH}_2\text{CH}_3$). All these results allow us to identify **IV.2** as $[(\equiv\text{Si-O})\text{Zr}(=\text{NEt})\text{NEt}_2]$. To the best of our knowledge, this is the first report of a well-defined single-site zirconium imido species supported onto silica.

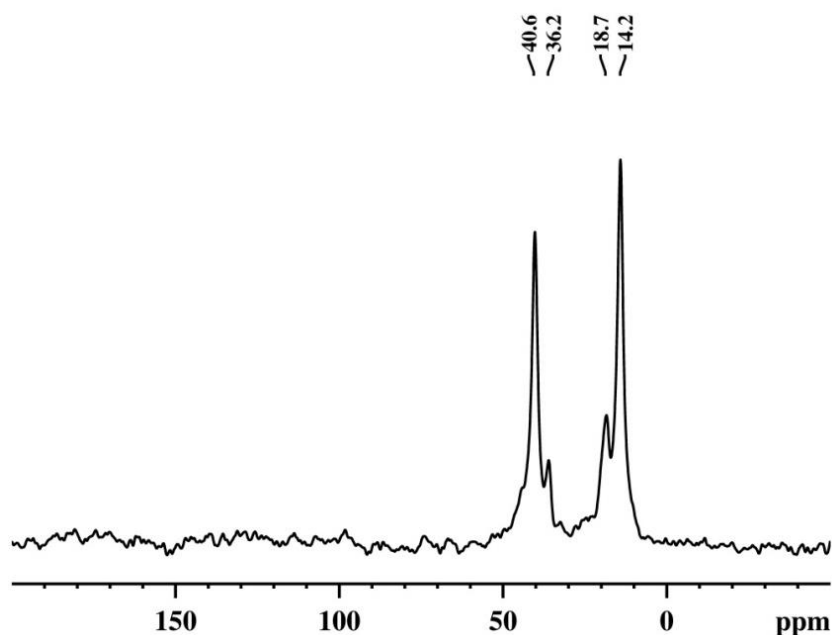
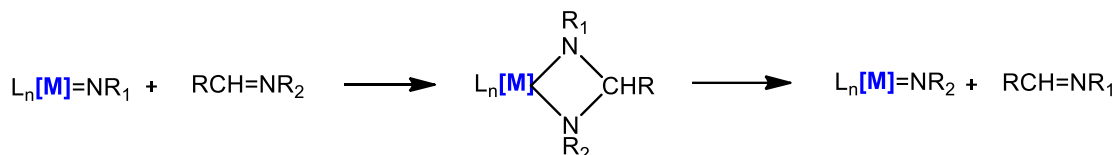


Figure 4.35: ^{13}C CP/MAS NMR spectrum of **IV.2**.

4.3.3 Imide/imine stoichiometric metathesis reaction

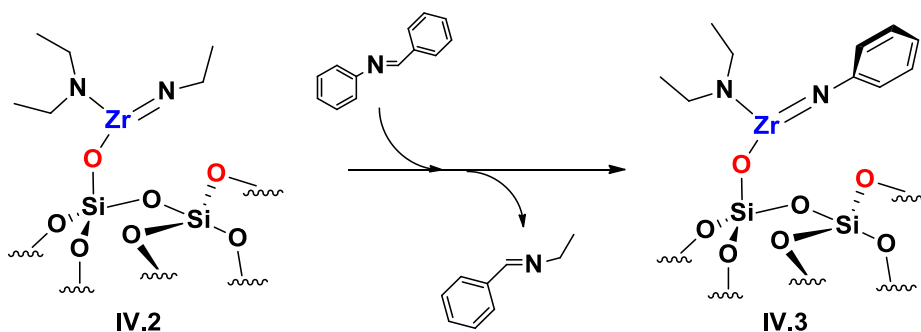
Previous works mainly described two types of NR transfer reactions: stoichiometric and catalytic. The former passes by imide/imine stoichiometric metathesis of a metal imide

with a one molecule of imine substrate and is regioselective. New metal imide and imine products are formed by transient 4-membered metallacycle (Scheme 4.61).



Scheme 4.61: Imide/imine stoichiometric metathesis via transient 4-membered metallacycle.

Treatment of **IV.2** by benzal(benzyl)amine (1.2 eq.) in toluene at 80°C yielded **IV.3** (Scheme IV.62) followed by filtration, washing and evacuation under high vacuum. The compound **IV.3** showed bands characteristic of the presence of an aromatic group around 3050 cm⁻¹ (aromatic C-H bending) and one at 1624 cm⁻¹ (ν_(C=C)) (Figure 4.31). A comparison of the FTIR spectra of **IV.2** and **IV.3** reveals notable decrease of the ν_(CH) (2970 -2843 cm⁻¹). Elemental analysis of **IV.3** gives 2.7% Zr, 3.7% C and 0.95% N with a ratio of Zr/C/N = 1/10.3/2.2 (+/-0.3) (expected 1/10/2). This is in agreement with one NEt₂ ligand in **IV.2** being replaced by an arylimido ligand.



Scheme 4.62: Silica-supported imide/imine metathesis.

¹H NMR of **IV.3** contains an intense signal at 7.1 ppm (Figure 4.36 A), absent from **IV.1** and **IV.2**, in addition to two overlapping peaks (a major one at 1.1 ppm with a minor one at 3 ppm). The ¹³C MAS spectrum displays also two new signals at 118 and 128

ppm consistent with aromatic carbon in addition to two signals at 14 ppm and 40 ppm (Figure 4.36 C). A correlation was observed in the HETCOR spectrum between the ^1H signal at 7.1 ppm and ^{13}C signals at 118 and 128 (Figure 4.36 D). Moreover, the DQ experiment shows a double autocorrelation for the 7.1 ppm resonance as expected for an aromatic CH proton (Figure 4.36 B). These observations are in line with the presence of aromatic group in **IV.3**. In the double-quantum (DQ) spectrum (Figure 4.36 B), the ^1H signals at 1.1 and 3.0 ppm displays strong auto-correlations that can be assigned to the NET_2 group similarly to that observed in **IV.1**.

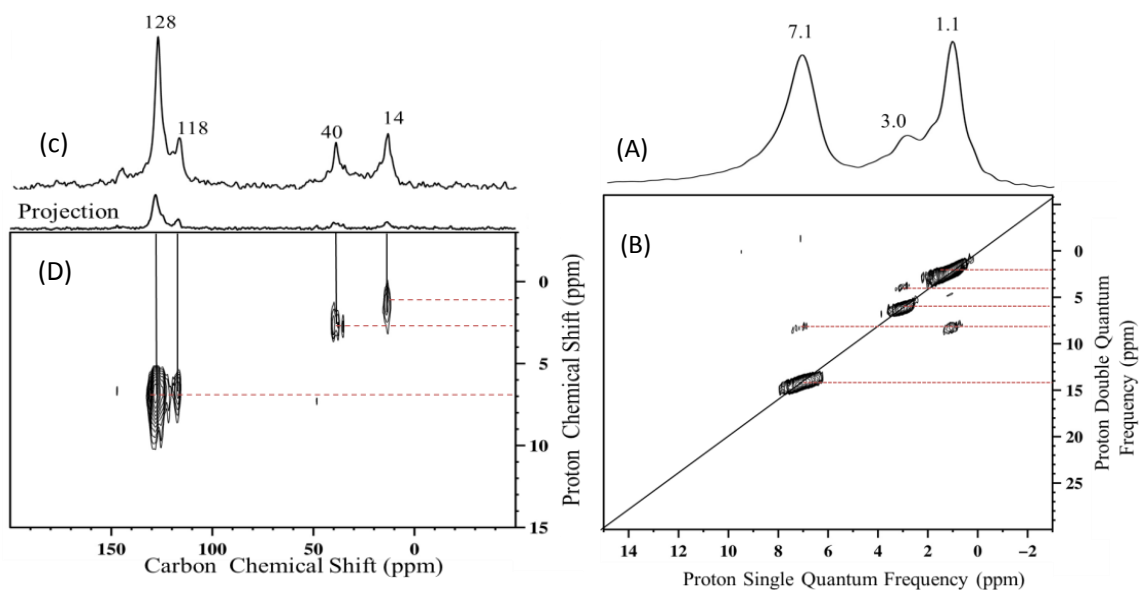
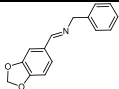
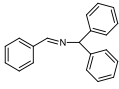
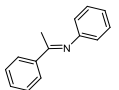
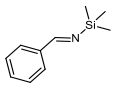
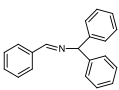


Figure 4.36: (A) 1D ^1H spin-echo MAS SS NMR spectrum of **IV.3**, (B) 2D ^1H - ^1H double-quantum (DQ), (C) ^{13}C CP/MAS NMR spectrum of **IV.3**, (D) 2D CP/MAS HETCOR NMR spectrum of **IV.3** (see section 4.5 for details).

4.3.3 Imine/imine catalytic metathesis reaction

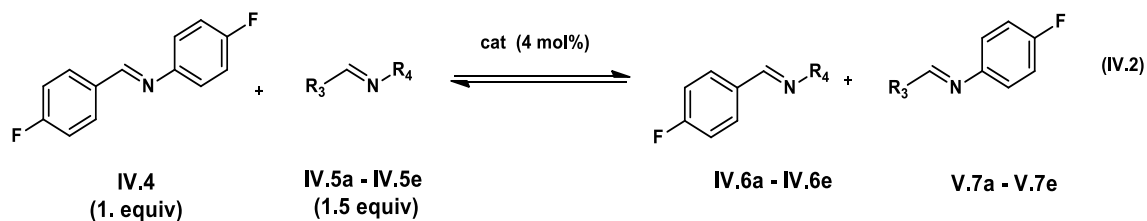
Species **IV.3** was investigated as a catalyst for the imine metathesis reaction. Selected imines substrates were tested. (Table 4.10).

Table 4.9: Catalytic imine metathesis substrates testing using catalysts **IV.3** and **IV.2**.

Entry	Imine V.5	Catalyst 4 mol%	Conv(%) ^a		
			2 hrs	6 hrs	12 hrs
1		IV.3	33	74	76
2		IV.3	28	62	65
3		IV.3	30	50	52
4		IV.3	25	47	49
5		IV.2	39	66	68

^a Determined by GC-FID using (4-fluorobenzylidene)-(4-fluorophenyl) as default substrate.

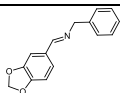
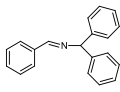
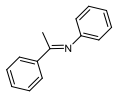
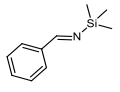
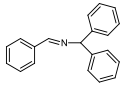
All runs were carried out under similar conditions (80 °C, 4 mol % catalysts, toluene (0.4 ml)) and terminated after 2, 4 and 12 hrs. The products monitored by gas chromatography-mass spectrometry were consistent with cross metathesis reaction (equation IV.2).



Reactions using imines such as N-(3,4-Methylenedioxybenzylidene)benzylamine (Entry 1) and benzal(benzhydryl)amine (Entry 2) occurred in high yields (around 70%). The use of phenyl-(1-phenylethylidene) (Entry 3) and N-Trimethylsilylbenzalimine (Entry 4) resulted in lower yields (around 50% after 12 hrs) (Table 4.11). When species **IV.2** was employed as a catalyst for the imine metathesis reaction in entry 5, the obtained yield was comparable to the same reaction using **IV.3** as catalyst in entry 2 (around 65% after 12 hrs).

The conversions for both substrates were similar and the corresponding products were obtained with around the same yield values. Each products pairs **IV.6** and **IV.7** are obtained with the same selectivities (ca. 50%) and no other products were observed.

Table 4.10: Conversion, yield and TON of the catalytic imine metathesis substrates testing using catalysts IV.3 and IV.2.

Entry	Imine V.5a-V.5	Cat	Conv (%) ^a	Yield (%)		TON
				V.6a-V.6e	V.7a – V.7e	
1		IV.3	75	76	74	19
2		IV.3	65	65	67	16
3		IV.3	54	52	51	13
4		IV.3	48	49	50	12
5		IV.2	66	68	68	17

^a Determined by GC-FID using (4-fluorobenzylidene)-(4-fluorophenyl) as default substrate after 12 hrs.

4.3.4 Catalyst regeneration

Additional experiments were performed to test the zirconium system reusability. After 12 hrs, the catalytic material was isolated by filtration, washed with toluene, dried under high vacuum, and reused in imine metathesis (Entry 1). This sequence was performed five times with only a slight loss of catalytic activity being observed (yield of 76% in the first cycle vs 72% in the fifth cycle) (Figure 4.37). FTIR of the catalysts after reaction was conducted and indicates that the catalytic active species are still present and no adsorbed products remains on the surface (Figure 4.38).

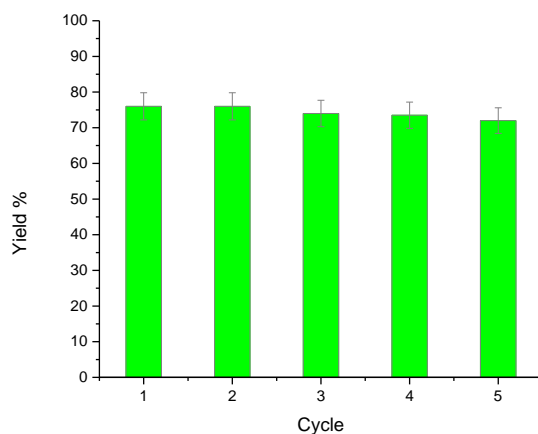


Figure 4.37: Reusability studies of IV.3 for the metathesis of imine metathesis (TableV.2, entry 1).

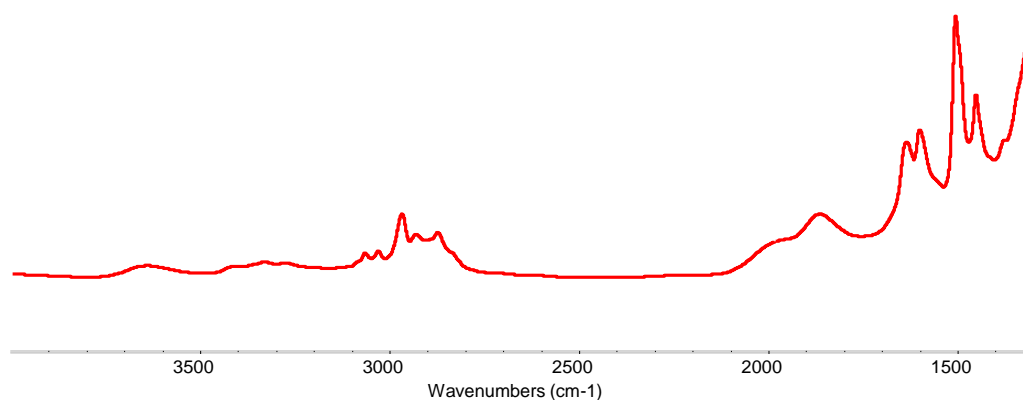
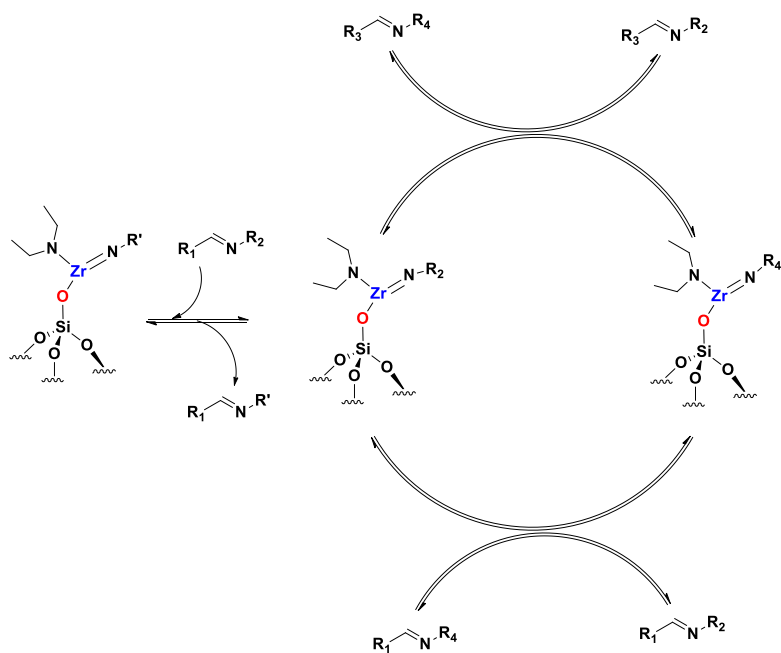


Figure 4.38: FTIR spectra of the catalyst IV.3 (Entry 1) after the first catalytic cycle.

4.4 Conclusion

In our investigation of the reactions of $Zr(NEt_2)_4$ with silica surface to give $[(\equiv Si-O)Zr(NEt_2)_3]$ (**IV.1**), thermal treatment of **IV.1** generate the imido complex $[(\equiv Si-O)Zr(=NR)NEt_2]$ (**IV.2**). **IV.2** can be converted to $[(\equiv Si-O)Zr(=NPh)NEt_2]$ (**IV.3**) by imine metathesis using $ArC=NPh$. Both **IV.2** and **IV.3** were tested as catalysts for imine metathesis using several imines and exhibited conversion ranging from 49 to 76%. **IV.2** and **IV.3** are the first report heterogeneous catalyst for imine metathesis.



Scheme 4.63: Silica-supported zirconium-imido complexes mediated heterogeneous imine metathesis.

4.5 Experimental

General

See chapter II section 5

Preparation procedures

Preparation of $[\equiv \text{Si-O-Zr}(\text{NEt}_2)_3]$ (IV.1): In a double Schlenk of $\text{Zr}(\text{NEt}_2)_4$ (132.4 mg) in slight excess (1.1 eq.) with respect to the amount of surface accessible silanols (0.3 mmol silanols groups per gram) was reacted with $\text{SiO}_2\text{-700}$ (1.000 g) at room temperature in pentane for 1 hr. After filtration and four washing cycles, all volatile compounds were evaporated and the white solid was dried for 1 hr under dynamic vacuum ($< 10^{-5}$ mbar).

Preparation of $[\equiv \text{Si-O-Zr}(=\text{NEt})\text{NEt}_2]$ (IV.2): In a glass reactor (230 mL), **IV.1** (1.000 g) was heated with the gradient room temperature to 200 °C (1 °C per minute) and then at 200 °C for 24 hrs under dynamic vacuum ($< 10^{-5}$ mbar). The resulting powder was then cooled to 22 °C analyzed by FTIR and SS NMR.

Preparation of $[\equiv \text{Si-O-Zr}(=\text{NPh})\text{NEt}_2]$ (IV.3): In a double Schlenk, an excess of benzal(benzyl)amine (1.5 eq.) was reacted with **IV.2** (0.500 g) at room temperature in toluene for 4 hr. After filtration and four washing cycles, all gas-phase products was analysed by GC-FID and the resulting solid was dried for 1 hr under dynamic vacuum ($< 10^{-5}$ mbar).

Catalytic imine metathesis reaction: A vacuum sealed ampule was charged, in a glove box, sequentially with the catalyst **IV.3** (0.04 equiv), toluene (400 μL), (4-fluorobenzylidene)-(4-fluorophenyl) amine (1.0 equiv), the imine **IV.5** (1.0 equiv) and a Teflon-coated stir bar. The ampules was then removed from the glove box and placed in a high vacuum line. The mixture was condensed by cooling with liquid nitrogen and the

ampules were evacuated ($< 10^{-5}$ mbar). After sealing, the ampules were placed in an oil bath (80 °C). The reaction mixture was heated for 4, 6 or 12 h and each time after reaction it was cooled to 22 °C. The product solution was filtrated to remove the catalyst and the remaining liquid product was analyzed by GC-FID and GC-MS

Catalyst recycling experiments: After 12 hrs, the catalytic material was isolated by filtration, washed with toluene four times, dried under high vacuum ($< 10^{-5}$ mbar) during 8 hrs (at 60°C), and reused in imine metathesis. This sequence was performed five times.

Details of the SS NMR spectra

Details about figure 4.3: (A) 1D ^1H spin-echo MAS SS NMR spectrum of **IV.2** (acquired on a 600 MHz NMR spectrometer under a 20 KHz MAS spinning frequency, number of scans = 8, repetition delay = 5 s), (B) ^{13}C CP/MAS NMR spectrum of **IV.2** (acquired on 600 MHz NMR spectrometer with 10 KHz MAS, number of scan = 20000, repetition delay = 4 s contact time = 2 ms, line broadening = 80 Hz). (C) 2D 1H-1H double-quantum (DQ)/single-quantum (SQ), (D) 1H-1H triple-quantum (TQ)/SQ (acquired on a 600 MHz NMR spectrometer under 22 KHz MAS spinning frequency with a back-to-back recoupling sequence, number of scans = 128, repetition delay = 5 s number of t1 increments = 128, with the increment set equal to one rotor period of 45.45 μs) and (E) 2D CP/MAS HETCOR NMR spectrum with short contact times of 0.2 ms under 8.5 KHz MAS, number of scans per increment = 4000, repetition delay = 4 s, number of t1 increments = 32, line broadening = 80 Hz).

Details about figure 4.6: (A) 1D ^1H spin-echo MAS SS NMR spectrum of **IV.3** (acquired on a 600 MHz NMR spectrometer under a 20 KHz MAS spinning frequency, number of scans = 8, repetition delay = 5 s), (B) 2D 1H-1H double-quantum (DQ)/single-quantum (SQ), (C) ^{13}C CP/MAS NMR spectrum of **IV.3** (acquired on 600 MHz NMR spectrometer with 10 KHz MAS, number of scan = 20000, repetition delay = 4 s contact time = 2 ms, line broadening = 80 Hz) and (D) 2D CP/MAS HETCOR NMR spectrum with short contact times of 0.2 ms under 8.5 KHz MAS, number of scans per increment = 4000, repetition delay = 4 s, number of t1 increments = 32, line broadening = 80 Hz).

4.6 References

- [1] E. Callens, N. Riache, K. Talbi, J. M. Basset, *Chem Commun* **2015**, 51, 15300-15303.
- [2] N. Riache, E. Callens, J. Espinas, A. Dery, M. K. Samantaray, R. Dey, J. M. Basset, *Catal Sci Technol* **2015**, 5, 280-285.
- [3] aL. K. Woo, *Chem Rev* **1993**, 93, 1125-1136; bJ. W. Bruno, X. J. Li, *Organometallics* **2000**, 19, 4672-4674; cM. Sun, J. Z. Zhang, P. Putaj, V. Caps, F. Lefebvre, J. Pelletier, J. M. Basset, *Chem Rev* **2014**, 114, 981-1019.
- [4] aA. Bokka, Y. D. Hua, A. S. Berlin, J. Jeon, *Acs Catal* **2015**, 5, 3189-3195; bC. A. Denard, M. J. Bartlett, Y. J. Wang, L. Lu, J. F. Hartwig, H. M. Zhao, *Acs Catal* **2015**, 5, 3817-3822; cJ. I. du Toit, C. G. C. E. van Sittert, H. C. M. Vosloo, *Monatsh Chem* **2015**, 146, 1115-1129.
- [5] J. M. McInnes, P. Mountford, *Chem Commun* **1998**, 1669-1670.
- [6] aV. C. Gibson, *Adv Mater* **1994**, 6, 37-42; bW. A. Nugent, B. L. Haymore, *Coordin Chem Rev* **1980**, 31, 123-175.
- [7] A. P. Duncan, R. G. Bergman, *Chem Rec* **2002**, 2, 431-445.
- [8] R. R. Schrock, A. H. Hoveyda, *Angew Chem Int Edit* **2003**, 42, 4592-4633.
- [9] P. D. Bolton, P. Mountford, *Adv Synth Catal* **2005**, 347, 355-366.
- [10] aR. L. Zuckerman, S. W. Krska, R. G. Bergman, *Journal of the American Chemical Society* **2000**, 122, 751-761; bK. E. Meyer, P. J. Walsh, R. G. Bergman, *J Am Chem Soc* **1994**, 116, 2669-2670; cK. E. Meyer, P. J. Walsh, R. G. Bergman, *J Am Chem Soc* **1995**, 117, 974-985.
- [11] P. Mountford, *Chem Commun* **1997**, 2127-2134.
- [12] G. K. Cantrell, T. Y. Meyer, *Organometallics* **1997**, 16, 5381-5383.
- [13] W. D. Wang, J. H. Espenson, *Organometallics* **1999**, 18, 5170-5175.
- [14] M. C. Burland, T. W. Pontz, T. Y. Meyer, *Organometallics* **2002**, 21, 1933-1941.
- [15] aJ. W. Nelson, L. M. Grundy, Y. F. Dang, Z. X. Wang, X. T. Wang, *Organometallics* **2014**, 33, 4290-4294; bJ. M. Bates, J. A. M. Lummiss, G. A. Bailey, D. E. Fogg, *Acs Catal* **2014**, 4, 2387-2394.
- [16] aB. Hamzaoui, M. El Eter, E. Abou-Hamad, Y. Chen, J. D. A. Pelletier, J. M. Basset, *Chem-Eur J* **2015**, 21, 4294-4299; bB. Hamzaoui, J. D. A. Pelletier, M. El Eter, Y. Chen, E. Abou-Hamad, J. M. Basset, *Adv Synth Catal* **2015**, 357, 3148-3154.
- [17] aP. Avenier, A. Lesage, M. Taoufik, A. Baudouin, A. De Mallmann, S. Fiddy, M. Vautier, L. Veyre, J. M. Basset, L. Emsley, E. A. Quadrelli, *J Am Chem Soc* **2007**, 129, 176-186; bP. Avenier, X. Solans-Monfort, L. Veyre, F. Renili, J. M. Basset, O. Eisenstein, M. Taoufik, E. A. Quadrelli, *Top Catal* **2009**, 52, 1482-1491; cF. Blanc, C. Coperet, J. Thivolle-Cazat, J. M. Basset, *Angew Chem Int Edit* **2006**, 45, 6201-6203; dF. Blanc, N. Rendon, R. Berthoud, J. M. Basset, C. Coperet, Z. J. Tonzetich, R. R. Schrock, *Dalton T* **2008**, 3156-3158; eF. Blanc, J. Thivolle-Cazat, J. M. Basset, C. Coperet, A. S. Hock, Z. J. Tonzetich, R. R. Schrock, *J Am Chem Soc* **2007**, 129, 1044-1045.
- [18] D. C. Bradley, I. M. Thomas, *Can J Chem* **1962**, 40, 1355-&.
- [19] K. J. Ahmed, M. H. Chisholm, K. Folting, J. C. Huffman, *J Am Chem Soc* **1986**, 108, 989-999.
- [20] M. Beaudoin, S. L. Scott, *Organometallics* **2001**, 20, 237-239.

Chapter 5. Atomic-Level Organization of Vicinal Acid-Base Pairs through the Chemisorption of Aniline and Derivatives onto Mesoporous SBA15

5.1 Introduction

One of the major current challenges in heterogeneous catalysis is the ability to develop multifunctional catalyst systems where each active site plays a distinct role in the overall catalytic process (cascade strategy). To date, two main approaches exist to introduce functionalities into mesoporous materials exist: the soft templating strategy for the synthesis of organic-inorganic hybrid materials ^[1] and the surface organometallic chemistry (SOMC) methodology for the generation of well-defined surface species.^[2]

In the soft templating method, the inorganic materials provide the surface area and the porosity. The organic active site, linked to the surface via an alkyl spacer can be randomly distributed or organized.^[3] However, the resulting materials are usually composed of complex mixtures of surface species that are difficult to characterize. Consequently, the structure of their active site is generally not known at the atomic and molecular level.

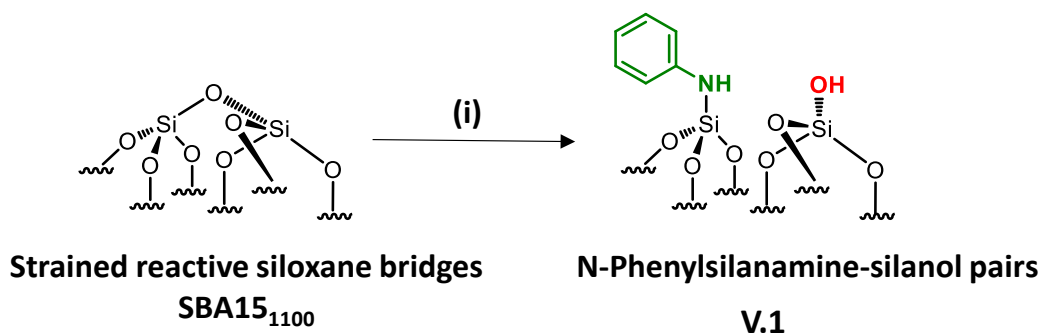
In the SOMC methodology, the generation of well-defined surface species is achieved by understanding the reaction of organometallic complexes with the inorganic materials which act as a rigid ligand. This approach presents the advantage of establishing a structure-activity relationship, and provides molecular-level insight for the design of new catalysts and reactions.^[4] Indeed, SOMC has been successful in designing “multifunctional” single site catalysts that are able to perform alkane metathesis via a multistep mechanism. However, the surface-complex bond is usually one or several σ -

bonded oxygen ligand, e.g., siloxy $[(\equiv\text{Si-O})\text{ML}_n]$, with M= metal and L = ligands, in the primary coordination sphere and the requirement for oxygen, in particular their proximity, limits the development of SOMC methods. It would then be highly desirable to tune the coordination sphere of the metal center by conceiving new surface ligands in close proximity to the surface to preserve the rigidity of the ensemble “surface ligand/complex”. By tuning the electronic and/or steric properties of the surface ligand new catalysts and reactions could be discovered.

In 2013, our group developed a new strategy to create an N-donor surface pincer ligand where the functional groups are well-organized into silylamine and silanol pairs on mesoporous SBA15 materials, named [N,O]SBA15. This was achieved through treatment with ammonia by opening strained siloxane bridges at 200 °C, by analogy with the ring opening of epoxides by ammonia.^[6] By reaction with an organometallic complex (Zirconium tetraneopentyl), the expected bipodal (siloxy-)(amido-)zirconium bis neopentyl was obtained.^[5] However, the successful formation of $[\equiv\text{Si-NH}_2][\equiv\text{Si-OH}]$ surface groups is associated with experimental, economical and safety disadvantages such as the need of the use of a high flow (200 mL/min) of pure, expensive and corrosive ammonia and the resulting materials is moisture sensitive. Aside from that approach, further chemical modifications of [N,O]SBA15 to offer opportunities to provide tunable steric and electronic properties which were impossible without affecting the structural parameter of the materials.

5.2 Scoop of the chapter

In this chapter, we investigate an alternative approach based on the chemisorption of dry aniline onto a highly dehydroxylated SBA15 (1100 °C) by opening siloxane bridges leading to N-phenylsilanamine - silanol pairs (Scheme 5.64). By contrast to ammonia, aniline allows one to bring some much more comprehensive approach of steric and electronic properties.



Scheme 5.64: Synthesis of paired N-phenylsilanamine/silanol V.1 via the chemisorption of dry aniline on SBA15₁₁₀₀ in toluene at 80 °C for 20h.

Advanced solid state magic angle spinning NMR methods including 2D ¹H-¹H double-quantum, ¹H-¹³C HETCOR experiments and dynamic nuclear polarization enhanced ²⁹Si and ¹⁵N spectra determine both the close proximity between the two functionalities and the formation of a covalent Si-N surface bond and confirm the generation of vicinal acid-base pairs. This methodology was successfully applied to the design of a series of aniline derivatives bifunctional mesoporous materials. An evaluation of the substituents effect, like nitro, chlorine, fluorine and methoxy group on a reaction model, the Knoevenagel condensation between the benzaldehyde and diethyl malonate is provided. The catalyst with 4-methoxy-N-phenylsilanamine-silanol pairs gave the best activity. This is explained by two factors: 1) The control of distance

between the acid-base functionalities and 2) The introduction of an electron-donating group involving higher basicity.

5.3 Results and discussion

5.3.1 Reaction of SBA15₁₁₀₀ with aniline

Well-ordered hexagonal mesoporous silica, SBA15, was chosen as a support because of its high thermal stability (up to 1200 °C), its high surface area (700 m².g⁻¹) and its large and uniform pore diameter (6 nm) and relatively thick walls (3 to 6 nm).^[6] Thermal treatment at 1100 °C under vacuum (10⁻⁵ mbar) yields the condensation of adjacent silanols and generates a support that contains a surface of mainly strained siloxanes along with a small amount of isolated silanols.^[7] As described in Scheme V.64, reaction of SBA15₁₁₀₀ with dry aniline was performed in solution in toluene at 80 °C for 20 h. The resulting material (**V.1**) was further evacuated at room temperature overnight under high vacuum (10⁻⁵ mbar) and characterized by FT-IR spectroscopy.

5.3.2 FT-IR characterization of the aniline modified SBA15

Comparison of the FT-IR spectra of SBA15₁₁₀₀ and **V.1** (Figure 5.39) reveals a slight increase in intensity of the characteristic [$\nu_s(\text{OH})$] band with a red shift from 3748 to 3745 cm⁻¹. Additionally, the typical single sharp infrared bands characteristic of secondary amines,^[8] here N-phenylsilylanamine appears, at 3435 and 1500 cm⁻¹. They correspond to the [$\nu(\text{NH})$] and [$\delta(\text{NH})$], respectively. Vibrational bands of the aromatic group are clearly visible at 3089-3023 cm⁻¹ [$\nu(\text{CH})$], at 1606 and 1500 cm⁻¹ [$\delta(\text{C}=\text{C})$] (overlap a NH band). Finally, the shoulder in the range of 3690-3585 cm⁻¹ is assigned to electronic interactions of the π system of the aromatic group with the newly formed adjacent silanol (π -OH interactions).^[9] It is important to mention that no aniline adsorption remains after reaction. Indeed, physical adsorption of aniline, which we do not see, would lead to a decrease of the isolated silanol band due to hydrogen bonding

between aniline and surface silanol, and the appearance of two bands at 3395 and 3300 cm^{-1} assigned to the N-H stretching vibration of physisorbed aniline.^[9]

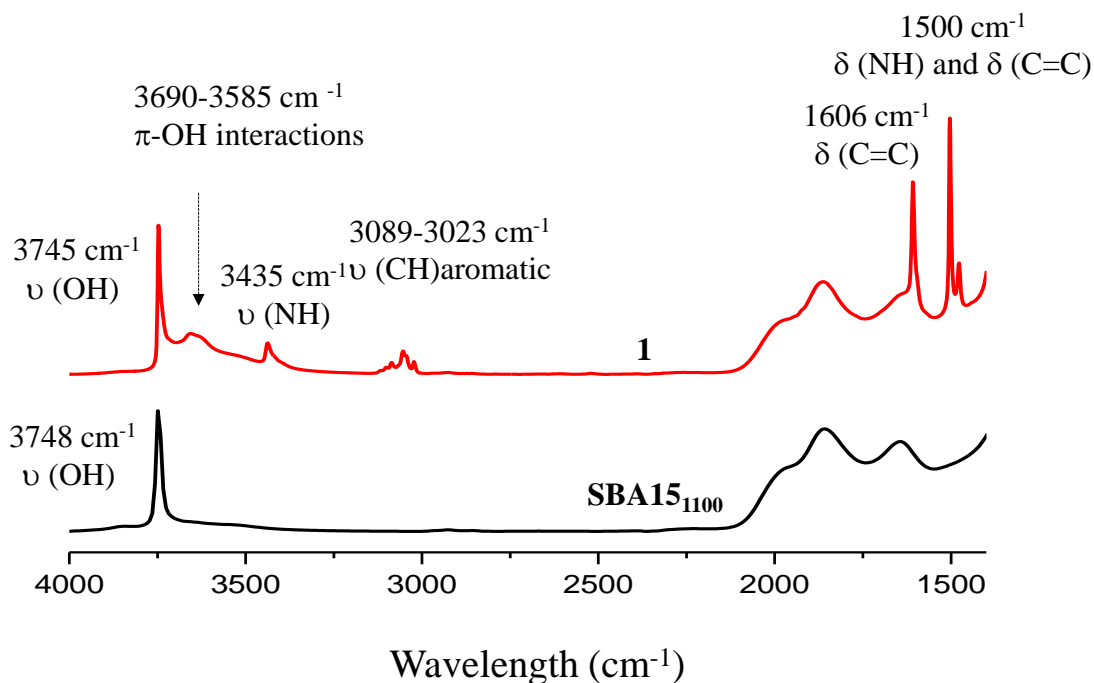


Figure 5.39: FT-IR spectra of the starting SBA15₁₁₀₀ (black) and V.1 (red).

5.3.3 NMR characterization of the aniline modified SBA15 and silsesquioxane

Solid state NMR was used to characterize the pairwise nature of the atomic-level organization of the supported organic functionalities, N-phenylsilanamine and silanol. The ¹H magic-angle-spinning (MAS) spectrum shows four clear resonances at 1.9, 3.4, 6.6 and 7 ppm (Figure 5.40). The chemical shift at 1.9 ppm is assigned to the $\equiv\text{SiOH}$ proton. Its value appears slightly downfield compared to the chemical shift of $\equiv\text{SiOH}$ (1.7 ppm) generated by treatment with ammonia.^[5a] This shift might be due to the proximity of the protons of the aromatic ring which induces π -OH interactions. The chemical shift at 3.4 ppm is attributed to the proton of the $\equiv\text{Si-NH-Ph}$.^[10]

The two intense signals at 6.6 ppm correspond to the protons of the aromatic ring in ortho (H_o) and para (H_p) positions. The proton in the meta position (H_m) appears at 7 ppm (Figure 5.2A).

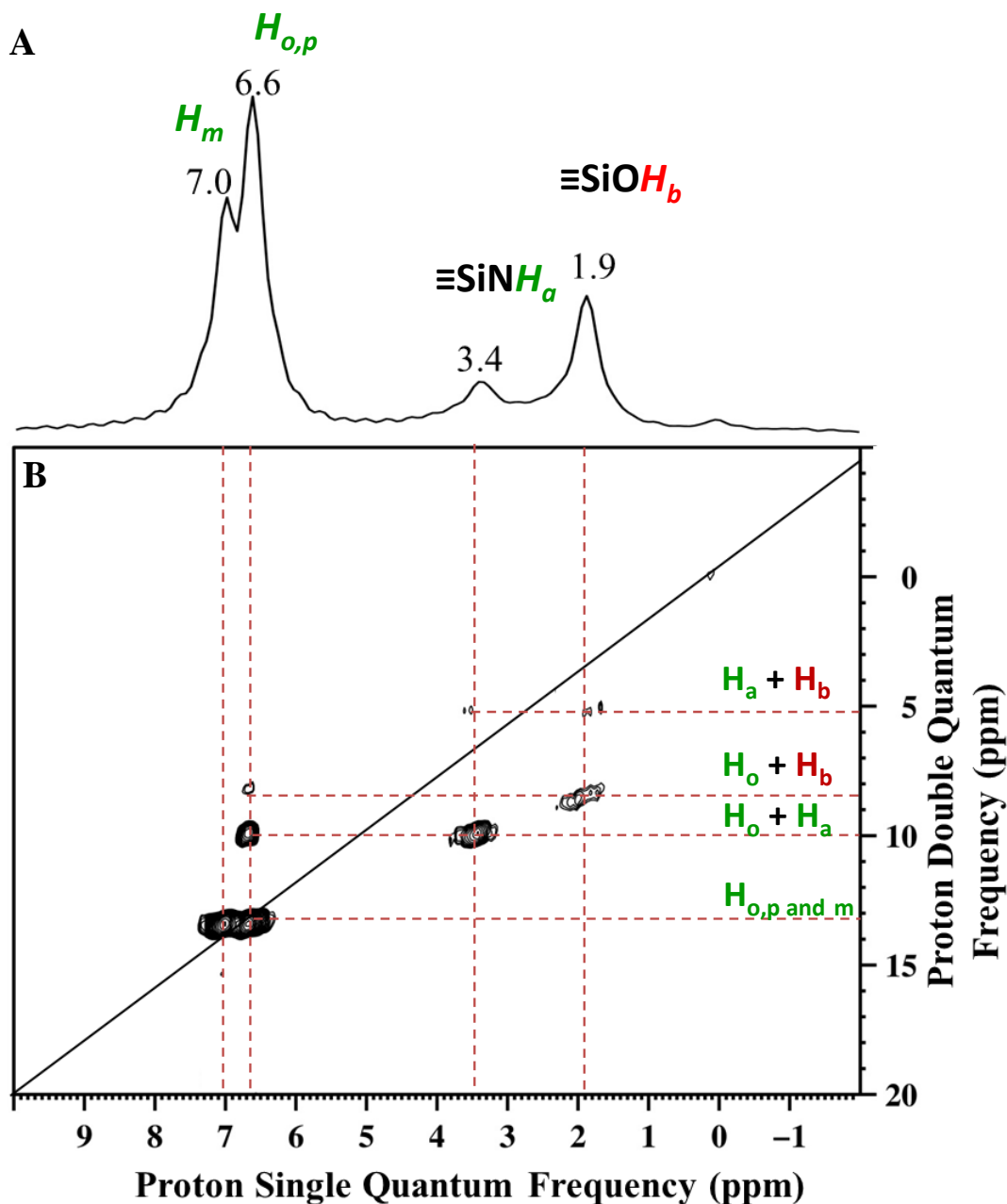
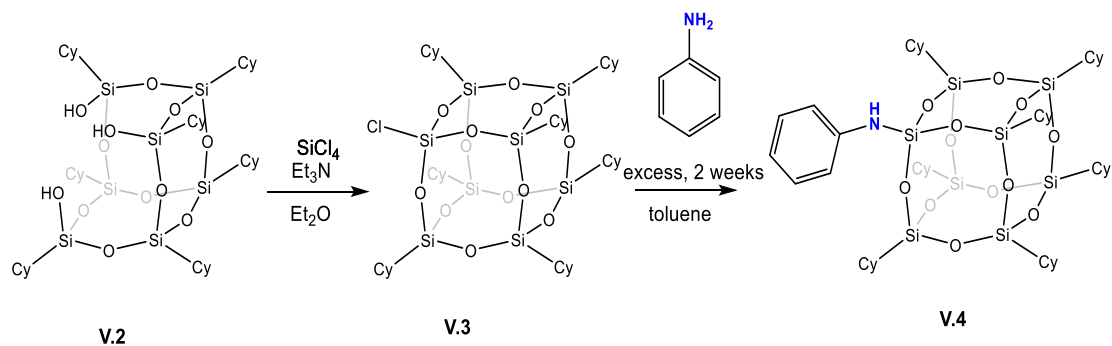


Figure 5.40: (A) ^1H MAS NMR spectrum of V.1. (B) DQ rotor-synchronized 2D ^1H MAS NMR spectrum of V.1.

To confirm these proton assignments, the synthesis of a model molecular silsesquioxane bearing N-phenylsilanamine group was carried out (Scheme 5.65).



Scheme 5.65: Synthesis of a model molecular silsesquioxane bearing N-phenylsilanamine group.

The ^1H liquid-state NMR spectrum (Figure 5.41) of the resulting silsesquioxane is in agreement with the ^1H MAS spectrum of **V.1** and confirms the formation of a σ bond between the nitrogen of aniline and the SBA15 surface.

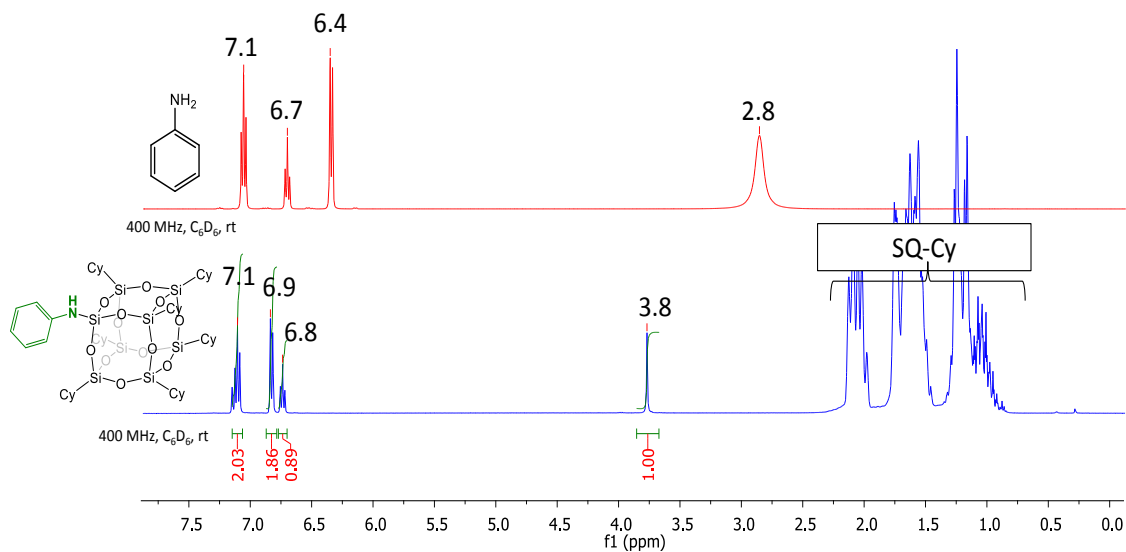
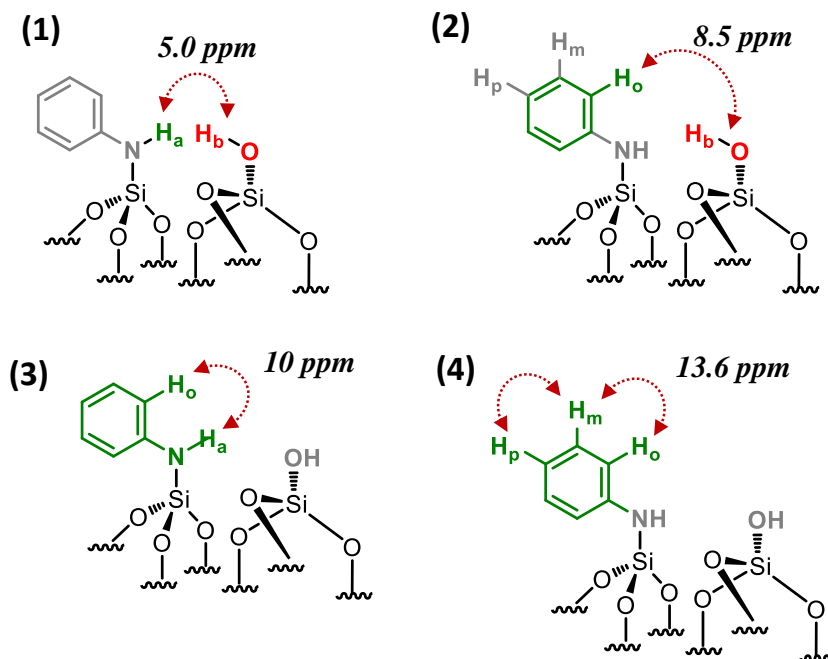


Figure 5.41: ^1H liquid NMR of aniline and **V.4 in C_6D_6 .**

Further information about the presence of vicinal functionalities was obtained from the 2D ^1H - ^1H double quantum (DQ) NMR spectrum (Figure 5.40 B). The 2D DQ

spectrum of **V.1** shows a weak correlation between the proton resonance of $\equiv\text{SiOH}$ at 1.9 ppm and the proton resonance of $\equiv\text{SiNHPh}$ at 3.4 ppm [5.3 ppm in F1: $\delta_{\text{H}}(\text{OH}) + \delta_{\text{H}}(\text{NH}) = 1.9 + 3.4$] (Scheme 5.3 (1)), indicating that the two protons are in close proximity, typically $< 5 \text{ \AA}$.

Moreover, the paired organization is reinforced by the presence of a correlation between the proton resonance of $\equiv\text{SiOH}$ and the aromatic proton resonances of the neighboring $\equiv\text{SiNHPh}$ at 6.6 ppm [8.5 ppm in F1: $\delta_{\text{H}}(\text{OH}) + \delta_{\text{H}}(\text{H}_o) = 1.9 + 6.6$] (Scheme 5.66 (2)).



Scheme 5.66: Schematic drawing showing of the observed proximities of the paired N-phenylsilanamine/silanol groups in **V.1** in the 2D ^1H - ^1H DQ NMR spectroscopy.

The correlation most likely arises from the ortho position H_o . Note that the H_m does not correlate with the silanol indicating that the aromatic ring is oriented in such a

way that the H_o is closest to the silanol. An additional correlation is observed between the proton resonance of $\equiv\text{SiNHPh}$ at 3.4 ppm and the proton of the aromatic ring in ortho position H_o at 6.6 ppm [10 ppm in F1: $\delta_H(\text{OH}) + \delta_H(H_o) = 3.4 + 6.6$] (Scheme 5.40 (3)). Finally, strong correlation peaks are observed between all the protons of the aromatic ring (Scheme 5.66 (4)).

We conclude that dry aniline reacts with strained siloxane bridges to generate vicinal N-phenylsilanamine and silanol groups. These results are consistent with those obtained with FT-IR spectroscopy.

In the ^{13}C CP-MAS NMR spectrum (Figure 5.42 A), the signals of the aromatic ring appear clearly at 118, 120, 129 and 143 ppm corresponding to the $C_o\text{H}$, $C_p\text{H}$, $C_m\text{H}$ and to the quaternary carbon linked to the nitrogen surface $\equiv\text{Si-NH-C}^V$, respectively. These assignments are in accordance with those of the silsesquioxane model (Figure 5.43).

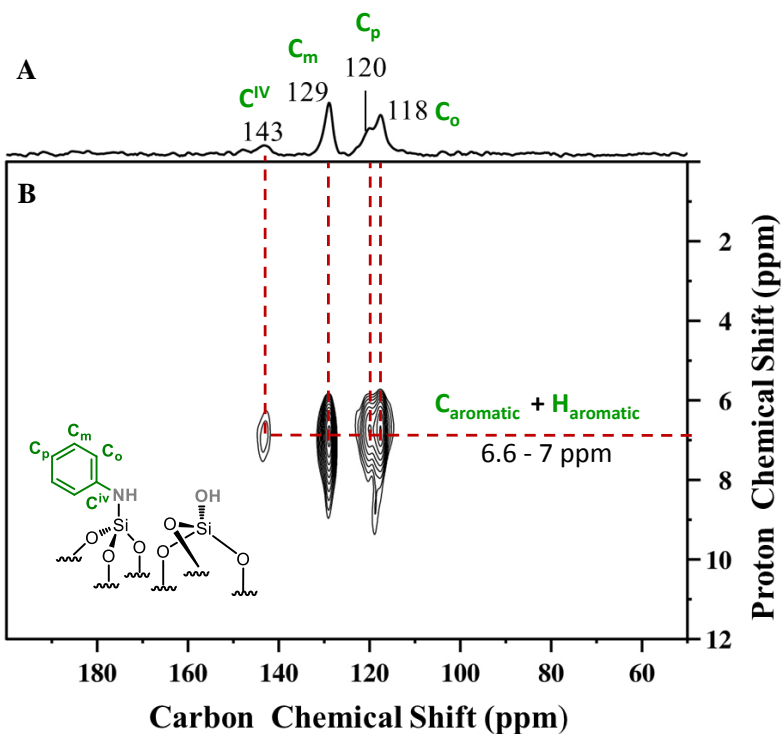


Figure 5.42: (A) ^{13}C CP-MAS NMR of V.1. (B) 2D contour plot of the aromatic region of ^1H - ^{13}C HETCOR spectrum of V.1.

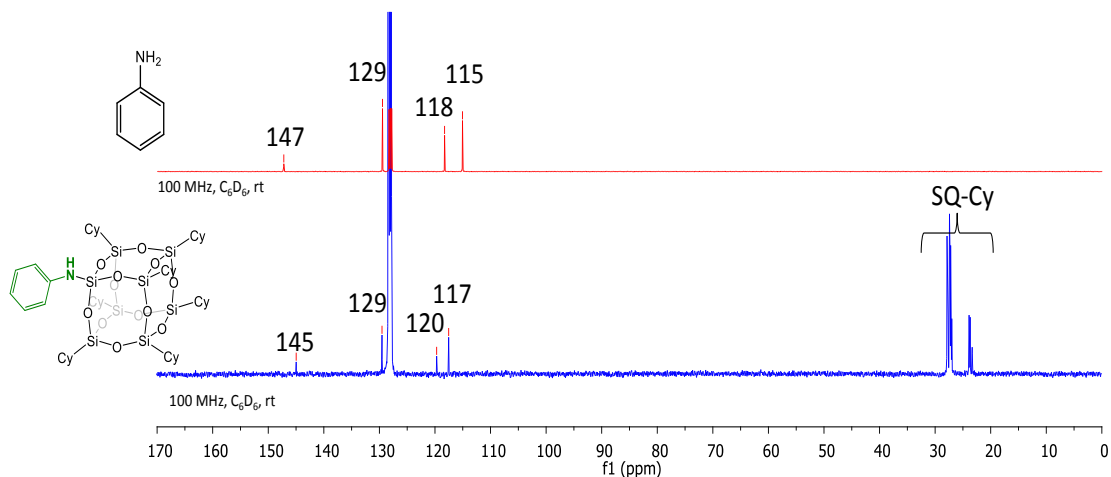


Figure 5.43: ^{13}C liquid NMR of aniline and V.4 in C_6D_6 .

The ^1H - ^{13}C HETCOR spectrum demonstrates strong correlation between these four carbon resonances and the proton resonances at 6.6 and 7 ppm attributed to the proton of aromatic group (Figure 5.42B). These results confirm that the integrity of the organic fragment is maintained under the reaction conditions.

5.3.4 Dynamic Nuclear Polarisation (DNP) characterization of the aniline modified SBA15

To identify the formation of a covalent bond between the silica surface and the organic fragment, $\equiv\text{SiNHPh}$, ^{29}Si and ^{15}N solid state NMR spectra are required, but are not practical using conventional methods due to low sensitivity at natural isotopic abundance. Dynamic Nuclear Polarization surface enhanced NMR (DNP SENS) ^[11] has recently been introduced and demonstrated to overcome these difficulties for the characterization of hybrid materials, and was used here.^[12] The natural abundance ^{29}Si DNP SENS spectrum of **V.1** (Figure 5.44 a) displays a signal centered at -100 ppm (intense) and a signal at -18 ppm (weak). According to the literature the former is attributed to both $[(\equiv\text{SiO})_3\text{SiOE}]$, with E = Si or H (commonly dubbed Q⁴ and Q³) ^[13] and the latter is assigned to the $[\equiv\text{SiNHPh}]$.^[14]

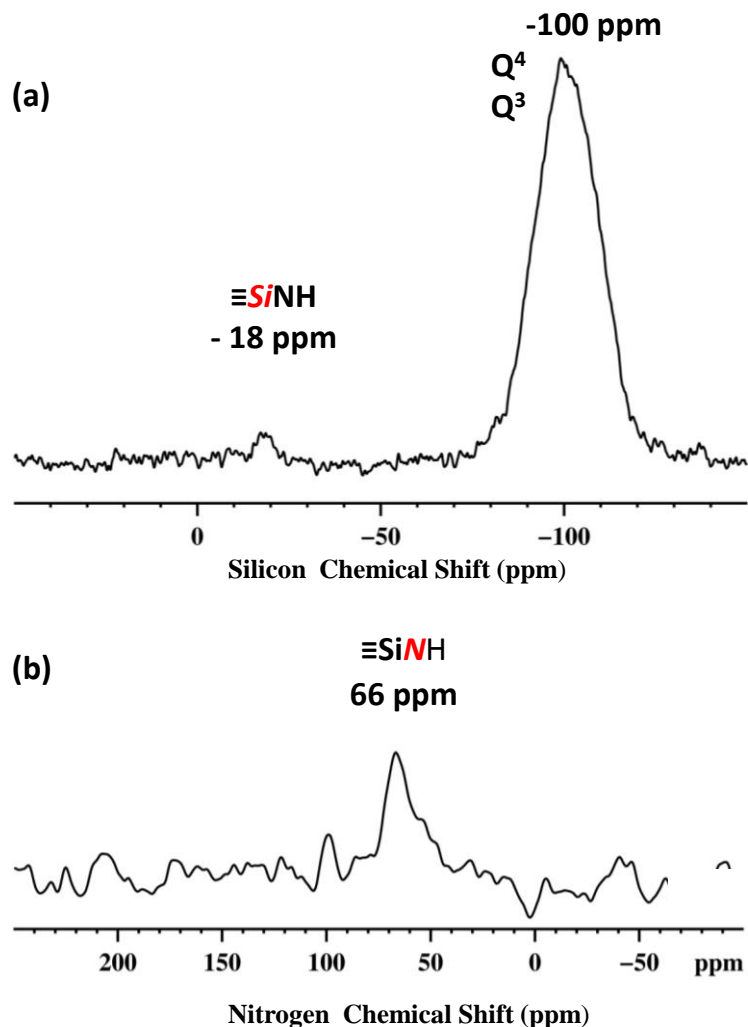


Figure 5.44: 400 MHz DNP SENS spectra of V.1 (20mg) impregnated with a 16mM solution of TEKPOL in 1,1,2,2-tetrachloroethane at 8 kHz MAS frequency with a sample temperature of 100K. (a) ^{29}Si DNP enhanced CP/MAS with a CP contact time of 5 ms, a 3 s polarization delay and 1024 scans. Exponential line broadening of 60 Hz was applied prior to Fourier transformation. (b) ^{15}N DNP enhanced CP/MAS with 5 ms CP contact time, a 3 polarization delay and 16000 scans. Exponential line broadening of 150 Hz was applied prior to Fourier transformation. In both (a) and (b) for comparison, spectra are shown with both for both μ wave on and off.

The natural abundance ^{15}N DNP SENS spectrum shows a single peak at 66 ppm (Figure 5.44 b) and it is in agreement with the ^{15}N liquid-state NMR spectrum of the model molecular silsesquioxane, for which the ^{15}N chemical shift appears at 62 ppm (Figure 5.45).

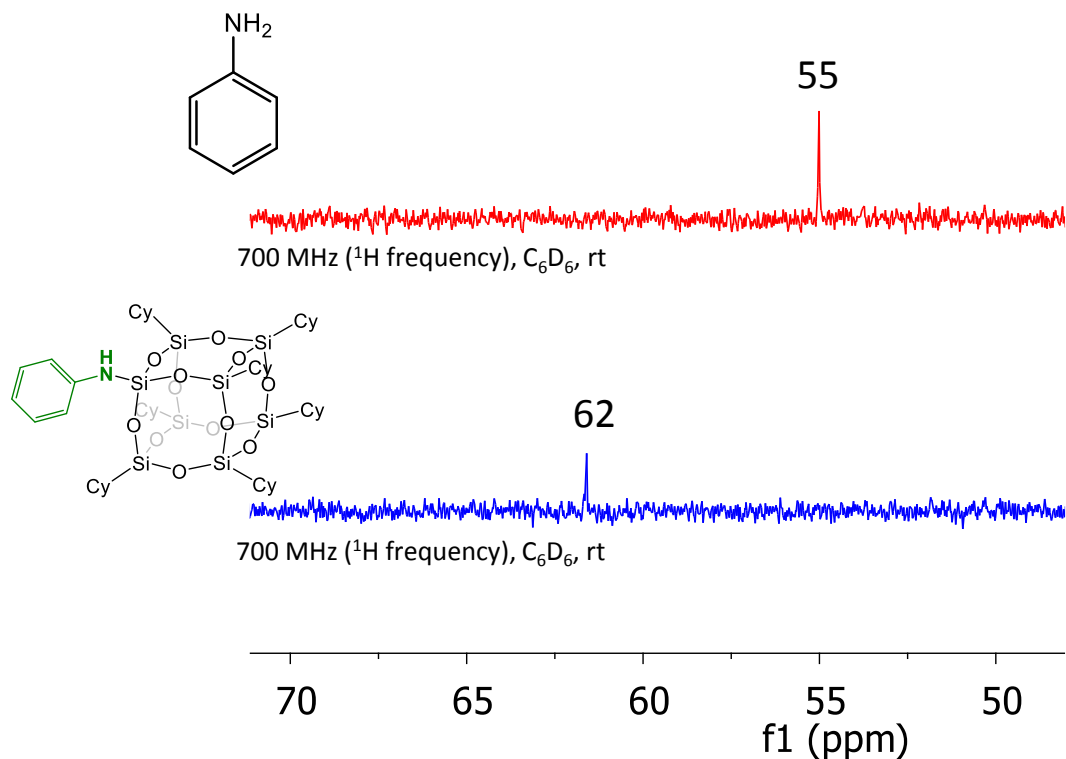


Figure 5.45: ^{15}N liquid NMR of aniline and V.4 in C_6D_6 .

5.3.5 Textural characterization of the aniline modified SBA15

Textural characterization was used to evaluate the preservation of the mesoporous materials, here by nitrogen adsorption/desorption porosimetry, X-ray diffraction (XRD), and Transmission Electronic Microscopy. The small angle X-ray diffraction patterns of **V.1** (Figure 5.46) exhibit three clear peaks (d_{100} , d_{110} and d_{200}) in the 2θ range of $0.7 - 4^\circ$. They confirm the presence of a well-ordered hexagonal mesophase with a d_{100} spacing of 86.28 \AA (Table 5.12). The structure of the mesoporous materials is thus maintained throughout the chemisorption of dry aniline.

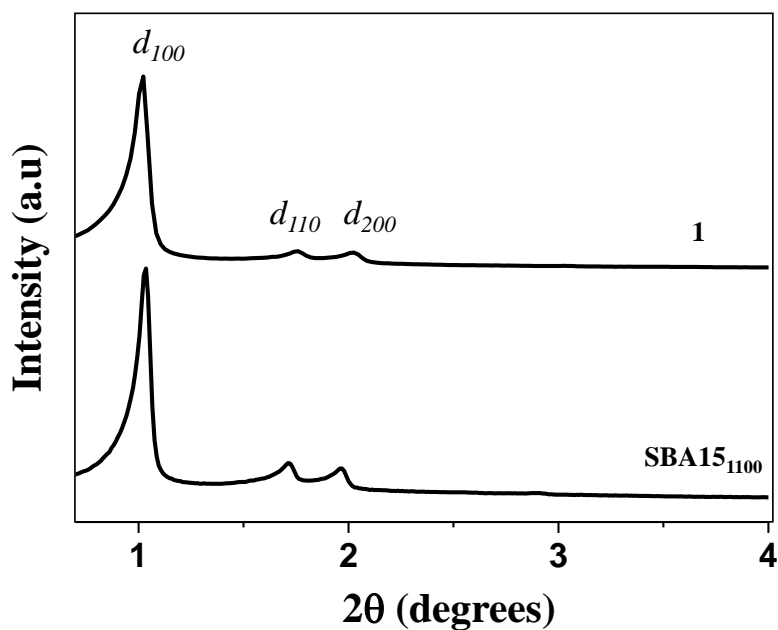


Figure 5.46: Small angle XRD patterns of SBA1₁₀₀ and V.1.

Table 5.11. Textural parameters of V.1 from Nitrogen sorption combined with small angle X-ray diffraction.

	$d_{100}^{[a]}$	$a_0^{[b]}$	Wall thickness ^[c]	$V_p^{[d]}$	$D_p^{[e]}$	S_{BET}
	(Å)	(Å)	(Å)	(cm ³ .g ⁻¹)	(Å)	(m ² .g ⁻¹)
SBA ₁₁₀₀	85.4	98.6	41.6	0.90	57	679
V.1	86.28	99.6	49	0.65	50	512

[a] d_{100} spacing. [b] $a_0 = 2d_{100}/\sqrt{3}$, hexagonal lattice parameter from XRD. [c]

Calculated by a_0 – pore size. [d] Total pore volume at $P/P_0 = 0.97$. [e] Pore size from desorption branch applying the BJH pore analysis.

Analyses of the nitrogen adsorption/desorption isotherms yielded BET surface areas of **V.1** of approximately 512 m²/g (versus 679 m²/g for SBA₁₁₀₀) and pore volumes of 0.65 cm³/g (versus 0.9 cm³/g for SBA₁₁₀₀). Also, **V.1** showed type IV isotherms (Figure 5.47), with clear H1-type hysteresis loops associated with capillary condensation in the mesoporous and with regular pore sizes of 50 Å. The textural parameters of sample **V.1** are summarized in Table 5.1 and are characteristic of mesoporous materials. The surface coverage α of the organic moieties based on the carbon content was calculated as described by Jaroniec *et al.* [15]

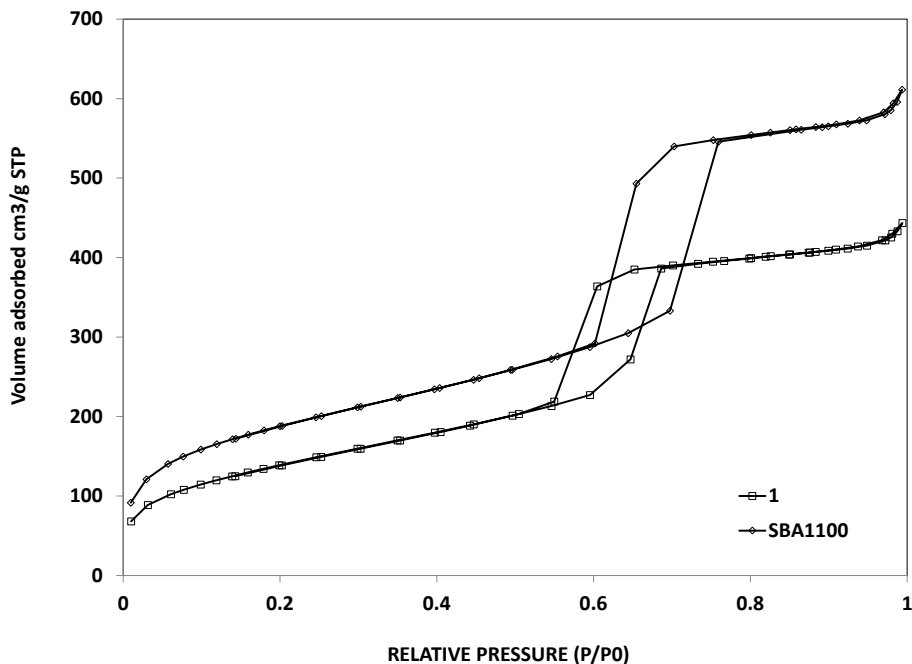


Figure 5.47: Nitrogen adsorption/desorption isotherm at 77 K of SBA₁₁₀₀ and **V.1**.

Using equation (S1) (see experimental), a carbon content of 1.42 wt. % was determined for **V.1**, which translates into a surface coverage of 0.3 $\mu\text{mol}\cdot\text{m}^{-2}$. The low

surface coverage supports the results of N₂ sorption experiments and indicates the functionalization of the SBA15₁₁₀₀.

Further evidence for a well-ordered hexagonal mesostructure is provided by the TEM images (Figure 5.48), which are representative of mesoporous SBA15. After the high thermal treatment (1100 °C, 10⁻⁵ mbar) and the dissociative chemisorption of aniline (80°C, toluene, 20 h), the mesoporous structure is still regular over the whole particle of V.1.

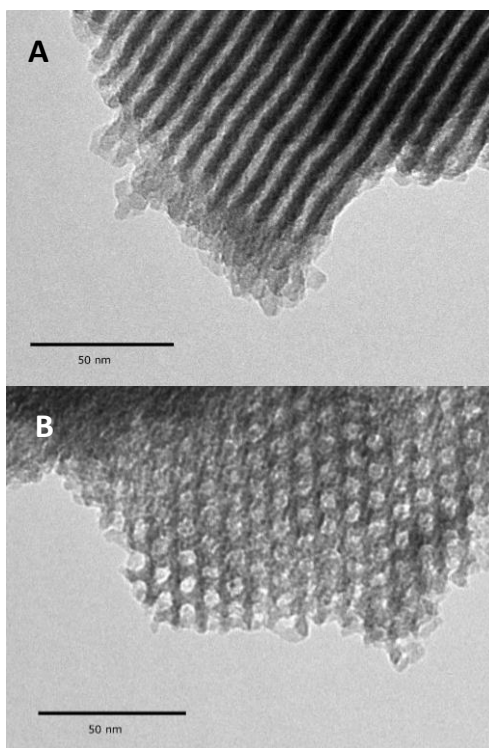
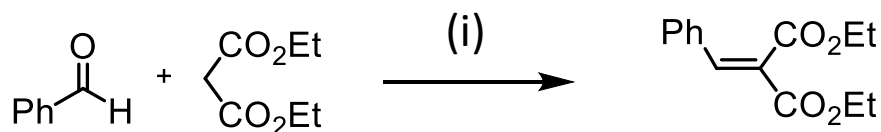


Figure 5.48: Transmission electron micrographs of V.1 at different tilt angles: in the direction perpendicular to the pore axis (A), and in the direction of the mesoporous axis (B).

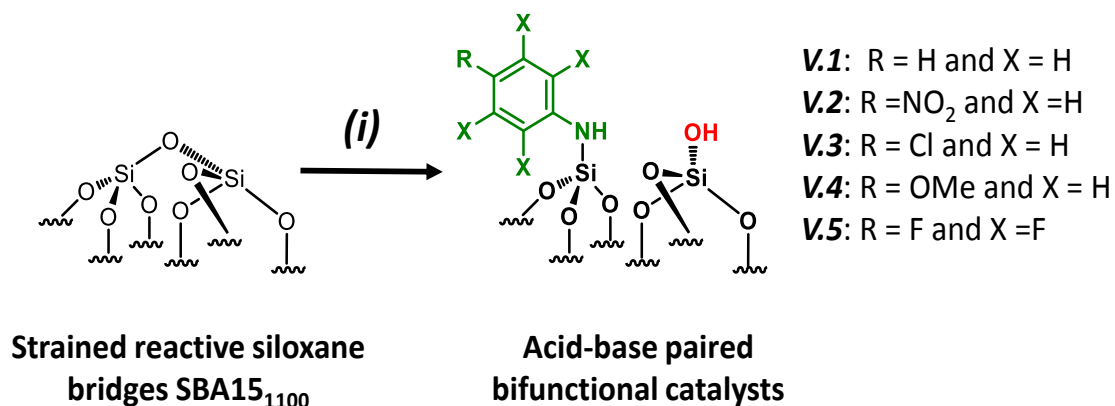
5.3.6 Catalytic behavior for the Knoevenagel condensation

A materials with atomic organization of acid-base pairs should exhibit cooperative catalytic behavior for the Knoevenagel condensation of benzaldehyde with diethyl malonate (pK_a =13) (Scheme 5.67).



Scheme 5.67: Knoevenagel condensation using benzaldehyde with diethylmalonate. (i) The reaction was performed in sealed flask in which each reactant (2 mmol) and the catalyst (20 mg) were dissolved in dry ethanol (5 mL) and the reaction mixture was refluxed in an oil bath at 80 °C for 24 h.

The Knoevenagel condensation between a carbonyl group and an activated methylene compounds is one of the most useful C=C bond forming reaction. It produces several important key intermediates such as α, β unsaturated widely used for the synthesis of therapeutic drugs, functional polymer and fine chemicals. In the literature, several studies have revealed an efficient catalysis by cooperative acid-base pairs well organized onto of mesoporous silica. In the mechanism, activation of the carbonyl group occurs on weak Brönsted acid sites and the basic sites extract the proton from methylene. In this case, the control of the distance is a key parameter to enhance the reactivity of the Knoevenagel condensation.



Scheme 5.68: Synthesis of acid-base paired catalysts via (i) the chemisorption of dry aniline derivatives on SBA_{15.1100} in toluene at 80 °C for 20h.

For comparison purpose, a series of aniline derivatives bifunctional mesoporous materials with different electronic properties were successfully synthesized through the

same approach (Scheme 5.68). All the materials were characterized by FT-IR and ^1H -MAS solid state NMR spectroscopy (Figure 5.49 and 5.50).

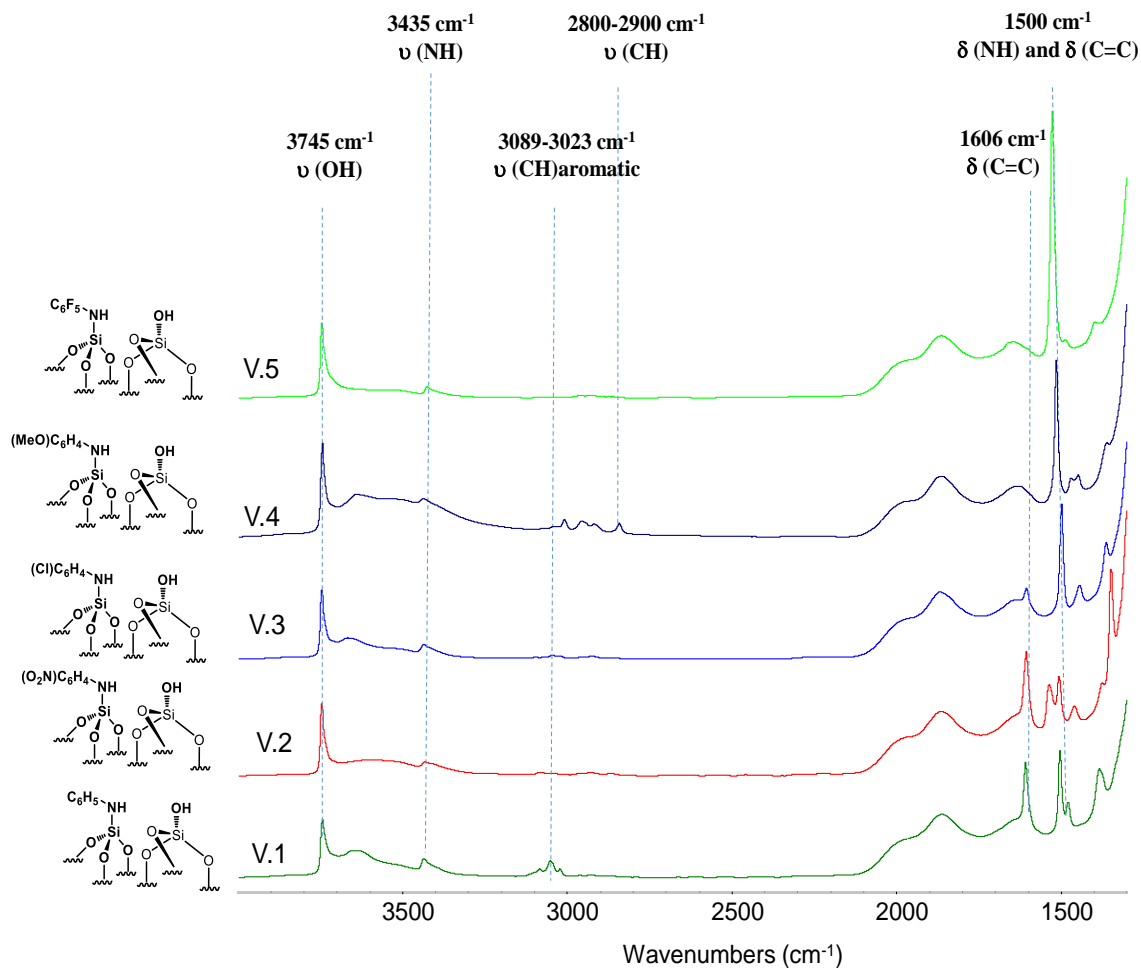


Figure 5.49: FT-IR spectra of materials V.1-V.5.

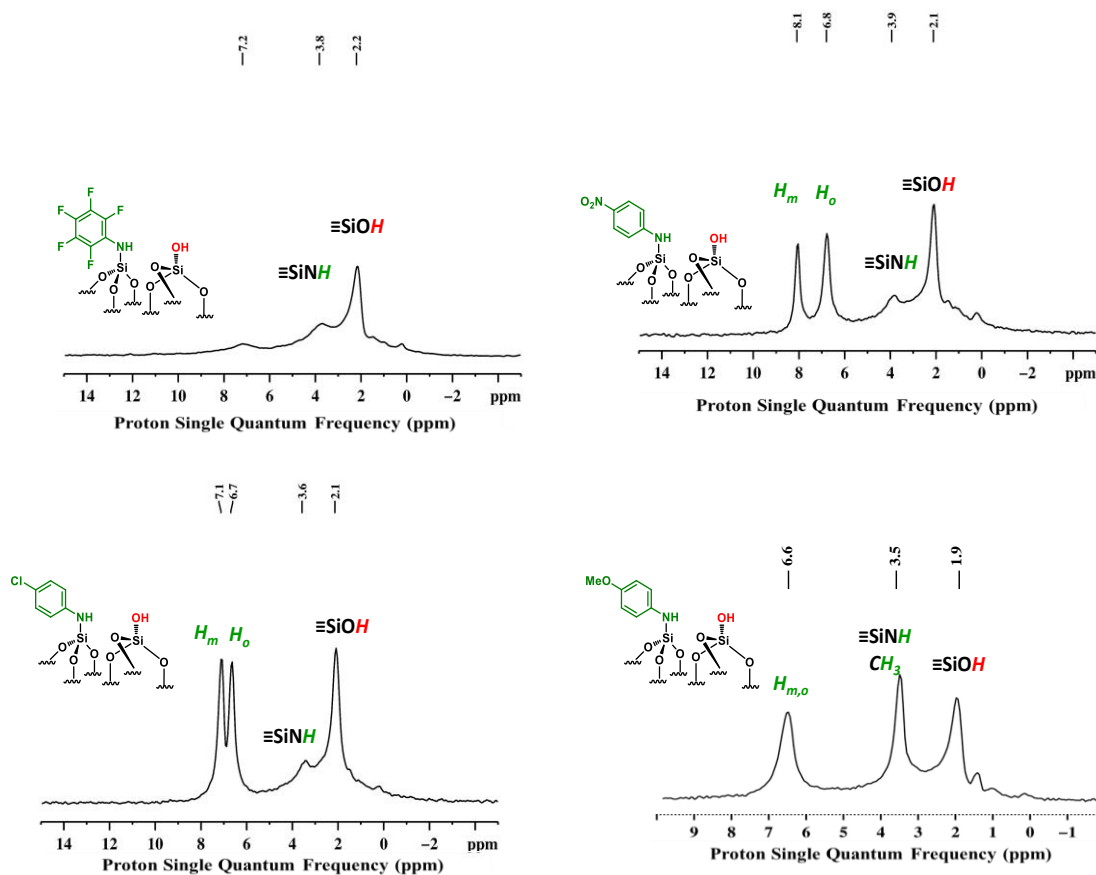
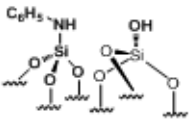
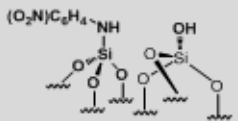
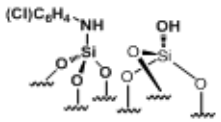
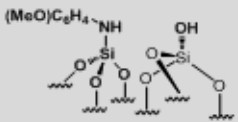
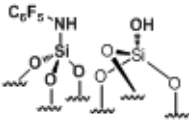
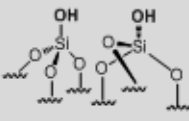
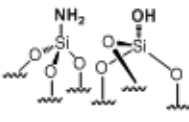
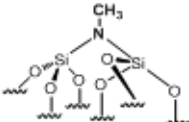


Figure 5.50: ^1H MAS solid state NMR of catalyst V.2-V.5

Their catalytic performances were tested (Table 5.13, Entry 1-5) and all the samples show good catalytic ability. Entry 1 show higher activity than Entry 2. The nitro group is strongly electron-withdrawing group (EWG) and thus, catalyst (**V.2**) is a weaker base than catalyst (**V.1**). A chloro group in para position is a slightly EWG, so catalyst (**V.3**) exhibit better activity than (**V.2**) and it is slightly less active than (**V.1**). Introducing an electron-donating group (EDG) as a p-methoxy group, in the catalyst (**V.4**) enhance the catalytic performance in the Knoevenagel reaction. Among all these catalysts, (**V.4**) exhibits the best performance where as (**V.5**) the lowest due to the base weakening effect.

Table 5.12 Knoevenagel condensation testing.

Entry	Catalyst	N loading ^a (mmol/g)	Yield (%) ^b	TON ^c
1		0.23	59	257
2		0.22	35	159
3		0.18	43	238
4		0.21	64	304
5		0.18	24	133
6		0	0	0
7		0.35	18	51
8		17.3	0	0
9		13.1	15	1.1

(a) Determined by elemental analysis. (b) Determined by GC analysis after 24h. (c)

Turnover number (TON) = number of mole of product per number of mole of active amine site.

Besides, the catalytic results of this series of acid-base paired catalysts (Table 5.13, entry 1-5) were compared to four others materials (Table 5.13, entry 6-9): an unmodified SBA15 displaying different silanols (vicinal, geminal) (**V.6**), [N,O] SBA15 where primary amine and silanol groups are proximal (**V.7**), ^[5a] a SBA15 containing a silazane bridges (**V.9**), and a methylated SBA15 (**V.9**). ^[16] As expected (**V.6**) shows no activity as no basic sites are present. (**V.7**) contains primary amines which are supposed to be the strongest base; yet it gives only 18 % conversion after 24h. (**V.1**) and (**V.4**) yield better conversion although their basicity is lower than that of (**V.7**). These results are explained by the higher stability of these catalysts under the experimental conditions (ethanol is the solvent and water is produced during the Knoevenagel reaction). Indeed, the $\equiv\text{SiNH}_2$ group is well-known to be easily hydrated.^[16-17]

5.3.7 Stability of the catalysts

The stability of (**V.7**) and (**V.1**) towards ethanol was monitored by FT-IR spectroscopy. After 5 min in contact with dry ethanol, the FT-IR spectrum (Figure 5.51) of (**V.7**) shows complete disappearance of the characteristic bands of the $\equiv\text{SiNH}_2$ group [$\nu_s(\text{NH}_2) = 3535$, $\nu_s(\text{NH}_2) = 3445$ and $\delta(\text{NH}_2) = 1550 \text{ cm}^{-1}$]. However the FT-IR spectrum of (**V.1**) shows the characteristic bands of $\equiv\text{Si-NHPh}$, [$\nu(\text{NH}) = 3435 \text{ cm}^{-1}$] even after 1 hr in contact with dry ethanol. In addition, during the catalytic test with catalyst **V.1**, no leaching of aniline was detected by both GC-FID (Figure 5.52).

Based, on previous work,^[16] catalysts (V.1-5) are also expected to be more active than (V.8) and (V.9) due to their higher basicity and the presence of a closer silanol, as it is well-known that Knoevenagel reaction is enhanced by through the cooperativity between acid/base pairs.^[1d, 3a-d]

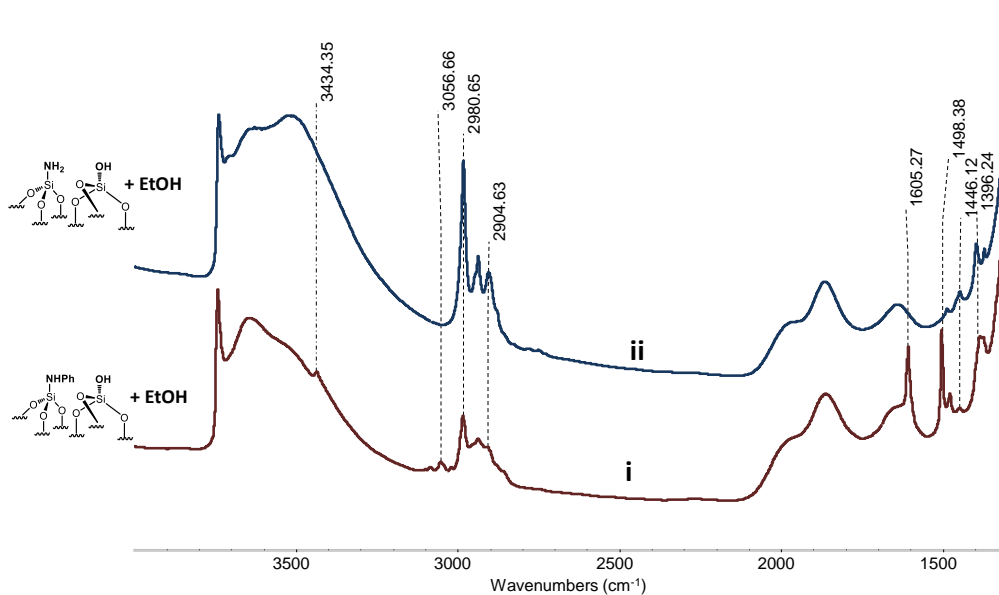


Figure 5.51: (i) FT-IR spectrum of [NHPh,O] SBA15, V.1 after 1hr in contact with dry ethanol and followed by evacuation at 10^{-5} mbar, 100 °C for 12h: the characteristic bands of $\equiv\text{SiNHPh}$, [$\nu(\text{NH}) = 3435 \text{ cm}^{-1}$] is still observed. (ii) FT-IR spectrum of [N,O] SBA15, after 5 min in contact with dry ethanol and followed by evacuation at 10^{-5} mbar, 100 °C for 12h: complete disappearance of the characteristic bands of $\equiv\text{SiNH}_2$ group [$\nu_s(\text{NH}_2) = 3535$, $\nu_{as}(\text{NH}_2) = 3445$ and $\delta(\text{NH}_2) = 1550 \text{ cm}^{-1}$].

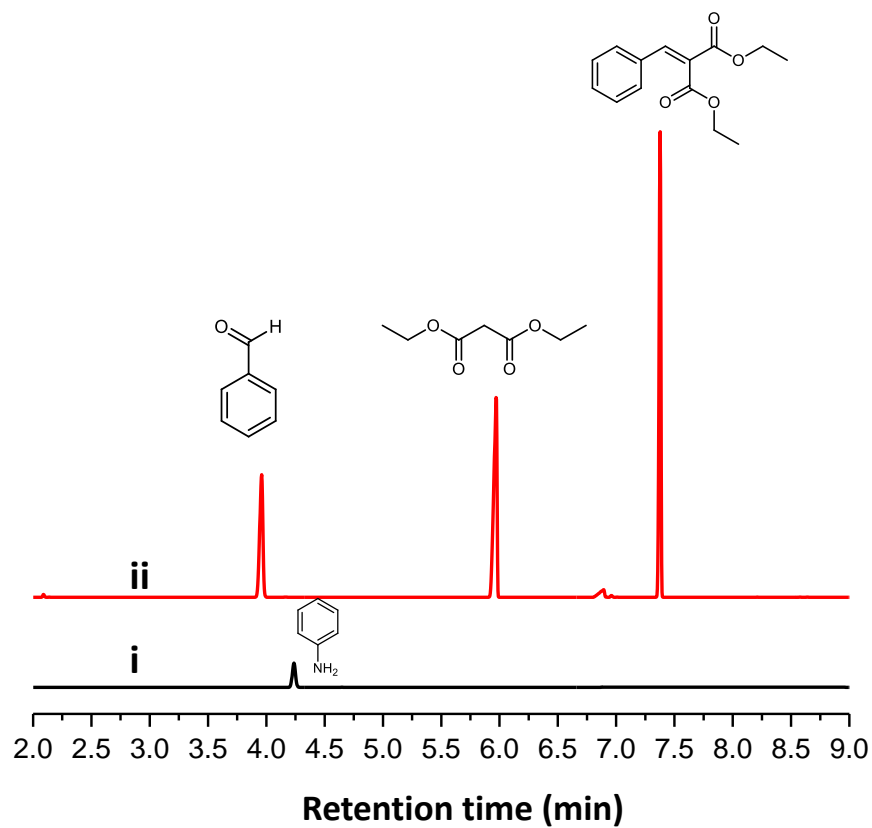


Figure 5.52:.(i) GC-MD Chromatogram of pure dry aniline and GC chromatogram of reactant and product of Knoevenagel condensation.

5.4 Conclusion

In summary, the opening siloxane bridges approach was successfully established to create an atomic organization of well-defined bi-functional acid-base pairs on mesoporous SBA15. This approach is based on an analogy between organic epoxides and strained siloxanes ($\equiv\text{Si-O-Si}\equiv$) of mesoporous SBA15₁₁₀₀ °C. The generation of well-defined adjacent N-phenylsilanamine-silanol pairs was unambiguously determined through FTIR, 2D solid state NMR, XRD, Nitrogen sorption and TEM. This way to design bi-functionalized mesoporous surface offers new opportunities to modify the electronic and steric properties of mesoporous silica useful for heterogeneous catalysis.

5.5 Experimental

5.5.1 DNP-solid state NMR. DNP experiments were performed on a 400 MHz (^1H /electron Larmor frequencies) Bruker Avance III solid-state NMR spectrometer equipped with a 263 GHz gyrotron. The sweep coil of the main super conducting coil was set so that microwave irradiation occurred at the positive enhancement maximum of TEKPOL. At low temperature double resonance 3.2 mm probe configured for ^{29}Si and after for ^{15}N CP/MAS. Sample temperature during DNP experiments were around 100K. DNP enhancements were measured by comparing the intensity of spectra acquired with and without continuous wave irradiation. A 20 mg of powdered material was impregnated with 20 μL of 16mM of TEKPOL tetrachloethane solution. Impregnated materials were then packed into sapphire rotors inside glovebox. For the CPMAS experiments the following sequence was used: 900 pulse on the proton, then cross-polarization with a contact time of 5 ms and finally acquisition of the ^{29}Si and ^{15}N signal

under high power decoupling. SPINAL-64 heteronuclear ^1H decoupling was employed during acquisition.

5.5.2 Transmission Electron Microscopy (TEM). Sample **V.1** was spread on a copper grid precoated with a holey carbon layer. Imaging was performed on a Tecnai Biotwin transmission electron microscope (FEI Company) operating at 120 kV. Data was acquired at 1 μm defocus and recorded on a Eagle CCD camera 4kx4k (FEI company)

V.5.3 Preparation of V.1 (impregnation method). In a schlenk, SBA15₁₁₀₀ C (0.5 g) was reacted with dry aniline (2.5 ml) in toluene for 24 h at 80°C. After filtration and four washing cycles, the resulting white powder was dried for 8 hr under dynamic vacuum ($< 10^{-5}\text{mbar}$).

Elemental analysis (mass. %): C (1.42) and N (0.35) corresponding to C/N ratio of 5.1

5.5.4 Preparation of N-phenylsilylanamine silsesquioxane V.4

1,3,5,7,9,11,13 - Heptacyclohexyltricyclo [7.3.3.15,11] heptasiloxane - 3,7,13 - triol **V.2** (1.0 g, 0.92 mmol, 1.0 eq.) was reacted with SiCl_4 (0.13 mL, 1.1 mmol, 1.2 eq.) in the presence of NEt_3 (0.40 mL, 2.9 mmol, 3.1 eq.) in dry Et_2O (50 mL) under inert conditions. The reaction was stirred overnight at reflux. After cooling down, the precipitate was filtered and the solvent was removed. The white solid residue was washed with hot acetonitrile/toluene, 1/1 (v/v), filtered and dried to dryness to isolate 1,3,5,7,9,11,14 - heptacyclohexyltricyclo [7.3.3.15,11] octasiloxane - 15 - chloride **V.3**.

Yield: 0.92 g (97 %) as white solid.

In a next step, toluene was added (20 mL) to react SQ-2 (0.92 g, 0.89 mmol, 1.0 eq.) with aniline (0.46 mL, 5.0 mmol, 5.7 eq.) in presence of NEt₃ (0.33 mL, 2.4 mmol, 2.7 eq.) under inert conditions. The reaction was stirred at room temperature for 18 days. Then, the white precipitate was filtered and the toluene was removed. To isolate 1,3,5,7,9,11,14 – heptacyclohexyltricyclo [7.3.3.15,11] octasiloxyl – 15 - aniline **V.4**, column chromatography was performed in DCM (R_f = 0.98) to remove the remaining aniline and in ethylacetate/hexane, 1/1 (v/v) to remove the remaining impurities. The purity of **V.4** was followed by ¹H NMR (400 MHz, C₆D₆) and ¹³C NMR (100 MHz, C₆D₆)

5.5.6 Catalytic performances for Knoevenagel reaction

In a typical experiment, the reactants were mixed in anhydrous ethanol and 0.02 g of the dried catalyst into the reactor and heated at 80 °C. After the reaction, the catalyst was separated by filtration. The products were analyzed using a Chrompak CP 9000 gas chromatograph (GC) equipped with 30 m × 0.32 mm RTX-50 capillary column and FID detector. Individual reaction product was identified by GC-mass spectrometry (HP5971 mass spectrometer connected with a 30 × 0.25 mm RTX-50 capillary column)

5.5.7 Determination of the surface coverage

The surface coverages (per m² of unmodified SBA15₁₁₀₀) of N-phenylsilanamine ligands (α) bonded to the surface were estimated from the carbon contents of the materials using Equation (V.1):

$$\alpha \text{ (mol/m}^2\text{)} = \frac{P_C}{1200n_C - P_C(M - 1)} / S_{BET}$$

Where, P_C = carbon percentage in the N-phenylsilanamine bonded phase; M are the molecular mass of the ligand attached, n_C are the number of carbon atoms per ligands attached and S_{BET} is the BET specific surface area in m^2/g

5.6 References

- [1] aF. Hoffmann, M. Cornelius, J. Morell, M. Fröba, *Angew. Chem. Int. Ed.* **2006**, *45*, 3216-3251; bA. Kuschel, M. Drescher, T. Kuschel, S. Polarz, *Chemistry of Materials* **2010**, *22*, 1472-1482; cD. E. De Vos, M. Dams, B. F. Sels, P. A. Jacobs, *Chemical Reviews* **2002**, *102*, 3615-3640; dA. P. Wight, M. E. Davis, *Chemical Reviews* **2002**, *102*, 3589-3614; eI. Sierra, D. Perez-Quintanilla, *Chemical Society Reviews* **2013**, *42*, 3792-3807; fM. Ogawa, K. Saito, M. Sohmiya, *European Journal of Inorganic Chemistry* **2015**, *2015*, 1126-1136.
- [2] aJ. M. Basset, R. Psaro, D. Roberto, R. Ugo, *Modern surface organometallic chemistry (hardback)*, **2009**; bC. Copéret, M. Chabanas, R. Petroff Saint-Arroman, J.-M. Basset, *Angewandte Chemie International Edition* **2003**, *42*, 156-181; cF. Lefebvre, in *Atomically-Precise Methods for Synthesis of Solid Catalysts*, The Royal Society of Chemistry, **2015**, pp. 1-26; dP. Sautet, F. Delbecq, *Chemical Reviews* **2010**, *110*, 1788-1806; eJ. D. Pelletier, J. M. Basset, *Acc Chem Res* **2016**, *49*, 664-677.
- [3] aE. L. Margelefsky, A. Bendjériou, R. K. Zeidan, V. Dufaud, M. E. Davis, *J. Am. Chem. Soc.* **2008**, *130*, 13442-13449; bV. Dufaud, M. E. Davis, *J. Am. Chem. Soc.* **2003**, *125*, 9403-9413; cE. L. Margelefsky, R. K. Zeidan, V. Dufaud, M. E. Davis, *J. Am. Chem. Soc.* **2007**, *129*, 13691-13697; dR. K. Zeidan, S.-J. Hwang, M. E. Davis, *Angewandte Chemie* **2006**, *118*, 6480-6483; eN. A. Brunelli, K. Venkatasubbaiah, C. W. Jones, *Chemistry of Materials* **2012**, *24*, 2433-2442; fA. T. Dickschat, F. Behrends, M. Bühner, J. Ren, M. Weiß, H. Eckert, A. Studer, *Chemistry – A European Journal* **2012**, *18*, 16689-16697; gA. T. Dickschat, F. Behrends, S. Surmiak, Wei, H. Eckert, A. Studer, *Chem. Comm.* **2013**, *49*, 2195-2197; hY. Huang, S. Xu, V. S. Y. Lin, *Angew. Chem. Int. Ed.* **2011**, *50*, 661-664; iK. K. Sharma, T. Asefa, *Angewandte Chemie* **2007**, *119*, 2937-2940; jN. R. Shiju, A. H. Alberts, S. Khalid, D. R. Brown, G. Rothenberg, *Angew. Chem. Int. Ed.* **2011**, *50*, 9615-9619.
- [4] aV. Vidal, A. Théolier, J. Thivolle-Cazat, J.-M. Basset, *Science* **1997**, *276*, 99-102; bV. Dufaud, J.-M. Basset, *Angew. Chem. Int. Ed.* **1998**, *37*, 806-810.
- [5] aA. Bendjeriou-Sedjerari, J. M. Azzi, E. Abou-Hamad, D. H. Anjum, F. A. Pasha, K.-W. Huang, L. Emsley, J.-M. Basset, *J. Am. Chem. Soc.* **2013**, *135*, 17943-17951; bF. A. Pasha, A. Bendjeriou-Sedjerari, K.-W. Huang, J.-M. Basset, *Organometallics* **2014**, *33*, 3320-3327.
- [6] aD. Zhao, J. Feng, Q. Huo, N. Melosh, G. H. Fredrickson, B. F. Chmelka, G. D. Stucky, *Science* **1998**, *279*, 548-552; bD. Zhao, Q. Huo, J. Feng, B. F. Chmelka, G. D. Stucky, *J. Am. Chem. Soc.* **1998**, *120*, 6024-6036.
- [7] aB. C. Bunker, D. M. Haaland, T. A. Michalske, W. L. Smith, *Surface Science* **1989**, *222*, 95-118; bB. A. Morrow, I. A. Cody, L. S. M. Lee, *Journal of Physical Chemistry* **1976**, *80*, 2761-2767.
- [8] Donald L. Pavia, Gary M. Lampman, George S. Kriz, J. R. Vyvyan, *Introduction to Spectroscopy- Fourth Edition*.
- [9] aM. J. D. Low, V. V. S. Rao, *Canadian Journal of Chemistry* **1969**, *47*, 1281-1287; bM. J. D. Low, M. Hasegawa, *Journal of Colloid and Interface Science* **1968**, *26*, 95-101.
- [10] M. J. Fuchter, C. J. Smith, M. W. S. Tsang, A. Boyer, S. Saubern, J. H. Ryan, A. B. Holmes, *Chem. Comm.* **2008**, 2152-2154.
- [11] aA. Lesage, M. Lelli, D. Gajan, M. A. Caporini, V. Vitzthum, P. Miéville, J. Alauzun, A. Roussey, C. Thieuleux, A. Mehdi, G. Bodenhausen, C. Coperet, L. Emsley, *J. Am. Chem. Soc.* **2010**, *132*, 15459-15461; bA. J. Rossini, A. Zagdoun, M. Lelli, A. Lesage, C. Copéret, L. Emsley, *Accounts of Chemical Research* **2013**, *46*, 1942-1951.
- [12] aT. Gutmann, J. Liu, N. Rothermel, Y. Xu, E. Jaumann, M. Werner, H. Breitzke, S. T. Sigurdsson, G. Buntkowsky, *Chemistry – A European Journal* **2015**, *21*, 3798-3805; bF. A.

- Perras, T. Kobayashi, M. Pruski, *J. Am. Chem. Soc.* **2015**, *137*, 8336-8339; cT. Kobayashi, F. A. Perras, I. I. Slowing, A. D. Sadow, M. Pruski, *ACS Catalysis* **2015**, *5*, 7055-7062; dA. J. Rossini, A. Zagdoun, M. Lelli, J. Canivet, S. Aguado, O. Ouari, P. Tordo, M. Rosay, W. E. Maas, C. Copéret, D. Farrusseng, L. Emsley, A. Lesage, *Angew. Chem. Int. Ed.* **2012**, *51*, 123-127.
- [13] aS. Leonardelli, L. Facchini, C. Fretigny, P. Tougne, A. P. Legrand, *J. Am. Chem. Soc.* **1992**, *114*, 6412-6418; bM. Lelli, D. Gajan, A. Lesage, M. A. Caporini, V. Vitzthum, P. Miéville, F. Héroguel, F. Rascón, A. Roussey, C. Thieuleux, M. Boualleg, L. Veyre, G. Bodenhausen, C. Coperet, L. Emsley, *J. Am. Chem. Soc.* **2011**, *133*, 2104-2107.
- [14] A. Y. Nikonov, I. V. Sterkhova, N. F. Lazareva, *Russian Journal of General Chemistry* **2015**, *85*, 1866-1869.
- [15] B. Buszewski, M. Jaroniec, R. K. Gilpin, *Journal of Chromatography A* **1994**, *673*, 11-19.
- [16] K. Sugino, N. Oya, N. Yoshie, M. Ogura, *J. Am. Chem. Soc.* **2011**, *133*, 20030-20032.
- [17] Y. Furukawa, M. Ogura, *J. Am. Chem. Soc.* **2014**, *136*, 119-121.

Appendix A: Selected NMR spectra

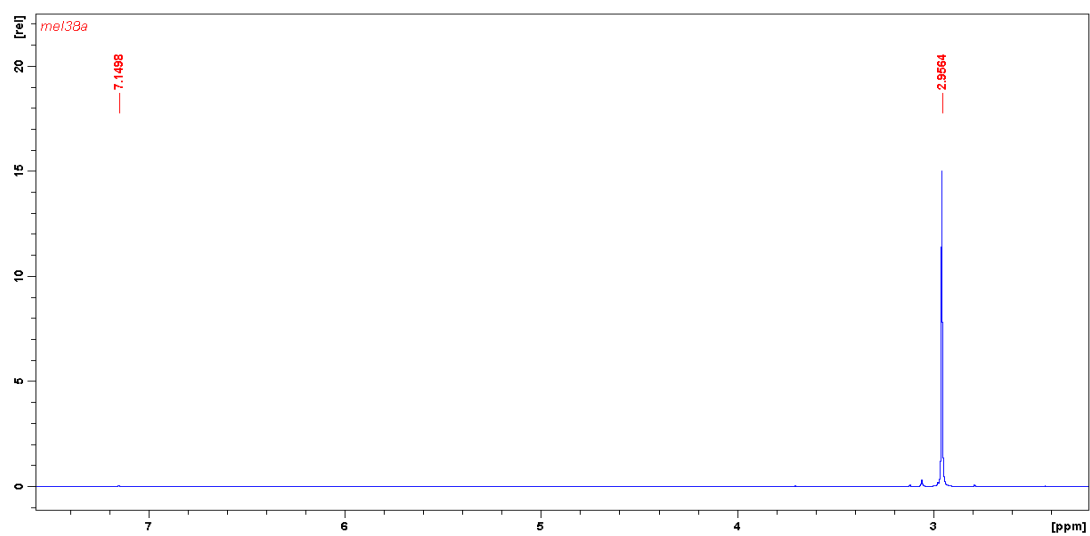


Figure A.1: ^1H NMR of $\text{Zr}(\text{NMe}_2)_4$ in C_6D_6

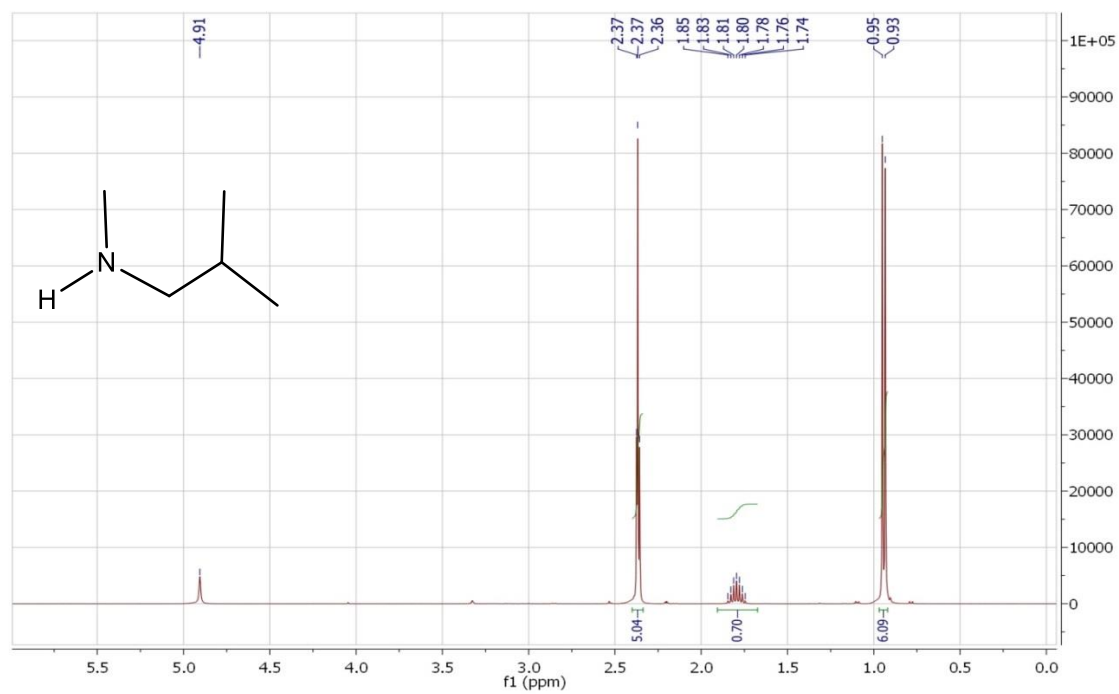


Figure A.2: ^1H NMR of N-methylisobutylamine on methanol- D_4

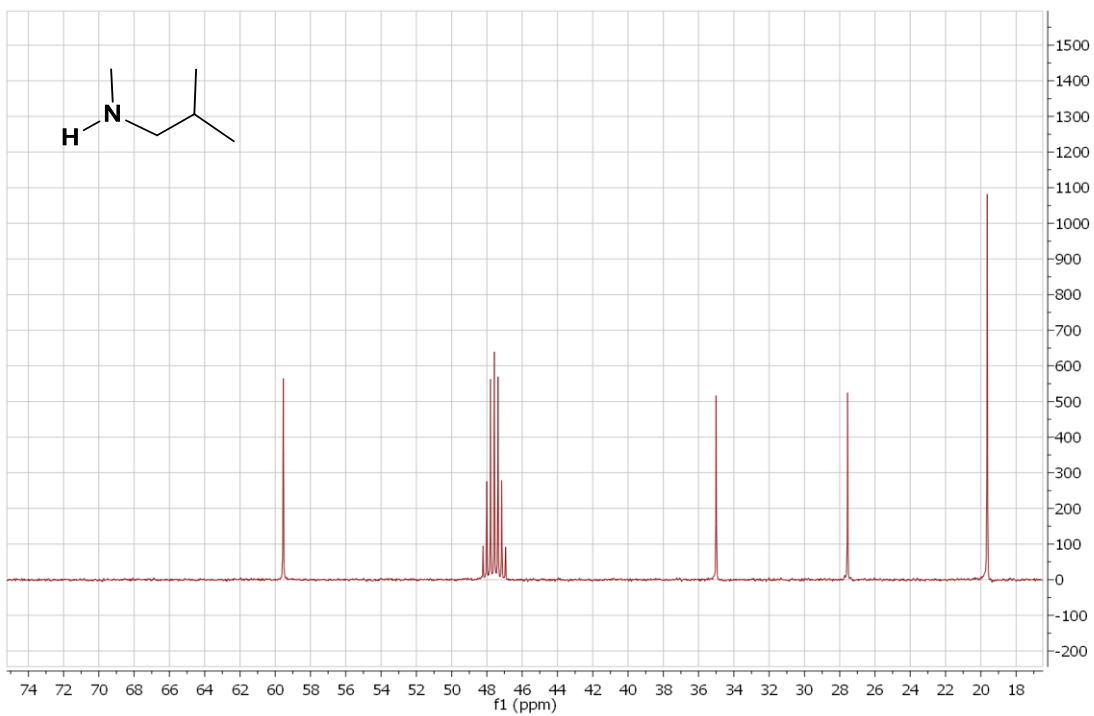


Figure A.3: ¹³C NMR of N-methylisobutylamine on methanol-D₄

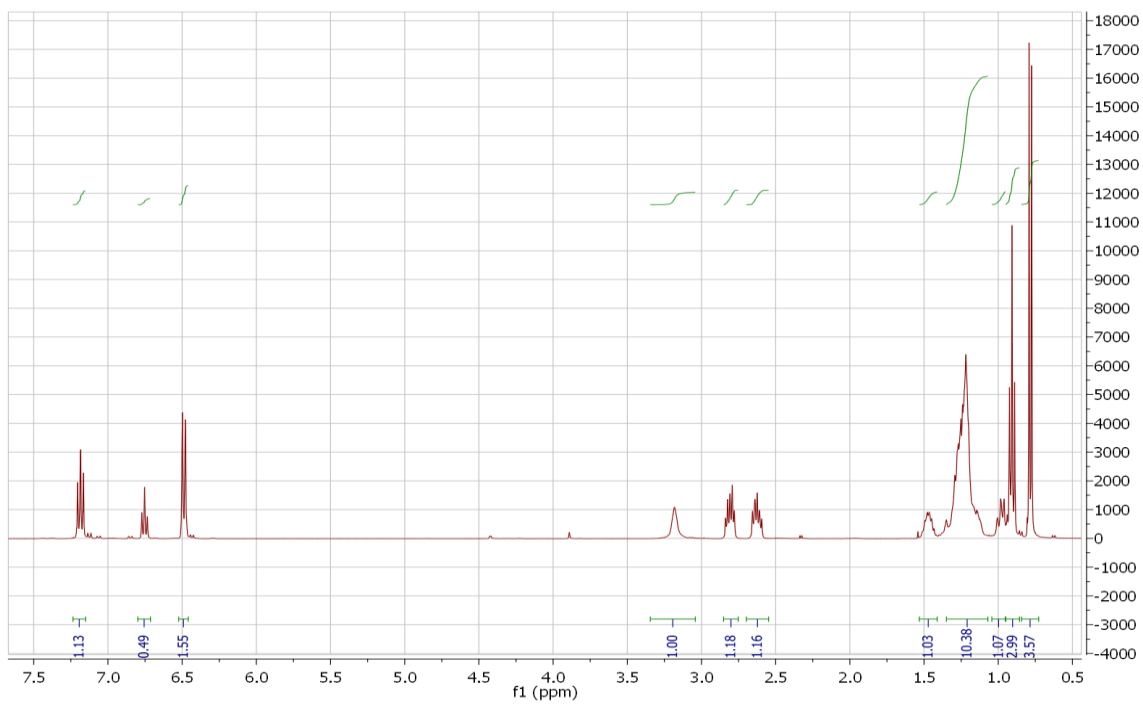


Figure A.3: ¹H NMR of the hydroaminoalkylated product (entry 1, table III.1) on C₆D₆

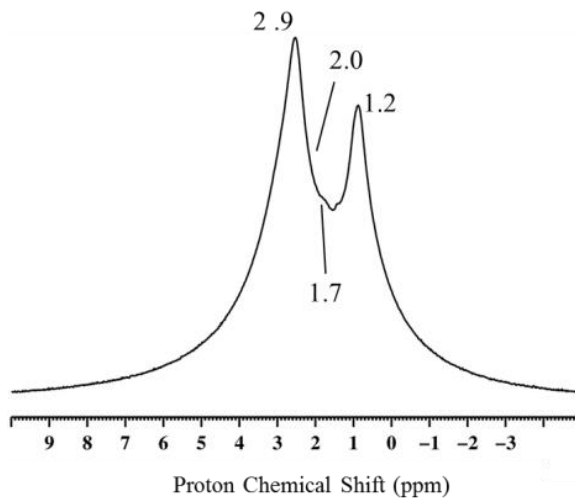


Figure A.4: ^1H SS NMR spectra of III.1 on SBA₇₀₀ surface

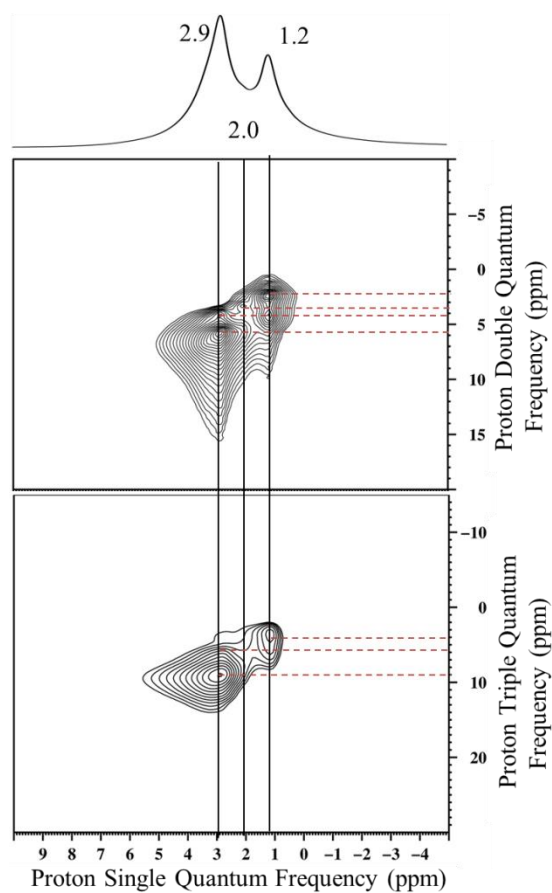


Figure A.5: ^1H MAS NMR, 2D contour plots of the aliphatic region of the DQ and TQ quantum proton SS-NMR correlation spectra of III.1 on SBA₇₀₀ surface

Appendix B: Selected GC-MS spectra

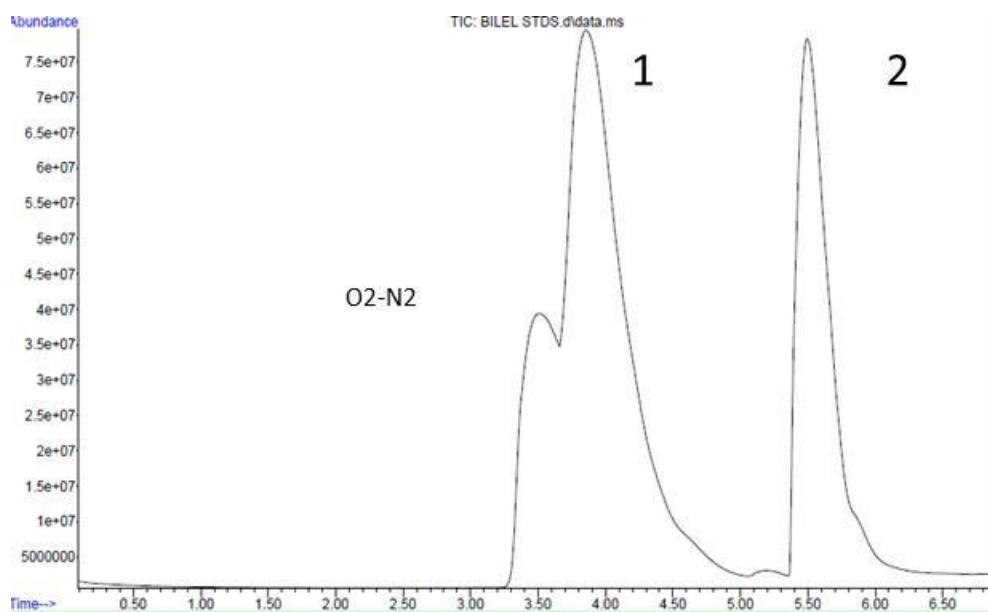


Figure B.1: GC/MS Characterization of the gas-phase products obtained after reaction of III.1 with HNMe_2+H_2

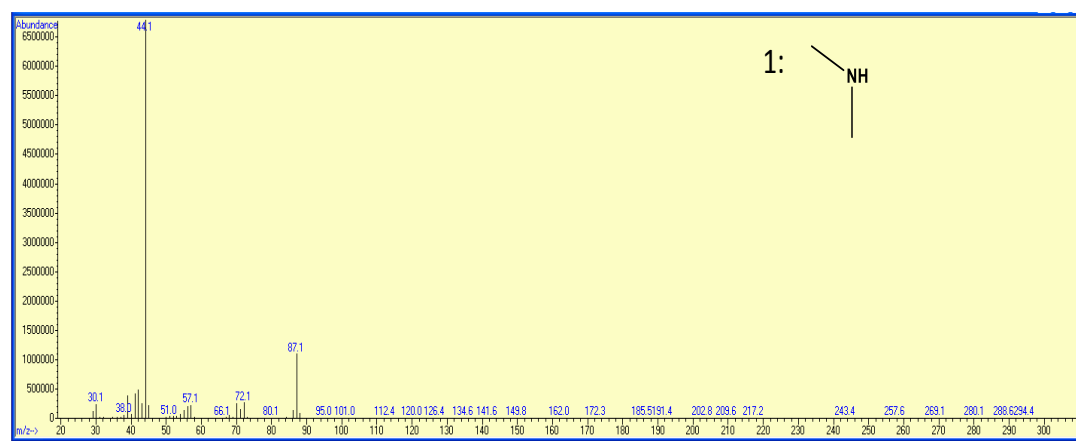


Figure B.2: Mass spectrum of diethylamide

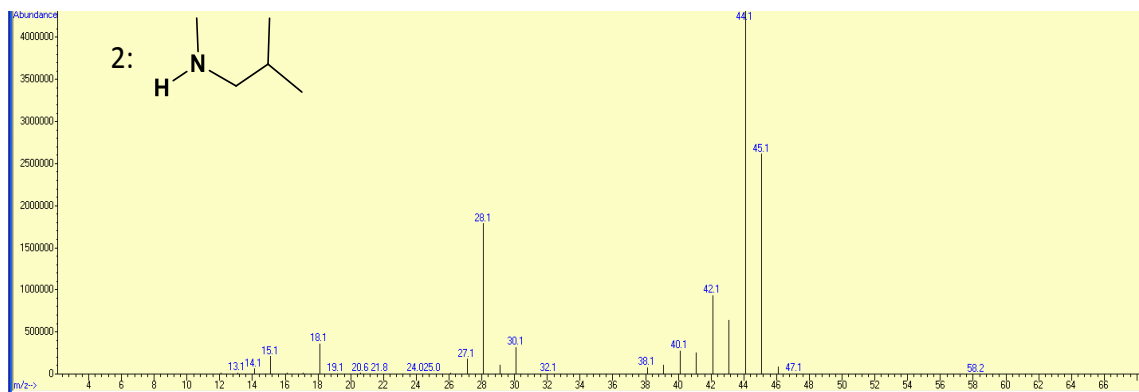


Figure B.3: Mass spectrum of 1-propanamine, N,2-dimethyl

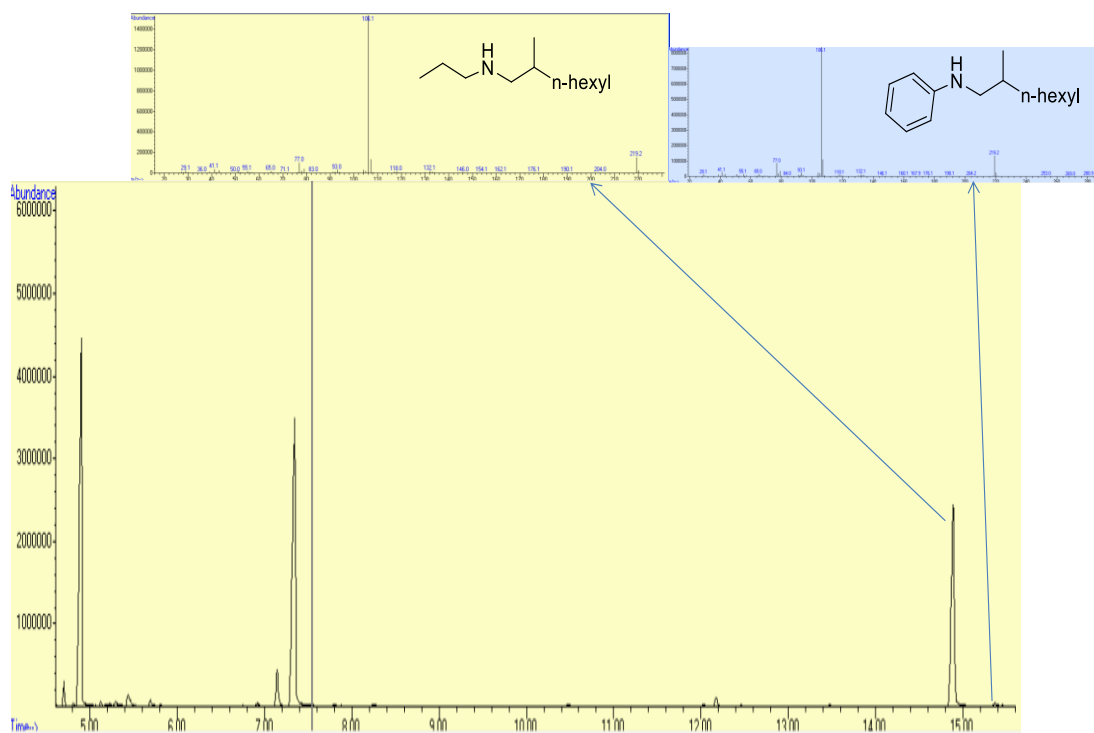


Figure B.4: GC/MS Characterization of the products obtained after reaction in table III.1 entry 9

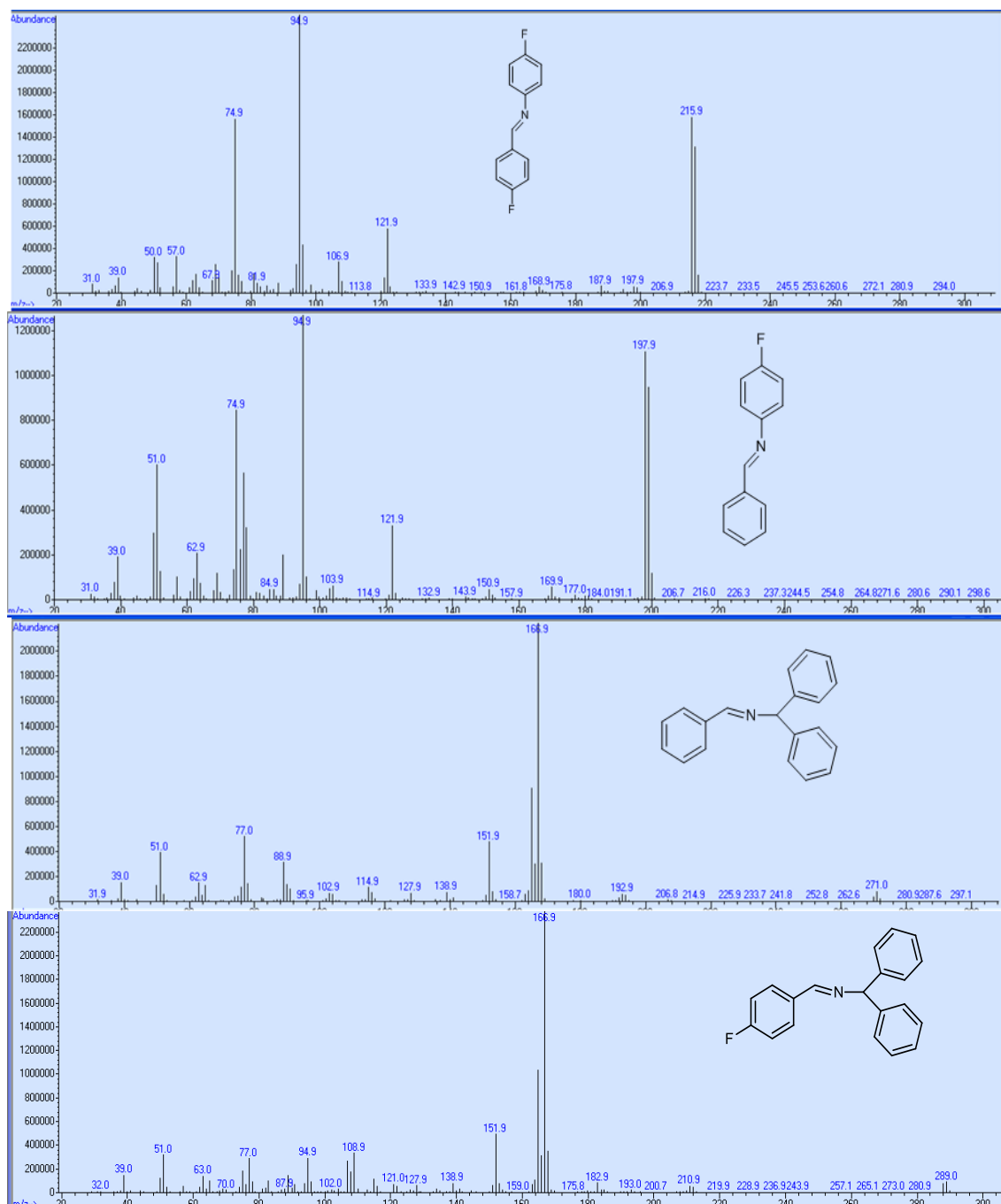


Figure B.5: GC/MS Characterization of the products obtained after reaction in table IV.2 entry 2

Appendix C: DFT calculated energies, frequencies, rate constants and optimized coordinates

We ran the following calculations using the split valence polarization basis set SVP as implemented in Gaussian09 (keyword : SVP), that is H[3s1p], C.[3s3p1d] and N[3s3p1d] for optimization and triple valence polarization basis sets as implemented in Gaussian09 (keyword: TZVP) for single point energies. For the Tantalum metal atom we used the basis set Ta:[6s5p3d] for valence electrons along with the Stuttgart effective core potential for core electrons. We present in table C.1 the calculated absolute and relative energies and frequencies of the transition states:

Table C.1: DFT calculated absolute and relative electronic and Gibbs free energies of the complexes at the PBE0-D3/TZVP/SDD with PBE/SVP/SDD thermal corrections at 298.15 K. Temperature corrections include both ZPE and TΔS term to get the free energy.

Me pathway					
Complex / Method	E(PBE/SVP/SDD) (au)	Thermal correction at 298.15 K (PBE/SVP/SDD) (au)	E(PBE0D3/TZVP/SDD) + Thermal corrections at 298.15 K (PBE/SVP/SDD) (au)	E(PBE0D3/TZVP/SDD) + Thermal corrections at 298.15 K (PBE/SVP/SDD) (kcal/mol) (Relative)	Transition states frequencies of vibration at PBE/SVP/SDD (cm-1)
1	-3890.008784	0.36916	-3892.7465467	0.00	*
2+HNMe2	-3889.9650347	0.347805	-3892.6965094	18.00	*
TS(1-2)	-3889.9532478	0.360996	-3892.6860721	32.83	-1352.7362
aryl	-326.2535836	0.108153	-326.6258371	*	*
HNMe2	-134.8734151	0.065045	-135.0448471	*	*

Ph pathway					
1-aryl+HNMe2	-4081.3889525	0.412268	-4084.3275367	0.00	*
TS(1-1b)	-4216.2440665	0.471071	-4219.3323289	*	-1207.8128
TS(1-1b)+HNMe2	-4081.3706514	0.406026	-4084.2874818	21.22	*
1b	-4081.3753903	0.416209	-4084.3269016	2.87	*
TS(1b-3)	-4081.3297627	0.40863	-4084.2759316	30.10	-1317.6529

3	-3946.4705975	0.331139	*	*	*
3+HNMe2	-4081.3440126	0.396184	-4084.2881019	14.65	*

Table C.2. Shows the calculated NMR normalized shifts for final compounds (2) and (3) with respect to tetramethylsilane (TMS). We optimized the geometry of the TMS at the PBE0/TZVP level. We evaluated NMR shifts of all our compounds including TMS at the PBE0/TZVP level from scalar relativistic ZORA Hamiltonian as from the ADF 2014 suite of programs.

Table C.2: Normalized DFT calculated ¹³C NMR shifts from scalar relativistic Hamiltonian at the PBE0/TZVP level of theory with respect to the reference 191.54 ppm and 31.49 ppm shifts respectively for Carbon and Hydrogen in TMS.

Atom type	Ta (2) NMR shifts(ppm)	Ta (3) NMR shifts(ppm)	Ta (2) normalized NMR shifts (ppm)	Ta (3) normalized NMR shifts(ppm)
Ta-HNMe2 ligand 1	143.96	144.45	47.58	47.09
Ta-HNMe2 ligand 2	143.2	141.72	48.34	49.82
Ta-HNMe2 ligand 3	138.28	137.54	53.26	54
Ta-HNMe2 ligand 4	149.52	150.091	42.02	41.45
Ta-HNMe2 ligands (average over 4)	*	*	47.8	48.08
Ta-CH2 (metallacycle)	140.504	133.28	61.06	58.26

The last section contains the optimized Cartesian coordinates for all the species at the PBE/SVP/SDD level involved in both Me and Ph pathways:

HNMe₂

```

C -31.683595 -0.010233 0.408171
H -31.507673 -0.193598 1.490761
N -30.843436 -0.888501 -0.382701
H -31.516622 1.088544 0.237777
H -32.753975 -0.224177 0.211373
C -29.424626 -0.630489 -0.231077
H -31.104714 -0.819512 -1.372698
H -29.110023 -0.852174 0.812229
H -29.107731 0.427240 -0.443515
H -28.840423 -1.298609 -0.896321

```

Aryl

```

C -6.90572 0.24378 0.46134
C -5.59590 0.73525 0.48391

```

C	-4.50524	-0.12803	0.21999
C	-7.14985	-1.10035	0.17860
C	-6.08481	-1.96152	-0.08327
C	-4.77301	-1.48071	-0.06281
H	-8.16530	-1.47466	0.16275
H	-7.73484	0.90951	0.66466
H	-5.46510	1.77889	0.70839
N	-3.13984	0.30978	0.22866
H	-6.27487	-3.00429	-0.30252
H	-3.95881	-2.16458	-0.26847
C	-2.68630	1.66313	0.48825
H	-2.40717	-0.39005	0.03439
H	-3.49134	2.38705	0.68494
H	-2.11396	2.02797	-0.38996
H	-2.01345	1.65716	1.37093

(1)

Si	4.112241	-2.205986	1.252074
Si	4.078071	2.303547	1.081820
Si	5.761941	0.008600	-0.353353
Si	2.419178	0.091416	2.682155
Si	1.911959	2.189888	-1.260343
O	3.017764	2.711853	-0.131002
O	3.287659	1.449586	2.267144
O	5.019787	-0.029331	-1.840327
O	5.328941	-1.331856	0.528881
O	3.334746	-1.265942	2.379701
O	3.032288	-2.726832	0.101011
O	1.005139	0.032778	1.824703
O	0.703233	1.329231	-0.528793
H	4.640378	3.541384	1.669095
Si	0.230133	-0.010272	0.348171
O	0.739958	-1.370578	-0.474100
O	5.322129	1.389595	0.460501
H	4.703471	-3.383918	1.927446
H	2.112319	0.145272	4.130323
O	-1.369354	-0.032150	0.565978
Si	1.957423	-2.300932	-1.095906
Ta	-3.350783	-0.006465	0.045410
H	1.382231	-3.536419	-1.678678
Si	3.602214	-0.099641	-2.706947
O	2.757725	-1.471949	-2.298379
H	7.230331	0.007865	-0.545198
O	2.681460	1.248943	-2.398564
H	1.330931	3.373303	-1.937134
H	3.923571	-0.144729	-4.152063
N	-3.702602	-0.923455	1.834121
C	-4.948905	-1.590219	2.191420

C	-2.792144	-0.926740	2.974539
N	-5.356607	0.108269	-0.438905
C	-6.129478	-0.744370	-1.324941
C	-6.235791	1.064952	0.222456
N	-3.041686	-1.202153	-1.538974
C	-2.757874	-2.621068	-1.414715
C	-2.932921	-0.694227	-2.892992
N	-3.216130	2.018741	-0.061499
C	-3.792813	2.847250	-1.105232
C	-2.433687	2.800489	0.884027
H	-2.588298	-1.970342	3.316101
H	-3.232942	-0.384283	3.846422
H	-1.826960	-0.459370	2.713499
H	-5.652956	-1.620247	1.340300
H	-5.459103	-1.084072	3.047851
H	-4.755344	-2.641778	2.515366
H	-6.995606	0.550359	0.860113
H	-6.804838	1.678727	-0.517582
H	-5.659807	1.754071	0.870275
H	-5.474175	-1.458827	-1.856315
H	-6.693083	-0.146336	-2.082937
H	-6.897909	-1.335368	-0.765344
H	-3.642552	-1.205110	-3.589481
H	-1.904558	-0.839672	-3.302358
H	-3.152355	0.393178	-2.930357
H	-2.886231	-2.954477	-0.365079
H	-1.707446	-2.850936	-1.711634
H	-3.434932	-3.234917	-2.057896
H	-1.551031	3.275635	0.391730
H	-3.046433	3.617944	1.335315
H	-2.048704	2.167542	1.705782
H	-4.420966	2.244154	-1.789071
H	-3.001148	3.348269	-1.713838
H	-4.433885	3.659359	-0.681586

TS(V.2-V.2b)

Si	4.782840	-2.296260	-0.207040
Si	4.646510	1.489390	2.251520
Si	6.396470	0.456990	-0.210220
Si	3.021190	-1.260660	2.252500
Si	2.517350	2.720710	0.221020
O	3.553560	2.492740	1.502750
O	3.901140	0.075810	2.707330
O	5.672870	1.225330	-1.494490
O	5.993710	-1.156150	-0.219790
O	3.922490	-2.194990	1.211190
O	3.768460	-2.059750	-1.502940
O	1.608480	-0.792381	1.522970

O	1.327680	1.568159	0.235600
H	5.180400	2.166400	3.455280
Si	0.869580	-0.034731	0.234300
O	1.410720	-0.740831	-1.174450
O	5.904290	1.153490	1.216290
H	5.389681	-3.643140	-0.310300
H	2.703320	-2.059340	3.458810
O	-0.742290	-0.141401	0.373430
Si	2.651170	-1.059120	-2.224330
Ta	-2.628150	-0.718371	-0.133560
H	2.113510	-1.735690	-3.427900
Si	4.263590	1.697660	-2.240250
O	3.386120	0.359190	-2.689870
H	7.866200	0.588981	-0.332050
O	3.367320	2.642690	-1.207920
H	1.901519	4.062760	0.337360
H	4.597860	2.485070	-3.448960
N	-4.549690	-1.257152	-0.634990
C	-5.459720	-0.449882	-1.442610
C	-5.215220	-2.494942	-0.249720
N	-2.056950	-2.660731	-0.193720
C	-4.670710	3.059608	-0.426770
C	-1.142859	-3.243021	0.778320
N	-2.339010	0.058679	-1.996900
C	-2.820890	-0.513271	-3.245030
C	-1.549720	1.251489	-2.268950
N	-2.978690	-0.685301	2.178300
C	-1.887980	-0.655351	3.151580
C	-4.115400	-1.408091	2.739070
H	-5.540260	-3.071982	-1.149410
H	-6.139700	-2.293142	0.342290
H	-4.550579	-3.136062	0.357460
H	-4.985140	0.495318	-1.761560
H	-6.376950	-0.183792	-0.870290
H	-5.788260	-1.011292	-2.350540
H	-2.167140	2.041809	-2.760020
H	-0.705450	1.019929	-2.961260
H	-1.118120	1.673659	-1.344750
H	-3.452510	-1.402701	-3.068660
H	-1.966520	-0.824061	-3.892690
H	-3.420240	0.223949	-3.831610
H	-3.899890	-2.495771	2.875610
H	-4.395740	-1.009651	3.744620
H	-5.003540	-1.322532	2.085510
H	-1.001560	-0.146311	2.732760
H	-1.571980	-1.681961	3.457580
H	-2.194180	-0.127761	4.087020
C	-4.528160	2.022408	0.529840
C	-5.701080	1.580738	1.192030

C	-6.957190	2.125198	0.887970
C	-7.083801	3.138158	-0.076920
C	-5.928381	3.602998	-0.726410
H	-5.616070	0.806738	1.968500
H	-7.847310	1.762788	1.426460
H	-8.068851	3.569698	-0.309990
H	-6.004971	4.403908	-1.479040
C	-2.346749	-3.599491	-1.264830
H	-3.082839	-3.183571	-1.977140
H	-2.755619	-4.559861	-0.868000
H	-1.422449	-3.851541	-1.837510
N	-3.267210	1.451019	0.845280
C	-2.210540	2.448939	1.055380
H	-1.915390	2.990969	0.129000
H	-1.299090	1.949729	1.429680
H	-2.529861	3.216659	1.796090
H	-1.591479	-4.140411	1.267970
H	-0.197479	-3.574731	0.285880
H	-0.872400	-2.516561	1.563920
H	-3.261690	0.525579	1.771120
H	-3.781231	3.439539	-0.950800

TS(V.2-V.3)

Si	4.193756	-1.041793	-2.227793
Si	4.030527	-1.146579	2.279439
Si	5.673536	0.543275	0.126148
Si	2.554397	-2.713891	-0.071008
Si	1.716000	1.057803	2.233893
O	2.842229	-0.068757	2.714314
O	3.390557	-2.342758	1.320287
O	4.853661	1.990384	0.125859
O	5.327762	-0.302592	-1.261594
O	3.463979	-2.281348	-1.396649
O	3.054101	0.068595	-2.707908
O	1.102508	-1.921689	-0.090935
O	0.566244	0.352124	1.274589
H	4.600659	-1.758686	3.501404
Si	0.209421	-0.517788	-0.106018
O	0.676003	0.398401	-1.420972
O	5.238932	-0.348855	1.459750
H	4.867024	-1.592390	-3.426218
H	2.320658	-4.175931	-0.110765
O	-1.369598	-0.865777	-0.183114
Si	1.885458	1.161032	-2.253814
Ta	-3.274530	-0.171531	-0.098448
H	1.321590	1.788945	-3.472044
Si	3.372591	2.746283	0.089087
O	2.566317	2.350829	-1.309183

H	7.128373	0.814348	0.177771
O	2.474321	2.290935	1.410974
H	1.064467	1.623766	3.438683
H	3.580578	4.212223	0.126993
N	-3.814013	-1.738619	-1.153075
C	-4.718939	-0.930110	-1.927619
C	-3.386894	-3.064468	-1.518630
N	-5.389477	0.641603	0.206666
C	-5.786614	2.035964	0.169191
C	-6.328789	-0.190004	0.944703
N	-2.804119	1.585596	-0.963948
C	-2.652099	1.849755	-2.380680
C	-2.390742	2.701926	-0.128449
N	-3.159881	-0.363213	1.918374
C	-3.663731	0.597738	2.880536
C	-2.489429	-1.480591	2.565927
H	-3.007963	-3.086162	-2.567659
H	-4.222771	-3.798309	-1.447858
H	-2.567352	-3.398800	-0.851398
H	-5.170409	0.090116	-1.033795
H	-5.762354	-1.331808	-1.939905
H	-4.395694	-0.723043	-2.975656
H	-7.376244	-0.055891	0.578438
H	-6.338364	0.035382	2.038615
H	-6.067041	-1.263169	0.836024
H	-5.183587	2.586909	-0.579484
H	-5.664158	2.560431	1.151758
H	-6.862275	2.146884	-0.111619
H	-2.974951	3.627336	-0.352385
H	-1.311517	2.942001	-0.280643
H	-2.525764	2.474143	0.949567
H	-2.985332	0.984051	-2.985670
H	-1.585741	2.052925	-2.637074
H	-3.251019	2.737265	-2.700102
H	-1.601711	-1.136108	3.149914
H	-3.173164	-2.006518	3.274632
H	-2.128462	-2.216797	1.823035
H	-4.210421	1.417840	2.377039
H	-2.831537	1.050792	3.473473
H	-4.364711	0.128459	3.613243

(V.2b)

Si	4.721098	0.487950	-2.489603
Si	4.545376	-2.023530	1.256642
Si	6.225262	0.528542	0.318170
Si	3.037308	-2.060885	-1.552142
Si	2.282448	-0.099929	2.438163
O	3.393188	-1.318657	2.226653

O	3.855398	-2.510215	-0.175408
O	5.410522	1.754026	1.090916
O	5.891726	0.567704	-1.310425
O	3.956517	-0.986935	-2.427099
O	3.612502	1.706718	-2.267926
O	1.588633	-1.360918	-1.141305
O	1.118650	-0.187818	1.254892
H	5.106600	-3.204441	1.950839
Si	0.776453	-0.138697	-0.370384
O	1.237661	1.325690	-0.995922
O	5.766672	-0.937726	0.953144
H	5.359770	0.647730	-3.815384
H	2.779210	-3.263257	-2.376164
O	-0.831808	-0.333635	-0.599197
Si	2.456243	2.411697	-1.304189
Ta	-2.695125	-0.569045	-0.058357
H	1.891418	3.587926	-2.003359
Si	3.960670	2.454241	1.502709
O	3.141942	2.906018	0.127882
H	7.680691	0.710782	0.517908
O	3.042971	1.376604	2.375891
H	1.635706	-0.258343	3.760658
H	4.217153	3.654533	2.330187
N	-2.870319	-2.117658	1.249325
C	-3.912484	-3.124570	1.304690
C	-1.904953	-2.269436	2.330382
N	-3.930826	0.815333	-1.028800
C	-5.129127	1.350584	-0.566340
N	-2.771605	0.685462	1.576300
C	-2.354786	2.062320	1.341078
C	-3.408234	0.554217	2.872086
H	-1.404984	-3.265839	2.268275
H	-2.379219	-2.205663	3.340043
H	-1.117500	-1.491607	2.278727
H	-4.592854	-3.036459	0.435641
H	-4.529653	-3.029945	2.232478
H	-3.485711	-4.156693	1.311409
C	-5.827952	0.703565	0.492279
C	-5.719670	2.524453	-1.111883
H	-2.693039	0.774849	3.702111
H	-4.263703	1.263306	2.984010
H	-3.801860	-0.469197	3.017244
H	-1.759237	2.155992	0.409121
H	-1.711844	2.427271	2.177082
H	-3.226082	2.756675	1.257086
C	-7.012598	1.231368	1.015777
C	-6.914066	3.038960	-0.586507
C	-7.567171	2.409906	0.484790
H	-5.231053	3.052998	-1.941963

H	-7.339274	3.955199	-1.026171
H	-5.434550	-0.246636	0.891778
H	-7.521822	0.702070	1.836685
H	-8.504729	2.819568	0.888966
C	-3.442431	1.269288	-2.324996
H	-3.108532	2.332743	-2.301419
H	-4.214304	1.176949	-3.124483
H	-2.570009	0.658918	-2.635287
N	-3.367180	-1.857126	-1.532857
C	-2.572552	-3.055303	-1.768297
C	-4.592468	-1.886555	-2.305499
H	-5.196975	-0.979244	-2.120861
H	-5.223517	-2.775759	-2.052368
H	-4.384129	-1.956710	-3.401230
H	-1.619275	-3.029895	-1.202561
H	-2.312943	-3.150282	-2.850063
H	-3.113770	-3.990421	-1.479919

TS(V.2b-V.4)

Si	-4.137509	1.809442	-1.885615
Si	-4.278183	0.635022	2.465122
Si	-5.997734	-0.094996	-0.127774
Si	-2.422490	2.525754	0.713006
Si	-2.321866	-1.824185	1.852841
O	-3.268148	-0.678540	2.599356
O	-3.428975	1.951053	1.909195
O	-5.391856	-1.583460	-0.556235
O	-5.450038	1.063159	-1.186813
O	-3.256269	2.605454	-0.724366
O	-3.186618	0.674492	-2.642507
O	-1.111542	1.526082	0.557816
O	-1.002038	-1.111664	1.146700
H	-4.842146	0.951169	3.797243
Si	-0.446324	0.071034	0.108263
O	-0.953117	-0.311087	-1.432968
O	-5.522541	0.281738	1.419669
H	-4.616466	2.786475	-2.889519
H	-1.967012	3.885126	1.083702
O	1.170549	0.167999	0.165027
Si	-2.191022	-0.647021	-2.480896
Ta	3.030501	-0.576109	-0.017120
H	-1.626127	-0.987013	-3.808085
Si	-4.052591	-2.553000	-0.730892
O	-3.067783	-1.949892	-1.927504
H	-7.476564	-0.141749	-0.183485
O	-3.217484	-2.629574	0.704065
H	-1.859817	-2.800375	2.867219
H	-4.489963	-3.916388	-1.109078

N	3.709964	1.250865	-0.445232
C	4.647088	0.659881	-1.372398
C	3.521156	2.622988	-0.257134
N	5.046592	-1.649931	0.023856
C	5.351797	-2.947848	-0.546142
C	6.009908	-1.238895	1.034337
N	2.493720	-1.825761	-1.494499
C	2.372999	-1.509310	-2.903801
C	1.942798	-3.124433	-1.143692
N	2.886216	-1.127171	1.931549
C	3.256380	-2.419049	2.476941
C	2.261077	-0.275602	2.933332
H	4.941257	-0.640704	-0.914226
H	5.705889	0.937762	-1.154221
H	4.430084	0.851366	-2.447626
H	7.058714	-1.294617	0.651996
H	5.968241	-1.870354	1.954331
H	5.822577	-0.191779	1.351991
H	4.735647	-3.125014	-1.449772
H	5.166546	-3.797469	0.160402
H	6.425631	-3.020792	-0.846121
H	2.442572	-3.953539	-1.700293
H	0.851681	-3.173269	-1.372757
H	2.058877	-3.332681	-0.059135
H	2.797590	-0.510917	-3.126201
H	1.303452	-1.500148	-3.220315
H	2.907762	-2.256196	-3.539450
H	1.284688	-0.695770	3.276161
H	2.917594	-0.169179	3.829117
H	2.066473	0.739816	2.540271
H	3.760648	-3.044615	1.715973
H	2.358494	-2.975539	2.842345
H	3.950742	-2.320711	3.346320
C	4.381593	3.565236	-0.873601
C	2.456699	3.102705	0.548775
C	4.188855	4.939935	-0.674791
H	5.204540	3.210009	-1.510452
C	3.139966	5.408246	0.131681
H	4.871659	5.654428	-1.161031
C	2.275379	4.477735	0.735442
H	1.754708	2.381892	0.989118
H	2.992913	6.487925	0.284586
H	1.437882	4.828473	1.359035

(V.3)

Si	3.623319	-3.579806	-2.324465
Si	0.011597	-4.021075	0.340601
Si	2.885179	-5.395181	0.198044

Si	0.757056	-2.206120	-2.176934
Si	1.185042	-1.777891	2.294121
O	0.236917	-2.949906	1.591078
O	-0.033777	-3.203959	-1.105718
O	3.678671	-4.597577	1.421540
O	3.435268	-4.856224	-1.275195
O	2.135672	-2.957884	-2.728971
O	4.557884	-2.401264	-1.617790
O	1.148485	-0.777432	-1.435977
O	1.388907	-0.508340	1.248502
H	-1.272943	-4.731143	0.536254
Si	1.921284	0.053600	-0.223905
O	3.560242	-0.210470	-0.346328
O	1.247791	-5.133867	0.321624
H	4.295788	-4.060469	-3.553020
H	-0.134037	-1.935596	-3.328314
O	1.584981	1.642533	-0.360269
Si	4.784733	-1.329230	-0.366440
Ta	1.839703	3.581890	0.014602
H	6.075753	-0.629676	-0.560749
Si	4.052344	-3.153229	2.155697
O	4.828012	-2.155754	1.076240
H	3.152322	-6.846999	0.312795
O	2.662834	-2.423423	2.704147
H	0.515990	-1.294419	3.524051
H	4.947700	-3.413406	3.305911
N	1.039536	4.739269	-1.422606
C	1.639427	4.817674	-2.747635
C	-0.140949	5.578480	-1.293714
N	3.776220	3.701361	-0.195696
C	4.997699	3.259806	-0.811285
N	0.820605	3.888007	1.715835
C	1.117250	4.398600	3.035421
C	-0.536685	3.364309	1.594932
H	-0.937507	5.284869	-2.019570
H	0.101257	6.650632	-1.489888
H	-0.566593	5.516487	-0.273275
H	2.540034	4.174686	-2.816245
H	1.951372	5.861454	-2.993086
H	0.926486	4.486891	-3.540311
H	5.713889	2.872051	-0.049204
H	5.509519	4.093084	-1.349039
H	4.799716	2.443861	-1.536940
H	-0.725769	2.526533	2.307591
H	-1.305912	4.152482	1.779337
H	-0.726553	2.959681	0.573100
H	2.169265	4.733573	3.085861
H	0.951247	3.623781	3.822510
H	0.463659	5.267002	3.291508

C	3.585302	4.637453	0.860992
H	4.021911	4.365547	1.850995
H	3.759978	5.712469	0.618408

(V.4)

Si	-2.682049	-2.595286	-2.255269
Si	-0.701939	-5.934069	0.049268
Si	0.127850	-4.096394	-2.433146
Si	-3.510326	-4.430907	0.218126
Si	0.575048	-3.796566	2.050001
O	0.143275	-5.205901	1.282047
O	-2.322438	-5.593592	0.204785
O	1.142613	-3.006178	-1.695462
O	-1.314429	-3.359933	-2.810042
O	-3.510648	-3.603521	-1.223082
O	-2.266398	-1.200992	-1.454904
O	-3.247711	-3.371591	1.474377
O	-0.789303	-3.010804	2.589624
H	-0.505920	-7.399310	0.126062
Si	-2.238141	-2.285489	2.223277
O	-1.983871	-0.972159	1.233834
O	-0.147904	-5.383906	-1.417455
H	-3.550983	-2.258247	-3.404948
H	-4.825891	-5.083536	0.404331
O	-1.619492	1.163688	-0.331127
Si	-1.414248	-0.456020	-0.246279
Ta	-2.299333	2.949414	0.087459
H	-2.874587	-1.814110	3.475322
Si	1.399034	-1.963732	-0.426132
O	0.193693	-0.822700	-0.380115
H	0.761999	-4.586736	-3.677428
O	1.412683	-2.814569	1.003899
H	1.436001	-4.119341	3.210091
H	2.704913	-1.291052	-0.603444
N	-4.316292	2.867603	-0.009359
C	-5.343318	3.554950	-0.760143
C	-4.873383	1.921474	0.949870
N	-1.143511	4.333421	-0.742598
C	0.053430	5.031685	-0.813785
N	-1.887984	3.486060	1.984779
C	-1.895574	2.463513	3.022718
C	-1.745922	4.831837	2.513038
H	-5.498388	1.145917	0.445106
H	-5.509433	2.421311	1.720605
H	-4.076266	1.366386	1.495310
H	-4.893067	4.279299	-1.462620
H	-6.045190	4.108482	-0.088624
H	-5.962847	2.839227	-1.353058

C	0.273318	5.999270	-1.825593
C	1.080537	4.794393	0.136451
H	-2.602921	5.110843	3.172860
H	-0.816485	4.931194	3.122363
H	-1.688001	5.568771	1.688566
H	-1.957242	1.441645	2.590284
H	-2.748789	2.585259	3.733885
H	-0.955994	2.499564	3.624231
C	-2.297520	4.375323	-1.575700
C	1.481959	6.708022	-1.876379
C	2.281178	5.509401	0.074109
C	2.492846	6.472065	-0.930601
H	0.912880	4.038731	0.919618
H	3.067632	5.311080	0.819390
H	-0.517893	6.182618	-2.568067
H	1.635302	7.455962	-2.670344
H	3.440299	7.029645	-0.976606
H	-2.191842	3.962571	-2.606478
H	-2.893447	5.316431	-1.567061

LIST OF PUBLICATIONS

- 7. **Bilel Hamzaoui**, Jeremie D. A. Pelletier, Edy Abou-Hamad and Jean-Marie Basset. Chem. Comm. **2016**, 52, 4617--4620. Well-defined silica-supported zirconium–imido complexes mediated heterogeneous imine metathesis
- 6. **Bilel Hamzaoui**, Jérémie D. A. Pelletier, Edy Abou-Hamad, Yin Chen, Mohamed El Eter, Edrisse Chermak, Luigi Cavallo, and Jean-Marie Basset. Chemistry - A European Journal **2016**, 22,1–10.

Solid-State NMR and DFT studies of well-defined silica-supported tantalaziridine formation: From synthesis to catalytic application.

- 5. **Bilel Hamzaoui**, Jérémie D. A. Pelletier, Mohamad El Eter, Yin Chen, Edy Abou-Hamada and Jean-Marie Basset. Advanced synthesis and catalysis. **2015**, 357, 3148 – 3154, Isolation and characterization of well-defined silica-supported azametallacyclopentane: a key intermediate in catalytic hydroaminoalkylation reactions
- 4. **Bilel Hamzaoui**, Dr. Mohamad El Eter, Dr. Edy Abou-hamad, Dr. Yin Chen, Dr. Jérémie D. A. Pelletier and Prof. Jean-Marie Basset. Chem. Eur. J. **2015**, 21, 4294 – 4299 Well-Defined Single-Site Monohydride Silica-Supported Zirconium from Azazirconacyclopropane
- 3. Yin Chen, Edy Abou-hamad, Ali Hamieh, **Bilel Hamzaoui**, Lyndon Emsley, and Jean-Marie Basset J. Am. Chem. Soc., **2015**, 137 (2), pp 588–591. Alkane Metathesis with the Tantalum Methylidene $[(\equiv\text{SiO})\text{Ta}(\text{=CH}_2)\text{Me}_2]/[(\equiv\text{SiO})_2\text{Ta}(\text{=CH}_2)\text{Me}]$ Generated from Well-Defined Surface Organometallic Complex $[(\equiv\text{SiO})\text{Ta}^V\text{Me}_4]$
- 2. Yin Chen, Bin Zheng, Edy Abou-Hamad, Ali Hamieh, **Bilel Hamzaoui**, Kuo-wei Huang and Jean-marie Basset. Chem. Commun., **2014**, 50, 11721—11723. The use of a well-defined surface organometallic complex as a probe molecule: $[(\text{SiO})\text{TaVCl}_2\text{Me}_2]$ shows different isolated silanol sites on the silica surface
- 1. Mohamad El Eter, **Bilel Hamzaoui**, Edy Abou-Hamad, Jeremie D. A. Pelletier and Jean-Marie Basset. Chem. Commun., **2013**, 49, 4616—4618. Well-defined azazirconacyclopropane complexes supported on silica structurally determined by 2D NMR comparative elucidation